

# **Manipulating Terahertz Radiation Using Nanostructures**

*A thesis submitted for the partial fulfilment of the  
requirements for the degree of*

**Doctor of Philosophy (Science)**

in

**Physics (Experimental)**

By

**Debanjan Polley**

**Department of Physics  
University of Calcutta**

**2016**

*dedicated to my parents...*

# Abstract

---

---

With the increasing popularity of terahertz (THz) frequency band and the unforeseen development in THz instrumentation in recent years, it is imperative to indulge in the study of THz devices and the theoretical interpretation of their performances. The present thesis is devoted in understanding different possible ways of using nanostructures and their composites in the passive modulation of the response in the THz frequency range. A new type of low-cost durable THz polarizer is demonstrated using magnetically aligned nickel nanostructures with tunable degree of polarization and frequency bandwidth. THz electromagnetic shielding effectiveness (SE) of single walled carbon nanotubes (SWNT)/polymer composite films is studied and its relation with the weight fraction of SWNT inclusion is established. The modification of the THz properties of composite materials is thoroughly investigated by varying the material parameters and morphology. We have established that while the real conductivity (also SE) can be increased up to  $\sim 80\%$  by simply changing the average length and weight fraction of the SWNT inside the polymer matrix, it can be tuned in a minuscule range ( $\pm 15\%$ ) by decorating the sidewalls of SWNT with gold nanoparticles (AuNP). The results are discussed in the light of a modified universal di-electric relaxation (UDR) model. The intrinsic THz conductivity and SE of self-standing multi-walled carbon nanotubes (MWNT) is studied as a function of MWNT structure parameters and the results are discussed to shed some light on the controversial origin of the THz conductivity peak (TCP) in carbon nanotubes (CNT). The intrinsic conductivity spectra are analysed using a combination of Maxwell-Garnett (MG) effective medium theory (EMT) and Drude-Lorentz (DL) model. The results indicate that the TCP arises mainly due to the surface plasmon resonance along the length of the MWNT and does not depend systematically on MWNT diameter. We have also performed a detailed analysis on the different contribution (reflection, absorption or multiple internal reflection) of shielding to the total SE and its dependence on the length and diameter of MWNT. It is found that the mechanism of shielding can be tuned significantly upon MWNT diameter variation. Lastly, the effect of oxidation on the THz conductivity of copper (Cu) thin films is studied. The conductivity spectra are analysed using a Drude model with reduced d.c. conductivity and increased scattering rate. The findings of this thesis open up exciting possibilities of the realization of new types of THz opto-electronic devices for the passive manipulation of THz radiation. The detailed study of THz conductivity and SE properties of CNT composites may lead to the better understanding of their performances in THz frequency range.

# Acknowledgement

---

---

I would graciously take this pleasant opportunity to acknowledge a lot of nice people who helped and encouraged me in one or another way during my PhD and without their help this work could not have been completed.

I am heartily thankful to my supervisor, **Dr. Rajib Kmar Mitra** and my co-supervisor, **Prof. Anjan Barman** for providing me the opportunity to work in their lab and guiding me to accomplish my goal. Their contagious encouragement, continuous support, numerous valuable discussions, helpful suggestions and insightful comments helped me to grow as a researcher and embrace my job whole-heartedly. Besides being patient guides and wonderful teachers, they are great human being and possess a beautiful sense of humour. It is always satisfying to talk with them, listen their views in different aspects of science and life as well. It has been a real privilege to work with both of you for five long years.

I would like to thank my labmates from “**THz Spectroscopy Lab**” and “**Ultrafast Nanomagnetism Lab**” for their supports and unconditional help. I would like to thank **Semanti di** for helping in my projects, teaching me to prepare presentable graphs, slides and to write scientific reports with all her love and care. I would like to thank **Susmita di** for her never ending enthusiasm in my research works, for always encouraging me to do well in life and above all for always believing in me. Again a big thanks to her for proof-checking my thesis. I would like to thank **Animesh da** and **Nirnay** for all those cheerful discussions and for helping me to understand THz spectroscopy in chemist’s point of view. I would like to thank **Dr. Dipak Das** for the fruitful discussions on lasers, optics and their alignments. I would like to thank **Dr. Jaivardhan Sinha** and **Samiran** for preparing thin films and lithographically patterned structures. I would like to thank **Arnab**, who is also my M.Sc. batch-mate, for all his helps. I would like to thank **Arindam, Debashis, Neeraj, Kallol, Chandrima, Sucheta, Santanu, Avinash** and **Kartik** for creating a cheerful and friendly lab environment. **Arnab** and **Santanu** are also good table tennis players and we spent a lot of evenings in the TT room. They are a great bunch of guys and I am really happy to share the labs with them.

I would like to thank *Carnival Cinemas* for all those wonderful and not-so-wonderful movie shows and *ABCOS* for those special and not-so-special dinners.

I would like to thank my friends at S. N. Bose National Centre for Basic Sciences; **Arijit** (now at SINP), **Arghya**, **Biplab**, **J.B.** (now in Germany), **Subhashis**, and **Sayani**. I really enjoyed spending those beautiful moments with them. I would also like to thank my friends **Arnab**, **Arpan**, **Abhrajit**, **Sannak**, **Subhojit** and **Nabadyuti**. We do not meet that much as we all are busy in pursuing our dreams in different parts of India, but we maintain a healthy and cheerful relationship.

A special thanks to my parents for their unconditional love, support and guidance throughout my life. They are the biggest inspiration of my life. They sacrificed a lot for me and I am indebted to them. I would like to thank **Kritanjan** (my brother) for being the perfect sibling; respecting me and pulling my leg at the same time.

Many great thanks to my childhood friend and colleague **Ishita** (who also happens to be my girlfriend) for always being there for me through the ups and downs of my life, for encouraging me to be myself, for those lovely moments, for all her love, for all those wonderful fights we had and for accepting me with all my madness. A special thanks to her for helping me in my last minute proof checking.

I would like to acknowledge the financial support of S. N. Bose National Centre for Basic Sciences and its common research facilities for all the basic characterization of the samples.

# LIST OF PUBLICATIONS

---

---

## Included in this thesis

1. "Polarizing effect of aligned nanoparticles in terahertz frequency region", **D. Polley**, A. Ganguly, A. Barman, and R. K. Mitra; *Optics Letters* 38, **2754** (2013).
2. "EMI shielding and conductivity of carbon nanotube-polymer composites at terahertz frequency", **D. Polley**, A. Barman, and R. K. Mitra; *Optics Letters* 39, **1541** (2014).
3. "Controllable terahertz conductivity in single walled carbon nanotube/polymer composites", **D. Polley**, A. Barman, and R. K. Mitra; *Journal of Applied Physics* 117, **023115** (2015).
4. "Length Dependent Terahertz Conductivity and Shielding Effect of Self-Standing Multi-walled Carbon Nanotubes Films" by **D. Polley**, A. Barman and R. K. Mitra (Manuscript to be submitted)
5. "Diameter Dependent Shielding Effectiveness and Terahertz Conductivity of Multi-walled Carbon Nanotubes", **D. Polley**, Kumar Neeraj, A. Barman and R. K. Mitra (Accepted for publication)
6. "THz Conductivity Engineering in Surface Decorated Carbon Nanotube Films" by **D. Polley**, A. Patra, A. Barman and R. K. Mitra (Manuscript being prepared)

## Not included in this thesis

7. "Magnetization reversal dynamics in Co nanowires with competing magnetic anisotropies", S. Pal, S. Saha, **D. Polley**, and A. Barman; *Solid State Communications* 151, **1994** (2011).
8. "Dielectric relaxation of the extended hydration sheathe of DNA in the THz frequency region", **D Polley**, A. Patra, and R. K. Mitra; *Chemical Physics Letters* 586, **143** (2013).
9. "Ultrafast Dynamics and THz Oscillation in [Co/Pd]<sub>8</sub> Multilayers" by S. Pal, **D. Polley**, R. K. Mitra and A. Barman; *Solid State Communication* 221, **50** (2015).

## Conference Proceedings

1. "Modulating Conductivity of Au/CNT composites in THz Frequency Range: A THz Resistor", **D.Polley**, A. Patra, A. Barman, and R. K. Mitra, *IRMMW\_THz 2014*, The University of Arizona, Tucson, USA, 14-19 September, 2014. **[Oral]**

2. "Controlling Terahertz Conductivity in SWNT/Polymer Composites", R. K. Mitra, **D. Polley**, and A. Barman, *IRMMW\_THz 2015*, The Chinese University of Hong Kong, Hong-Kong, 23-28 August, 2015. **[Poster]**
3. "Nickel nanochain composite: An improved terahertz shielding material", **D. Polley**, A. Barh, A. Barman, and R. K. Mitra, *2015 Applied Electromagnetic Conference (AEMC 2015)*, IIT Guwahati, Assam, 18-21 December, 2015. **[Oral]**

# Some Useful Abbreviations

---

---

2D: two-dimensional	LN: lithium niobate
a.c.: alternating current	LT-GaAs: low temperature grown GaAs
ADC: analog to digital converter	MG: Maxwell-Garnett
AR: aspect ratio	MHz: megahertz ( $10^6$ Hz)
ARC: anti-reflection coating	MWNT: multi walled carbon nanotubes
AuNP: gold nanoparticles	NiNC: nickel nanochains
BG: Bruggeman	NiNP: nickel nanoparticles
BSE: back scattered electrons	PBS: polarizing beam splitter
BSP: back substrate polarizer	PC: photo conductive
CCD: charge coupled device	PPLN: periodically poled lithium niobate
CNF: carbon nanofiber	PVA: poly vinyl alcohol
CNT: carbon nanotubes	QCL: quantum cascade laser
CVD: chemical vapour deposition	QS: quasi space
d.c.: direct current	RF: radio frequency
DI: de-ionized	rGO: reduced graphene oxide
DL: Drude-Lorentz	S/N: signal to noise
DOP: degree of polarization	SE: shielding effectiveness
DSO: digital storage oscilloscope	SEM: scanning electron microscope
DWNT: double walled carbon nanotubes	SHG: second harmonic generation
EBSD: diffracted backscattered electrons	SI: semi insulating
EDX: energy dispersive x-ray analysis	SP: surface plasmon
EG: ethylene glycol	SVMFAF: spatially moving average filter
EMI: electromagnetic interference	SWNT: single walled carbon nanotubes
EMIS: electromagnetic interference shielding	TCP: terahertz conductivity peak
EMT: effective medium theory	TEM: transmission electron microscope
ER: extinction ratio	TES: terahertz emission spectroscopy
FFT: fast Fourier transform	THz: terahertz ( $10^{12}$ Hz)
FP: Fabry Perot	THz-TDS: THz time domain spectroscopy
FSP: free standing polarizer	TRTS: THz time resolved spectroscopy (optical pump-THz probe)
FTIR: Fourier transform infrared spectroscopy	TV: total variation
GHz: gigahertz ( $10^9$ Hz)	UHV: ultra-high vacuum
GO: graphene oxide	UV: ultra-violet
HDPE: high density polyethylene	WGP: wire grid polarizer
KK: Kramers-Kronig	
LD <sup>f</sup> : reduced linear dichroism	

# Contents

---

---

<b>1.</b>	<b>INTRODUCTION .....</b>	<b>14</b>
<b>2.</b>	<b>GENERAL BACKGROUND .....</b>	<b>21</b>
2.1.	Brief History of Generation and Detection of THz Radiation Using Photo-Conductive Antenna.....	21
2.2.	Generation and Detection of THz Radiation .....	25
2.2.1.	Generation of THz Radiation.....	27
2.2.2.	Detection of THz Radiation .....	30
2.3.	THz Spectroscopy of Exotic Nanostructures.....	31
2.3.1.	Nanowires .....	32
2.3.2.	Graphene and Other Two Dimensional Materials.....	33
<b>3.</b>	<b>INSTRUMENTS AND DATA ANALYSIS .....</b>	<b>38</b>
3.1.	THz Time Domain Spectrometer.....	38
3.1.1.	T-Light 780 .....	38
3.1.2.	Second Harmonic Generation .....	40
3.1.3.	Periodically Poled Lithium Niobate Crystal .....	40
3.1.4.	Absorptive Neutral Density Filter .....	41
3.1.5.	Mirrors .....	41
3.1.6.	Wave Plates.....	41
3.1.7.	Polarizing Beam Splitter .....	42
3.1.8.	Motorized Delay Stage and Vibration Generator.....	43
3.1.9.	Antenna for THz Generation and Detection .....	43
3.1.10.	Direct Digital Synthesizer .....	45
3.1.11.	Lock-in Amplifier .....	46
3.1.12.	Oscilloscope.....	47
3.1.13.	Working Principle.....	49
3.1.14.	Alignment of the Spectrometer .....	51
3.2.	Scanning Electron Microscopy .....	55

---

3.3.	Transmission Electron Microscopy .....	58
3.4.	UV-Visible Spectrometer .....	60
3.5.	Data Analysis.....	61
3.5.1.	Measurement and Data Recording .....	61
3.5.2.	Transmittance Calculation .....	62
3.5.3.	Optical Parameter Extraction .....	62
<b>4.</b>	<b>TERAHERTZ POLARIZER.....</b>	<b>69</b>
4.1.	Introduction.....	69
4.2.	Background Study .....	70
4.2.1.	Wire Grid THz Polarizer.....	71
4.2.2.	Aligned Carbon Nanotube Polarizer .....	72
4.2.3.	Other types of Polarizers.....	73
4.3.	Basic Theory .....	74
4.4.	Sample Preparation.....	75
4.5.	Measurement and Analysis.....	77
4.6.	Conclusion .....	85
<b>5.</b>	<b>TERAHERTZ ELECTROMAGNETIC SHIELDING.....</b>	<b>88</b>
5.1.	Introduction.....	88
5.2.	Background Study .....	89
5.3.	Basic Theory .....	90
5.4.	Sample Preparation.....	92
5.5.	Measurement and Analysis.....	92
5.6.	Conclusion .....	97
<b>6.</b>	<b>CONDUCTIVITY MANIPULATION IN SWNT/POLYMER COMPOSITE FILMS.....</b>	<b>99</b>

6.1.	Introduction.....	99
6.2.	Background Study .....	100
6.3.	Basic Theory .....	104
6.4.	Length Dependent Conductivity in SWNT/Polymer Composite.....	105
6.4.1.	Introduction.....	105
6.4.2.	Sample Preparation .....	106
6.4.3.	Results and Discussions .....	106
6.5.	Conductivity Manipulation in Surface Decorated Carbon Nanotube Composite.....	110
6.5.1.	Introduction.....	110
6.5.2.	Sample Preparation .....	111
6.5.3.	Results and Discussions .....	113
6.6.	Conclusion .....	120
<b>7.</b>	<b>TERAHERTZ SHIELDING EFFECTIVENESS AND CONDUCTIVITY OF SELF- STANDING MWNT FILM.....</b>	<b>122</b>
7.1.	Introduction.....	122
7.2.	Background Study .....	123
7.3.	Basic Theory .....	126
7.3.1.	Shielding Analysis .....	126
7.3.2.	Effective Medium Theory .....	126
7.3.3.	Drude-Lorentz Theory .....	129
7.4.	Length Dependent Shielding and THz Conductivity.....	133
7.4.1.	Sample Preparation .....	133
7.4.2.	Results and Discussions .....	134
7.5.	Diameter Dependent Shielding and THz Conductivity .....	140
7.5.1.	Sample Preparation .....	140
7.5.2.	Results and Discussions .....	141
7.6.	Conclusion .....	147

<b>8.</b>	<b>PROBING OXIDATION IN COPPER THIN FILM.....</b>	<b>150</b>
8.1.	Introduction.....	150
8.2.	Background Study .....	150
8.3.	Basic Theory.....	152
8.4.	Sample Preparation.....	153
8.5.	Measurement and Analysis.....	153
8.6.	Conclusion .....	158
<b>9.</b>	<b>CONCLUSION AND FUTURE DIRECTION .....</b>	<b>160</b>
9.1.	Conclusion .....	161
9.2.	Future Direction.....	164
<b>10.</b>	<b>REFERENCES.....</b>	<b>166</b>
<b>11.</b>	<b>APPENDICES.....</b>	<b>179</b>
11.1.	Kramers Kronig relation.....	179
11.2.	Transmittance Calculation.....	179
11.3.	Analysis of THz Polarizer .....	181
11.4.	Shielding Analysis.....	182
11.5.	Universal Di-electric Relaxation Model.....	184
11.6.	Thin Film Conductivity .....	185

# **Chapter One**

# 1. Introduction

Terahertz (THz) means  $10^{12}$  hertz. In the context of the present thesis, THz denotes an electromagnetic radiation which lies in the gap between microwaves and infrared frequency range in the electromagnetic spectrum. THz spectral region roughly spreads from 0.1 THz (wavelength  $\lambda \sim 3000 \mu\text{m}$ ) to 10 THz (wavelength  $\lambda \sim 30 \mu\text{m}$ )[1, 2]. In some of the literatures, it was also argued that the THz spectral region is defined between 0.3 THz to 3 THz, but this is just a matter of convention and in the present thesis, all the experimental works are demonstrated in the frequency range of 0.2 THz to 2.7 THz. The position of THz spectral range in the electromagnetic spectrum is shown in Fig. 1.1. One THz corresponds to a timescale of 1 ps, a wave length of  $300 \mu\text{m}$ , an energy content of 4.1 meV, and wave number of  $33.33 \text{ cm}^{-1}$ .

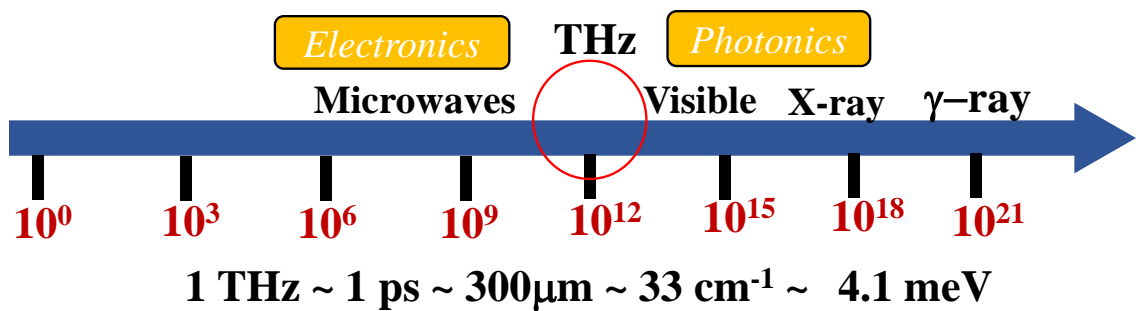


**Fig. 1.1: THz frequency region in electromagnetic spectrum**

The so-called “THz Gap” has historically been defined by the relative lack of convenient and inexpensive sources, detectors, and systems operating in this elusive THz frequency range. However, the universe is filled with THz/microwave radiation coming from different galaxies, stars and even every living being are also constantly emitting THz/microwave radiation. But, they remain undetected due to the unavailability of efficient detectors. Using electronic sources, one can’t go beyond 0.3 THz, due to the inherent restriction in the fast electron oscillation time. Using semiconductor materials, we cannot generate or detect radiation below 10 THz because the conventional band gaps of such materials are of the order of few eV, an order of magnitude higher than the energy related to THz gap, which is only few meV. Hence unless multi-photon absorption, which is difficult to observe, one can’t generate THz waves using semiconductor devices. That’s why, we don’t have conventional laser sources (like lasers in optical or far-infrared

frequency range) working in THz frequency range. However, for frequencies below 0.3 THz, electronic components are commercially available, and millimetre-wave imaging systems are also becoming available. Above 10 THz, thermal (black-body) sources are an increasingly efficient means for generating electromagnetic radiation, thermal cameras are also commercially available, and optical techniques are more readily and easily applicable. Due to its unique energy range, THz radiation can't be produced or detected using common lasers or commercial photodiodes. Special techniques by combining both electronics and optics have been invented and vigorously studied to manipulate THz waves. In the THz regime, energy level ( $1 \text{ THz} \cong 4.1 \text{ meV}$ ) is much smaller than the quantized thermal unit of radiation  $k_B T$ , which is the thermal energy at room temperature ( $1 k_B T \cong 25 \text{ meV}$  at  $T = 300 \text{ K}$ ). So, one can generally neglect the quantized nature of the radiation field. THz regime is therefore a natural bridge between the quantum mechanical and classical descriptions of electromagnetic waves and their interactions with materials. The two orders of magnitude of frequency spectrum in between were, relatively speaking, much less explored because of these difficulties until the last decade. Because of the works of various devoted research groups all around the world, the term "THz Gap" has now become practically non-existent. Within last 15 years many new THz techniques have been studied, which were motivated in part by the vast range of possible applications for THz imaging, sensing, and spectroscopy. The research field of THz radiation has been experiencing an unprecedented growth and a paradigm shift since last few years due to the invention of new THz generators and THz detectors. In the 1990s and early 2000s, researchers were mainly interested in studying efficient ways to generate and detect THz radiation with sufficient energy which includes the use of new types of photo-conductive (PC) antennas, electro-optic materials, multi-ferroic materials and intense femtosecond lasers down to 15 fs and some basic spectroscopic study of polar liquids and thin films. Riding on the advantage of extremely low energy, broadband nature, high signal-to-noise (S/N) ratio and the information of both the amplitude and the phase of this unique frequency range, THz spectroscopy has been used in various aspects of science in the last few years. There are many applications of THz spectroscopy covering diverse areas of science including solid state physics, semiconductors physics, nano-science and molecular spectroscopy, biology, pharmaceuticals, standoff detection and security, and art conservation. Now-a-days, researchers are mostly interested in application based THz research ranging from THz manipulating devices (like THz polarizers and wave-plates[3-8], THz shielding[9-11], THz conductivity manipulation), THz giant-magneto resistance

---

materials and spintronics[12-16], ultrafast data storage[17-21], computer performing operations at the rates of teraflops[22, 23], THz communication systems[24-27], gas sensing electronic devices on the picoseconds time scale[28] to THz astronomy[29-32], THz applications in security, imaging and healthcare[1, 33-41] etc.. A beautiful review about the progress of THz technology in different aspect of science has been provided by Tonouchi et al.[42] in 2007. THz radiation can be transmitted to a reasonable distance through air, many plastics, cardboard, paper, clothing, and many other materials, with the notable exceptions of metals and water. THz radiation is therefore useful for imaging applications. In the simplest case, the sample is scanned across the focus of the THz beam and the amplitude and phase of either the broadband pulse or the individual frequency components can be mapped. THz imaging has potential applications including security screening, biomedical testing, pharmaceuticals, and art conservation. THz spectroscopy provides important information on the basic structure of molecules and is a useful tool of radio astronomy. Rotational frequencies of light molecules fall in this spectral region, as do vibrational modes of large molecules with many functional groupings, including many biologic molecules that have broad resonances at THz frequencies. Several research groups are also involved in studying exotic fundamental studies in the field of superconductor carrier dynamics, ultrafast demagnetization mechanisms, magnon propagation in anti-ferromagnets, phonon modes in nanostructures, understanding water dynamics, carrier relaxation mechanism in two-dimensional (2D) systems (like graphene, molybdenum sulphide, boron nitrate) etc.. Undoubtedly, from the early days of adolescence, THz research has reached its vibrant youth. A recent report from the National Academics outlines that electronic and optics are combining to open up a new “Tera-Era”[43]. There are three different types of THz spectroscopy measurements carried out, namely i) THz time domain spectroscopy (THz-TDS), ii) THz time resolved spectroscopy (TRTS) and iii) THz emission spectroscopy (TES). In THz-TDS, the ground state properties of the samples can be obtained in a non-invasive way. THz-TDS has become a widely used technique, and the great majority of THz studies have employed this method. Even though the measurement is made in the time domain, it is not a time-resolved technique. It is equivalent to a Fourier transform infrared spectroscopy (FTIR) method, and does not provide time-resolved dynamical information. It has several notable advantages relative to other methods in the far-infrared and a detailed discussion is given later. In TRTS, the sample is excited via an optical pulse and a THz pulse passes through the sample to detect the photo-excited carrier dynamics of the sample. In TES, a sample

---

is photo-excited and radiates a THz pulse due to a change in the current and/or a change in the polarization in the sample, and the radiated THz waveform is analyzed to uncover the dynamics of the underlying process. In the present thesis we have studied the ground state THz properties of various nanostructures using THz-TDS.

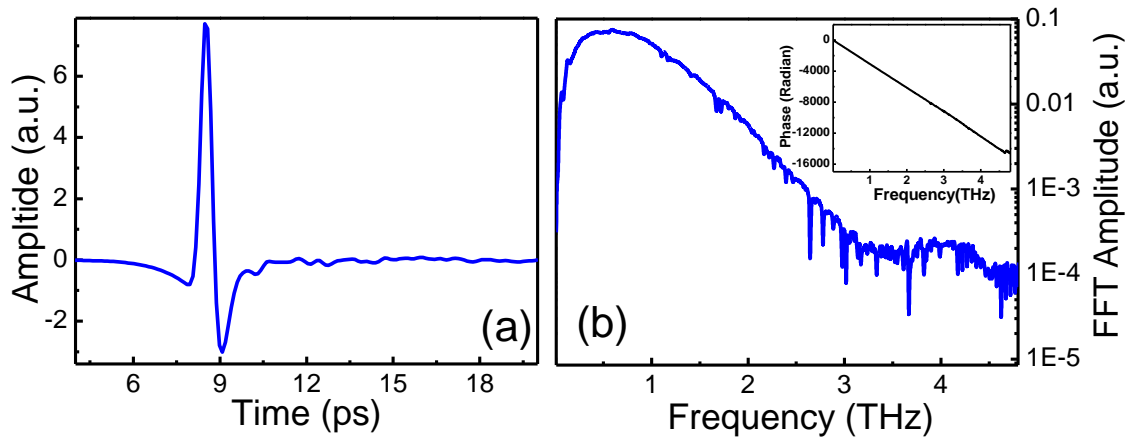


**Fig. 1.2: A typical (a) THz pulse and its (b) fast Fourier transform, phase of the pulse is shown at the inset**

A typical time-domain THz waveform, measured in air purged with dry nitrogen ( $N_2$ ) is shown in Fig. 1.2. Dry  $N_2$  is used to get rid of the water vapour absorption lines. The oscillatory features, which follow the initial single-cycle transient are due to the small amount of water vapour still present in the beam path, which becomes prominent in higher frequency region. The spectral amplitude  $|\tilde{E}(\omega)|$  or the fast Fourier transform (FFT) amplitude is shown at the right panel on a log scale. Small water vapour absorption lines can also be seen. The inset shows the spectral phase, also derived from the THz-TDS measurement. This is essentially linear, as expected for a single-cycle pulse. There are several advantages of THz time domain spectroscopy over conventional FTIR which also covers the THz frequency range.

1. In THz-TDS, we measure both the amplitude and the phase of the transmitted THz pulse simultaneously. Both the real and imaginary dielectric constants of the systems can be retrieved without using the completed Kramers-Kronig (KK) analysis (described briefly at the appendices). In KK analysis we require the knowledge of the real (or imaginary) response function over the entire frequency range (0 to infinity) to get the imaginary part (real) of the response function. A distinct advantage of coherent THz pulses is that the amplitude and the phase of the electric field can be measured directly, because the THz fields are coherent with the femtosecond pulses from which they are

generated. Using THz-TDS, both the real and imaginary parts of the response functions, such as the complex dielectric function as shown below;

$$\tilde{\epsilon}(\omega) = \epsilon_{Real}(\omega) + i\epsilon_{Imag}(\omega), \quad (1)$$

where,  $\tilde{\epsilon}$  is the complex di-electric function,  $\epsilon_{Real}$  and  $\epsilon_{Imag}$  are the real and imaginary component of the di-electric function respectively and  $\omega$  is the probing frequency, can be obtained directly without the need for KK transforms. The complex dielectric constant of the material is related to the complex conductivity ( $\tilde{\sigma}(\omega)$ ) of the system according to the following equation;

$$\tilde{\sigma}(\omega) \equiv \sigma_{Real}(\omega) + i\sigma_{Imag}(\omega) = i\omega\epsilon_0[1 - \tilde{\epsilon}(\omega)], \quad (2)$$

where  $\sigma_{Real}$  and  $\sigma_{Imag}$  are the real and imaginary component of the conductivity and  $\epsilon_0$  is the d.c. di-electric constant of the material. The conductivity describes the current response as the following;

$$\tilde{J}(\omega) = \tilde{\sigma}(\omega)\tilde{E}(\omega), \quad (3)$$

of a many-body system to an electric field, an ideal tool to study conducting systems. Here  $\tilde{J}$  is the complex current density and  $\tilde{E}$  is the complex electric field.

2. THz-TDS is a coherent detection technique and the signal to noise ratio is quite high. For example, in our experimental setup the highest S/N ratio is around 50 dB at 0.4 THz.

3. THz-TDS is a useful technique to measure the optical properties of a sample in a non-invasive manner, which is extremely advantageous in case of measuring nanostructured samples because there is no chance of getting the samples damaged by any kind of contact and also one does not need to put any kind of connecting wires to the sample which may slightly alter the response of the sample.

In the present thesis entitled “*Manipulating Terahertz Radiation Using Nanostructures*”, I shall be describing the works that I have carried out during my Ph.D. tenure. It is basically centred around the fabrication of different types of nanostructures and films, their structure and morphology characterization, extracting their THz opto-electronic properties and/or their demonstration in manipulating the THz radiation.

The structure of the present thesis is as follows. The thesis can be divided into two main parts. Chapter 1 to chapter 3 discuss the introduction of THz radiation, its history and the instruments and data analysis techniques. Chapter 4 to Chapter 8 discuss all the works that I have done during my PhD. An overall conclusion is provided in chapter 9 and

references are given in chapter 10. In [chapter 1](#), a general introduction is given about the THz radiation, its unique properties and its advantages. The [second chapter](#) briefly describes the history of the progress of filling up the so called “THz Gap” by using antenna structures and also some important THz-TDS studies in nanostructures are revisited. The major instruments and the data analysis procedure are described in [chapter 3](#). In [chapter 4](#), the preparation of a low-cost durable THz polarizer using magnetically aligned nickel nanostructures is described and the THz polarizing behaviour is demonstrated. THz electromagnetic shielding (EMIS) of single walled carbon nanotube (SWNT)/polymer composites with increasing SWNT content is described in [chapter 5](#). The conductivity manipulation in two different and efficient ways is described in [chapter 6](#). In [chapter 7](#), the conductivity and EMIS of self-standing multi-walled carbon nanotube (MWNT) films is described as a function average length and diameter of MWNT. The oxidation in copper thin films and its effect on the THz conductivity properties of the Cu film is discussed in [chapter 8](#). Finally, [chapter 9](#) presents the overall summary of the main findings of the thesis and offers some recommendations for future works based on this thesis.

# **Chapter Two**

## 2. General Background

---

---

### **2.1. Brief History of Generation and Detection of THz Radiation Using Photo-Conductive Antenna**

THz spectroscopy grew out primarily due to the efforts of Daniel Grischkowsky (who was working at IBM Watson Research Center) and David Auston and Martin Nuss (who were working at the Bell Labs) to generate and detect ultrashort electrical transients as they propagated down a transmission line. David H. Auston started working in femtosecond excitation of electro-optic crystals to generate sub-ps pulses at Bell Lab. They found that defects in lithium niobate (LN) favour the far-infrared generation by optical excitation[44]. The idea of using photoconductors rather than ion doped crystals to generate the electrical signals came shortly afterwards he began experimenting with silicon-based transmission-line structures. In the earliest experiments, very fast rise time electrical signals could be generated, but long carrier recombination times in silicon limited the bandwidth through the rather slow decay times. To terminate the electrical pulse, he deployed a second optical pulse to create a short-circuit in the transmission line. Detection of the signal was accomplished by using a second pair of optical pulses further down the transmission line, which is used to open and close the circuit in a similar fashion. This general approach for generating and detecting extremely fast electrical pulses by optical techniques became known as the "Auston Switch"[45, 46]. At that time, the idea of using the optical pulses not just to excite a photo conductor, but to actually generate a localized current that could be swept up and radiated by a localized radio frequency (RF) antenna, began to take shape and the coherent generation and detection of free space radiating RF fields using fast optical pulses was demonstrated[47, 48]. At about this time, would be THz pioneer Daniel Grischkowsky started working with sub-ps pulses and was able to launch and detect sub picosecond electrical pulses propagating on a coplanar waveguide transmission line[49], after his important innovation (which was later commercially implemented by Spectra Physics) on the area of pulse compression and pulse reshaping[50, 51]. They generated electrical pulses (shorter than 0.6 ps) in a coplanar transmission line with 80 fs laser pulses which broadened to only 2.6 ps after

propagating 8 mm on the transmission line. For the reduction of this pulse broadening effect, he started to work on the propagation of sub-ps radiation in free spaces and succeeded in the demonstration of THz generation, its free propagation in air up to 10 cm and then its detection using dipolar antennas[52]. As understood from Maxwell's equations, a time-varying electric current will radiate an electromagnetic pulse. Thus, it was realized that these transmission lines were also radiating short bursts of electromagnetic radiation. These reports[48, 52], where THz pulse propagated through air between the generator and detector antenna paved the way for modern day THz spectrometers. At this stage, significant number of studies were focused on the generation of THz radiation via photo-mixing two diode laser on suitable antenna structure. McLantosh et al.[53] studied the performance of photo-mixer structure on low temperature grown GaAs (LT-GaAs) and excited it with optical pump power generated from two Ti:Al<sub>2</sub>O<sub>3</sub> (Ti-Sapphire) lasers operating in the range of 720-820 nm to get THz radiation across the range 0-5 THz. By reducing the area of the electrode region, they had pushed the RC limit (RC constant of an equivalent circuit is defined as the time required to charge the capacitor, through the resistor, by  $\approx 63.2\%$  of the difference between the initial value and final value and here the frequency ( $f$ ) is related with the RC time constant  $\tau$  as;  $\tau = 1/2\pi f$ ) for the photo-mixer beyond 2 THz. This allowed them to measure a lifetime-limited 3 dB bandwidth of 650 GHz in a mixer with a 250 fs photo-carrier lifetime, and leads to a 50 times increase in power at a frequency of 2.5 THz. Matsuura et al.[54] demonstrated the generation of continuous-wave THz radiation at frequencies up to 3.5 THz by photo-mixing in LT-GaAs photoconductors with printed dipole antennas.

Kono et al.[55] prepared a dipole type PC detector antenna on an LT-GaAs wafer. The 1.5 mm thick LT-GaAs layer was grown at 250 °C on the GaAs substrate whose thickness was 0.4 mm. Using a 12 fs Ti-Sapphire light, they succeeded in detecting THz radiation up to 20 THz, however, with a strong phonon resonance dip around 8 THz. Tani et al.[56] studied PC dipole antennas fabricated on semi-insulating (SI) GaAs and SI-InP to detect THz pulses. The SI-InP based photoconductive detector showed a higher responsivity and a better S/N ratio than the LT-GaAs based photoconductive detector at low gating laser powers. They have also studied[57] THz emission with several designs of PC antennas (three dipoles, a bow tie, and a coplanar strip line) fabricated on LT-GaAs and SI-GaAs, and compared them. The radiation spectra for the antennas fabricated on LT-GaAs and SI-GaAs did not show significant differences, indicating that the high-frequency components of radiation were not greatly limited by the carrier lifetime of the

---

substrate semiconductor. Liu et al.[58] studied the performance of InP:H<sup>+</sup> PC antennas as the ultra-broadband THz detector and compared it with an LT-GaAs. They found that the peak THz signal of the InP:H<sup>+</sup> ( $10^{15}$  ions.cm<sup>-2</sup>) PC antenna was slightly higher than that of the LT-GaAs one, while the SNR of the former was about half as high as the latter. Salem et al.[59] measured the characteristics of PC antenna emitters fabricated on GaAs:As, GaAs:H, GaAs:O and GaAs:N ion-implanted substrates and compared them with those obtained for a similar emitter fabricated on SI-GaAs substrate. In all the cases (except for GaAs:N), they found better THz integrated intensity for emitters made on ion-implanted substrates. Dreyhaupt et al.[60] demonstrated a planar large-area PC emitter for impulsive generation of THz radiation. The device consisted of an interdigitated electrode (metal-semiconductor-metal (MSM)) structure which was masked by a second metallization layer isolated from the MSM electrodes. The second layer blocked optical excitation in every second period of the MSM finger structure. Hence charge carriers were excited only in those periods of the MSM structure which exhibited a unidirectional electric field. Constructive interference of the THz emission from accelerated carriers led to THz electric field amplitudes up to  $85 \text{ V.cm}^{-1}$  when excited with fs optical pulses from a Ti:sapphire oscillator with an average power of 100 mW at a bias voltage of 65 V applied to the MSM structure. Upadhyaya et al.[61] studied the generation of THz transients in photoconductive emitters by varying the spatial extent and density of the optically excited photo-carriers in asymmetrically excited, biased LT-GaAs antenna structures. They found a pronounced dependence of the THz pulse intensity and broadband ( $> 6.0 \text{ THz}$ ) spectral distribution on the pump excitation density and simulate this with a three-dimensional carrier dynamics model. Miyamaru et al.[62] studied the dependence of the emission spectrum of THz radiation on the geometrical parameters of the dipole antenna, and the relationship between these parameters and the temporal characteristics of the transient current that generate THz radiation. They found that the frequency bandwidth became narrower as the dipole length increased and the emission efficiency of the dipole antenna decreased with decreasing aspect ratio (AR) of the dipole antenna. Park et al.[63] presented a nanoplasmonic PC antenna with metal nanoislands for enhancing THz pulse emission. The whole photoconductive area was fully covered with metal nanoislands by using thermal dewetting of thin metal film at relatively low temperature. The metal nanoislands served as plasmonic nanoantennas to locally enhance the electric field of an ultrashort pulsed pump beam for higher photo-carrier generation and two times higher enhancement for THz pulse emission power than a conventional PC antenna was

---

demonstrated. Hou et al.[64] investigated the relationship between THz wave emission efficiency, noise, and stability to the material properties of fabricated LT-GaAs and SI-GaAs antennas with the same structure, and compared their emission power, S/N ratio, and stability under the same experimental conditions. Using both theoretical and experimental analysis, they concluded that the LT-GaAs antenna provides high THz wave emission efficiency, low noise, and high stability due to its short carrier lifetime and high resistivity. Ropagnol et al.[65] demonstrated the generation of intense THz pulses at low frequencies, and THz pulse shaping, using a ZnSe interdigitated large aperture PC antenna. They experimentally measured a THz pulse energy of  $3.6 \pm 0.8 \mu\text{J}$ , corresponding to a calculated peak THz electric field of  $143 \pm 17 \text{ kV}\cdot\text{cm}^{-1}$ . The focused THz intensity spot size was  $7.3 \text{ mm}^2$ ; close to the diffraction limit. They also used a binary phase mask instead of a traditional shadow mask with their interdigitated PC antenna, which allowed them to generate THz field profiles that ranged from a symmetric single-cycle THz pulse to an asymmetric half-cycle THz pulse.

THz systems operated at  $1.5 \mu\text{m}$  wavelength can benefit from the large variety of lasers and fiber components developed and matured originally for telecom applications. Thus, compact, flexible and cost effective THz sensor systems can be assembled. So, people got excited to use the advantage of lossless well-known communication wavelength  $1.5 \mu\text{m}$  for excitation of THz radiation. Unfortunately, GaAs is usually not sensitive at  $1.5 \mu\text{m}$  wavelength because the optical band gap is  $1.43 \text{ eV}$  at room temperature, corresponding to a wavelength of  $867 \text{ nm}$ . Gupta et al.[66] prepared LT-GaAs and LT-InGaAs using MBE technique at various growth temperatures and studied the corresponding ultrafast carrier lifetime. The carrier lifetime of un-annealed LT-GaAs decreased from  $70 \text{ ps}$  to less than  $0.4 \text{ ps}$  as the growth temperature decreased from  $400 \text{ }^\circ\text{C}$  to  $190 \text{ }^\circ\text{C}$ . Carrier lifetime of un-annealed LT-InGaAs decreased from  $\sim 70 \text{ ps}$  to  $2.5 \text{ ps}$  with decreasing growth temperature. Application of THz detector using LT-InGaAs and  $1.55 \mu\text{m}$  excitation wavelength was studied. Sekine et al.[67] studied the ultrafast carrier response of ion-implanted Ge thin films and found a photo-carrier mobility as high as  $100 \text{ cm}^2\text{V}^{-1}\text{s}^{-1}$  and carrier lifetime as low as  $0.6 \text{ ps}$ . They also studied THz emission using PC antenna array excited by  $1.55 \mu\text{m}$  radiation. Erlig et al.[68] studied the THz radiation from LT-GaAs antenna using  $1.55 \mu\text{m}$  wavelength and concluded that two-photon absorption was the origin of the radiation, however, Tani et al.[69] suggested that the two-step photon absorption mediated by mid-gap states, formed by the excess As (1% - 2%) in LT-GaAs, contributed to the photoconductivity at relatively low excitation power ( $5 \text{ mW}$ ) rather than

---

the two-photon absorption at 1.55  $\mu\text{m}$  and found 10% higher efficiency than 780 nm excitation. Suzuki et al.[70] deposited un-doped 1.5  $\mu\text{m}$  thick  $\text{In}_{0.53}\text{Ga}_{0.47}\text{As}$  layers using metalorganic chemical vapour deposition on semi-insulating  $\text{InP}:\text{Fe}$  substrates and implanted with Fe ion of 340 keV at the dose of  $1.0 \times 10^{15} \text{ cm}^{-2}$  which was then annealed at different temperatures (400, 580, and 640  $^{\circ}\text{C}$ ). They found that annealing at 580  $^{\circ}\text{C}$  of Fe-implanted PC antennas affected the shape of photocurrent signals, and increased the amplitude of the signals and concluded that Fe-implanted  $\text{InGaAs}$  PC antennas after annealing was one of the potential candidates for applications as an efficient THz detector triggered by the optical communication light of 1.55  $\mu\text{m}$  wavelength. The Group of Martin Schell at the Fraunhofer Institute for Telecommunications, Berlin was engaged in fabricating THz generators and detectors operating at 1.5  $\mu\text{m}$  telecom wavelength for the realization of all-fiber THz time domain spectrometer. They[71, 72] studied the novel LT- $\text{InGaAs}/\text{InAlAs}$  multi-layer structures at various growth temperatures to prepare efficient THz emitter and detector antennas working at 1.55  $\mu\text{m}$ . To overcome the problem of decreasing in-plane electrical field component, they also studied the mesa-type structures with electrical side contacts. The electrical field was directly applied even to deeper layers, and the current in the receiver did not need to traverse hetero-structure barriers which increased the THz peak-to-peak voltage about  $\sim 27$  times than planar THz antenna. Bekar et al.[73] demonstrated an all-optoelectronic continuous-wave THz photo-mixing system from microwave frequencies to beyond 1.0 THz that uses LT- $\text{InGaAs}$  devices both for emitters and coherent homodyne detectors. The photo-conductive  $\text{InGaAs}$  layers were grown on SI- $\text{GaAs}$  by MBE at a nominal growth temperature of 230  $^{\circ}\text{C}$ . The excellent material properties were achieved by applying a post-growth anneal, in which the surfaces were passivated by contact with SI- $\text{GaAs}$  wafers. Ramer et al.[74] studied the generation and detection of THz radiation at 1560 nm based on LT- $\text{GaAs}$  PC antennas. A THz-TDS system employing LT- $\text{GaAs}$  PC antennas pumped at 1560 nm was also demonstrated which reached a bandwidth of 4.5 THz and a peak S/N ratio of 29 dB, while the reference measurement at 780 nm reached 40 dB and a bandwidth of approximately 3 THz.

## 2.2. Generation and Detection of THz Radiation

Generation and detection of THz pulses occur through the non-linear interactions of the driving optical pulse with a material with fast response. Any process that crates time-dependent change in the material properties  $\mu$ ,  $\sigma$ , or  $\varepsilon$  can act as a source term that can

---

result in emission of THz radiation. There are mainly two major classifications of producing THz generation and detection namely i) photo-conductive antenna and ii) non-linear electro-optic crystals. But, there are also some other techniques like i) photo-mixing, ii) THz quantum cascade laser (QCL), iii) THz generation from air plasma etc. Since all the studies reported in this thesis are based on PC antenna, in this chapter, only the mechanism of THz generation and detection using PC antenna will be discussed.

As the main equations governing the generation and detection of any radiation are the Maxwell's equations, in this section, the Maxwell's equations in vacuum and in material will be briefly revisited in the context of wave equation, whose solution gives us an electric field as a function of time (or frequency). Electromagnetic radiation and its properties can be efficiently expressed by the Maxwell's equations[75, 76] as given below;

$$\nabla \cdot \mathbf{E} = \rho / \epsilon_0, \quad (4)$$

$$\nabla \times \mathbf{E} = -\partial \mathbf{B} / \partial t, \quad (5)$$

$$\nabla \cdot \mathbf{B} = 0, \quad (6)$$

$$\nabla \times \mathbf{B} = \mu_0 \epsilon_0 \partial \mathbf{E} / \partial t + \mu_0 \mathbf{J}, \quad (7)$$

where,  $\mathbf{E}$  and  $\mathbf{B}$  are the electric field vector and magnetic induction vectors,  $\epsilon_0$  and  $\mu_0$  are the vacuum permittivity and permeability,  $\rho$  and  $\mathbf{J}$  are the charge and current density.

The speed of light is defined as,  $c = \frac{1}{\sqrt{\mu_0 \epsilon_0}}$ . Now, using the identity  $\nabla \cdot (\nabla \times \mathbf{B}) = 0$ , we find the following equation which is also known as the continuity equation,

$$\partial \rho / \partial t = \nabla \cdot \mathbf{J}. \quad (8)$$

The charge density ( $\rho$ ) of a medium can be expressed as the combination of external charges due to free electrons ( $\rho_{ext}$ ) and the polarization charges ( $\rho_{pol}$ ) which is related to the polarization density  $\mathbf{P}$  according to  $\rho_{pol} = -\nabla \cdot \mathbf{P}$ . The total current density ( $\mathbf{J}$ ) is also expressed as a combination of conduction current density ( $\mathbf{J}_{cond}$ ) and displacement current density ( $\mathbf{J}_{disp}$ ), which is related with the polarization density according to  $\mathbf{J}_{disp} = \partial \mathbf{P} / \partial t$ .

The electric displacement  $\mathbf{D}$  and magnetic field strength  $\mathbf{H}$  are the material-related parameters, which for a linear isotropic non-magnetic dielectric are given by,

$$\mathbf{D} = \epsilon \mathbf{E} = \epsilon_0 \mathbf{E} + \mathbf{P} = \epsilon_0 (1 + \chi) \mathbf{E}, \quad (9)$$

$$\mathbf{H} = \mathbf{B}/\mu_0, \quad (10)$$

where,  $\varepsilon$  is the dielectric constant and  $\chi$  the dielectric susceptibility.

So, the Maxwell's equations in the presence of materials[76, 77] can be written as;

$$\nabla \cdot \mathbf{D} = \rho_{ext}/\varepsilon_0, \quad (11)$$

$$\nabla \times \mathbf{E} = -\partial \mathbf{B}/\partial t, \quad (12)$$

$$\nabla \cdot \mathbf{B} = 0, \quad (13)$$

$$\nabla \times \mathbf{H} = \varepsilon_0 \partial \mathbf{D}/\partial t + \mathbf{J}_{cond}. \quad (14)$$

These are the Maxwell's equations in presence of materials. Now, in the absence of free charges, these equations can be combined into the general wave equation as given below,

$$\nabla^2 \mathbf{E} - \frac{1}{c^2} \frac{\partial^2 \mathbf{E}}{\partial t^2} = \mu_0 \left( \frac{\partial \mathbf{J}_{cond}}{\partial t} + \frac{\partial^2 \mathbf{P}}{\partial t^2} \right). \quad (15)$$

The two time-varying source terms are the conduction current  $\mathbf{J}_{cond}$  and the polarization  $\mathbf{P}$ . The far-field on-axis solution of this equation relates the temporal shape of an electromagnetic signal emitted by a slab of material with a time-varying spatially uniform conduction current  $\mathbf{J}_{cond}$  and/or the polarization  $\mathbf{P}$  at the axis normal to the slab at a distance. The solution has been presented by several authors[78-82] which looks like the following,

$$\mathbf{E}_{rad}(t) \approx \frac{\mu_0 S}{4\pi z} \left( \frac{\partial \mathbf{J}_{cond}(t)}{\partial t} + \frac{\partial^2 \mathbf{P}(t)}{\partial t^2} \right), \quad (16)$$

where,  $S$  is the emitting area and  $z$  stands for the distance between the emitter surface and the detection surface. This solution is important since it allows for reconstruction of the polarization and carrier dynamics in an electromagnetic signal, under the assumption that the radiated field is properly detected.

### 2.2.1. Generation of THz Radiation

Photoconductive THz generation occurs when optical excitation induces conductivity changes in a semiconductor. This is a resonant interaction and the photons are absorbed through inter-band transitions. For THz generation using PC antennas an ultrashort optical pulse incident on the semiconductor causes rapid transient changes to the macroscopic parameters represented by  $\mu(t)$ ,  $\sigma(t)$ , and  $\varepsilon(t)$ . The major change caused by the optical pulse is assumed to be in the conductivity  $\sigma$ . The rapid, optically induced

change of  $\sigma$  on a femto-second time scale is the origin of the ultrafast THz pulses generated through photoconduction. It is important to note that many physical processes occur when ultrafast pulses are absorbed by semiconductors, and, from an experimental point of view, they are not easily separable. Both resonant (absorption of a photon to create charge carriers), and non-resonant effects (nonlinear optical difference frequency generation), can contribute to THz pulse generation. A common example of a material in which both processes contribute to THz generation is LT-GaAs. The geometry of a photoconductive THz source (schematic) is shown in Fig. 2.1.

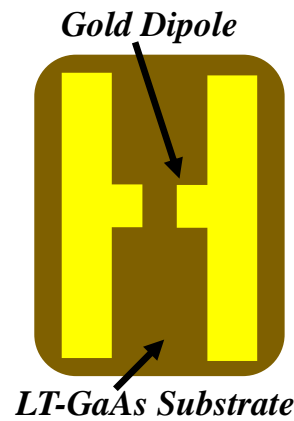


**Fig. 2.1: Schematic of photo-conductive antenna**

A coplanar transmission line of gold (Au) is fabricated on a semiconductor substrate with high mobility ( $\mu$ ) and fast carrier recombination time ( $\tau$ ), usually GaAs or LT-GaAs. The coplanar transmission lines are d.c. biased to produce a field on the order of  $10^6$  V/m near the breakdown threshold for air. The electric field near the surface of the semiconductor is represented by the parallel arrows between the lines (Fig. 2.2a). Energy is stored by the capacitive structure, with capacitance of the order of several pF. At first step, the ultrafast optical pulses excite the semiconductor device. The wave length of the excitation photon has to be chosen such that the photon energy ( $h\nu$ ) must be greater than the band gap energy ( $E_{gap}$ ) of the semiconductor. As a result, electron-hole pairs are created in the semiconductor. A focused ultrafast optical pulse incident between the metal lines generates a thin conductive region down to approximately the absorption depth  $1/\alpha$ . The optically generated electron-hole pairs form electrically neutral plasma near the semiconductor surface as shown in the Fig. 2.2b.

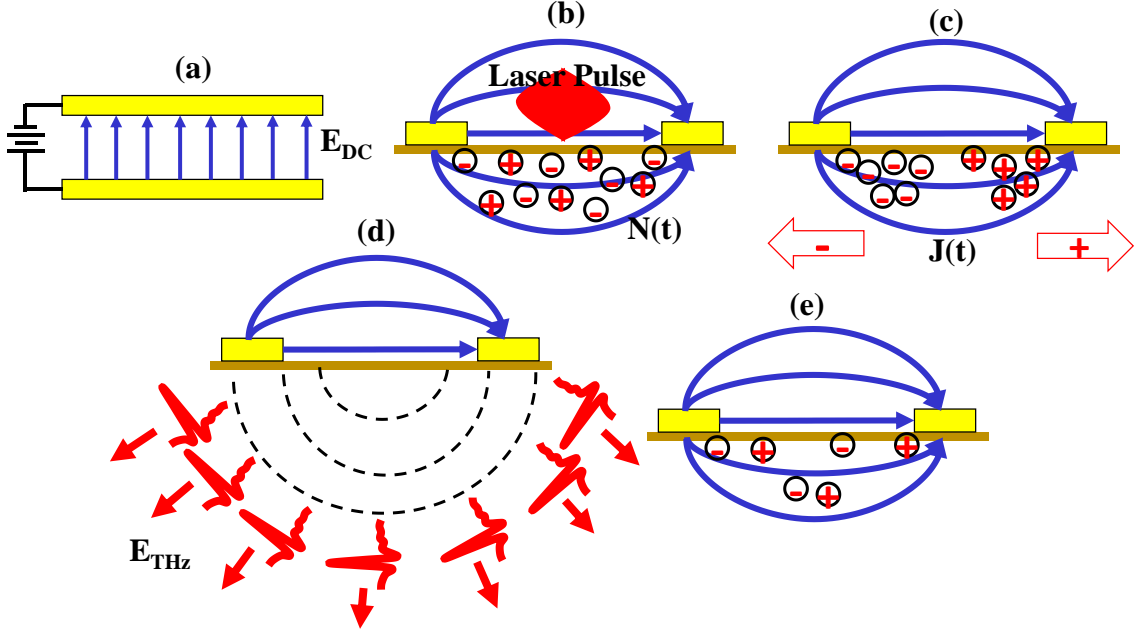


**Fig. 2.2: Schematic of THz generation via photo-conductive antenna (schematic is based from Ref. 43)**

The time evolution of the charge density is given by  $N(t)$  with the total carrier density as the sum of that of the electrons and the holes i.e.,

$$N(t) = N_e(t) + N_h(t). \quad (17)$$

At low-excitation influences, the charge density is proportional to the intensity profile of the optical pulse  $I(t)$ . The time evolution of the carrier density is given by this expression,

$$N(t) = \int_0^t G(t)\delta t - N_0 \exp\left(-\frac{t}{t_c}\right), \quad (18)$$

where,  $t_c, N_0$  are respectively the carrier lifetime and total number of generated carrier. The first term describes carrier density at time scales of the laser pulse and the second term describes the evolution of the carrier density at longer times. Here  $G(t)$  is the optical carrier generation rate determined by the optical pulse profile. The free carriers affect the conductivity by,

$$\sigma(t) = N(t)e\mu. \quad (19)$$

The current density is,

$$J(t) = \sigma(t)E, \text{ or } J(t) = N(t)ev(t), \quad (20)$$

with  $v(t)$  being the carrier velocity. Immediately after the generation of the carriers in the semiconductor the accelerating field is  $E(t = 0^+) = E_{DC}$ . The time dependence has

been written explicitly to illustrate the transient nature of the photoconductivity on sub-picosecond time scales. It is the transient current,  $J(t)$ , that generates the THz pulse. The carriers are accelerated in the applied electric field,  $E_{DC}$ . The time evolution of carrier velocity is determined by the initial acceleration of carriers with effective mass  $m^*$  and by rapid carrier scattering with a characteristic time, which is determined by phonon scattering, carrier scattering from the dopants and the photon energy, or where in the conduction band carriers are generated. In summary, a d.c. biased semiconductor (Fig. 2.2a) has electron-hole plasma created in femtosecond time scales by an optical pulse (Fig. 2.2b). The rapid acceleration and separation of the electrons and holes create a current transient (Fig. 2.2c). The transient electric field determined (approximately) by the time derivative of the current results in a radiated pulse front in THz frequency range (Fig. 2.2d). Equilibrium is reached after long time (Fig. 2.2e).

### 2.2.2. Detection of THz Radiation

The detections of THz pulses are performed by using the phenomenon of ultrafast pulse excitation in a semiconductor causing rapid changes in conductivity. The photoconductive detection process is shown schematically in Fig. 2.3. The ultrafast laser pulse is incident on the antenna from the left and the THz pulse propagating from the right. As in the case of the generation of THz pulse where an ultrafast laser pulse generates an electron and hole plasma. The arrival of the laser pulse is analogous to closing a switch, which allows the antenna gap to conduct due to the creation of electron-hole plasma. But, these electron-hole plasma cannot conduct due to the absence of any electric field. It can only conduct when the THz field falls on the antenna providing the necessary bias voltage. The short recombination time of the semiconductor causes the gap resistance to change from nearly insulating to conducting (closing the switch) then back to insulating (opening the switch) on a picoseconds time scale. The coplanar strip line is connected to a high-sensitivity current amplifier that detects any current flow through the antenna gap with sub-pA resolution. If the resistance of the metal lines is negligible the resistance of the antenna is determined by the antenna gap. The current flows according to Ohms law  $I(t) = V(t)/R(t)$ , where the antenna bias voltage is provided by the THz pulse:  $V(t) \cong E_{THZ}(t)h$ . In Fig. 2.3a, the THz pulse has not arrived at the antenna, the bias voltage is zero, and there is no net current flowing through the antenna. In Fig. 2.3b, the positive gating peak of THz pulse is incident on the antenna and at the same instance the optical

gating pulse arrives. In this case  $E_{THz} > 0$ , and the current flows from the lower half of the antenna to the upper are determined by the electric field direction.

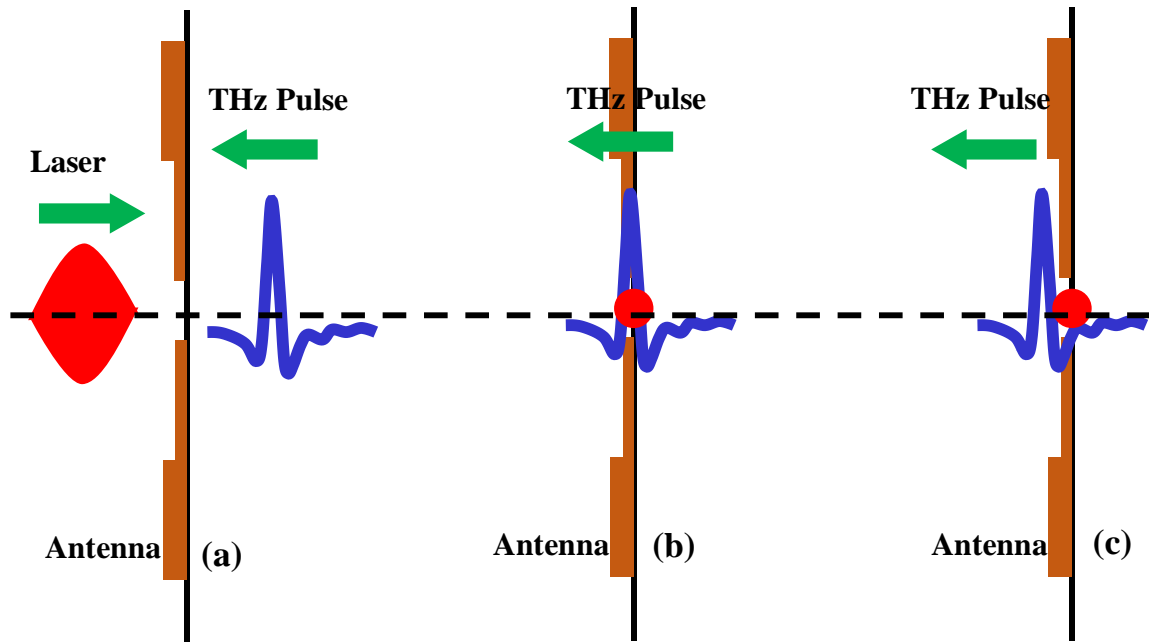


**Fig. 2.3: Schematic of THz detection using photo-conductive antenna (Schematic is taken from Ref. 43)**

The measured time average current is proportional to the THz electric field. After the current is measured, the delay between the laser generating and gating pulses is again changed to advance the THz pulse in time. Fig. 2.3c corresponds to a point on the pulse where the electric field is opposite in sign. The time resolved measurement of the THz pulse electric field is thus made by changing the delay between the optical gating pulse and the generating pulse, i.e. the time delay between the pump and probe laser beams. It is clear that to measure the electric field with high temporal resolution, the response time of the semiconductor must be short compared to the rate of change of the THz field. The two semiconductor materials most commonly used for photoconductive THz detectors are LT-GaAs and ion-implanted silicon on sapphire.

### 2.3. THz Spectroscopy of Exotic Nanostructures

The application of THz spectroscopy in the field of THz optics (THz polarizer, THz EMIS, THz neutral density filter), THz conductivity in CNT and their composites, THz conductivity of thin metallic films has been reviewed in this thesis at the beginning of the later chapters in this thesis. However, here a brief review of some recent THz spectroscopic works on carrier dynamics (both time-resolved and time domain study) of

nanostructured semiconductors and active THz devices using novel 2D materials (graphene, transition metal dichalcogenides MoS<sub>2</sub> and WeS<sub>2</sub>) is provided.

### 2.3.1. Nanowires

Parkinson et al.[83] investigated the time-resolved conductivity of isolated GaAs nanowires by TRTS. They found that the electronic response exhibited a pronounced surface plasmon mode within 300 fs before decaying within 10 ps as a result of charge trapping at the nanowire surface. Hendry et al.[84] studied the electron mobility in nanoporous and single-crystal titanium dioxide using THz-TDS. They determined the electron mobility after carrier thermalization with the lattice but before equilibration with defect trapping states. The electron mobility reported for single-crystal rutile ( $1 \text{ cm}^2 \text{ V}^{-1} \text{ s}^{-1}$ ) and porous TiO<sub>2</sub> ( $10^{-2} \text{ cm}^2 \text{ V}^{-1} \text{ s}^{-1}$ ) therefore represent upper limits for electron transport at room temperature for defect-free materials. The large difference in mobility between bulk and porous samples was explained using Maxwell-Garnett (MG) effective medium theory (EMT). They demonstrated that electron mobility is strongly dependent on the material morphology in nanostructured polar materials due to local field effects and cannot be used as a direct measure of the diffusion coefficient. George et al.[85] studied the ultrafast relaxation and recombination dynamics of photo-generated electrons and holes in epitaxial graphene using TRTS. They found that the conductivity in graphene at THz frequencies depend on the carrier concentration as well as the carrier distribution in energy. They concluded that carrier cooling occurred on sub-picosecond (sub-ps) time scales and that inter-band recombination times were carrier density dependent. Hoffmann et al.[86] demonstrated the ability to accelerate free carriers in doped semiconductors to high energies by single cycle THz pulses. They observed that, for GaAs, a fraction of carriers undergoes inter-valley scattering, leading to a drastic change in the effective mass. They also found that, in the case of InSb, the carrier energy could exceed the impact ionization threshold, leading to an increase of carrier concentration of about one order of magnitude. They observed the energy exchange between the hot electrons and the lattice, lead to population change of the longitudinal optical phonon. Hebling et al.[87] observed the non-equilibrium carrier distribution in *n*-type Ge, Si and GaAs semiconductors at room temperature using intense single cycle THz pulses. A review on the THz conductivity of different types of bulk and nanostructured semiconductors was given by Ulbricht et al.[88]. A detailed description of the ultrafast carrier dynamics of various types of semiconductor nanostructures could be found in a recent book by Jagdeep

---

Shah[89]. Joyce et al.[90] performed a comparative study of ultrafast charge carrier dynamics in a range of III-V nanowires using TRTS. InAs nanowires exhibited the highest electron mobilities of  $6000 \text{ cm}^2 \text{ V}^{-1} \text{ s}^{-1}$ , which highlighted their potential for high mobility applications, such as field effect transistors. InP nanowires exhibited the longest carrier lifetimes and the lowest surface recombination velocity of  $170 \text{ cm s}^{-1}$ . Such low surface recombination velocity made InP nanowires suitable for applications in photovoltaics. In contrast, the carrier lifetimes in GaAs nanowires were extremely short, of the order of picoseconds, due to the high surface recombination velocity, which was measured to be  $5.4 \times 10^5 \text{ cm s}^{-1}$ .

### **2.3.2. Graphene and Other Two Dimensional Materials**

Ryzhii et al.[91] studied the dynamic a.c. conductivity of a non-equilibrium 2D electron-hole system in optically pumped graphene. Considering the contribution of both inter-band and intra-band transitions, they demonstrated that at sufficiently strong pumping the population inversion in graphene can lead to the negative net a.c. conductivity in the THz frequency range. Hong et al.[92] performed THz spectroscopy on reduced graphene oxide (rGO) network films coated on quartz substrates from dispersion solutions by spraying method. They obtained the frequency-dependent conductivities and the refractive indexes of the rGO films and analyzed the results using Drude free-electron model. They concluded that the THz conductivities could be manipulated by controlling the reduction process, which was correlated well with the d.c. conductivity above the percolation limit. Tamagnone et al.[93] demonstrated a graphene based THz frequency-reconfigurable antenna. The antenna exploited dipole-like plasmonic resonances, which could be frequency-tuned on large range via the electric field effect in a graphene stack. Vakil et al.[94] theoretically showed that by designing and manipulating spatially inhomogeneous, non-uniform conductivity patterns across a flake of graphene, one could obtain a one-atom-thick platform for infrared metamaterials and transformation optical devices. Varying the graphene chemical potential by using static electric field, the authors had shown tunable conductivity in the THz and infrared frequencies. Horng et al.[95] reported measurements of high-frequency conductivity of graphene from THz to mid-IR at different carrier concentrations. The conductivity exhibited Drude like frequency dependence and increased dramatically at THz frequencies, but its absolute strength was lower than theoretical predictions. This anomalous reduction of free-electron oscillator strength was corroborated by corresponding changes in graphene inter-band transitions,

---

as required by the sum rule. Jnawali et al.[96] measured the THz frequency dependent sheet conductivity and its transient response following femtosecond optical excitation for single-layer graphene samples grown by chemical vapour deposition (CVD). The THz conductivity was analysed using Drude model, which yielded an average carrier scattering time of 70 fs. Upon photoexcitation, they observed a transient decrease in graphene conductivity. The THz frequency-dependence of the graphene photo-response differed from that of the unexcited material but remained compatible with a Drude form. They showed that the negative photoconductive response arises from an increase in the carrier scattering rate, with a minor offsetting increase in the Drude weight. The photo-induced conductivity transient had a picosecond lifetime and was associated with non-equilibrium excitation conditions in the graphene. Bonaccorso et al.[97] wrote a review on the different synthesis procedure of graphene and its use in opto-electronic devices. Ju et al.[98] explored plasmon excitations in engineered graphene micro-ribbon arrays and demonstrate that graphene plasmon resonances could be tuned over a broad THz frequency range by changing micro-ribbon width and electrostatic doping. The ribbon width and carrier doping dependences of graphene plasmon frequency demonstrated a power-law behaviour characteristic of 2D massless Dirac electrons. Vicarelli et al.[99] demonstrated THz detectors operating at 0.3 THz based on antenna-coupled graphene field-effect transistors by exploiting the nonlinear response to the oscillating radiation field at the gate electrode, with contributions of thermoelectric and photoconductive origin. Lee et al.[100] demonstrated substantial gate-induced persistent switching and linear modulation of THz radiation by inserting an atomically thin, gated 2D graphene layer in a 2D metamaterial. Their device could modulate both the amplitude of the transmitted wave by up to 47% and its phase by  $32.2^\circ$  at room temperature. Hwang et al.[101] reported strong THz-induced transparency in CVD grown graphene where 92-96% of the peak-field is transmitted compared to 74% at lower field strength. TRTS studies revealed that the absorption recovered in 2-3 ps. The induced transparency was believed to be arising from nonlinear pumping of carriers in graphene, which suppressed the mobility, and consequently the conductivity in a spectral region where the light-matter interaction is particularly strong. Xia et al.[102] showed ultrafast transistor-based photodetectors made from single and few layer graphene whose photo-response remained un-degraded for optical intensity modulations up to 40 GHz. Meang et al.[103] measured the frequency dependent optical sheet conductivity of graphene which showed electron-density dependence characteristics, and can be understood by a simple Drude model. In a

---

low carrier density regime, the optical sheet conductivity of graphene was constant regardless of the applied gate voltage, but in a high carrier density regime, it showed nonlinear behaviour with respect to the applied gate voltage.

Shen et al.[104] used THz absorption and spectroscopic ellipsometry to investigate the charge dynamics and electronic structures of CVD grown monolayer MoS<sub>2</sub> films. THz conductivity displayed a coherent response of itinerant charge carriers at zero frequency. Drude plasma frequency ( $\sim 7$  THz) was found to be decreasing with decreasing temperature while carrier relaxation time ( $\sim 26$  fs) remained temperature independent. The absorption spectrum of monolayer MoS<sub>2</sub> showed a direct 1.95 eV band gap and charge transfer excitations that were  $\sim 0.2$  eV higher than those of the bulk counterpart. Docherty et al.[105] measured the ultrafast charge carrier dynamics in monolayers and tri-layers of MoS<sub>2</sub> and WSe<sub>2</sub> using a combination of time-resolved photoluminescence and TRTS. They observed a photoconductivity and photoluminescence response time of 350 fs from CVD grown monolayer MoS<sub>2</sub>, and 1 ps from trilayer MoS<sub>2</sub> and monolayer WSe<sub>2</sub>. Lui et al.[106] observed a pronounced transient decrease of conductivity in doped MoS<sub>2</sub>, using ultrafast TRTS. In particular, the conductivity was reduced to only 30% of its equilibrium value at high pump fluence. This anomalous phenomenon arises from the strong many-body interactions in the 2D system, where photo-excited electron-hole pairs joined the doping-induced charges to form trions, bound states of two electrons and one hole. The resultant substantial increase of the carrier effective mass helped in diminishing the conductivity. Kar et al.[107] reported the dynamics of photo-induced carriers in a free-standing MoS<sub>2</sub> laminate consisting of a few layers (1-6 layers) using TRTS. The relaxation of the non-equilibrium carriers shows both the fast and slow relaxation dynamics. They established that the fast relaxation time occurred due to the capture of electrons and holes by defects via Auger processes, while the slower relaxation happened since the excitons are bound to the defects, preventing the defect-assisted Auger recombination of the electrons and the holes. Kong et al.[108] theoretically demonstrated the feasibility of ultra-high-frequency operation in a vertical three-terminal electronic device by exploiting the advantages of 2D crystal heterostructures. They modelled a gapped 2D material as the tunnel barrier between a graphene base and a metallic emitter, while the Schottky contact with an *n*-type substrate formed the base-collector junction. With proper optimization, they showed that their device was capable of reaching the intrinsic cut-off frequencies over a few THz even under realistic constraints, indicating a technological pathway beyond the current limit. Cao et al.[109] demonstrated a new type of optically

---

tunable THz modulator based on multilayer MoS<sub>2</sub> and silicon. They showed that the THz transmission could be significantly modulated by changing the power of the pumping laser and the modulation was better than graphene based devices. Lee et al.[110] for the first time reported MoS<sub>2</sub> based metal semiconductor field-effect transistors (MESFETs) with NiO<sub>x</sub> Schottky electrode, where the maximum mobilities or carrier transport behaviour of the Schottky devices may hardly be interfered by on-state gate field. Our MESFETs with single-, double-, and triple-layered MoS<sub>2</sub> respectively showed high mobilities of 6000, 3500, and 2800 cm<sup>2</sup>/Vs at a certain low threshold voltage of -1 ~ -2 V. The thickness-dependent mobility difference in MESFETs was theoretically explained with electron scattering reduction mechanisms.

# **Chapter Three**

## 3. Instruments and Data Analysis

---

---

### 3.1. THz Time Domain Spectrometer

A compact and affordable table-top THz spectrometer, developed by Menlo Instruments and named as Tera K8 Terahertz Spectrometer, is being used for all the THz measurements. The detailed description of different components of the instrument is given below.

The list of components that are needed to develop the spectrometer is the following;

- 1) [T-Light 780 \(a femtosecond fibre laser\)](#)
- 2) [Absorptive Neutral Density Filter](#)
- 3) [Mirrors](#)
- 4) [Wave Plates](#)
- 5) [Polarizing Beam Splitter](#)
- 6) [Motorized Delay Stage and Vibration Generator](#)
- 7) [Antenna for Generation and Detection of THz Waves](#)
- 8) [Direct Digital Synthesizer](#)
- 9) [Lock-in-Amplifier](#)
- 10) [Oscilloscope](#)
- 11) [Working Principle](#)
- 12) [Alignment of the THz Spectrometer](#)

The set-up is covered with a glass-top and we purge extra-pure N<sub>2</sub> gas into the covered area and keep the humidity strictly < 10% inside the whole box to get rid of unwanted water vapours affecting our measurements.

#### 3.1.1. T-Light 780

This is an erbium doped fiber laser with 780 nm and 65 mW output. The fiber laser uses the same physics principles as any other laser, but there are several properties that made it special and very useful. Unlike a conventional laser which is constructed from components such as mirrors, dispersive crystals, rods and lenses, fiber laser is an all bulk material device. The laser rod is effectively substituted by several meters long doped active fiber. The rest of the components are also all fibre devices each of which are spliced together to form a laser resonator. There is no need for alignment, adjustment or subsequent cleaning of optical surfaces once the laser has been built, which means little or effectively no maintenance is required.

---

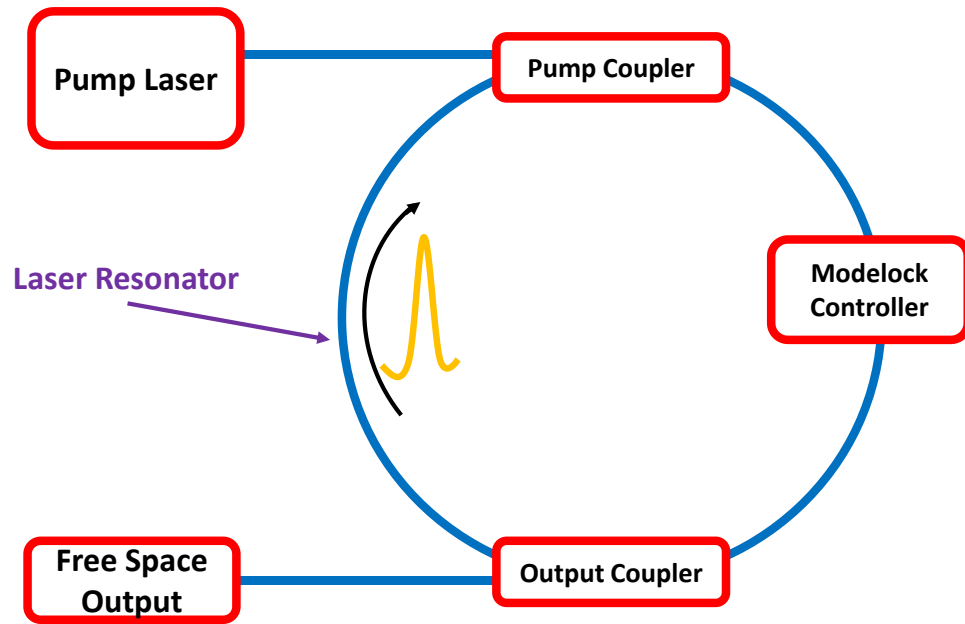


**Fig. 3.1: Schematic of the fiber laser working principle**

Very small amount of rare earth material erbium is added to the core of the glass fibre to prepare the erbium doped fibre laser. The erbium atoms have very useful energy levels. There is an energy level that can absorb photons with a wavelength of 980nm, and then it decays to a meta-stable state of 1560 nm. A diode laser of 980 nm is used to pump the fibre laser via a pump coupler and we get an output of 1560 nm. The microcontroller driven actuators built into the fiber ring rotate and maintain stable mode-locking automatically. The mode-lock controller consists of four wave plates and these can be rotated along their axis manually or automatically using a rotatable motor via a software interface. The fundamental wavelength at 1560 nm is then efficiently frequency doubled using a periodically poled lithium niobate crystal via second harmonic generation technique, which offers higher quasi phase matching, and therefore high conversion efficiency when compared to conventional wavelength conversion crystals, and we get a 780 nm laser beam in free space.  $ER^{3+}$  doped silica fiber is used as gain medium instead of a laser crystal. The schematic of the working principle of the fibre laser is shown in Fig. 3.1. The main features of the laser are tabulated below:

1. Repetition rate:  $100 \text{ MHz} \pm 1 \text{ MHz}$
2. Centre wavelength:  $780 \pm 10 \text{ nm}$
3. Average output power:  $\sim 65 \text{ mW}$
4. Pulse width: 100-120 fs
5. Polarization: Linearly Polarized

### 3.1.2. Second Harmonic Generation

Second harmonic generation (SHG; also called frequency doubling) is a technique via which the fundamental wavelength is passed through a non-linear crystal and is frequency doubled i.e. wavelength becomes half of its fundamental value. The non-linear material efficiently combines two incident photon of same energy to a new photon of twice the energy. The optical response of a material can be written as;

$$\vec{P} = \varepsilon_0 \chi \vec{E}, \quad (21)$$

where,  $\chi$  is the susceptibility tensor,  $\vec{P}$  is the polarization vector and  $\vec{E}$  is the electric field vector. Now, if we expand the above equation in a Taylor series each component of the polarization vector  $P_k$  ( $k = x, y, z$ ) can be written as;

$$P_k = \varepsilon_0 (\chi_{ij}^1 E_i + \chi_{ijk}^2 E_i E_j + \chi_{ijkl}^3 E_i E_j E_k + \dots), \quad (22)$$

where, the coefficients  $\chi^n$  correspond to the tensor of the n-th order nonlinear process. We can consider up to 2<sup>nd</sup> order non-linear process for sufficiently strong incident radiation for most of the practical applications. If we write the incident radiation component as  $E_i = \mathcal{E}_i \exp(-i\omega t) + c. c$ , then the 2<sup>nd</sup> order non-linear term of k<sup>th</sup> component of polarization can be written as;

$$P_k^2(nl) = \varepsilon_0 (\chi_{ijk}^2 \mathcal{E}_i \mathcal{E}_j \exp(-i2\omega t) + c. c + \mathcal{E}_i \mathcal{E}_j^* + \mathcal{E}_i^* \mathcal{E}_j). \quad (23)$$

Neglecting the d.c. term, we can see that a polarization component arises with a frequency twice to that of the fundamental incident radiation. This polarization component gives rises to the frequency doubled radiation. The SHG is possible only with non-linear crystals having broken inversion symmetry and strong incident radiation.

### 3.1.3. Periodically Poled Lithium Niobate Crystal

Periodically poled lithium niobate crystals (PPLN) are highly efficient, engineered, and quasi-phase matched non-linear material for SHG. For effective non-linear frequency doubling, it is necessary that the phase relation of the incident and generated photons remain constant throughout the length of the crystal otherwise the photons will destructively interfere and the resultant intensity for frequency doubled photons will be negligible. For a particular wavelength, we can calculate the length ( $l_{nl}$ ) of the crystal when the phase of the generated photon of frequency  $2\omega$  will be  $180^\circ$  out of the phase with the incident photon of frequency  $\omega$ . Lithium niobate (LN) being a ferroelectric material,

its structural direction can be flipped spatially by introducing a spatially variable electrode and strong radiation. Thus, LN is periodically poled with a period determined by  $l_{nl}$ , as a result, the number of generated photons will grow as the light propagates through the PPLN, yielding a high conversion efficiency of input to generated photons. The fundamental wavelength 1560 nm of the Erbium doped fiber laser can be effectively converted to the 780 nm laser light by frequency doubling in the PPLN crystal, which offers higher quasi phase matching and therefore high conversion efficiency when compared to conventional wavelength conversion crystals. The PPLN crystal used in the setup has multiple grating structures. This allows phase matching to a wide range of wavelengths via combination of temperature and selection of poled period.

### 3.1.4. Absorptive Neutral Density Filter

We use two filters directly after the laser beam output i) to get rid of any unwanted 1560 nm laser in the output beam and ii) to get the required laser power for the excitation of THz generator and THz detector antenna.

The first absorber  $A_1$  with an optical density of 0.05 ( $T \sim 89\%$  at 780 nm) is mainly used to get rid of any unwanted 1560 nm signal present in the laser beam. Then ( $A_2$ ) a neutral density filter (NE506A, ThorLabs) with optical density 0.5 ( $T \sim 35\%$  at 780 nm) is used to reduce the laser power at 780 nm at a value ( $\sim 20$  mW) which is suitable for THz generator and detector antenna excitation otherwise they will get burnt due to excessive laser heating.

### 3.1.5. Mirrors

Silver-coated highly reflecting mirrors (PF10-03-PO1, ThorLabs) are used to guide the 780 nm laser beam through the setup. A  $\text{SiO}_2$  coating of 100 nm is applied on the coated surface to prevent oxidation. The typical reflectivity of these mirrors at 780 nm is  $> 97.5\%$ , thereby ensuring negligible power loss even after multiple passes.

### 3.1.6. Wave Plates

Wave plates are made of birefringent crystal (Quartz, Mica) of appropriate thickness such that they change the polarization state of the light beam passing through it. The crystal is cut into a plate in such a way that the optic axis of the crystal is parallel to the surfaces of the plate. These results in two axes in the plane of the cut: the ordinary axis, with index of refraction  $n_o$ , and the extraordinary axis, with index of refraction  $n_e$ . The ordinary axis

---

is perpendicular to the optic axis. The extraordinary axis is parallel to the optic axis. For a normally incident light beam, polarization component along the ordinary axis travels through the crystal with a speed  $v_o = \frac{c}{n_o}$ , while the polarization component along the extraordinary axis travels with a speed  $v_e = \frac{c}{n_e}$ . This leads to a phase difference ( $\Gamma$ ) between the two components as they exit the crystal. The relative phase that is imparted between the two components for a crystal length  $L$  and wavelength  $\lambda_0$  is given by the following relation;

$$\Gamma = \frac{2\pi(n_e - n_o)L}{\lambda_0}. \quad (24)$$

Quarter wave plates introduce a phase shift of  $\frac{\pi}{2}$  and half wave plates introduce a phase shift of  $\pi$  between the two components and thereby changing the polarization state of the emitting light beam. Linearly polarized light from laser falls on a half wave plate ( $W_1$ ) in such an angle that it becomes diagonally polarized. This diagonally polarized light is incident on a polarizing beam splitter and  $p$ -polarized light is transmitted and  $s$ -polarized light is reflected. The reflected  $s$ -polarized light passes through a quarter wave plate ( $W_2$ ) at  $45^\circ$ , falls on a mirror mounted on a motorized delay stage and reflects back through  $W_2$  and thereby changing its polarization state orthogonally i.e. become  $p$ -polarized.

### 3.1.7. Polarizing Beam Splitter

A polarizing beam splitter (PBS) is an optical device which can split any unpolarized light beam into two light beams with mutually orthogonal ( $s$  and  $p$ ) polarization. Two birefringent prisms of same material are mounted together using a commercial gum such that their optic axis remains perpendicular to each other. The light whose polarization is perpendicular to the optic axis of the 1<sup>st</sup> prism passes un-deviated through it and the other polarized light reflects at the interface of two prisms and deviated by  $90^\circ$ . Designed for broadband applications, TECHSPEC® broadband polarizing cube beam-splitters offer a transmission of greater than 90% for  $p$ -polarized light and a reflection efficiency of greater than 99% for  $s$ -polarized light across the entire design wavelength range. Each beamsplitter consists of a pair of precision high tolerance right angle prisms cemented together with a dielectric coating on the hypotenuse of one of the prisms. An anti-reflection coating (ARC) has been applied to each face of the beamsplitter to achieve less than 0.5% reflection per surface.

### 3.1.8. Motorized Delay Stage and Vibration Generator

The motorized delay (Physik Instrumente, PI-M403.42S) stage offers a maximum 100 mm travel range, i.e. a time delay as high as 300 ps, which is extremely useful when measuring thick samples and their Fabry-Perot (FP) reflections. A two phase stepper motor (24 Volt, 4.8 W) with maximum speed of 6400 rev/minute and minimum incremental motion of 0.2  $\mu\text{m}$  is used to drive the delay stage.

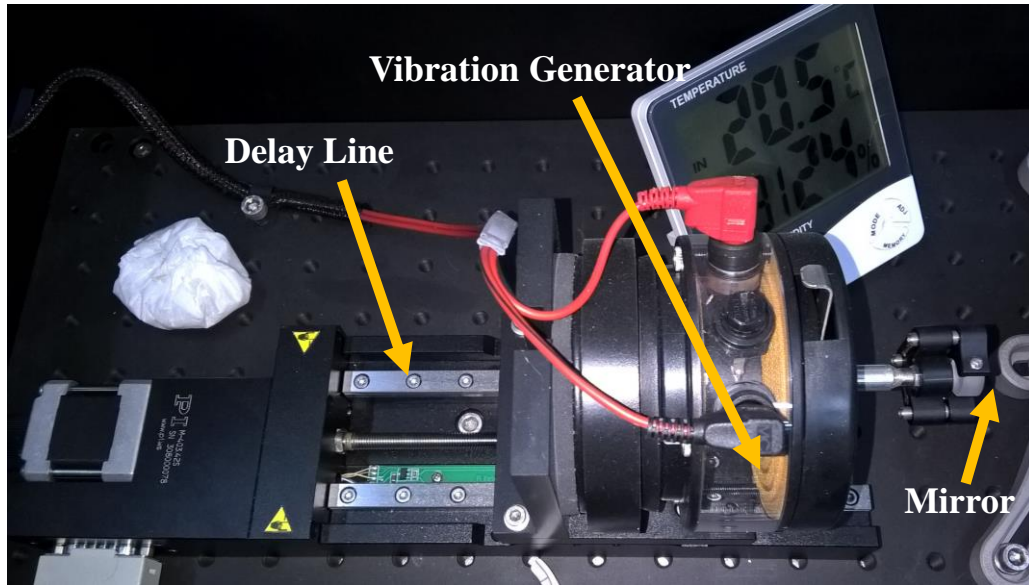


**Fig. 3.2: Motorized delay stage and vibration generator**

The vibration generator is mounted on this delay stage over which a mirror is attached to reflect the pump laser beam and to provide the required time delay between pump and probe laser beam. A small sinusoidal voltage (1-2 V, 3 Hz) is applied to this vibration generator to create the vibration. The mirror vibrates around its mean position. During alignment, this helps us to find the position of the THz peak and we also use it during peak-to-peak THz amplitude optimization. During experimental scan, this vibration generator remains off and only delay line operates.

### 3.1.9. Antenna for THz Generation and Detection

Similar types of PC antenna have been used both for THz generation and detection. LT-GaAs is used as the semiconductor substrate offering fast carrier recombination time due to increased defect state and on top of that a unique spiral-dipole Au antenna (dipole length = 20  $\mu\text{m}$  and dipole gap = 5  $\mu\text{m}$ ) has been deposited. The active region of the antenna is of the order of  $\sim 5 \mu\text{m}^2$ .

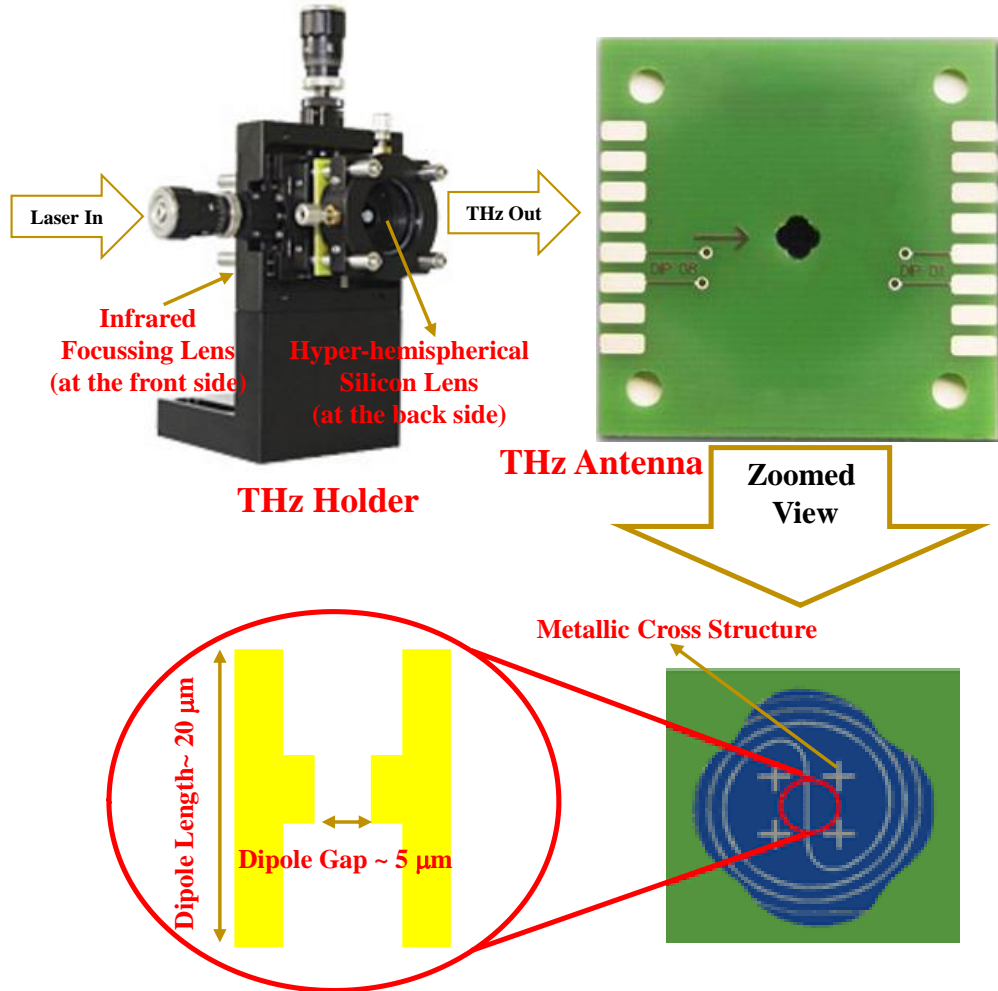


**Fig. 3.3: THz photo-conductive antenna**

An external bias voltage of 20V/30V (depending on the dark and photo current produced at the antenna at the time of experiment and also on the absorptive nature of the sample), 10 kHz is provided to the antenna for THz generation. The optical image of the THz antenna and the THz holder is shown in Fig. 3.3 and the zoomed in view schematically shows the dipole structure at the middle of the antenna and spiral structure at the periphery of the antenna. An infrared focussing lens ( $f = 7.5 \text{ mm}$ , ARC for 600-1050  $\text{nm}$ ) is used at the front side of the antenna to focus the laser beam at the THz antenna structure. A high resistive silicon lens is also used (hyper-hemispherical shape,  $\varphi = 10 \text{ mm}$ ) to focus the generated THz radiation in air (for THz emitter) and also to direct the incoming THz radiation efficiently into the THz dipole structure (for THz detector).

### 3.1.10. Direct Digital Synthesizer

It is basically a two channel waveform generator (MiniDDS) from Menlo Systems GmbH, which uses direct digital synthesis technique to generate highly stable and high voltage sine waves, square waves and d.c. in channel 1 and highly stable and high current sine wave (up to 1 A) in channel 2. The MiniDDS is operated with a touch screen and wheel knob. Remote computer operation is supported vis USB and RS232 interface. The optical image of the miniDDS and the lock-in amplifier is shown in Fig. 3.4.

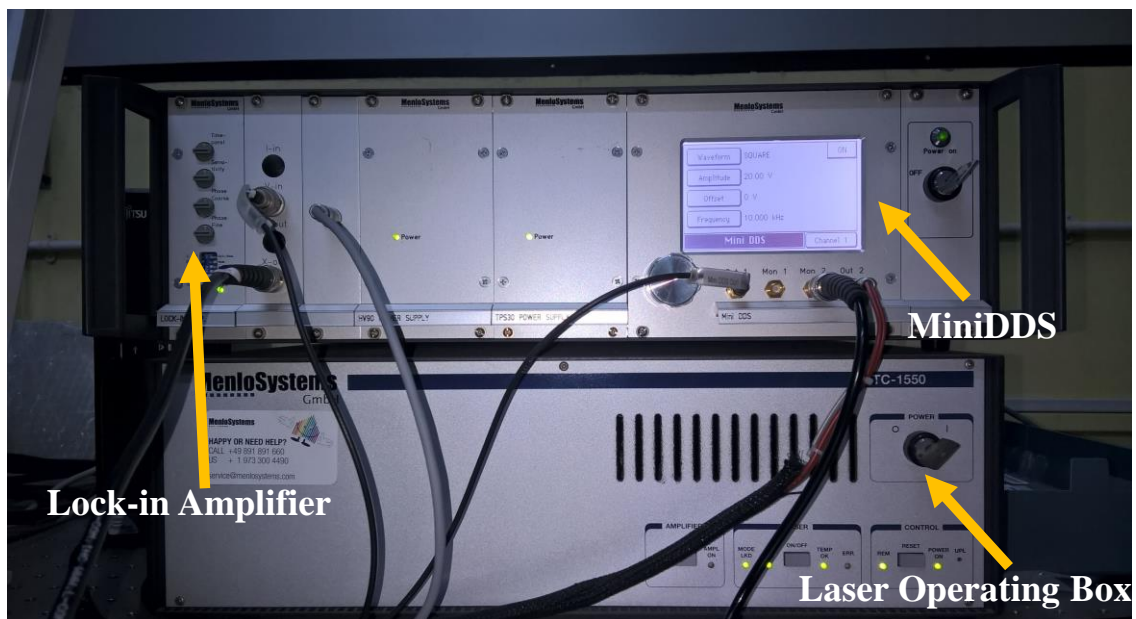


**Fig. 3.4: MiniDDS and lock-in amplifier**

For the control electronics it requires a power of  $\pm 15$  V and for the voltage amplifier in channel 1 it requires  $\pm 75$  V. The current amplifier in channel 2 require  $\pm 15$  V power. The specifications for the two channels are given below.

#### Channel 1

**Waveform:** Symmetric Sine Wave, Positive Sine Wave, Symmetric Square Wave, Positive Square Wave and DC. 50% Duty Cycle and the frequency range is 0-100 kHz with a frequency resolution of 1 Hz. Maximum current produced is 100 mA.

**Amplitude:** 0 V to 40 V, 0.25 V step resolution.

#### Channel 2

**Waveform:** Symmetric Sine Wave. 50% Duty Cycle and the frequency range is 0-100 kHz with a frequency resolution of 1 Hz. Maximum RMS current produced is 1 A.

---

**Amplitude:** 0 V to 10 V, 0.1 V step resolution.

### 3.1.11. Lock-in Amplifier

A lock-in or phase-sensitive, amplifier is a type of amplifier that can extract a signal with a known carrier wave from an extremely noisy environment. It may also be looked upon simply as a fancy a.c. voltmeter. Along with the input, one supplies it with a periodic reference signal. The amplifier then responds only to the portion of the input signal that occurs at the reference frequency with a fixed phase relationship. Depending on the dynamic reserve of the instrument, signals up to 1 million times smaller than noise components, potentially fairly close by in frequency, can still be reliably detected. By designing experiments that exploit this feature, it's possible to measure quantities that would otherwise be overwhelmed by noise. Lock-in amplifier is an integrated part of any time of spectroscopic precision measurement technique. In the present THz spectrometer, we use a lock-in amplifier to efficiently record the THz spectra. The control parameters of the lock-in amplifier is added as an additional menu in the MiniDDS system, from where (touch screen) we can change the time constant, sensitivity and phase parameters of the lock-in amplifier. The simplified working procedure of a typical lock-in amplifier is given below. Let us consider a sinusoidal a.c. signal of the form:  $V_{in}(t) = V_0 \sin(\omega t + \phi)$ . Suppose we also have a reference signal as  $V_R(t) = V_0 \sin(\Omega t)$ . The product of these two signals gives beats at sum and difference frequency,

$$V_{in}(t)V_R(t) = \frac{V_0}{2} \{ \cos[(\omega - \Omega)t + \phi] - \cos[(\omega + \Omega)t + \phi] \}. \quad (25)$$

When the input signal has a frequency different from the reference frequency  $\Omega$ , the product oscillates in time with an average value of zero. However, if  $\omega = \Omega$  we get a sinusoidal output, offset by a d.c. (zero frequency) level,

$$V_{in}(t)V_R(t) = \frac{V_0}{2} \{ \cos[\phi] - \cos[2\omega t + \phi] \}; \quad \omega = \Omega. \quad (26)$$

If we can extract the d.c. component of this product, and are able to adjust  $\phi$ , we get a direct measure of the signal amplitude  $V_0$ .

The schematic of the working procedure of a simple lock-in amplifier is given in Fig. 3.5. The input signal  $V_{in}(t)$  passes through a capacitor, blocking any pre-existing d.c. offset, and is then amplified. The reference signal  $V_R(t)$  passes through an adjustable phase-shifter ( $\phi$ ). These two results are then multiplied, and any resulting d.c. component is extracted by the low-pass filter. In the THz spectrometer, a square wave a.c. voltage

---

(30 V, 10 kHz) is applied at the THz generator antenna for the efficient generation of THz radiation. So, a frequency modulation of 10 kHz in the emitted THz field is inherently introduced. The input voltage is modulated at 10 kHz and the same reference signal is provided at the lock-in amplifier for the phase sensitive detection of THz signal.

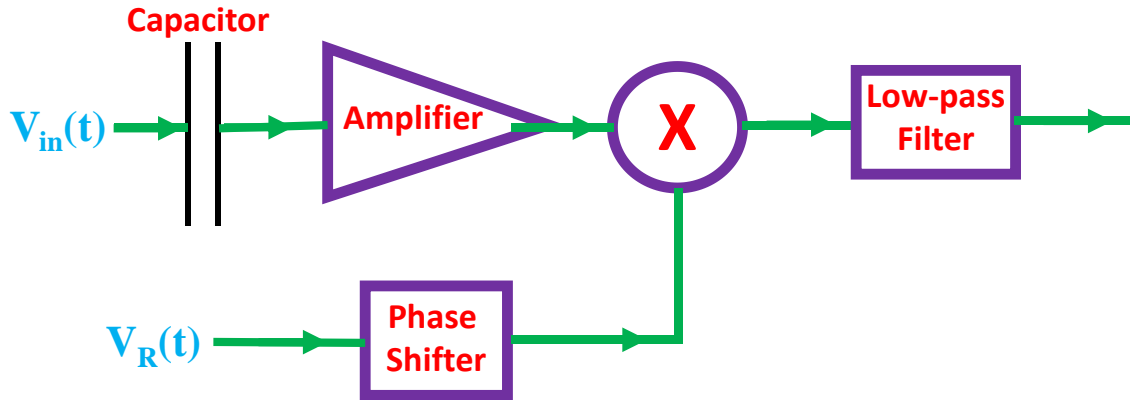


**Fig. 3.5: Schematic of working principle of a lock-in amplifier**

The reference frequency is chosen in such a way that it is much larger than the electrical connection frequency (50 Hz) and also much smaller than the THz frequency.

### 3.1.12. Oscilloscope

An oscilloscope, previously called an oscillograph and informally known as a scope, CRO (for cathode-ray oscilloscope), or DSO (for the more modern digital storage oscilloscope), is a type of electronic test instrument that allows observation of constantly varying signal voltages, usually as a 2D plot of one or more signals as a function of time. Other signals (such as sound or vibration) can be converted to voltages and displayed. We have used such a DSO (Tektronix, DPO 4104B-L) in our lab to monitor the THz signal especially during laser alignment as shown in Fig. 3.6. An analog oscilloscope works by directly applying a voltage being measured to an electron beam moving across the oscilloscope screen. The voltage deflects the beam up and down proportionally, tracing the waveform on the screen. This gives an immediate picture of the waveform. In contrast, a digital oscilloscope samples the waveform and uses an analog-to-digital converter (ADC) to convert the voltage being measured into digital information. Finally, it converts the resulting signal in a picture format to be displayed on the screen of the scope. Since the waveform is stored in a digital format, the data can be processed either within the oscilloscope itself, or even by a computer connected to it. One advantage of using the DSO is that the stored data can be used to visualize or process the signal at any time. Another

important advantage of DSO compared to analogue instruments is the possibility of internally executing some calculations on the stored data.

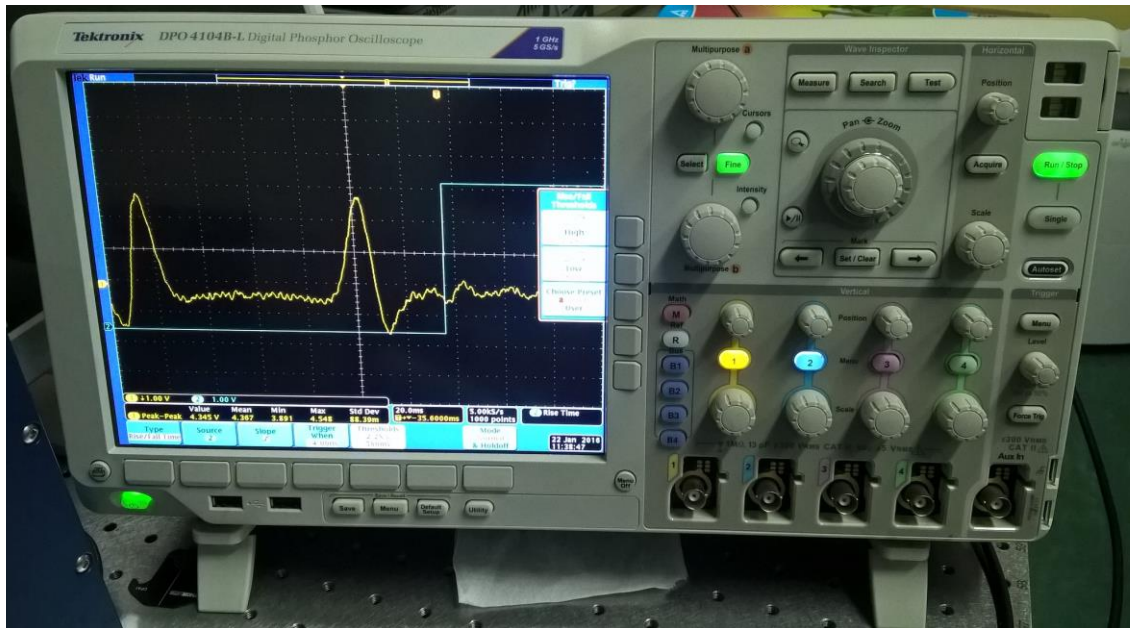


**Fig. 3.6: Digital oscilloscope**

Thus peak values of signals, temporal and amplitude differences, time periods, signal frequencies etc. are easy to measure. The analog to digital conversion is not continuous, but at discrete periodic times, the so called sampling points. The frequency at which a signal is scanned is determined by the sampling rate or sampling frequency ( $f_a$ ); its reciprocal value is the sampling interval ( $T_a = 1/f_a$ ). The higher the sampling rate  $f_a$ , that is the smaller  $T_a$ , the more precisely the temporal course of the input signal can be represented. The DSO used for the measurements has a sampling rate of 5 GHz/s and bandwidth of 1 GHz. According to the sampling theorem, the highest possible sampling frequency  $f_a$  simultaneously determines the maximum frequency  $f_s$  of a harmonic input signal that can be acquired by a DSO. The correct signal recording the condition is given below, otherwise error will occur.

$$f_a > 2f_s \quad (27)$$

So, it is pretty obvious that we cannot truly measure THz radiation using the Tektronics oscilloscope. During the alignment, we actually perturb or modify the THz wave at a particular frequency (3 Hz, from channel 2 of the MiniDDS) using the mechanical oscillation of the mirror attached with the delay stage using the vibration generator. So, the THz waves oscillate at a much lower frequency (3 Hz) and we measure the peak-to-

peak amplitude of this THz wave. During laser alignment, we optimize this peak-to-peak voltage by properly focussing the laser spot at the dipole gap. Another important factor of a DSO is its bandwidth. We know, the more the bandwidth, the more it will cost. The bandwidth of an oscilloscope actually indicates the point at which the measured amplitude on an amplitude/frequency chart has decreased by -3 dB (or 70.7%) of the original value. The measure frequency will be good up to and perhaps even slightly beyond the maximum rating of the scope, but at the maximum rated frequency, the amplitude will be  $\sim 70\%$  the actual value. So if we are measuring 5 V signal at the highest frequency, it will actually show up as  $\sim 3.5$  V. We need to be careful not only about the bandwidth of the oscilloscope but the about the bandwidth of the probe as well. The other important feature of a DSO is its rising time. The faster the rise time, the more accurately we can measure the fast transitions in the signal. Rise time is defined as,

$$t_r = k / \text{bandwidth}, [k \sim 0.35 - 0.45]. \quad (28)$$

To measure a 4 ns rising time, ideally one should have a DSO with 800 ps rise-time.

### 3.1.13. Working Principle

We get a 780 nm laser beam in free space from the erbium doped fiber laser after frequency doubling. A frequency selective filter (transmission close to 1 in 400-800 nm and close to 0 beyond that) blocks any unwanted 1560 nm laser that might be present in the output and passes only the 780 nm laser. A neutral density filter with optical density  $\left(OD = -\log \frac{P_{out}}{P_{in}}\right)$  0.5 is used to control the power of the laser, which restricts the output laser to the desired level (20 mW). The linearly polarized (*s*-polarized) 20 mW output laser is now reflected through two lenses before passing through a half wave plate and changes the angle of the linear polarization from vertical to approximately  $45^\circ$  between horizontal and vertical. Now, this diagonally polarized light is incident upon a polarizing beam splitter (PBS) which splits the beam into two parts that are commensurate with the projection of that “diagonal” polarization onto the vertical (*s*-polarized) and horizontal (*p*-polarized) axes of the beam splitter. *P*-polarized beam transmits through the PBS and goes to the THz detector antenna. The *s*-polarized passes through the quarter wave plate at  $45^\circ$  angle, becomes circularly polarized, gets reflected from a mirror attached on the tip of a vibrator mounted on the motorized delay stage, again passes through the quarter wave plate and becomes *p*-polarized. This beam passes through the PBS and excites the THz emitter antenna guided by two mirrors. The THz antenna is basically a gold dipole-

spiral structure fabricated on top of LT-GaAs semiconductor substrate with a dipole gap or active region of 5  $\mu\text{m}$ . The emitter antenna is externally biased with a 30 V square wave of frequency 10 kHz (this frequency is later used as the reference of the lock-in amplifier). The generated THz radiation passes through a pair of focussing polymer lenses and gets focussed on the sample plane. THz radiation passes through the sample (undergoes changes depending on the sample characteristics) and advances towards the THz detector antenna, which is gated by the other part of the  $p$ -polarized laser beam. TPX polymer lenses are used because the material (TPX) has a very small absorption coefficient in the THz frequency range.

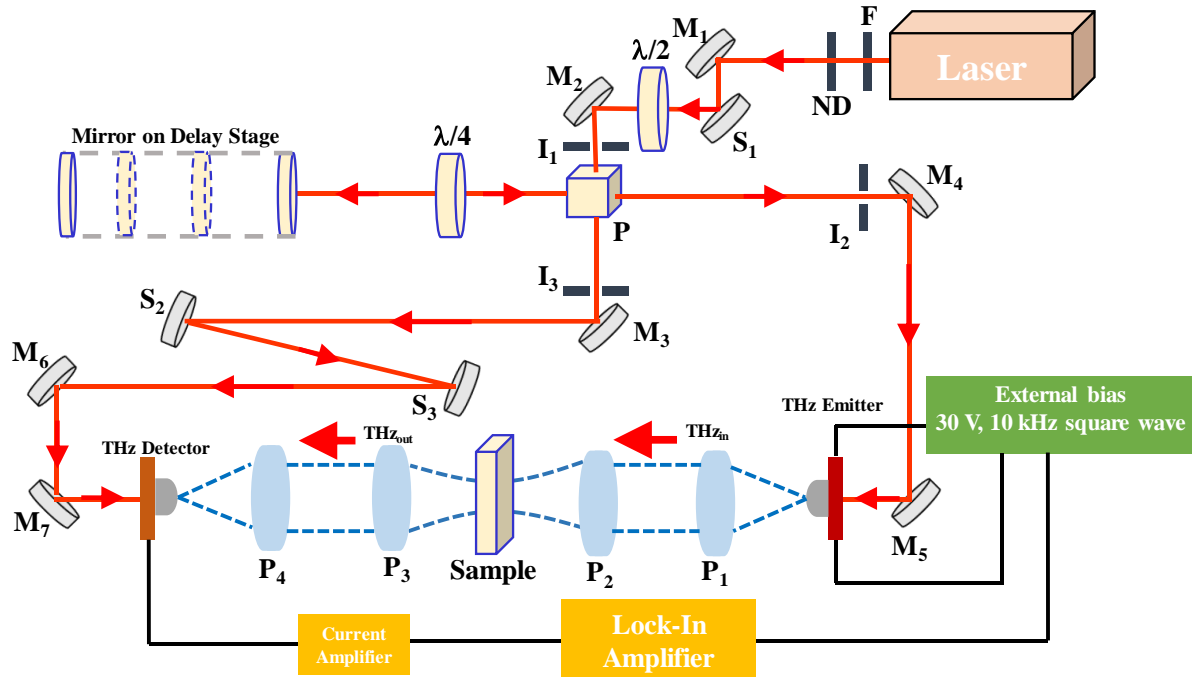


**Fig. 3.7: Schematic of the THz spectrometer**

No external voltage is applied at the detector antenna as the THz voltage itself acts as the bias voltage to manipulate the detector current, which is detected in a coherent fashion using a voltage amplifier and a lock-in amplifier. By varying the motorized delay stage, we can introduce up to 300 ps time delay between the pump and the probe laser beam and thereby we can map the full THz spectrum in time domain with at least two FP reflections even with samples with significant optical thickness. The whole set up is covered with a glass-top and the internal environment is purged with ultrapure nitrogen gas (> 99% pure  $\text{N}_2$  gas) to get rid of the unwanted water vapour absorption lines in the obtained THz spectra. The spectral range essentially extends from 0.1-3.5 THz with

highest S/N ratio of 50 dB at 0.4 THz which then reduces to 30 dB at 3.5 THz. 3.5 THz. The schematic of the spectrometer is shown in Fig. 3.7.

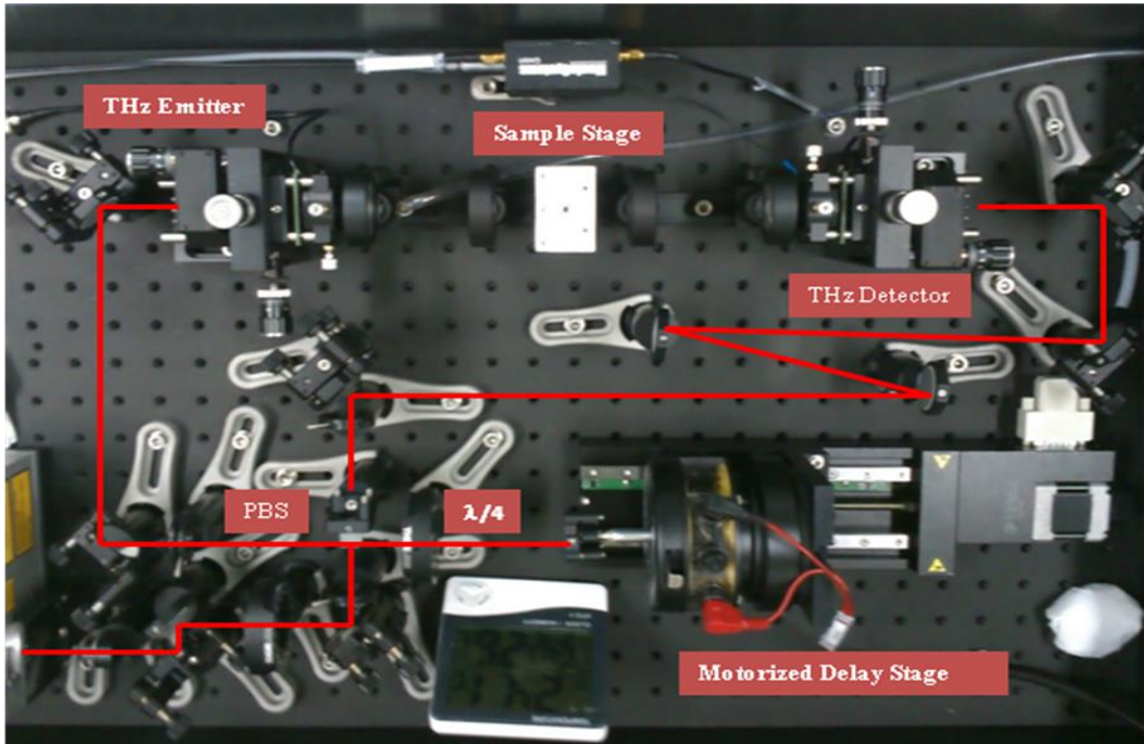


**Fig. 3.8: Optical image of the THz spectrometer**

When a THz pulse is incident on a sample it undergoes an amplitude reduction according to the absorption characteristics of the sample and a finite time shift with respect to the THz radiation passing through air due to the finite optical thickness of the sample. We analyze the transmission spectra of the sample to obtain the complex refractive index of the sample using Fresnel's transmission coefficient. The complex dielectric function and the complex conductivity of the sample can be extracted from the complex refractive index of the system. The optical image of the THz Spectrometer (Tera K-8) is shown in Fig. 3.8.

### 3.1.14. Alignment of the Spectrometer

The THz spectrometer from Menlo systems is in general very stable and does not require daily alignment. But, if the laser gates misaligned or if we need to change the emitter or detector, we need to thoroughly align the THz spectrometer. The alignment procedure is explained in detail in the following paragraph.

1. At first, we need to check the power of the fiber laser. Immediately after the laser output head, we have a filter to block any unwanted 1560 nm laser output that might

be present in the system. After removing this filter and the ND filter, we check the laser power. The laser power is in general  $\sim 65$  mW. After putting the filters, the laser power should be 20 mW, which gets divided equally after the PBS in the two arms.



**Fig. 3.9: Control panel of the FiberLaser software**

So, both in the emitter and detector arm, laser power would be  $\sim 10$  mW. The laser power can be increased by optimizing the mode-lock state, but one should be careful that the power does not exceed beyond 10 mW in any arms. If the laser is emitting, then it is in the mode lock state. But, sometimes a new optimized mode-lock state increases the output power of the laser. We can search for a new mode-lock state (only if the laser power at the output is less than 60 mW) using the software namely FiberLaser associated with the laser system. The basic window displays the laser power button, the mode-lock and the temperature status. The position of the four waveplates can also be seen in the control panel. The image of the control panel of this software is shown in Fig. 3.9. There are two different mode-lock options; i) global mode lock search and ii) vicinity mode-lock search. Global mode-lock search is the default process and it performs a wide search (rotate the waveplates) and tries to reach a maximum waveplates combination and runs until a

mode-lock state is found. In case of vicinity mode-lock search, all the waveplates move together in a small range or the waveplates move inside the same range but one at a time. Manual adjustment of the waveplates using the scroll bars is also possible but not recommended. Memory bank remembers the position of waveplates for the last eight mode-lock states and can be recalled. When the laser is turned on, the mode-lock search tab and controls window is enabled, showing the current position of the waveplates and using these controls it is possible to perform automatic mode lock search. The AC value characterizes the quality of the mode-lock state and the DC value is proportional to the average power in the fundamental wavelength of the laser. The optimized laser power can be verified using the power meter and a qualitative idea can be obtained by checking the higher AC and DC value provided by the software. Sometimes, it also happens that although the laser power after P is  $\sim 20$  mW, they are not evenly distributed along the emitter and detector arm. Then we need to adjust the two wave plates ( $\lambda/2$  and  $\lambda/4$ ) such that the polarization state of the laser gets properly modified and hence the laser power gets distributed evenly along the two arms.

2. After the laser power is optimized, we need to make sure that the laser pulse passes through the three irises ( $I_1$ ,  $I_2$  and  $I_3$ ) by adjusting the mirrors  $M_1$ ,  $M_2$  and the mirror attached at the delay stage.

3. Guiding by the lenses, both the pump and probe laser pulse are made to pass through the view-pointer hanging in the THz emitter and detector holder (the emitter and detector antenna is already removed). At first we block the probe beam and remove all the TPX lenses ( $P_1$ ,  $P_2$ ,  $P_3$  and  $P_4$ ). The pump beam is made to go through the view-pointer hanging at the front side (the side which faces the pump laser) of the THz emitter holder and adjusted by using the  $M_4$  mirror (near adjustment). Then the view pointer is hanged at the backside (the side which faces the incoming THz beam) of THz detector holder and made to pass through it using the  $M_5$  mirror (far adjustment). This process is repeated until the pump laser passes through the view-pointer hanging on THz emitter holder and THz detector holder simultaneously. Similar procedure is applied to align the probe laser beam (after blocking the pump laser beam) using  $M_6$  and  $M_7$  mirrors. Now, both the pump and probe laser becomes parallel and coincides with each other and passes through the view pointers.

4. Now THz antennas are inserted in the THz emitter and THz detector holders. An infrared focussing lens is inserted on top of the antenna to focus the pump and probe

---

laser beam at the antenna. Both the antenna and holder are similar in nature and design. Silicon lenses are inserted at the front side of the antenna holders to guide THz waves effectively and in a unidirectional way into the free space. The four TPX lenses are also inserted between the two THz antennas to guide the generated THz wave to the detector antenna.

5. Now we try to measure the photo current for THz emitter antenna. An external bias voltage (20 V, d.c.) is applied at the antenna and moving the horizontal and vertical displacement screws we try to make sure the laser pulse hits the dipole region. This part is a bit tricky because the dipole active region is  $\sim 5 \mu\text{m}^2$  and we don't have any illumination system so that we can view the laser pulse falling on the antenna structure. Some metallic cross structures and concentric circles are therefore patterned on the antenna structure (shown in Fig. 3.3). Whenever laser beam falls on these structures, it reflects and the reflected beam can be viewed if we place a white card with a small hole in the path of the laser beam. The laser beam passes through the hole and the reflected beam falls on the white card. Thus seeing the reflection images, we get the idea about the position of the laser pulse on the antenna and by moving the horizontal and vertical screws, we coincide the dipole gap with the laser beam. When the laser beam falls near the dipole region, the photo current suddenly increases and we maximize this photocurrent. When the laser falls exactly at the dipole gap, a beautiful reflection pattern can be seen which confirms the position of the dipole. Similar techniques are also used to focus the probe laser beam on the THz detector antenna. The photo currents are in the range 20-30  $\mu\text{A}$  (for both the antennas at 20 V bias) depending on the laser alignment.

6. Now, a bias voltage (30V, 10 kHz) is provided to the THz emitter antenna and the detector antenna is attached with the current amplifier. A fast scan is performed to find the zero delay position (position of the THz peak).

7. Now, the delay is kept fixed at the zero delay position and vibration generator is started (channel 2 of the MiniDDS is ON and a sinusoidal voltage of 1V, 10 Hz is given) so that the mirror moves slowly around the THz peak position, time is set at 100  $\mu\text{s}$  and using an oscilloscope we can now view the THz pulse. If the pulse shape is distorted, it means that THz radiation is not getting properly focused and is not unidirectional. This can be rectified using the silicon lens position at the emitter and detector antenna and the position of the TPX lenses. Next, the THz peak to peak voltage is maximized using the small movement of the lenses ( $M_4$ ,  $M_5$ ,  $M_6$  and  $M_7$ ) and the horizontal and vertical displacement screws of the emitter and detector antennas. As we can directly observe the

---

THz pulse in oscilloscope, this adjustment is relatively easy although time consuming. Thus we can align the THz spectrometer. For a perfectly aligned setup, we get the following parameters as listed in Table 1.

**Table 1: Typical THz antenna parameters for an aligned THz spectrometer**

Optical Power at each antenna	DC Bias Voltage	Emitter Dark Current	Detector Dark Current	Emitter Photo Current	Detector Photo Current	AC Bias Voltage	THz peak-to-peak amplitude
10 mW at 780 nm	20 V	0.3 $\mu$ A	0.3 $\mu$ A	30 $\mu$ A	26 $\mu$ A	30 V, 10 kHz	8 (a.u.)

### 3.2. Scanning Electron Microscopy

Scanning electron microscope (SEM) is a type of electron microscope that produces images of a sample by scanning over it with a focused beam of electrons. The focused beam of high-energy electrons generates a variety of signals at the surface of solid specimens. The signals that derive from electron-sample interactions reveal information about the sample including external morphology (texture), chemical composition, and crystalline structure and orientation of materials making up the sample. Specimens can be observed in high vacuum, low vacuum and in environmental SEM specimens can be observed in wet conditions. The SEM is an instrument (schematic is shown in Fig. 3.10) that produces a largely magnified image (magnification ranging from 20X to 30,000X) by using electrons instead of light to form an image. A beam of electrons is produced at the top of the microscope by an electron gun. The electron beam follows a vertical path through the microscope, which is held within a vacuum. The beam travels through electromagnetic fields and lenses, which focus the beam down toward the sample. When the primary electron beam interacts with the sample, the electrons lose energy by repeated random scattering and absorption within a teardrop-shaped volume of the specimen known as the interaction volume, which extends from less than 100 nm to around 5  $\mu$ m into the surface. The size of the interaction volume depends on the electron's landing energy, the atomic number of the specimen and the specimen's density. The energy exchange between the electron beam and the sample results in the reflection of high-energy electrons by elastic

scattering, emission of secondary electrons by inelastic scattering and the emission of electromagnetic radiation, each of which can be detected by specialized detectors.

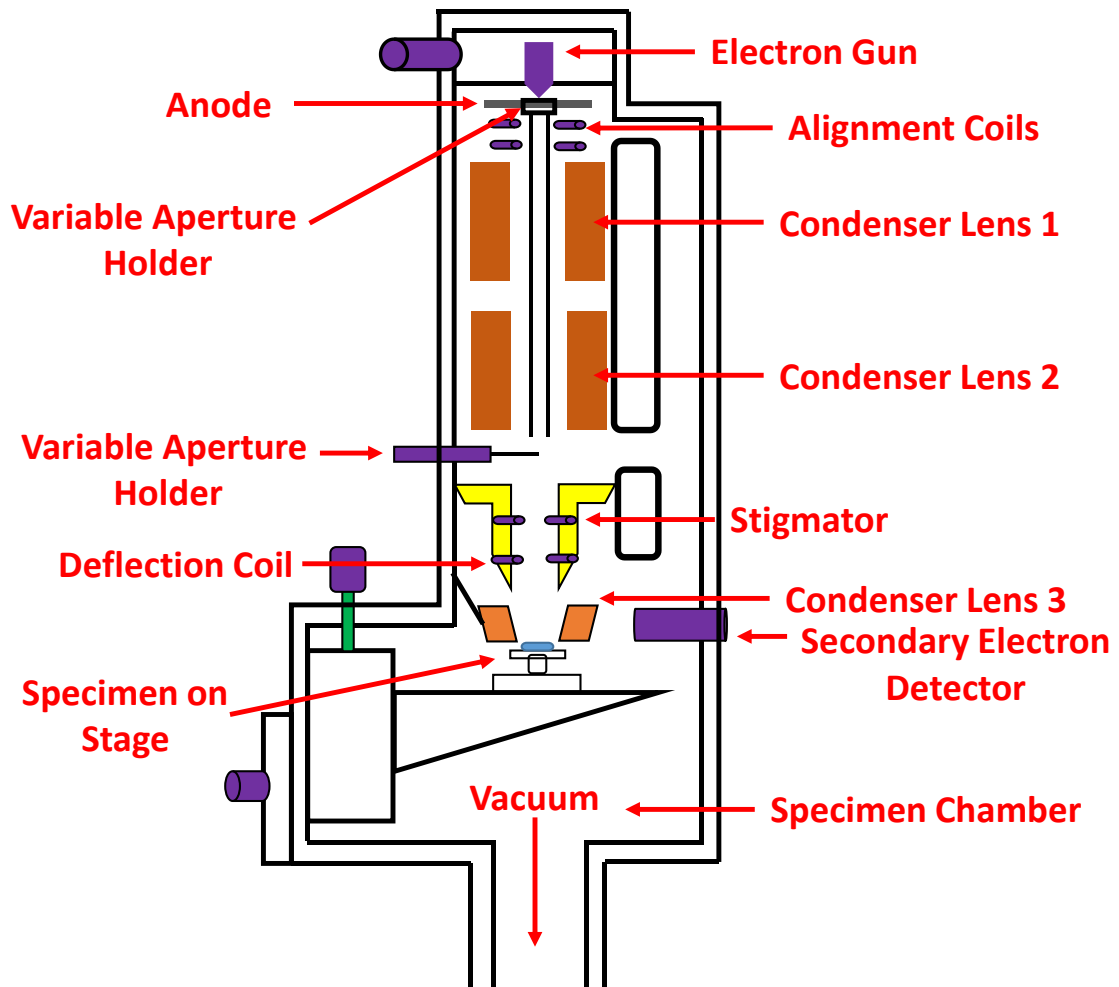


**Fig. 3.10: Schematic of scanning electron microscope**

Accelerated electrons in an SEM carry significant amounts of kinetic energy, and this energy is dissipated as a variety of signals produced by electron-sample interactions when the incident electrons are decelerated in the solid sample. These signals include secondary electrons (that produce SEM images), backscattered electrons (BSE), diffracted backscattered electrons (EBSD that are used to determine crystal structures and orientations of minerals), photons (characteristic X-rays that are used for elemental analysis and continuum X-rays), visible light (cathodoluminescence, CL), and heat. This is also schematically shown in Fig. 3.11. The secondary electrons are first collected by attracting them towards an electrically biased grid at about +400 V, and then further accelerated towards a phosphor or scintillator positively biased to about +2,000 V. The accelerated secondary electrons are now sufficiently energetic to cause the scintillator to emit flashes of light, which are conducted to a photomultiplier outside the SEM column

via a light pipe and a window in the wall of the specimen chamber. The amplified electrical signal output by the photomultiplier is displayed as a 2D intensity distribution that can be viewed and photographed on an analogue video display, or subjected to analog to digital conversion and displayed and saved as a digital image. This process relies on a raster scanned primary beam. The brightness of the signal depends on the number of secondary electrons reaching the detector.

Secondary electrons and backscattered electrons are commonly used for imaging samples: secondary electrons are most valuable for showing morphology and topography on samples and backscattered electrons are most valuable for illustrating contrasts in composition in multiphase samples (i.e. for rapid phase discrimination). X-ray generation is produced by inelastic collisions of the incident electrons with electrons in discrete orbitals (shells) of atoms in the sample. As the excited electrons return to lower energy states, they yield X-rays that are of a fixed wavelength (that is related to the difference in energy levels of electrons in different shells for a given element).

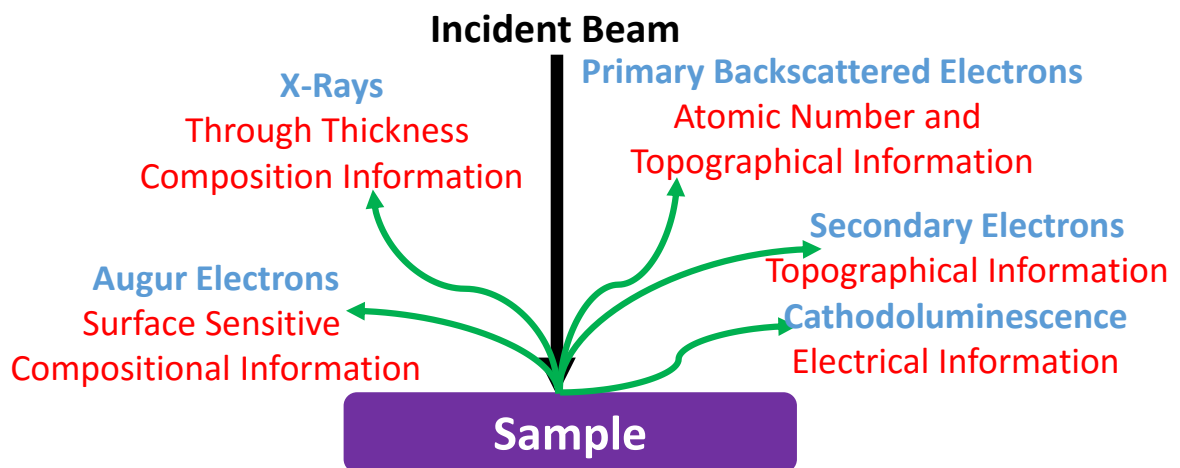


**Fig. 3.11: Electron beam-sample interaction**

Thus, characteristic X-rays are produced for each element in a mineral that is "excited" by the electron beam. SEM analysis is considered to be "non-destructive"; that is, x-rays generated by electron interactions do not lead to volume loss of the sample, so it is possible to analyze the same materials repeatedly.

Because the SEM utilizes vacuum conditions and uses electrons to form an image, special precautions must be taken to prepare the sample. In the present thesis, SEM is used to characterize different types of CNT and their polymer composite films. All water must be removed from the samples because the water would vaporize in the vacuum. All

metals are conductive and require no preparation before being used. Nanostructure dispersion (in alcohol) are drop-casted on small piece (1 cm<sup>2</sup>) Si substrates and attached with the sample holder. Films or structured samples on Si substrates can also be measured easily. All non-metals need to be made conductive by covering the sample with a thin layer of gold conductive material using a "sputter coater".

### **3.3. Transmission Electron Microscopy**

Transmission electron microscopy (TEM) is a microscopy technique whereby a beam of electrons is transmitted through an ultra-thin specimen, interacting with the specimen as it passes through. An image is formed from the interaction of the electrons transmitted through the specimen. From the top down (schematically shown in Fig. 3.12), the TEM consists of an emission source, which may be a tungsten filament, for tungsten, this will be of the form of either a hairpin-style filament, or a small spike-shaped filament. By connecting this gun to a high voltage source (typically ~ 100-300 kV) the gun will, given sufficient current, begin to emit electrons by thermionic emission in vacuum. The upper lenses of the TEM allow for the formation of the electron probe to the desired size and location for later interaction with the sample. Manipulation of the electron beam is performed using two physical effects.

1. The interaction of electrons with a magnetic field will cause electrons to move according to the right hand rule, thus allowing for electromagnets for manipulating electron beams. The use of magnetic fields allows for the formation of a magnetic lens of variable focusing power, the lens shape originating due to the distribution of magnetic flux.

2. Additionally, electrostatic fields can cause the electrons to be deflected through a constant angle. Coupling of two deflections in opposing directions with a small intermediate gap allows for the formation of a shift in the beam path, this being used in TEM for beam shifting, subsequently this is extremely important to STEM.

The optical configuration of a TEM can be rapidly changed, unlike that for an optical microscope, as lenses in the beam path can be enabled, have their strength changed, or be disabled entirely simply via rapid electrical switching, the speed of which is limited by effects such as the magnetic hysteresis of the lenses. The original form of electron microscope, the TEM uses a high voltage electron beam to create an image. The electrons are emitted by an electron gun, commonly fitted with a tungsten filament cathode as the electron source.

---

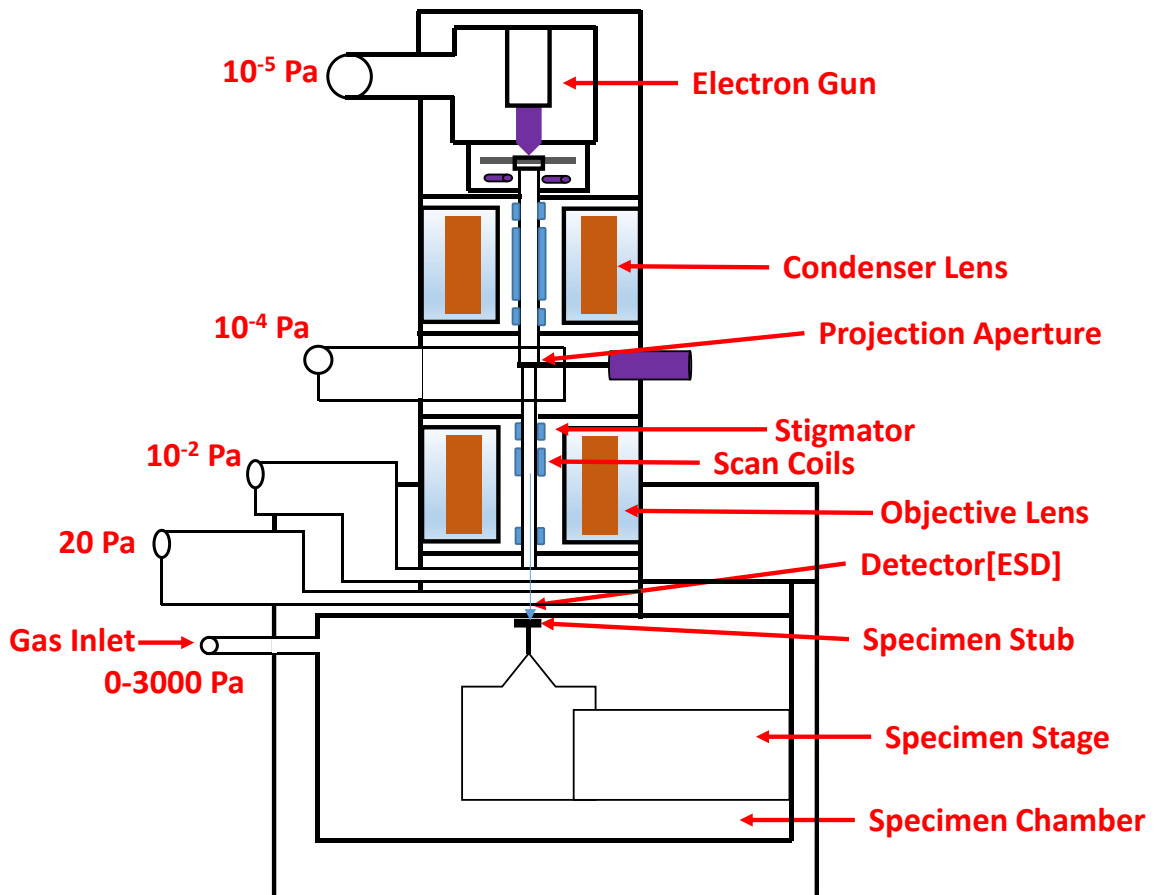


**Fig. 3.12: Schematic of transmission electron microscope**

When the electron beam transmits through the specimen, it carries information about the structure of the specimen that is magnified by the objective lens system of the microscope. The spatial variation in this information (the "image") is viewed by projecting the magnified electron image onto a fluorescent viewing screen coated with a phosphor or scintillator material such as zinc sulfide. The image can be photographically recorded by exposing a photographic nanostructures or plate directly to the electron beam, or a high-resolution phosphor may be coupled by means of a lens optical system or a fiber optic light-guide to the sensor of a CCD (charge-coupled device) camera. The image detected by the CCD may be displayed on a monitor or computer. Because the TEM utilizes vacuum conditions and uses electrons to form an image, special preparations must be done to the sample. All water must be removed from the samples because the water would vaporize in the vacuum. In the present thesis, TEM is used to characterize different types of carbon nanotubes and gold nanoparticles.

In general, very small amount of the sample is dispersed in ethanol and then carefully drop casted (100-300  $\mu\text{l}$ ) on a Cu mesh (300  $\times$  300). Then the Cu mesh is kept

---

under normal bulb for 4-6 hours for drying. Slight increase in the sample concentration will cause agglomerated particles or carbon nanotubes and we will not be able to spatially resolve them. Specially designed finger tweezers have been used to handle the fine Cu mess structures, because the use of normal tweezers can damage the mess easily due to excessive pressure.

### 3.4. UV-Visible Spectrometer

When continuous radiation passes through a material, a portion of the radiation gets absorbed depending on the absorption coefficient of the sample in the prescribed frequency range. If such a situation occurs, the transmitted radiation has some gaps in the electromagnetic spectrum which is called the absorption spectrum. In the case of ultra-violet (UV)-visible spectroscopy, the absorption of electromagnetic radiation occurs due to the transitions between lower energy electronic state to higher energy state. An electronic transition of a molecule is always associated with both vibrational and rotational transitions. So each electronic transition consists of a vast number of lines spaced so closely that spectrophotometer cannot resolve them. Rather, the instrument traces an 'envelope'. That's why the UV spectrum of a molecule usually consists of a broad band centered near the wavelength of the major transition.

Regarding the extent of absorption of a molecule there is an empirical equation known as Beer-Lambert law.

$$A = \log_{10} \left( \frac{I_0}{I} \right) = \epsilon cd \quad (29)$$

Where  $A$  is the absorption,  $I_0$  is the intensity of light incident upon sample cell,  $I$  is the intensity of light leaving sample cell,  $\epsilon$  is molar absorptivity,  $c$  is the molar concentration of solute and  $d$  is the length of sample cell.

UV-visible absorption spectra were measured with Shimadzu UV-2450 in our lab and the schematic ray diagram is shown in Fig. 3.13. It can measure absorption spectrum from 190-1100 nm with a spectral resolution of 0.1 nm. A Deuterium light ( $D_2$ ) is used as ultraviolet light source and tungsten light ( $W_1$ ) used as visible light source with a lamp interchange wavelength of 290-370 nm. The monochromator used in this instrument consist high performance blazed holographic diffraction grating; its role is to spread the beam of light into its component wavelengths.

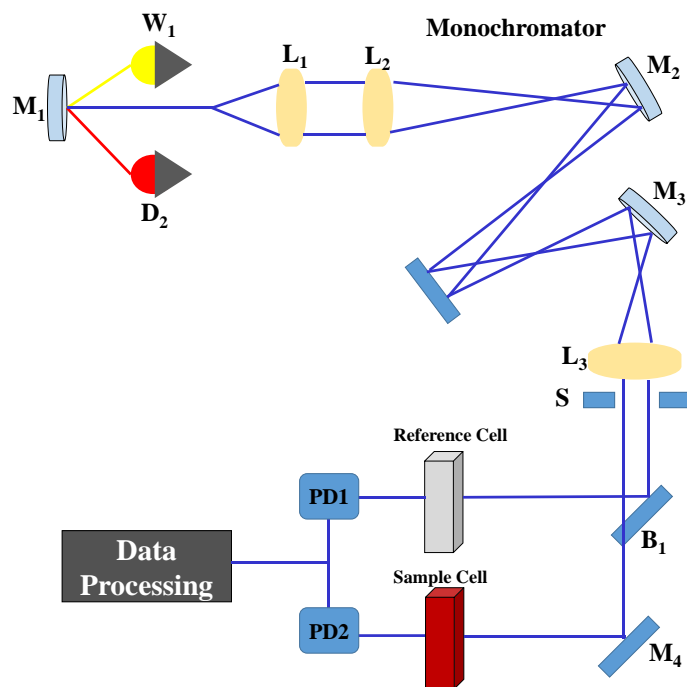


**Fig. 3.13: Schematic of UV-visible spectrometer**

This is a typical double beam instrument; the light emanating from source is split into two beams the reference beam and sample beam. Photodiodes (PD<sub>1</sub> and PD<sub>2</sub>) are used to detect the transmitted amplitude.

## 3.5. Data Analysis

### 3.5.1. Measurement and Data Recording

The analysis of the data from THz spectroscopic measurements is a little bit tricky. The detailed procedures of the data extraction and analysis are given in this section. As shown in the schematic diagram of the THz spectrometer (Fig. 3.7), a stepper motor is used to change the time delay between the pump and the probe beam. By changing the time delay and recording the corresponding photocurrent response of the THz detector at each point, whole THz spectrum is recorded. The delay line enables highest time delay of 300 ps which is enough even for samples in thick quartz cell. Each step of the stepper motor introduces a time delay of 0.82 ps. The path length of the laser is designed in such a way that, reference THz peak (in air) appears around 10 ps in time domain. Start and end points of the stepper motor are adjusted according to the experimental requirement. The number of points is generally chosen as a power of 2 (either 512 or 1024). Increasing the total number of points increases the resolution of the experimental configuration and

increasing number of point, increases the measurable highest frequency according to the Fast Fourier Transform (FFT) theorem. The highest measurable frequency ( $f_n$ ) and resolution ( $\Delta f = f_{n+1} - f_n$ ) of the setup depends on the total number of points ( $n$ ) and data sampling ( $\Delta$ ) according to the following equation.

$$f_n = \frac{n}{N\Delta}, n = -\frac{N}{2}, \dots, \frac{N}{2} \quad (30)$$

The time constant is kept fixed at 100 ms during the experiment. It means that, the stepper motor will wait for 100 ms at each point and the average photo-response of the THz detector antenna will be recorded. An external bias voltage (30 V, 10 kHz square wave) is provided at the THz emitter antenna to excite THz radiation. The time constant of the lock-in amplifier is kept three times (300 ms) than the time constant of the stepper motor for better averaging of the measured data. A typical datasheet contains three columns; i) first column gives provides the time domain data, ii) second column provides the THz electric field and iii) third column provides the relative position of the delay line (stepper motor) starting from zero. Reference spectra (air) and sample spectra are recorded three times and for several positions of the sample to minimize the error.

### 3.5.2. Transmittance Calculation

The calculation of transmission is required for extracting different parameters like degree of polarization (DOP), extinction ratio (ER) and shielding effectiveness (SE). First of all, using FFT technique from time domain data is converted to the frequency domain data. The FFT spectra consists of frequency, FFT amplitude and phase. The transmittance of a sample is calculated using the following formula;

$$T(\omega) = \left| \frac{\tilde{E}_{sample}(\omega)}{\tilde{E}_{reference}(\omega)} \right|^2, \quad (31)$$

where,  $\tilde{E}_{sample}(\omega)$  and  $\tilde{E}_{reference}(\omega)$  are the complex THz field passing through sample and reference. Transmittance have been usually calculated using Origin Software or MATLAB programming. A typical matlab code is given in the appendices.

### 3.5.3. Optical Parameter Extraction

A commercial software namely teralyzer is used to calculate the optical parameters (complex refractive index and complex dielectric function) of the samples in the corresponding frequency range. We will only discuss the required theories for complex

optical parameter extraction for single layered films. The theoretical background of the software is based on various literatures, some of which are briefly described below. Duvillaret et al.[111] presented a novel method for improving the determination of optical constants in THz-TDS. This method, which could be applied to any material of low absorption, could be used to determine the thickness of the sample with accuracy better than 1%. They minimized the error in determination of optical constants by the accurate measurement of sample thickness. They obtained the refractive index with enhanced precision ( $\sim \Delta n \approx 10^{-2}$  for a sample thickness of  $\sim 1$  mm). They concluded that their method could be applied not only to THz-TDS but also to any kind of optical constant measurement in the time domain. Dorney et al.[112] presented a robust algorithm for extracting material parameters from measured THz waveforms. Their algorithm simultaneously obtained both the thickness and the complex refractive index of an unknown sample under certain conditions. Most spectroscopic transmission measurements required the knowledge of the sample's thickness for an accurate determination of its optical parameters. Their approach relied on a model-based estimation, a gradient descent search, and the total variation measure. They explored the limits of their technique and compared the results with literature data for optical parameters of several different materials. Pupeza et al.[113] tried to improve the existing data extraction algorithms for THz-TDS in two aspects. They merged the up-to-date knowledge of THz-TDS signal processing into a single powerful optical material parameter extraction algorithm and also introduced a novel iterative algorithm that further enhanced the accuracy of the parameter extraction. They were able to reliably investigate samples with thicknesses as small as 100  $\mu\text{m}$ , samples with low indexes of refraction, i.e. close to 1, as well as samples with sharp peaks in the material parameter curves. Scheller et al.[114] proposed a method for the extraction of material parameter and thickness information from sub-100- $\mu\text{m}$  thin samples using non-differential transmission THz-TDS. Their approach relied on an additional Fourier transform of the frequency dependent material parameters to a quasi-space regime. By iterative minimization of the discrete peaks arising due to periodic FP oscillations, the highly precise thickness information along with the refractive index and absorption coefficient of the sample was extracted. Experimental verification of the approach was also provided. We need to acquaint with some of the terminologies used in the algorithm as well as in the abovementioned studies described below.

---

### Fabry-Perot (FP) Oscillation

When a THz electromagnetic pulse passes through a material a significant amount (depending on the absorption coefficient of the sample in the corresponding frequency range) of the THz radiation transmits but some part of the radiation reflects from the 2<sup>nd</sup> surface of the sample. This reflected radiation traverses through the sample backwards and then again reflects from the 1<sup>st</sup> surface and traverses in forward direction. The abovementioned process is repeated until the radiation dies down. This causes multiple peaks in the transmitted THz pulse which is called FP oscillation. These FP oscillation causes ripples in the measured optical constants if the thickness of the sample is not calculated accurately.

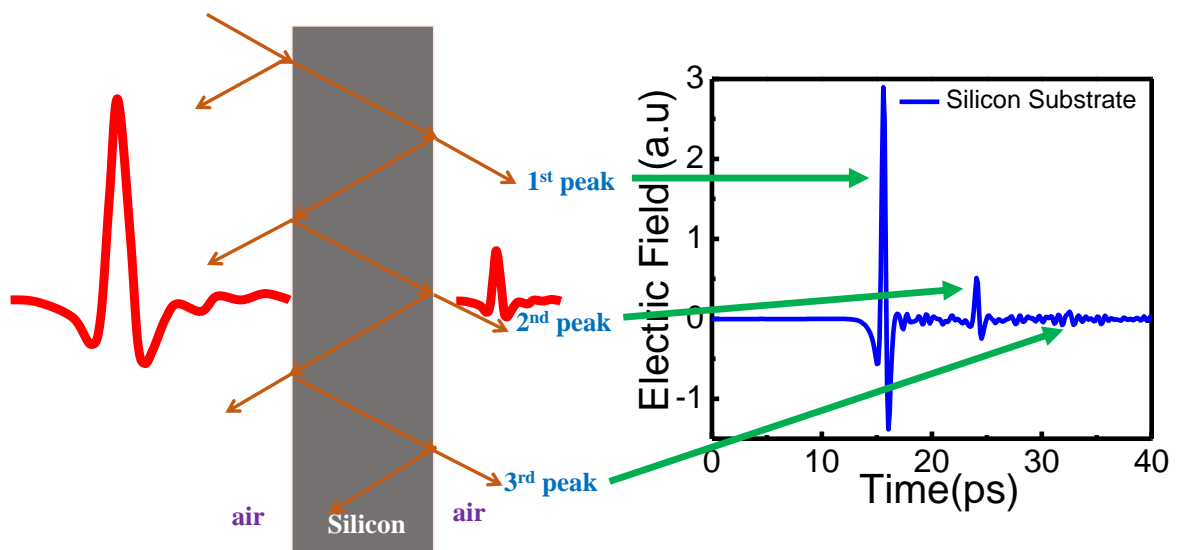


**Fig. 3.14: Appearance of the Fabry-Perot oscillation peak**

For successful determination of the optical constant, we need to get rid of this unwanted ripples in the frequency dependent optical constants of the sample. If the sample is thin and low absorptive in nature, the FP oscillation coincides with the main transmitted THz pulse and hence becomes difficult to extract optical parameters. The appearance of the FP oscillations in case of a silicon substrate is shown in the following figure. The 2<sup>nd</sup> and 3<sup>rd</sup> transmitted THz peak as shown in Fig. 3.14 is called the FP oscillation peak while the 1<sup>st</sup> THz peak is the main transmitted THz radiation.

### Dynamic Range

Dynamic range is the difference between the smallest and largest usable signal through a transmission or processing chain or storage medium. It is measured as a ratio,

or as a base-10 (decibel) logarithmic value. The noise floor of the THz spectrometer that we have used in all my works is shown in Fig. 3.15.

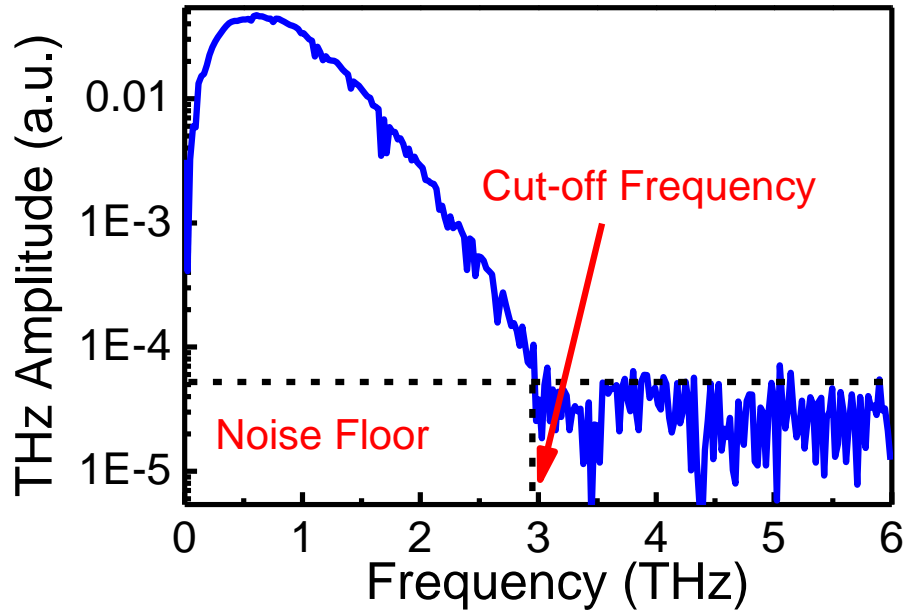


**Fig. 3.15: Noise floor and cut-off frequency**

As rightfully described by Jepson et al.[115], owing to the typical single-cycle nature of the THz pulse, the corresponding frequency spectrum extends from the low GHz to several THz. At high frequencies the spectrum is characterized by a gradual roll-off, until the detected signal level approaches that of the noise floor of the experiment. The noise floor is normally independent of frequency and corresponds to the spectrum recorded with a completely blocked THz beam path. The origin of this noise is of an electronic nature, whereas fluctuations of the THz signal itself are caused mainly by laser intensity fluctuations.

### **Nelder-Mead Simplex Algorithm**

It is a renowned optimization technique used by various scientist in different fields of research. It is a simplex method for finding a local minimum of a function of several variables which has been devised by Nelder and Mead in 1965[116]. For two variables, a simplex is a triangle, and the method is a pattern search that compares function values at the three vertices of a triangle. The worst vertex, where  $f(x, y)$  is largest, is rejected and replaced with a new vertex. A new triangle is formed and the search is continued. The process generates a sequence of triangles (which might have different shapes), for which the function values at the vertices get smaller and smaller. The size of the triangles is reduced and the coordinates of the minimum point are found. The algorithm is stated

using the term simplex (a generalized triangle in  $N$  dimensions) and will find the minimum of a function of  $N$  variables. It is effective and computationally compact.

A reference pulse with an empty THz-TDS system and a sample pulse with the sample in the THz beam path are measured. The ratio of the corresponding Fourier spectra yields the measured transfer function as given below,

$$H_{meas}(\omega) = \left| \frac{\tilde{E}_{sample}}{\tilde{E}_{reference}} \right|. \quad (32)$$

In case of a single layer sample, the theoretical transfer function takes the following form,

$$H_{theory}(\omega) = (1 - r^2)e^{-i(\tilde{n}-1)k_0\Delta} \sum_{m=0}^M (r^2 e^{-i2\tilde{n}k_0\Delta})^m, \quad (33)$$

where,  $r$  is Fresnel reflection coefficient,  $k_0$  is the free-space wave number,  $c_0$  is the speed of light in vacuum,  $\Delta$  is the thickness of the sample,  $\tilde{n}$  is the complex index of refraction and  $m$  is the number of echo pulses included in the corresponding measured transfer function accounting for the limited length of the measurement time window. The difference between the measured and the theoretical transfer function was minimized using an implementation of the Nelder-Mead simplex algorithm. The thickness of the sample is determined by superimposing the FP oscillations on the refractive index data. These oscillations are the results of FP oscillation pulses which are included in the time window of the measurement and should disappear at the correct sample thickness. For analysing the FP oscillations two approaches are employed: The first one is the quasi-space (QS) method. Here, a Fourier transform of the frequency dependent refractive index and the frequency dependent extinction coefficient is performed so that the sinusoidal FP oscillations result in a distinct peak. By minimizing this peak, the correct thickness is determined and the correct complex refractive index of the sample is obtained. As second approach, the total-variation (TV) method is employed. The TV denotes the total variation of the neighbouring values of the refractive index and the extinction coefficient. The FP-oscillations will result in an increased TV value. However, since all variations are considered, also absorption peaks and noise induced features will result in a high TV. Thus, in most cases the QS-approach is the method of choice for analysing the thickness, especially for samples that are thinner than 500  $\mu\text{m}$  as the TV method starts to fail for very thin samples. For relatively thick samples in the range of several tens of mm, the TV approach perform better. The reason for that is that the TV method also works if the FP oscillation period is close to the frequency resolution of the measurement. The FP

oscillation pulses are essential for employing the thickness determination feature of the TeraLyzer software. One has to be careful that the chosen time window of the measurement includes at least one of these oscillation pulses. One can estimate the necessary length of the time window by considering the time difference between the FP oscillation and the pulse that propagates directly through the sample,

$$\Delta T_{FP} = \frac{2n\Delta}{c_0}. \quad (34)$$

Keeping in mind that the first FP oscillation is delayed by  $\Delta T_{FP}$  in respect to the directly transmitted sample pulse, a too short time window will compromise the thickness extraction process. As rule of thumb, it is advisable to choose a time window that includes at least one FP oscillation. In this case, the frequency resolution of the measurement will be sufficient to be enabled for a reliable thickness determination. The second important parameter is the bandwidth of the measurement. The time difference between the FP oscillations is the inverse of the FP oscillation period  $\Delta F_{FP}$ :

$$\Delta F_{FP} = \frac{c_0}{2n\Delta}. \quad (35)$$

To analyze the perturbing FP oscillations, it is necessary that the extracted material parameters comprise at least a single complete FP period. That means the bandwidth of the measurement has to be larger than  $\Delta F_{FP}$ . The difference  $D$  between the measured and theoretical transfer function is minimized by Nelder-Mead algorithm based code.

$$D = H_{theory} - H_{meas} \quad (36)$$

The optimized complex refractive index  $\tilde{n}(\omega)$  is extracted. From the complex refractive index all the required optical functions are measured according to the following relation as described below;

$$\tilde{n}(\omega) = n(\omega) + ik(\omega), \quad (37)$$

$$\begin{aligned} \tilde{\varepsilon}(\omega) = \tilde{n}^2(\omega) &= (n^2(\omega) - k^2(\omega)) + i2n(\omega)k(\omega) = \\ &\varepsilon_{real}(\omega) + i\varepsilon_{ima}(\omega). \end{aligned} \quad (38)$$

It is essential to notice that the extracted material parameters are just valid in the range of the confidence interval of the measurement. That means within this interval there is no evidential truth which value is the real physical one but depending on the chosen width of the confidence interval there is a given probability that the true value lies within its borders.

# Chapter Four

## 4. Terahertz Polarizer

### 4.1. Introduction

With the advent of new compact devices for generating and detecting high power THz radiation[117, 118] and the simultaneous advancement in bridging the THz gap[119], the application of THz spectroscopy has increased by leaps and bounds in various fields of research[33, 120-126]. With such a dramatic advancement comes the great demand of high quality quasi-optic components like phase shifters, filters, polarizers, etc. efficiently working in the THz frequency range.

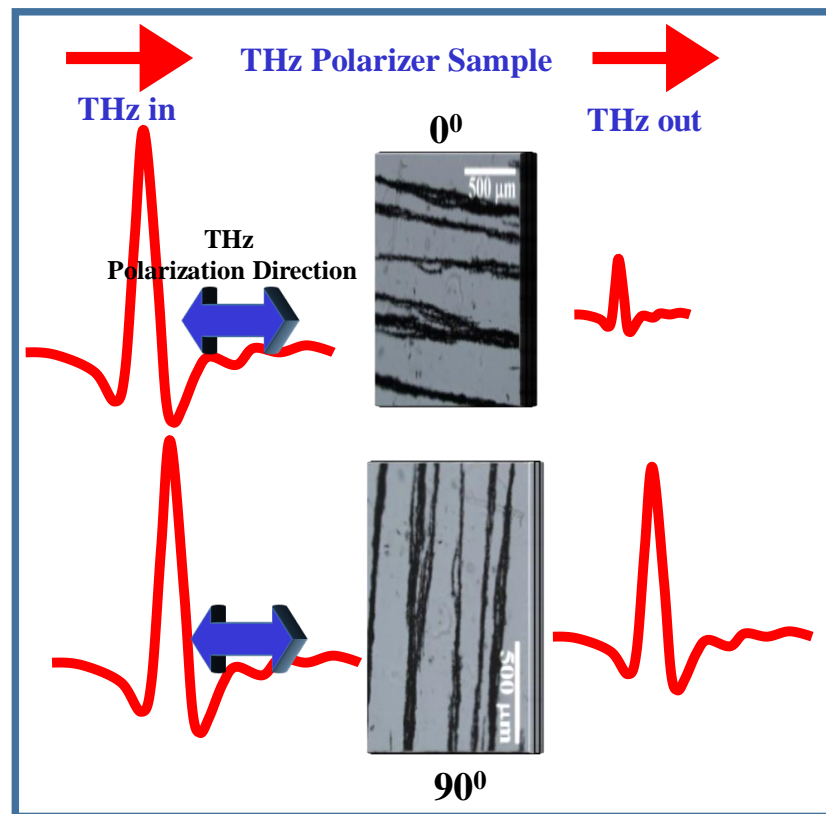


**Fig. 4.1: Schematic of the working procedure of the THz polarizer**

For several applications like THz ellipsometry[127-130] polarizers are the most important optical components as the accuracy of these measurements strongly depends on the polarization degree of the electromagnetic waves. Although some efforts have already been made in the realization of THz polarizers, preparation of a high performance, robust, durable, and cheap THz polarizer remains a challenging job.

In the present chapter, we explore the idea of using aligned magnetic nanostructures (nickel nanoparticles and nickel nanochains) in PVA matrix as a potential robust polarizer in the THz frequency range. The novelty of the work lies on the simple preparation procedure as well as the robustness and durability of the so obtained polarizer. The schematic of the project studied in this chapter is pictorially depicted in Fig. 4.1. The work presented in this chapter is largely based on our published paper[6].

## 4.2. Background Study

There are mainly two types of polarizers available in the present literatures; i) wire-grid type reflective polarizer (WGP) and ii) aligned nanotube absorptive polarizer, while some scattered efforts have also been made in other types of polarizers like i) nematic crystal polarizer, ii) brewster angle polarizer, but with severe limitation either in frequency bandwidth or incident angel of THz radiation.

**Table 2: Advantages and disadvantages of different types of polarizers**

Types of Polarizer	Advantages	Disadvantages
Wire-grid Polarizer	High Degree of Polarization High Extinction Ratio	Complicated Preparation Technique (Lithography, Nano-imprinting Technique) Multiple internal reflection
Nematic Crystal Polarizer	High Degree of Polarization High Extinction Ratio	Works in a limited frequency and temperature range Complicated preparation technique
Brewster angle Polarizer	High DOP in a limited frequency window	Limited range of THz incident angel
Aligned Carbon Nanotube	High DOP over a large frequency range	Costly Preparation, Small Extinction Ratio, Careful Handling of the sample

Depending on the effect of substrate it can also be divided into two groups namely i) back substrate polarizer (BSP) and ii) free standing polarizer (FSP). Compared with FSP, BSP requires a substrate as a mechanical backup to sustain the shape of the metal wire or stripes. Commercially available wire-grid FSPs usually have large apertures, high ER, and high DOP. However, such FSPs require a tedious, labour intensive coil-winding manufacturing process[131]. Though BSP type wire-grid polarizers offer comparable

extinction ratio to the FSP polarizers, they also introduced FP reflection in the transmitted THz signal due to high refractive index and finite width of the substrate. The advantages and disadvantages of the different types of polarizers are given below in the Table 2.

#### 4.2.1. Wire Grid THz Polarizer

This type of polarizer is the oldest among all the THz polarizers available. They can be both FSP and BSP types. FSPs are even commercially available in the market. BSPs are basically lithographically patterned metallic stripes on high resistive silicon or quartz substrates. The width and spacing of the structure, thickness of the metallic layer determines the DOP, ER and the frequency bandwidth of the device. Yamada et al.[8] fabricated aluminium WGP with a grating constant of 3  $\mu\text{m}$  on Si substrate and demonstrated an ER of  $\sim 23$  dB in the frequency range of 0.5-3 THz. Young et al.[8] fabricated THz WGP and THz band-pass filter devices on high-density polyethylene substrates using simple photolithographic fabrication technique. They had successfully demonstrated the use of standard fabrication techniques to produce large-aperture free-standing THz optical devices on low-absorption polymer materials with the advantage of low cost using a simple fabrication process. The fabricated polarizer had better than 30 dB ER at 3 THz. Band-pass filters were demonstrated at three different centre frequencies (1.5, 1.8, 2.9 THz) with a 3 dB insertion loss. Sun et al.[132] proposed a layout for high ER polarizer which was composed two dense metal wire gratings separated in parallel and by numerical analysis they showed very high ER ( $\sim 180$  dB) in the frequency range of 0.3-3 THz. Deng et al.[133] experimentally verified the idea proposed by Sun et al. and they prepared a bilayer WGP by UV-lithography, one step etching and metal decomposition process and showed an ER of  $\sim 70$  dB in the frequency range of 0.5-3 THz. Shiraishi et al.[134] reported a simple, robust, and large-aperture polarizer that utilizes thin metal-film gratings with sinusoidal or triangular cross section profile. The calculated ER using numerical simulation between the TM- and TE-waves for a 50 nm-thick gold film grating (period = height = 30  $\mu\text{m}$ ) on a tsurupica resin substrate was greater than 60 dB for the frequency range of 0.5-3 THz. Furthermore, the polarizer was shown to have high tolerance to deviations in structural parameters and input angle. The polarizer with a 25 nm-thick gold-film triangular grating (period = 25  $\mu\text{m}$ , height = 40  $\mu\text{m}$ ) was fabricated using a simple mechanical fabrication method. The measured transmission loss for the TE-waves was greater than 50 dB while the corresponding transmission loss for the TM-

waves was lower than 1 dB in the frequency range of 1.0-2.5 THz. Cetnar et al.[135] designed a THz polarizer based on aluminium stripes on polycarbonate substrate and by varying the separation of the structures they achieved variable ER as high as  $\sim 40$  dB in the frequency range of 100-550 GHz. Huang et al.[131] prepared a single layer WGP of aluminium deposited on a thin layer of SiO<sub>2</sub> supported by a Si substrate and coated the metallic layer with polymer to get rid of the FP reflections in similar WGP. Their structure offered a high ER and very low insertion loss in the frequency range of 0.2-2 THz. Berry et al.[136] reported the design and experimental characterization of a PBS based on a sub-wavelength metallic grating fabricated on a high density polyethylene (HDPE) substrate. The THz polarizing beam splitter consisted of a silver grating on a HDPE substrate. The grating consisted of 2  $\mu\text{m}$  thick, 12  $\mu\text{m}$  wide silver lines with 20  $\mu\text{m}$  periodicity. When placed at an oblique angle relative to an incident THz beam, TE polarization was reflected while TM polarization was found to be transmitted. Their device offered less than 0.3 dB transmission loss over 0.1-2 THz, and ERs of 21 dB and 16 dB at 0.5 THz and 1 THz, respectively. Das et al.[137] studied the performance of a polarizer prepared by inkjet printing method. Short length CNF stripes were printed on marlyn film with a width and separation of 100  $\mu\text{m}$  each and they found a promising DOP of  $\sim 0.32$  in the frequency range of 0.57 THz to 0.63 THz and concluded that DOP and ER can be increased by decreasing the width and separation of the structure. Grady et al.[138] showed that polarization of reflected THz beam could be rotated by 90° (*s* to *p* polarization) in the frequency range of 0.7-1.9 THz by using a gold ground plane and gold cut wires aligned 45° with respect to the incident THz polarization separated by a dielectric spacer. Hunag et al.[139] proposed a tuneable bilayer aluminium wire-grid structure on thin silica layer by micro-fabrication technique working in the frequency range of 0.2-2.0 THz. They achieved ER  $\sim 50$  dB and transmission loss  $< 1$  dB in the frequency range of interest.

#### 4.2.2. Aligned Carbon Nanotube Polarizer

Anisotropic one dimensional conduction properties of CNTs has recently been deployed in manufacturing prototype polarizer devices working in THz frequency range although the anisotropic conduction of aligned CNT in THz frequency range had been experimentally demonstrated almost ten years back by Jeon et al.[140]. Ren et. al.[3] first experimentally observed the excellent polarizing properties of aligned CNT structures. Vertically aligned SWNTs were grown on silicon substrate using a CVD technique and then they were efficiently transferred onto a sapphire substrate. Polarization dependent THz

transmission measurements were performed on both the SWNT film sample on a sapphire substrate and a reference sapphire sample with the same thickness as the sample substrate. The symmetry axis of the structure was rotated corresponding to the polarization axis of the THz radiation and the corresponding transmitted signal was recorded. For perpendicular orientation of the sample ( $\theta = 90^\circ$ ), there was virtually no interaction (THz absorption). For parallel orientation ( $\theta = 0^\circ$ ), transmitted THz signal was found to be the smallest dictating strongest interaction and highest THz conductivity in this orientation. The measured DOP was  $\sim 1$ , while the measured reduced linear dichroism ( $LD^r$ ) was  $\sim 3$ , corresponding to an order parameter of 1 in the frequency range of 0.1-1.8 THz. Kyoung et al.[4] studied the polarizing performance of micro-meter thick freestanding CNT polarizer excellently working in the frequency range of 0.1-2.0 THz. A MWNT forest was deposited using CVD technique and then using a motorized coil-winding process freestanding MWNT polarizer was prepared using a polyethylene support. DOP was found to be 0.999 and ER  $\sim 37$  dB in the measured frequency range. Ren et. al.[5] had showed excellent polarizing behaviour of aligned SWNT polarizer using multilayer stacks of aligned SWNT in the frequency range of 0.4-2.2 THz. Fragouli et al.[141] decorated the surface walls of CNFs and then dispersed them in polymer matrix in the presence of external magnetic field thereby aligning the CNFs. Besides, anisotropic magnetic and electric properties, the aligned CNFs showed anisotropic THz transmission in the frequency range of 570-630 GHz and a DOP  $\sim 0.5$  was found in the measured frequency range.

### 4.2.3. Other types of Polarizers

Some other types of THz polarizers and wave plates has also been demonstrated in recent past. Hirota et al.[142] fabricated a four-contact PC antenna, which has four metal contacts on a LT-GaAs substrate by a standard photolithographic and chemical etching method. By rotating the bias voltages by  $90^\circ$ , the polarization direction of THz radiation was alternated between the  $+45^\circ$  and  $-45^\circ$  direction at a rate of more than several kHz. These linearly polarized THz radiations were converted to circularly polarized radiations by using the total reflection within a high-resistivity Si prism; the  $s$  polarized component of electromagnetic radiation was phase-retarded against  $p$  polarized one by the total reflection and its phase-shift depends on the reflection angle. The internal reflection angle of the Si prism was designed to give rise to a  $\pi/2$  phase-shift so that the linearly polarized radiations at  $+45^\circ$  becomes left-handed circularly polarized radiations, and, in the same

way, the ones at  $-45^\circ$  become right-handed circularly polarized radiations. Thus using the combination of a four-contact PC antenna and a Si prism, they had built a broadband, circularly polarized THz radiation source and modulator. Masson et al.[7] prepared an achromatic THz quarter wave plate by precisely stacking six birefringent quartz plates. The de-phasing was found to be in the range of  $90^\circ \pm 3\%$  in the broad frequency range of 0.25-1.75 THz. A Feussner-type THz polarizer with a nematic liquid crystal (NLC) layer between two fused-silica prisms was demonstrated[143]. The DOP and ER of the polarizer exceeded 0.99 and  $10^5$ , respectively in the frequency range of 0.3-1.0 THz. NLC was introduced in a rectangular parallelepiped space in a fused silica crystal and external magnetic field is used to align the NLC. Wojdyla et al.[144] demonstrated the performance of a THz linear polarizer made from a stack of silicon wafers at aligned at the Brewsters angel. Using four industrial grade silicon wafers they obtained a power  $ER > 6 \times 10^3$  in the frequency range of interest. Scherger et al.[145] prepared a low-cost THz wave plate based on the birefringence of normal paper/air gaps working in 100-450 GHz frequency range. The performance of the device as an efficient half-wave plate was shown at 244 GHz. Cong et al.[146] discovered a unique approach to efficiently rotate the polarization state of incoming THz radiation by using a tri-layer meta-surface. Three sets of metallic gratings were separated by a dielectric spacer and the axis of the gratings were rotated with the previous by  $45^\circ$ . The device was tailored to rotate the polarization axis of a linearly polarized terahertz wave by any desired angle, especially to the orthogonal direction, and the rotation occurred with a high power conversion efficiency of about 85% at a broadband frequency. The FP interference theory explained the underlying mechanism of the ultrahigh transmittance.

### 4.3. Basic Theory

The performance of a polarizer is depicted by its DOP, which is defined as the amount of a particular type of polarization present in the transmitted radiation if unpolarised radiation passes through the polarizer and the ER, which is defined as the ratio of transmittance of a plane polarized radiation when the polarizer axis is placed in parallel and perpendicular orientation with respect to the incident polarization direction. The DOP is calculated as,

$$DOP = \frac{A_{0^\circ} - A_{90^\circ}}{A_{0^\circ} + A_{90^\circ}}, A_{0^\circ(90^\circ)} = -\log_{10} \left( T_{0^\circ(90^\circ)} \right), \quad (39)$$

where  $A_{0^\circ(90^\circ)}$ , and  $T_{0^\circ(90^\circ)}$  are the absorbance and transmittance in parallel and perpendicular orientations, respectively and the ER is defined as;

$$ER(\omega) = -10 \log_{10} \left( \frac{T_{0^\circ}}{T_{90^\circ}} \right) \text{ in dB.} \quad (40)$$

A simple MATLAB code as described in the appendices is used to extract the necessary parameters required to describe a THz polarizer.

#### 4.4. Sample Preparation

Nickel nanoparticles (NiNP) and nickel nanochains (NiNC) were prepared by a simple chemical route. Nickel chloride salt was reduced by hydrazine hydrate in the ethylene glycol (EG) matrix in the presence of sodium hydroxide.



**Fig. 4.2: Schematic of nickel nanostructure preparation**

EG provided the spherical structure of the nanoparticles while diameter of the NiNP were optimized by concentration of the reactants and the reaction environment. Nickel chloride ( $\text{NiCl}_2 \cdot 6\text{H}_2\text{O}$ ; Merck) was reduced by hydrazine hydrate ( $\text{N}_2\text{H}_5\text{OH}$ ; Merck) in ethylene glycol ( $\text{HO}-\text{CH}_2-\text{CH}_2-\text{OH}$ ; Merck) environment (provides the spherical shape of the nanostructures) at  $\sim 80^\circ\text{C}$  by vigorous magnetic stirring in presence of sodium hydroxide ( $\text{NaOH}$ ; Merck), which controlled the length of the nanostructures (important in the preparation of NiNC). The colour of the solution progressively turned green to violet to black indicating the formation of nickel nanostructures. The collected nanostructures were washed thoroughly with ethanol ( $\text{CH}_2-\text{CH}-\text{OH}$ ; Merck) and de-ionized (DI) water (Millipore) and then separated magnetically prior to further use. The nanostructures were anisotropically dispersed in polymer solution in presence of external magnetic field to align them along the magnetic field lines for the preparation of a wire grid like structure. The main idea behind preparing these two structures are to create nanostructures with

drastically different magnetic anisotropy so that they can be aligned differently using optimized external magnetic field.

## Nickel Nanostructures in Polymer Matrix



**Fig. 4.3: Schematic of magnetic alignment of nickel nanostructures**

1 g PVA is dissolved in 10 ml DI water, freshly prepared NiNP (NiNC) are mixed with it and ultrasonicated for 15 minutes. The solution is then poured in a Petri dish for slow drying process and placed in external magnetic field of  $\sim 6$  kOe for NiNP (300 Oe for NiNC) to align the NiNP (NiNC) inside the polymer matrix and then slow drying of the liquefied polymer. The schematic of the magnetic alignment procedure of the chemically synthesized nickel nanostructures in polymer matrix is shown in Fig. 4.3.

**Table 3: Reactants for preparation of nickel nanostructures and the THz polarizer**

Reactants or External Perturbations	Amount
Ethylene Glycol	Required Amount
Nickel Chloride	45 mM
Hydrazine Hydrate	0.9 M
Sodium Hydroxide	0.1 M for NiNPs and 0.15 M for NiNCs
Temperature while stirring	80 °C
Poly-Vinyl Alcohol	1 g

Two opposite poles of bar magnets are kept in a structured groove in thermocol and the Petri dish containing the nickel nanostructures immersed in liquefied PVA is kept in the middle point of these two bar magnets. The magnitude of the magnetic field is varied by changing the distance between the bar magnets and their strength. PVA has been used as the matrix because of the twofold reason; i) it has an uncharacteristic optical response in the THz frequency range ( $n \sim 1.8$  and  $\alpha = 40 \text{ cm}^{-1}$  at 1 THz) and ii) it provides robustness to the polarizer[8, 147, 148]. The concentration of the different reactants required for the preparation of the nickel nanostructures and the aligned THz polarizer are given in Table 3.

### 4.5. Measurement and Analysis

SEM images in Fig. 4.4 show that the average diameter of the NiNP are  $\sim 165 \text{ nm}$  and the average diameter and length of NiNC are  $\sim 300 \text{ nm}$  and  $\sim 4 \mu\text{m}$ , respectively. The NiNPs are spherical in structure as seen in the image and the NiNCs seems to be formed by adding the individual NPs in a chain like fashion. The chemical purity of the samples have been confirmed using EDX study (not shown here). The optical image of both the NiNP and NiNC THz polarizer structure is given in Fig. 4.5. The anisotropy of the chemically synthesized NiNC are much larger than the NiNC due to the structure or shape anisotropy of the sample and we have also optimized the external magnetic field (for nickel nanostructure alignment) and thus we have efficiently changed the structure constants (width and separation of the structure). The average width of the aligned NiNP and NiNC structures are  $40$  and  $90 \mu\text{m}$  respectively and the corresponding average separations are  $170$  and  $80 \mu\text{m}$ .

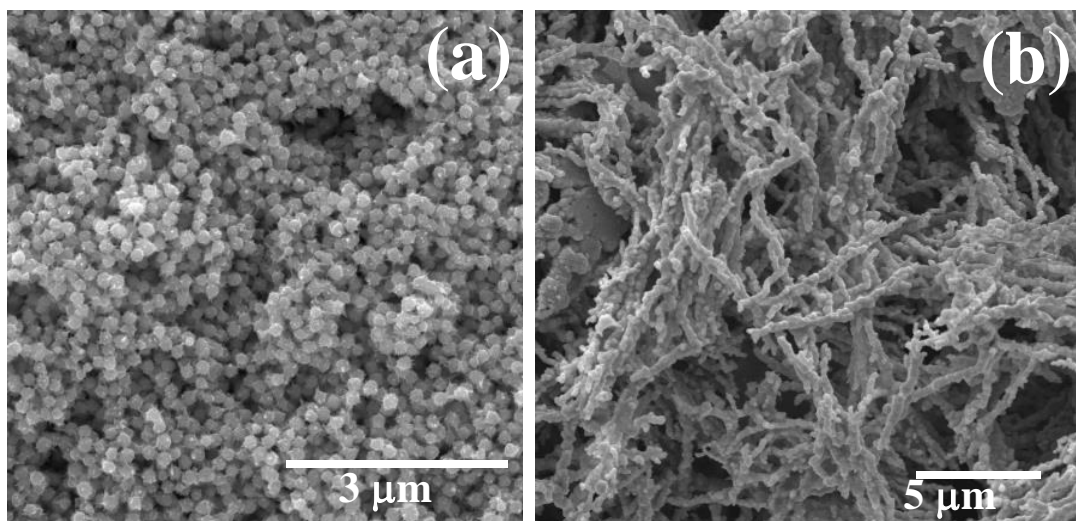


**Fig. 4.4: SEM images of the chemically synthesized (a) NiNPs and (b) NiNCs**

Width of the structure increases with increasing anisotropy and decreasing external magnetic field (for the case of NiNC polarizer) due to higher cohesion energy of longer wire like structures and the separation decreases due to weaker magnetic field.

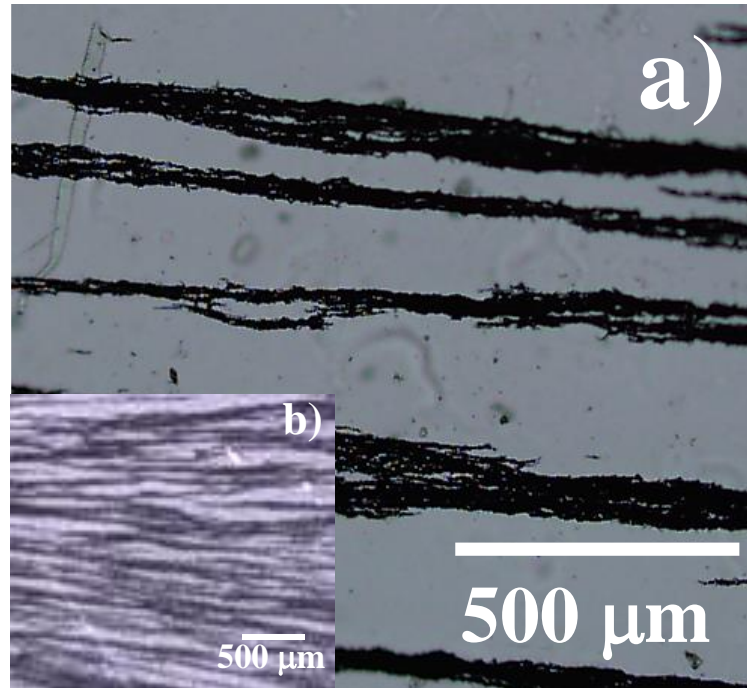


**Fig. 4.5: Optical image of the a) NiNP and b) NiNC THz polarizer**

The use of the word ‘average’ is important because the width and separation may be varied due to various reasons like i) non-uniformity of the external magnetic field, ii) non-uniform size of the nanostructures, iii) thermal fluctuations in the polymer matrix, iv) misalignment of the polymer matrix plane with that of the external magnetic field. So, we have analysed several images and then calculated an average measurement. The thickness of the NiNC and NiNP THz polarizers are  $210 \pm 30$  and  $300 \pm 30$   $\mu\text{m}$  respectively and bare PVA films of similar thicknesses are also prepared for reference measurements.

THz measurements were carried out in a commercial THz spectrophotometer (TERA K8, Menlo Systems) at room temperature in transmission geometry (details given Chapter 3). A 780 nm Er doped fiber laser having pulse width of  $< 100$  fs and repetition rate  $\sim 100$  MHz is used to excite a dipolar type PC antenna which produces a THz radiation having bandwidth up to 2.5 THz ( $< 50$  dB). The radiation transmitted through the sample was then focused on a similar antenna and detected coherently. The frequency dependent power and phase of the transmitted pulse was obtained using Fourier analysis of the measured electric field amplitude. Polarization of THz pulse depends on the pump

beam polarization and the bias voltage direction in the THz antennas and in the present case it is aligned along the horizontal direction (along x axis or  $p$  polarization).

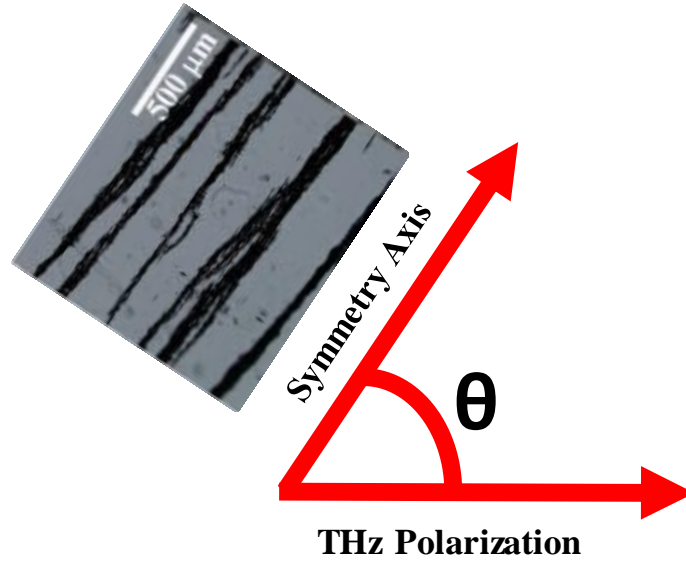


**Fig. 4.6: Schematic of the measurement of the anisotropic THz transmittance of the device**

The polarization of the THz pulse remained fixed and we varied the angle between the symmetry axis of the polarizer structure and the THz polarization and measure THz transmittance in the frequency range of 0.2-2.5 THz. The schematic of the measurement of the anisotropic THz transmission is given in Fig. 4.6.

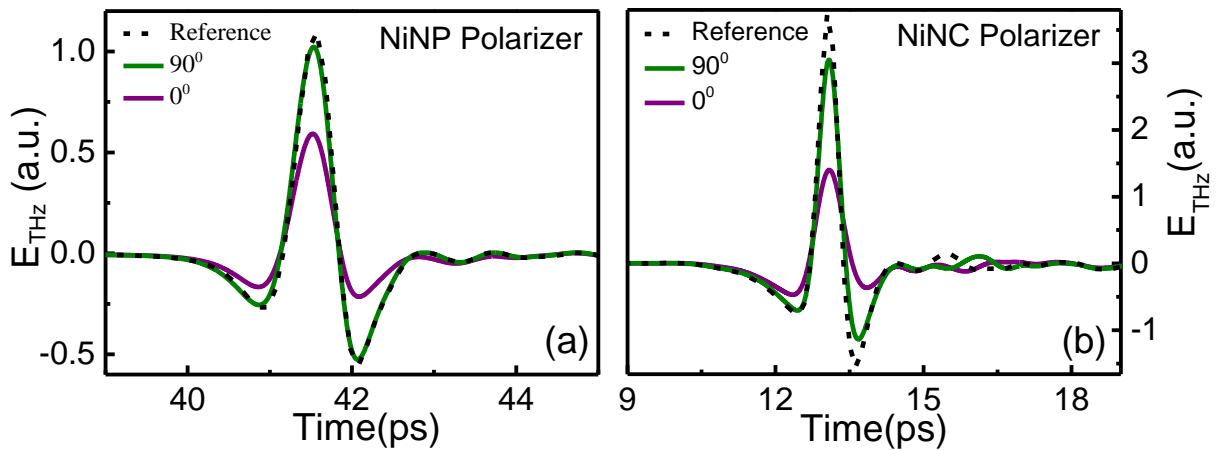


**Fig. 4.7: Transmitted THz pulse in time domain through bare PVA, parallel ( $0^\circ$ ) and perpendicular ( $90^\circ$ ) position of the sample with respect to the THz polarization for (a) NiNP and (b) NiNC THz polarizer**

The transmitted THz signal in time domain through the bare PVA film ( $E_{PVA}(t)$ ), parallel ( $E_{0^\circ}(t)$ ) and perpendicular ( $E_{90^\circ}(t)$ ) orientation of the sample with respect to the

THz polarization is shown in Fig. 4.7 for both the polarizers. In perpendicular configuration transmitted pulse is almost identical with the bare PVA film for both the cases indicating very small interaction of THz photons with the free electrons in the system. However, if we analyze NiNP and NiNC polarizer, the transmittance (in perpendicular orientation) is smaller in NiNC polarizer (as shown in Fig. 4.8). This is due to the increased width of the NiNC structure which allows more interaction with the horizontally polarized THz photons with the free electrons of the system.

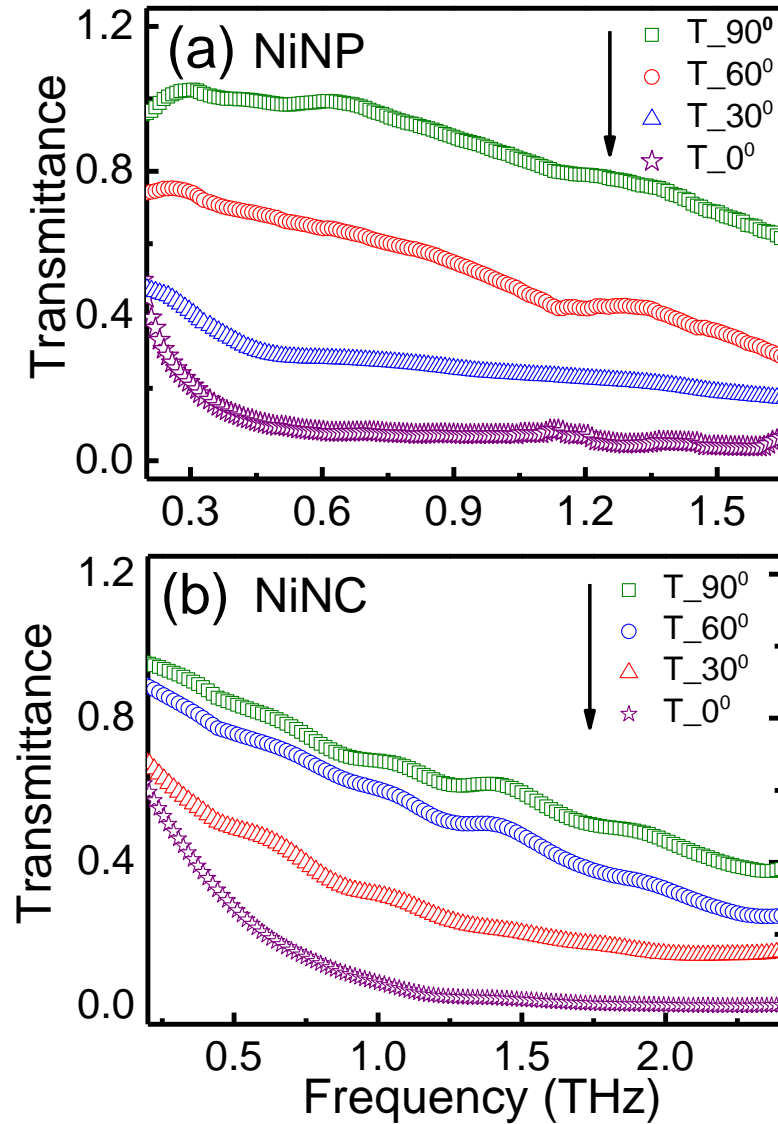


**Fig. 4.8: THz transmittance for different angle of rotation for (a) NiNP and (b) NiNC polarizer**

If we consider  $\tilde{E}_{PVA}(\omega)$ ,  $\tilde{E}_{0^\circ}(\omega)$ , and  $\tilde{E}_{90^\circ}(\omega)$  as the frequency domain complex transmitted THz signal in frequency domain through bare PVA, parallel and perpendicular orientation of the sample, then the transmittance is calculated as  $T_\theta(\omega) = \left| \frac{\tilde{E}_{\theta^\circ}(\omega)}{\tilde{E}_{PVA}(\omega)} \right|^2$ ;

where  $\theta$  indicates the angle between the symmetry axis of the structure and the polarization of the incoming THz radiation as shown in Fig. 4.6.

The transmittance is shown in Fig. 4.8 for both the polarizers in the THz frequency range for different angle of rotation. Beautiful anisotropic transmittance behaviour has been observed for both the polarizers in the frequency range of interest. For NiNP polarizer, data can be obtained in the frequency range of 0.2-1.65 THz while for NiNC polarizer we have obtained data in the extended frequency range of 0.2-2.5 THz beyond noise floor.

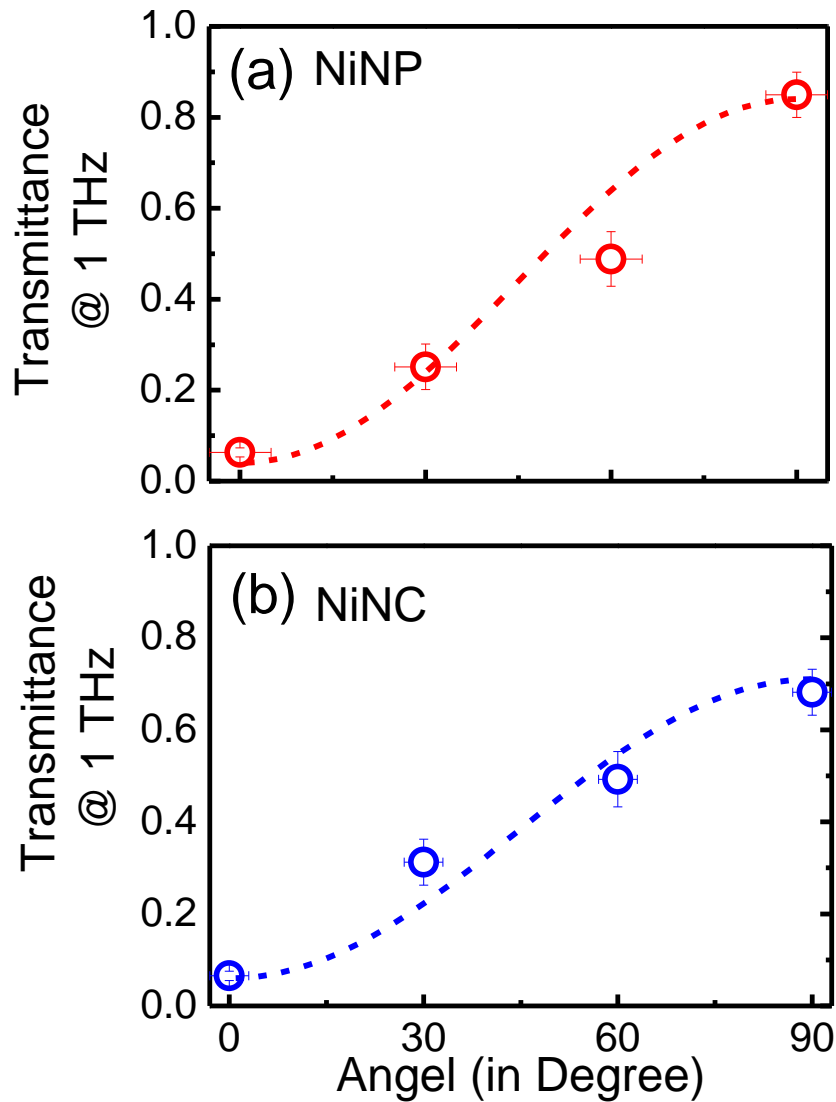


**Fig. 4.9: Malus' law for (a) NiNC and (b) NiNP THz polarizer**

For NiNP polarizer, the transmittance is  $\sim 0.92$  between 0.2-0.9 THz followed by a gradual decrease down to 0.65 at 1.6 THz with an average value of  $\sim 0.86$  for the perpendicular orientation, whereas it remains  $\sim 0.09$  in the entire frequency region for the parallel

orientation. The observed anisotropic nature of the transmittance is due to the one-dimensional character of confined carriers and phonons in aligned NP structure.

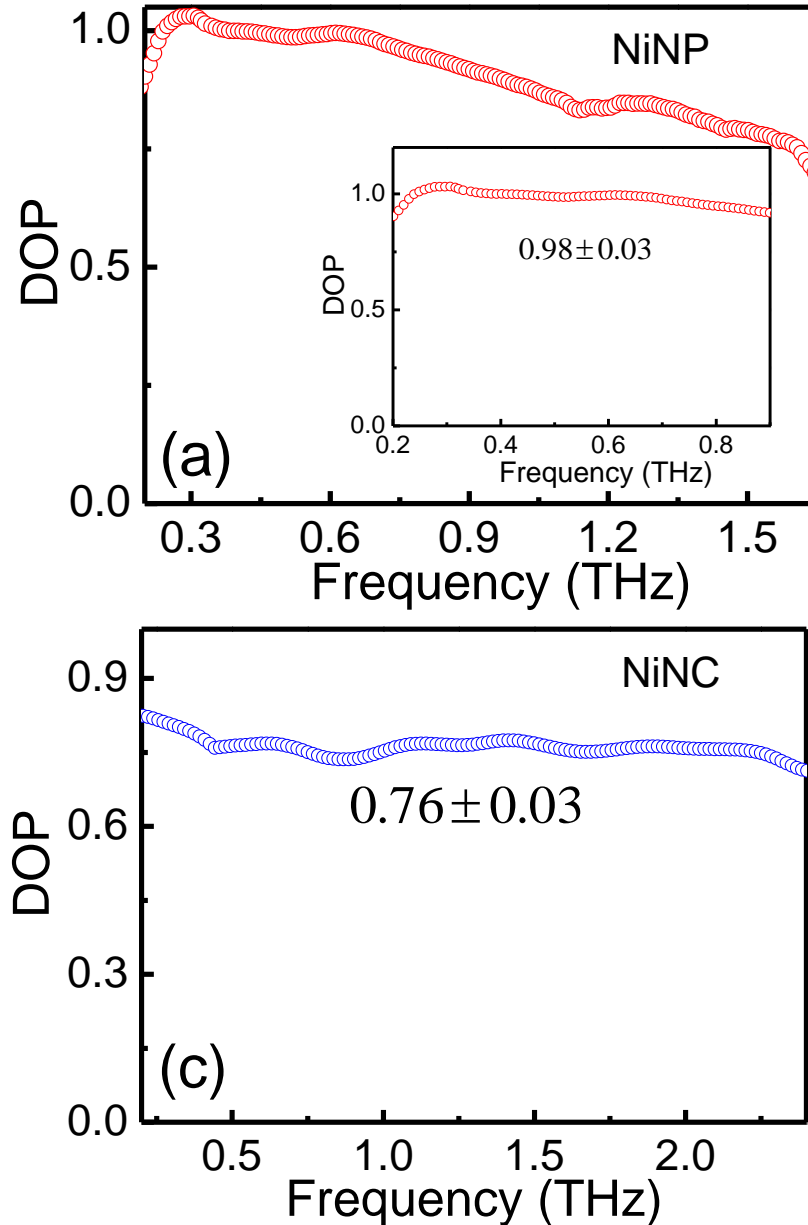


**Fig. 4.10: DOP of the NiNP polarizer in the frequency range of (a) 0.2-1.65 THz and the zoomed in view in the frequency range of (b) 0.2-0.9 THz with DOP  $\sim 0.98 \pm 0.03$ . (c) A constant DOP of  $0.76 \pm 0.03$  is found for NiNC polarizer in the extended frequency range of 0.2-2.4 THz**

This can be explained in the following manner: Fig. 4.5 reveals a wire like structure of the aligned NP in PVA film and the calculated width of the wire-like structure is  $\sim 40 \mu\text{m}$  and the average separation is  $\sim 170 \mu\text{m}$ , which is of the same order of magnitude as that of THz wavelength. So, the conduction electrons follow effectively a one-dimensional path through the wire-like structures. When THz polarization is parallel to the symmetry axis

of the structure, THz photons can interact with the conduction electrons inside the wire-like structure and hence cannot pass through the polarizer producing a minimum in the transmission. No such interaction occurs in the perpendicular orientation and a maximum in transmission is observed. A regular increase in the transmittance with increasing the angle of orientation strongly supports this argument. In addition, ideally the periodicity or pitch, of the grid of parallel lines should be as small as possible, but to be efficient as a polarizer the pitch must be about less than the wavelength of the light to be polarized. Here, the condition is reasonably satisfied for frequencies between 0.2 and 0.9 THz (1500 and 333  $\mu\text{m}$ ). However, at larger frequencies the condition does not satisfy anymore and the efficiency of polarization reduces[149]. Similar interpretation is also applied for the case of NiNC polarizer. As the pitch of the NiNC polarizer ( $\sim 170 \mu\text{m}$ ) is much smaller than the pitch of the NiNP polarizer ( $\sim 210 \mu\text{m}$ ), the anisotropic behaviour is observed over a larger frequency bandwidth of 0.2 and 2.4 THz (1500 and 125  $\mu\text{m}$ ). However, the transmittance in perpendicular orientation decreases rapidly with increasing frequency due to larger width of the structure.

According to Malus' law, which is named after Étienne-Louis Malus, when a perfect polarizer is placed in a polarized beam of light, the intensity ( $I$ ) of the light that passes through is given by  $I = I_0 \cos^2 \phi$ , where  $I_0$  is the initial intensity, and  $\phi$  is the angle between the light's initial polarization direction and the axis of the polarizer. Here, the axis of the polarizer means the pass axis of the polarizer and not the symmetry axis of the polarizer (these two axes are perpendicular with each other). So, in our case  $\phi = \pi/2 - \theta$  and the redefined Malus' law is  $I = I_0 \sin^2 \theta$  where  $\theta$  is defined in Fig. 4.6. Our devices obey the abovementioned law excellently and the transmittance at different angle of rotation ( $\theta$ ) for both the NiNP and NiNC polarizer are fitted with this redefined Malus' law and plotted in Fig. 4.9. One of the most important factors for a polarizer is its DOP and ER. It is a measure of the polarizing performance of the device in the measured frequency range of interest. DOP describes the amount of a particular type of polarization present in the transmitted radiation if unpolarised radiation passes through the polarizer while ER denotes the ratio of transmittance of a plane polarized radiation when the polarizer axis is placed in parallel and perpendicular orientation with respect to the incident polarization direction. A good polarizer should have DOP close to 1 and high ER over the allowed frequency range. The DOP is calculated as  $DOP = \frac{A_{0^\circ} - A_{90^\circ}}{A_{0^\circ} + A_{90^\circ}}$ ,  $A_{0^\circ(90^\circ)} = -\log_{10}(T_{0^\circ(90^\circ)})$ ; where  $A_{0^\circ(90^\circ)}$ , and  $T_{0^\circ(90^\circ)}$  are the absorbance and transmittance in

parallel and perpendicular orientations, respectively and the ER is defined as  $ER(\omega) = -10 \log_{10} \left( \frac{T_{0^\circ}}{T_{90^\circ}} \right)$  in dB. The DOP of both the polarizers are shown in Fig. 4.10. For NiNP polarizer in the lower frequency range DOP remains very high almost  $\sim 1$  but with increasing frequency DOP decreases and at 1.65 THz it becomes  $\sim 0.6$ . The DOP is as high as  $0.98 \pm 0.03$  in the frequency range of 0.2-0.9 THz. However, in higher frequency range, the corresponding wavelength becomes comparable or much lower than the grating constant of the polarizer, and its performance deteriorates. However, for the NiNP polarizer, as the grating constant is much smaller it works in the large frequency range and we get a constant DOP  $\sim 0.76 \pm 0.03$  in the extended frequency range of 0.2-2.4 THz. Although the DOP is somewhat lower than the NiNC polarizer, it remains constant over a larger frequency range of interest and we have also option to optimize the DOP by manipulating the thickness, NiNC length and grating constant of the device. The ER of both the polarizers is shown in Fig. 4.11. The ER is relatively smaller than the conventional wire-grid type polarizers. For, NiNP polarizer, ER is  $\sim 11$  dB in the higher frequency range of interest however, for the NiNC polarizer, ER increases linearly with increasing frequency and reaches a maximum value of  $\sim 25$  dB at 2.2 THz before decreasing slightly. It could be noted here that MWG and aligned SWNT often offer a DOP  $\sim 0.9$  or greater in the frequency range of interest.

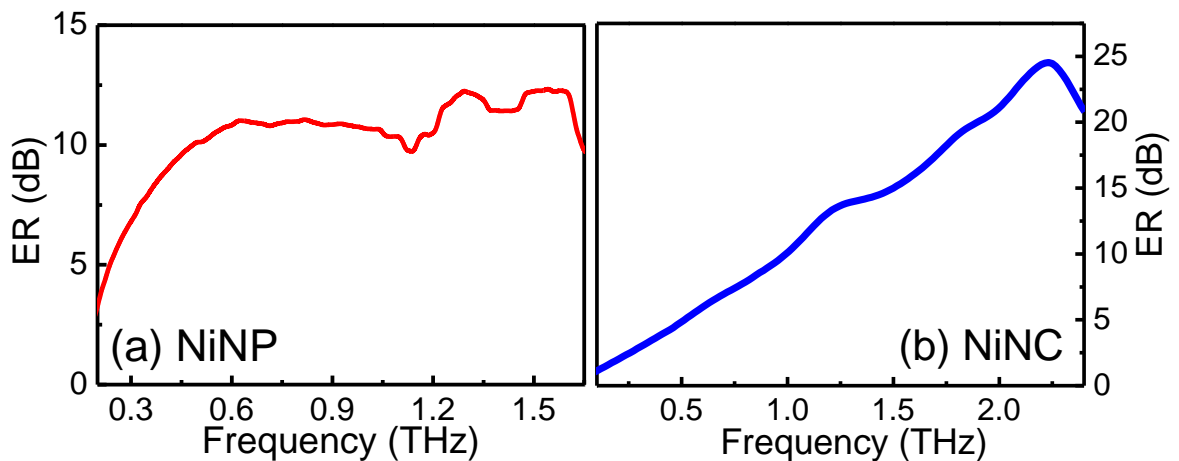


**Fig. 4.11: Extinction ration of (a) NiNP and (b) NiNC polarizer**

So, considering the ease of preparation without deploying any sophisticated lithographic technique the observed DOP is of considerable interest for both the polarizers even though the presence of the restricted frequency bandwidth in NiNP polarizer and lower value of DOP in an extended frequency bandwidth for NiNC polarizer. The average ER value is obtained to be  $\sim 11.08 \pm 0.56$  dB in the frequency range of 0.5-1.65 THz for NiNP polarizer.

This value is in comparable interest with that obtained in commercially available polarizer (25 dB)[8] or CNT polarizers (10-37 dB)[3-5] .

The other important parameter for a good polarizer are reduced linear dichroism ( $LD^r$ ) [150, 151].  $LD^r$  is defined as  $LD^r = \frac{LD}{A_0}$  where  $LD = A_{0^\circ} - A_{90^\circ}$  and  $A_0 = \frac{A_{0^\circ} + 2A_{90^\circ}}{3}$ .  $LD$  is a measure of the degree of alignment of NPs in PVA matrix, whereas  $LD^r$  is normalized by the unpolarised, isotropic absorbance ( $A_0$ ) of the system[152]. From microscopic theory,  $LD^r$  can also be expressed as  $LD^r = 3 \left[ \frac{3\cos^2\alpha - 1}{2} \right] S$ , where  $\alpha$  is the angle between the transition moment and the long axis of the sample (assumed to be 0 for the present samples) and  $S$  is the nematic order parameter which describes the degree of alignment of the sample;  $S = 0$  when the NPs are randomly oriented while for perfectly oriented NPs,  $S = 1$ . An ideally aligned polarizer should offer  $LD^r = 3$  and  $S = 1$ . We have plotted  $LD^r$  and  $S$  as a function of frequency. The average value of  $LD^r$  and  $S$  is found to be  $2.59 \pm 0.25$  and  $0.86 \pm 0.11$  in this frequency range of 0.2-1.65 THz for NiNP polarizer respectively. The average value of  $LD^r$  and  $S$  is found respectively to be  $2.04 \pm 0.07$  and  $0.68 \pm 0.02$  in this frequency range of 0.2-2.4 THz for NiNC polarizer as shown in Fig. 4.12. Keeping in mind that anisotropy is entirely due to confined motion of carriers, the obtained average DOP of the present polarizer concludes that the alignment of the NPs inside the matrix is not perfect which is also reflected from the measured nematic order parameter.

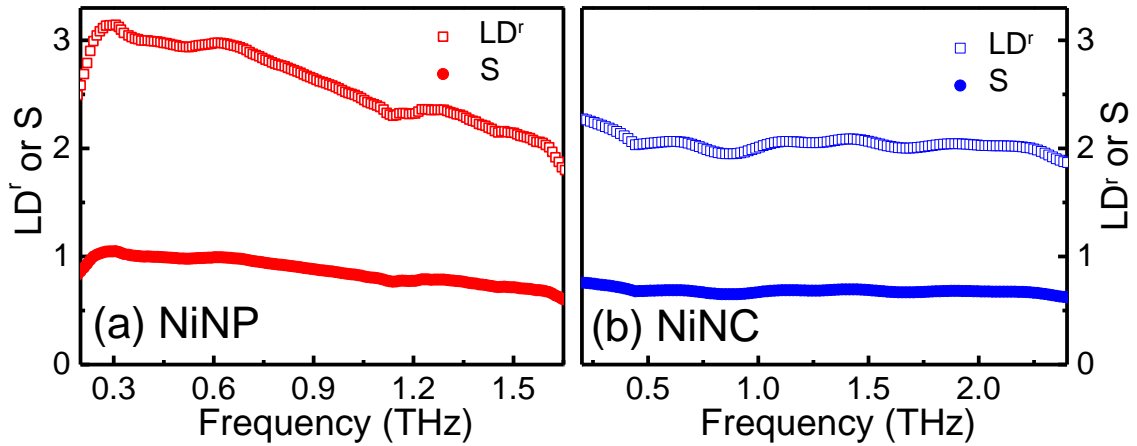


**Fig. 4.12: Reduced linear dichroism ( $LD^r$ ) and nematic order parameter ( $S$ ) for the (a) NiNP and (b) NiNC polarizer**

## 4.6. Conclusion

In summary, we demonstrate an easy route to prepare robust and durable THz polarizer using NiNP and NiNC in polymer matrix. We have synthesized NiNP of average diameter

$\sim 165$  nm and NiNC of diameter  $\sim 300$  nm and length  $\sim 4$   $\mu\text{m}$  via simple chemical route. The nanostructures are aligned inside polymer matrix using an optimized external magnetic field for the preparation of the polarizer. The width and separation of the NiNP polarizer structure are found to be  $\sim 40$   $\mu\text{m}$  and  $\sim 170$   $\mu\text{m}$  respectively and for the NiNC polarizer the width and separation are found to be  $\sim 90$   $\mu\text{m}$  and  $\sim 80$   $\mu\text{m}$  respectively. THz transmittance of both the polarizers decreases systematically with increasing  $\theta$ . Thus, we have demonstrated the fabrication and realization of a robust, easy to prepare and low cost polymer based THz polarizer which provide a high and constant DOP in an extended frequency range. For NiNP polarizer, the average DOP is found to be  $\sim 0.98 \pm 0.03$  in the frequency range of 0.2-0.9 THz which decreases to  $\sim 0.6$  at 1.65 THz and using the NiNC polarizer, we have found a constant DOP of  $\sim 0.76 \pm 0.03$  in the frequency range of 0.2-2.4 THz. The alignment of NPs and NCs could easily be tuned by using more uniform external magnetic field, which could increase the nematic order parameter and DOP and consequently its polarizing behaviour. Considering its good polarizing performance, easy and cheap preparation process, durability, robustness and low maintenance, aligned magnetic nanostructures offer bright prospect to emerge as a popular THz polarizer.

# **Chapter Five**

---

# 5. Terahertz Electromagnetic Shielding

---

## 5.1. Introduction

With the development of high frequency electronic devices comes the essential need of electromagnetic interference (EMI) shielding in the corresponding frequency range. EMI is defined as the adverse effect caused by the electromagnetic waves emanating from some sources on the performance of other equipment's operating nearby at similar frequency range[153]. Therefore, development of EMI shielding materials is gaining much needed attention of scientific community in the present era. Researchers have used both SWNT and MWNT, CNF with large AR and dispersed in different polymer matrices for the preparation of composite materials to use as effective shielding materials. Most of the works till today regarding SE are concentrated in MHz to GHz frequency range[154-157], mainly due the large number of commercially available and technologically important microwave communication systems like mobile phones, radars, wireless communication. Only recently with the increasing popularity and significance of THz spectroscopy new types of devices and optical components are being investigated in this elusive frequency regime. Here, comes the importance of studying shielding mechanism in THz frequency range. SWNTs have extensively been used in a broad spectrum of science including electromagnetic shielding in a large frequency range due to their fascinating electronic, optical and mechanical properties. SWNTs dispersed in polymer matrices have attracted a great deal of attention for their unique combination of conductivity, mechanical flexibility, resistance to corrosion and processing advantages.[154] SWNT/polymer composites have been explored extensively for their excellent lightweight shielding properties at frequencies ranging from 10 MHz to several GHz using network analyzer systems[154, 158]. Scientists are now paying attention on the shielding properties in the elusive THz frequency range[9, 11, 159, 160], mainly using CNT/polymer composites and also including metallic nanostructural inclusions in it. The schematic of the THz shielding procedure as discussed in detail in this chapter is schematically shown in Fig. 5.1. The works presented in this chapter are largely based on our published paper[161].

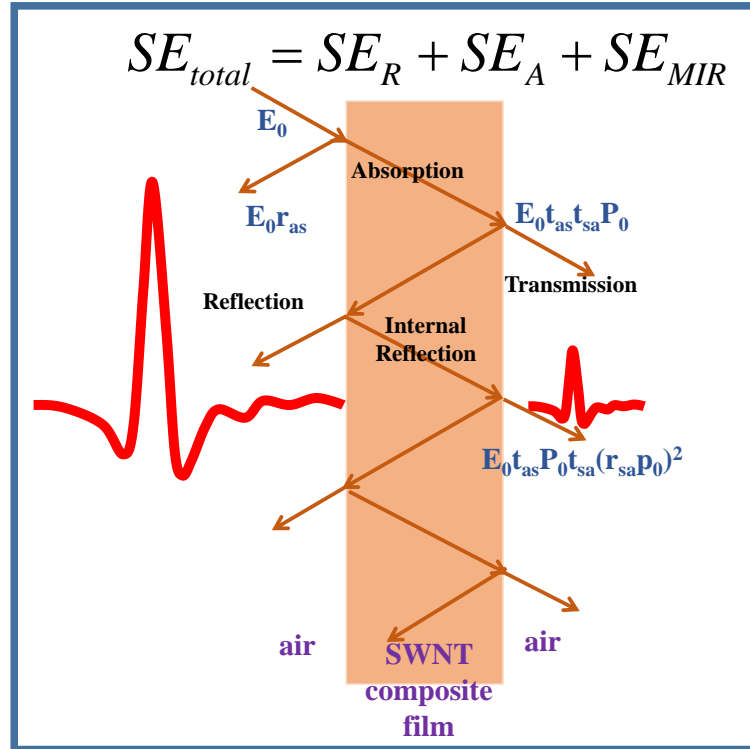


Fig. 5.1: Schematic of THz shielding

## 5.2. Background Study

EMIS of SWNT/Polymer composite had been studied for a long time mainly in the MHz and GHz frequency range. Recently with the invention of efficient THz sources and THz detectors, those studied have been extended in THz frequency region as well. A few of those important works have been mentioned in the present section. Liu et al.[156] studied the SE of SWNT/Polyurathin composites in X-band (8.0-12.0 GHz). They studied the mechanism of shielding in detail and found out that the shielding mechanism was initially reflection type but with increasing SWNT content in the polymer matrix and also with increasing probing frequency absorptive shielding started dominating. They had also theoretically showed how to extract the effect of absorption, reflection and multiple internal reflection to the total shielding of the composite. We have applied these methods to extract the proper mechanism of shielding for our composites also. Al-Saleh et al.[155] investigated the mechanism of CNT composites shielding in detail in microwave frequency range. They showed both analytically and experimentally that the contribution of multiple internal reflection remained negative for such composites in microwave frequency region and by properly tuning the thickness of the system, such negative effect can be minimized over a particular frequency range of interest. Berres et al.[162] had

analytically studied the response of an isolated, infinitely long MWNT in RF-THz frequency range using a semi-classical approach. They discussed the effect of number of tube walls, the radius of the outermost tube wall and the presence of an inner gold core on the scattering and shielding of the MWNT. Agnandji et al.[10] studied the experimental SE in the frequency range of 0.1-4 THz using  $\sim 0.15$  mm thick polyaniline films with different amount of doping (0.2, 0.5, 1, 5 and 10%). They had also studied the conductivity of the system and made a comparison between the theoretical and experimentally found SE in THz frequency range. They obtained  $\sim 40$  dB SE for 10% doped polyaniline film in the frequency range of interest which was interesting in application point of view. Arindam das et al.[159] prepared a super-hydrophobic CNF/polymer composite and studied the SE and composite conductivity of the system and there dependence on the hydrophobicity of the system in the frequency range of 570 GHz to 630 GHz. They found out a maximum attenuation of 32 dB in the frequency range of interest and the attenuation increased with increasing CNF content in the sample. Macutkevic et al.[163] studied the THz spectroscopy of onion like carbon (OLC) nanofiber/PMMA polymer composites in recent past. The EMI shielding quasi-resonant behaviour in the frequency range near 0.3-0.5 THz and the observed resonant properties depend significantly on the composite films preparation and concentration of OLC inclusions. The observed absorption bands were supposed to be associated with excitation of plasmon modes. Seo et al.[9] studied the dielectric constant engineering and shielding mechanism of graphite powder/PMMA composites by varying weight fractions of graphite powders inside the polymer matrix in the frequency range of 0.1-1.6 THz. For the highest graphite (35.7%) powder weight fraction, the absorption was mainly due to absorption particularly in the higher frequency range ( $> 1$  THz). At a particular frequency, SE was found to be increasing linearly with increasing graphite content in the matrix. The real dielectric function of the composite containing highest graphite powder showed Drude behaviour but the other composites did not.

### 5.3. Basic Theory

Total SE of a system is governed by three processes namely reflection, absorption and multiple internal reflection;

$$SE_{tot}(\omega) = SE_R(\omega) + SE_A(\omega) + SE_{MIR}(\omega) \quad (41)$$

Shielding also depends upon various physical parameters like i) conductivity, ii) permittivity and permeability and iii) thickness with most of these factors being cross-

linked to each other. Now-a-days composite materials (conductive filler in dielectric host) are particularly gaining much attention as a potential shield material due to their unique properties like i) tunable conductivity, ii) resistance to corrosion, iii) flexibility and iv) low cost[154]. Experimentally, one can calculate the transmittance in frequency domain ( $T(\omega)$ ) and from that total SE can be easily achievable using the following formula;

$$SE(\omega) = -10 \log_{10} \left( \left| \frac{\tilde{E}_{samp}(\omega)}{\tilde{E}_{ref}(\omega)} \right|^2 \right) \quad (42)$$

where  $\tilde{E}_{samp}(\omega)$  and  $\tilde{E}_{ref}(\omega)$  are the complex transmitted field in frequency domain passing through sample and air. There are three different contributions to the SE of a system, namely absorption, reflection and multiple internal reflection. The SE of a composite system can be written as[75, 76, 156, 164],

$$\begin{aligned} SE(\omega) &= SE_A(\omega) + SE_R(\omega) + SE_{MIR}(\omega) \\ &= 8.68\alpha(\omega)l + 20 \log_{10} \left( \frac{|1 + \tilde{n}(\omega)|^2}{4|\tilde{n}(\omega)|} \right) \\ &\quad + 20 \log_{10} \left| 1 - \frac{(1 - \tilde{n}(\omega))^2}{(1 + \tilde{n}(\omega))^2} e^{(-2\alpha(\omega)l)} \right| \end{aligned} \quad (43)$$

where  $\tilde{n}(\omega)$ ,  $\tilde{\gamma}(\omega)$  and  $l$  are the complex refractive index, complex propagation constant and thickness of the sample under consideration. The complex propagation constant is described as;

$$\begin{aligned} \tilde{\gamma}(\omega) &= \alpha(\omega) + i\beta(\omega); \\ \alpha(\omega) &= \frac{2\pi}{\lambda} \left( \sqrt{\frac{(\sqrt{1 + \tan^2 \delta(\omega)} - 1) \varepsilon_r(\omega)}{2}} \right), \\ \beta(\omega) &= \frac{2\pi}{\lambda} \left( \sqrt{\frac{(\sqrt{1 + \tan^2 \delta(\omega)} + 1) \varepsilon_r(\omega)}{2}} \right), \end{aligned} \quad (44)$$

where  $\tan \delta(\omega) = \frac{\varepsilon_i(\omega)}{\varepsilon_r(\omega)}$  is the loss tangent. Shielding due to multiple internal reflection ( $SE_{MIR}(\omega)$ ) is dominant for films where the thickness of the film is comparable or smaller than the skin depth of the material at that particular frequency. If the thickness of the film is thicker than the skin depth, the conductive material will absorb the reflected wave from the internal surface, and thus multiple-reflection can be ignored. However, if the shield is thinner than the skin depth, the influence of multiple-reflection will be significant in decreasing overall EMI shielding[155]. It was argued in many

literatures[164, 165] that the effect of multiple internal reflection can be neglected if  $SE_R(\omega) \geq 15 \text{ dB}$ . The matlab code given in the appendices is used to extract the different contributions to the total shielding and their subsequent analysis. The complex optical parameters are obtained using teralyzer software, which is then fed into the matlab code for further analysis.

## 5.4. Sample Preparation

SWNT (> 90% carbon content, > 77% SWNT, diameter ~ 0.9-1.2 nm) and PVA (> 99% hydrolyzed) were purchased from Sigma-Aldrich and used without further purification. 1 g granular PVA was dissolved in 10 ml DI water with continuous magnetic stirring for 45 minutes at 80 °C to produce a clear solution. Required amount of SWNT powder was mixed with 5 ml DI water and ultrasonicated for 30 minutes to produce a uniform dispersion. Uniformly dispersed SWNT solution was then added with the clear PVA solution and magnetically stirred for another 45 minutes before pouring into a glass Petri dish, which was then kept at an ambient condition for slow drying for 10 days to prepare the samples for spectroscopic measurements. A pure PVA film was also prepared for the reference measurements.

## 5.5. Measurement and Analysis

Different concentration of SWNT powder is mixed with the polymer solution for the preparation of the composite and we have prepared six composite films namely S1, S2, S3, S4, S5 and S6; containing 1, 4, 8, 10, 16 and 20 mg SWNT powder respectively. A bare PVA film has also been prepared. The optical image of the S2 and S5 is shown in the Fig. 5.2.

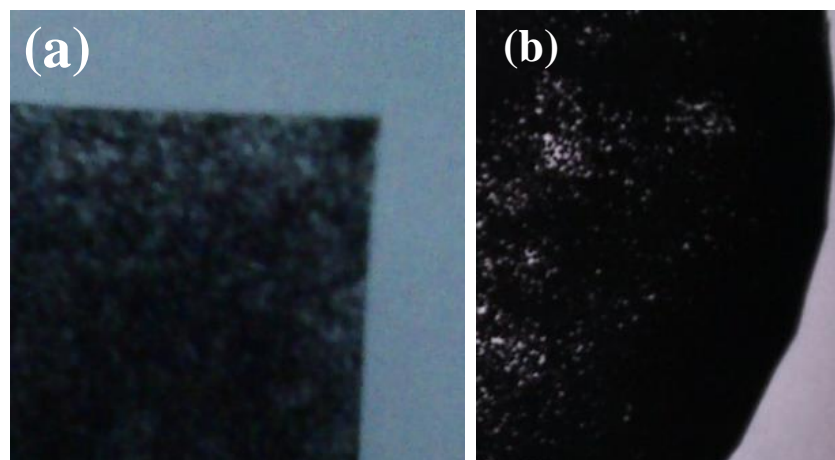
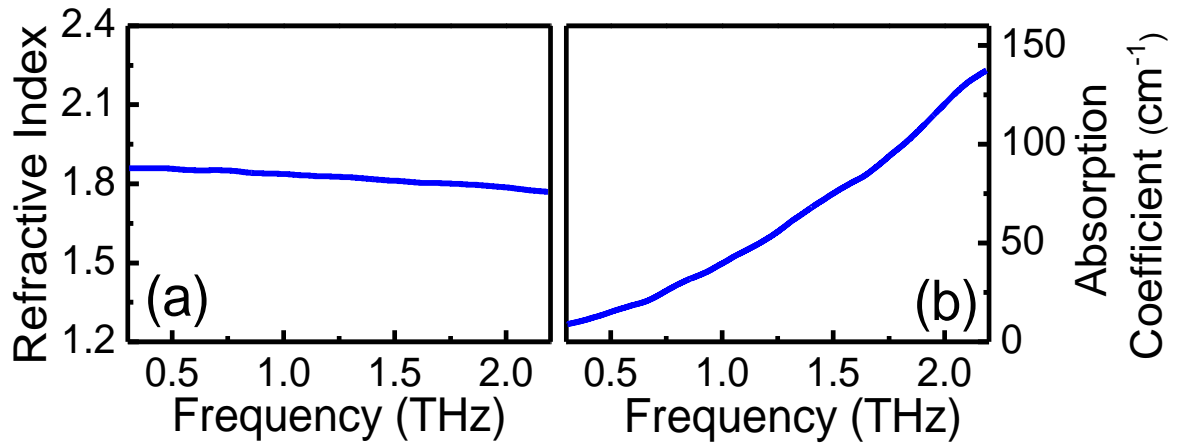


Fig. 5.2: Optical image of (a) S2 and (b) S5 film

The importance of using PVA as the matrix is twofold: i) it provides the necessary tensile strength to the film besides supporting the dispersed CNTs and also ii) PVA has a flat refractive index over the frequency range of interest and provides some attenuation especially in larger frequency. The refractive index and absorption coefficient of a bare PVA film of thickness  $290\ \mu\text{m}$  is shown in Fig. 5.3. The refractive index remains constant at  $1.82 \pm 0.02$  in the frequency range of 0.3-2.2 THz whereas absorption coefficient continuously increases and reaches  $135\ \text{cm}^{-1}$  at 2.2 THz.



**Fig. 5.3: (a) Refractive index (b) absorption coefficient of a bare PVA film**

The thickness of the films has been calculated from cross sectional SEM images (not shown here) and found to be around  $300 \pm 30\ \mu\text{m}$ . The THz time domain amplitude through bare PVA sample and SWNT/PVA composites and the corresponding FFT amplitude in frequency domain are shown in Fig. 5.4.

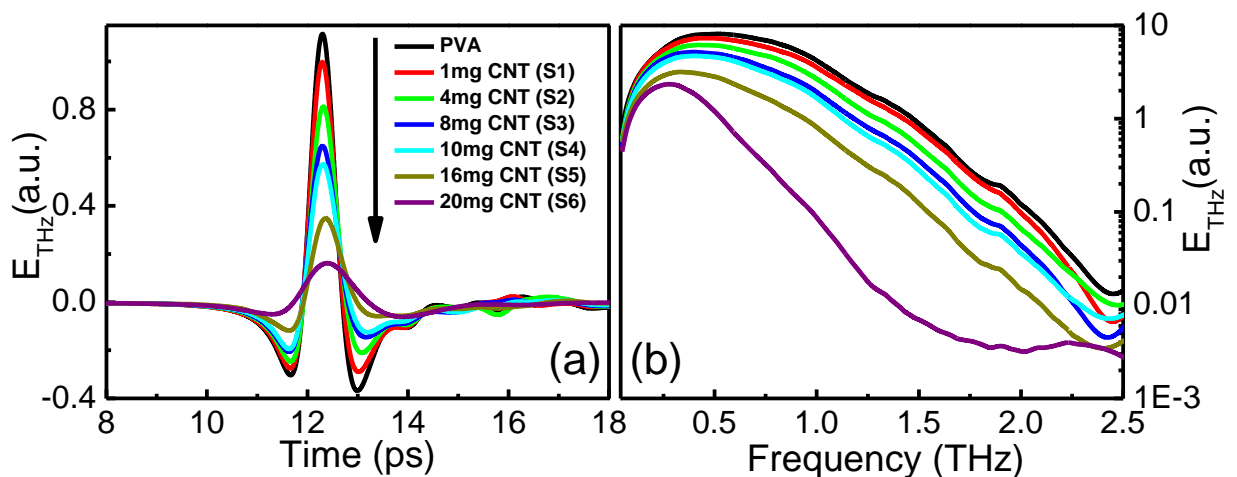


**Fig. 5.4: Transmitted THz amplitude through the composite films in (a) time domain and (b) frequency domain**

The peak-to-peak THz amplitude decreases with increasing SWNT content in the polymer due to highly percolated behaviour of the SWNTs with increasing weight fraction which is also clearly visible from the frequency domain spectrum. The FFT spectrum of the sample S6 is limited by the S/N ratio of up to 1.4 THz, whereas for the remaining samples FFT spectra can be analyzed from 0.3 to 2.1 THz frequency range with good S/N ratio. We have not considered sample S6 for further analysis. Transmittance ( $T$ ) profile of all the samples in the aforementioned frequency range is depicted in Fig. 5.5a. Transmittance is defined as  $T(\omega) = \left| \frac{\tilde{E}_{samp}(\omega)}{\tilde{E}_{ref}(\omega)} \right|^2$  where  $\tilde{E}_{samp}(\omega)$  and  $\tilde{E}_{ref}(\omega)$  are the complex THz electric fields passing through the sample and incident on the sample, respectively in frequency domain.

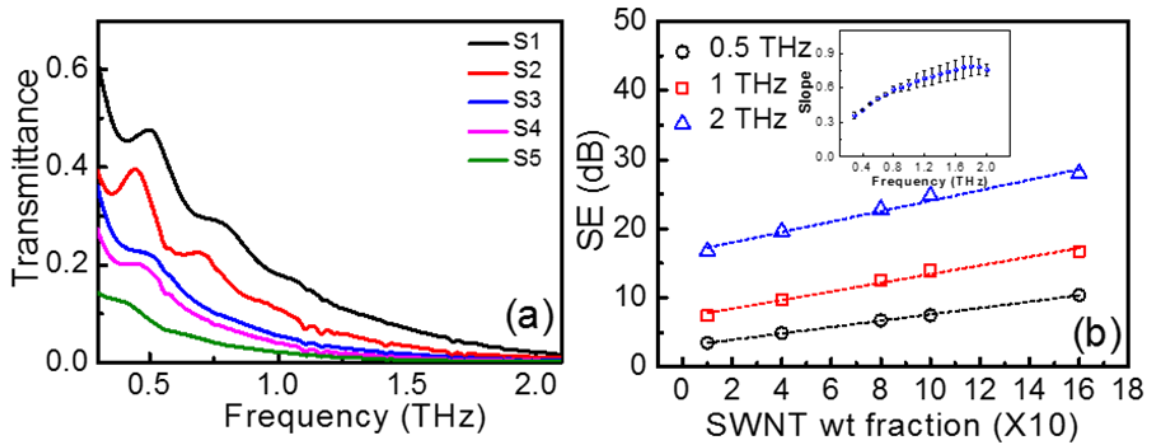


**Fig. 5.5: (a) Frequency dependent transmittance, (b) SE at three different frequencies fitted with a straight line as a function of SWNT weight fraction. Inset shows the slopes of these fitted straight lines as a function of frequency.**

As evident from the figure, transmittance for all the samples decreases steadily with increasing frequency due to high absorption of SWNT at higher THz frequencies. This also indicates that the present composites are capable of acting as good low band-pass filters that effectively screen THz wave beyond 1.25 THz especially for samples with higher SWNT content (S3, S4 and S5). SE of the samples are calculated using the formulae;  $SE_{tot}(\omega) = -10 \log(T(\omega))$ . It can be noted that total SE is a combination of absorptive, reflective and multiple internal reflection type shielding and later we have extracted the contribution of each type of shielding separately for a proper understanding of the shielding mechanism in our polymer composites. We have plotted the total shielding at three different frequencies at; 0.5, 1.0 and 2.0 THz for all the composites with

increasing SWNT content and fitted with a straight line as a function of increasing SWNT weight fraction as shown in Fig. 5.5b.

**Table 4: SE at different probing frequencies**

Frequency	Expression of measured SE (SE of bare PVA matrix at that particular frequency) + (SWNT weight fraction x 1000 x slope)
0.5 THz	$(3.02 \pm 0.07) + (\text{SWNT weight fraction} \times 1000 \times 0.45)$
1.0 THz	$(7.19 \pm 0.42) + (\text{SWNT weight fraction} \times 1000 \times 0.63)$
2.0 THz	$(16.49 \pm 0.50) + (\text{SWNT weight fraction} \times 1000 \times 0.75)$

We found that, at a particular probing frequency, SE increases linearly with increasing SWNT content in the composite and the fitted parameters are given in Table 4 at three different probing frequencies. So, to estimate the SE of a composite at a particular frequency, we need three factors; i) SE of the bare PVA matrix at that particular frequency, ii) SWNT weight fraction, iii) Slope of the fitted straight line. SE of a bare PVA matrix can be experimentally measured easily in the frequency range of interest and we know the slope of fitted straight lines at different frequencies for over a significant range of SWNT inclusions. This enables us to prepare a shielding device working at a particular frequency, according to the required SE using appropriate amount of SWNT inclusion inside the polymer matrix.

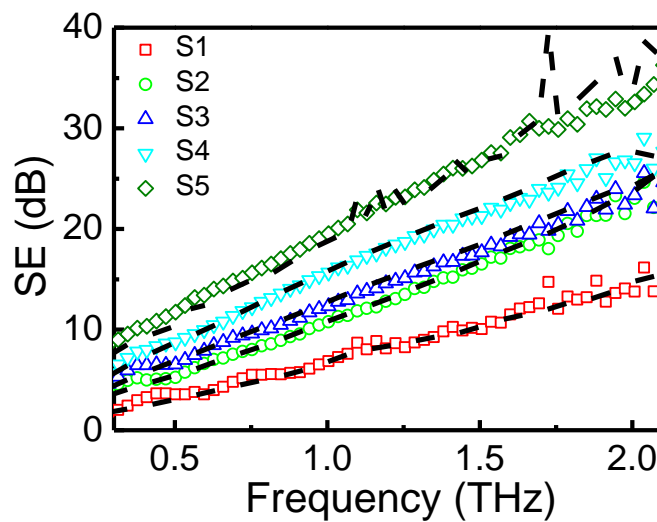


**Fig. 5.6: Shielding effectiveness of the composite films in the frequency range of 0.3-2.1 THz and fitted with a phenomenological model**

Thus SE of these composites can be predicted in the prescribed frequency range without performing direct measurements if one knows the SWNT weight fraction in the composite. The slopes of the fitted straight lines are found to be increasing with increasing probing frequency. But, in higher frequency range (1.2 THz to 2.1 THz), the slope remains constant at  $0.73 \pm 0.07$  as shown in the inset of Fig. 5.5b.

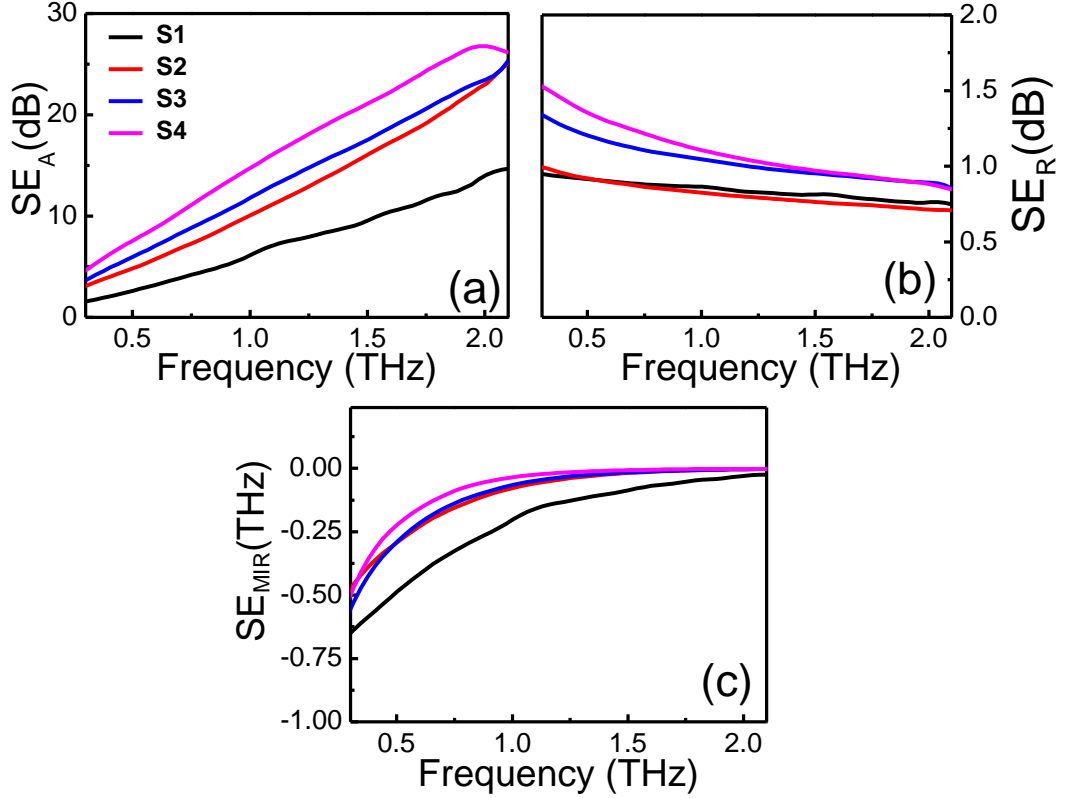


**Fig. 5.7: The contribution of (a) absorption, (b) reflection and (c) multiple internal reflection to shielding of the composite films in the frequency range of 0.3-2.1 THz**

It can be shown[75, 156] that SE of a composite system can be written as;

$$SE(\omega) = SE_A(\omega) + SE_R(\omega) + SE_{MIR}(\omega)$$

$$= 8.68\alpha(\omega)l + 20 \log_{10} \left( \frac{|1 + \tilde{n}(\omega)|^2}{4|\tilde{n}(\omega)|} \right) + 20 \log_{10} \left| 1 - \frac{(1 - \tilde{n}(\omega))^2}{(1 + \tilde{n}(\omega))^2} e^{-2\alpha(\omega)l} \right|,$$

where  $\tilde{n}(\omega)$ ,  $\tilde{\gamma}(\omega)$  and  $l$  are the complex refractive index, complex propagation constant and thickness of the sample under consideration. The details of the equation have been described in the theory section.  $SE_{total}$  increases with increasing probing frequency and also with increasing SWNT content (as shown in Fig. 5.6) due to i) high absorption of THz waves by SWNT at high frequencies and ii) well percolated region with increasing SWNT content, respectively. Experimentally obtained  $SE_{total}(\omega)$  has been plotted in Fig. 5.6 and fitted with the theoretical model described earlier. We have also extracted the

contribution of absorption ( $SE_A(\omega)$ ), reflection ( $SE_R(\omega)$ ) and multiple internal reflection ( $SE_{MIR}(\omega)$ ) to the total shielding using and plotted in Fig. 5.7. Absorption is the dominating factor in shielding for all the composites and it increases with increasing frequency and increasing SWNT weight fraction. Such absorptive nature of the EMIS has been found in various literatures studying the shielding of CNT/Polymer composite in different frequency range of interest mainly in MHz and GHz frequency region. Reflection remains very small ( $< 1.5$  dB) and decreases with increasing frequency. Multiple internal reflection remains very small ( $< 0.75$  dB) and negative (which increases to 0 with increasing frequency) and can be neglected for all the composites.

## 5.6. Conclusion

In summary, we have prepared SWNT-polymer composite samples via slow drying method with varying SWNT content in PVA matrices. Transmittance is found to be significant at lower frequencies (between 0.3 and 0.8 THz) but is close to zero at higher frequencies (beyond 1.25 THz) showing a possible application of these composites especially with higher amount of SWNT contents for low band-pass THz filters. Shielding properties of the samples were studied in the frequency range of 0.3 THz to 2.1 THz. SE shows a linear relationship with SWNT weight fraction at a particular probing frequency and in a broad frequency range from 1.2 to 2.0 THz, SE can be expressed as  $SE \propto (0.73 \pm 0.075) \cdot w$  where  $w$  is the SWNT weight fraction. SE of the 1.6% SWNT composite was found to be greater than 20 dB at 1.25 THz and rises steadily up to 29 dB at 2.1 THz. The different contributions (absorption, reflection and multiple internal reflection) to the total shielding is extracted using a theoretical formula. The effect of absorption is found to be dominating and it increases with increasing probing frequency.

# **Chapter Six**

---

# 6. Conductivity Manipulation in SWNT/Polymer Composite Films

---

## 6.1. Introduction

In last decade, THz spectroscopy has emerged as a salient technique to explore the high frequency optical properties of thin films[166-168], nanomaterials[83, 169-171], CNT[140, 172-175] in a non-invasive way due to the availability of powerful and compact THz sources and THz detectors. Scientists are now trying to develop different types of THz optics like THz shielding devices[11, 159, 161, 176], THz attenuator[161], THz polarizer[3, 5, 6, 8], THz band-pass filter[177, 178] to manipulate THz radiation in an effective way and high quality SWNT's[179, 180] are acting as a building block in most of the cases due to their fascinating optoelectronic response in this frequency range. Significant amount of work has already been conducted to understand the frequency dependent conductivity properties of CNT/polymer composite materials from d.c. to GHz frequency[181-183] range and now with the newly unfolded THz technique, significant amount of work are being carried out in this frequency window[161] particularly in the last decade. Conductivity of SWNTs and MWNTs in THz frequency region has been studied extensively in the last decade, although its origin remains a debatable issue. The inclusion of CNTs in a polymer matrix results in an increased electrical conductivity as well as mechanical stability of the polymer and it depends on various cross related issues like AR, weight fraction, chirality, conductivity, tube-tube interaction, functionalization and solubility of CNTs. Conductivities of 0.01-0.1  $\text{Scm}^{-1}$  can be obtained for CNT/polymer composites with a CNT loading of 5%. CNT/polymer materials have important applications in the field of solar cells, charge storage and electromagnetic shielding devices hence governing electrical properties of such composites seems to be very important for successful device applications. Electromagnetic frequency response of such materials can be tuned by chemically modifying the CNT or controlling CNT aggregate structure[184]; however they are extremely complicated and difficult process. A recent study has shown that dimensions of CNTs specially their length are effective[184] in modifying frequency dependent (near d.c. to GHz) conductivity of such composites using a modified UDR theory[185]. Scientists have also tried to modulate the conductivity of

CNT composites by functionalization, acid treatment, sidewall modification etc. In a recent report[186], it was shown that nanoparticles (both metallic and semiconductor) attached at the CNT surfaces act as a local carrier trapping potential and thereby reduce conductivity of pristine SWNT in THz frequency range.

Here in the present chapter, we have tried to manipulate the conductivity properties of SWNT/Polymer composites by two distinct methods; i) SWNT length variation and ii) SWNT sidewall modification with Au nanoparticles. The Schematic of these two methods is shown in Fig. 6.1. The works described in this chapter are largely based on one of our published papers[187] and a conference presentation[188].

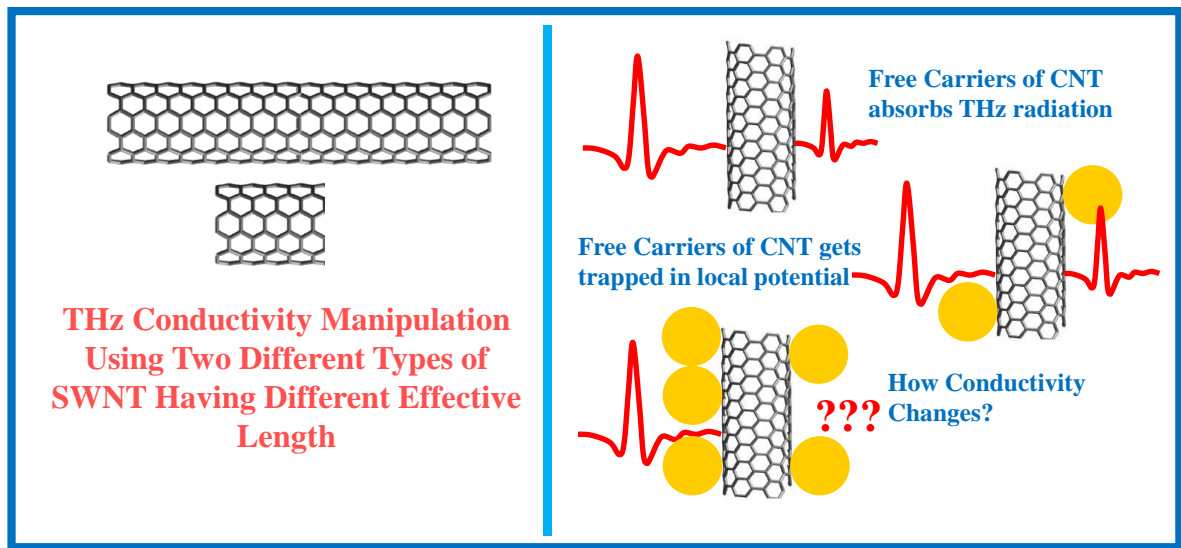


**Fig. 6.1: The two conductivity manipulation mechanisms; (a) SWNT of different lengths and (b) different concentration of AuNP decoration on the sidewalls of SWNT**

## 6.2. Background Study

THz conductivity of different types of CNT films have been investigated extensively in last few years. Manipulation of THz conductivity by aligned, doped or acid treated CNTs has also been experimented in a handful of studies. CNTs show a broad TCP in the frequency range of 1.5-30 THz[189, 190]. According to one group of scientists, THz conductivity depends on the inter-band transitions in a narrow gap in the vicinity of the Fermi point arising out due to the finite radial curvature of CNTs[191] and TCP depends on tube diameter ( $f_{TCP} \propto \frac{1}{D^2}$ ). Whereas, the other group says the electromagnetic response of a single or a collection of SWNT's depend strongly on its length ( $f_{TCP} \propto \frac{1}{L}$ ) in THz regime where localised surface plasmon resonance is responsible for its conductivity and the TCP

increases with decreasing SWNT length[189, 190, 192]. The increase in TCP is also related with intensity decrement of THz conductivity of short SWNT's due to their weak scattering ability, damaged sidewalls and smaller electron relaxation time. Recently Shuba et. al.[192] showed that TCP was increased from 4.5 to 30 THz which decreasing SWNT length and the effect has been solely attributed to excitation of localized surface plasmon resonance. Whatever, the reason may be due this appearance of TCP in CNT composites, the THz conductivity of such composites and their manipulation became very important aspect of research for the application of CNT based devices in THz optoelectronics. The composite conductivity of the system becomes important rather than the intrinsic conductivity of the CNTs for its successful function as a composite material. The composite dielectric function and the conductivity of such composite materials has been studied significantly in MHz-GHz frequency region over the last two decades and with the increasing popularity of THz technology, such studies are now being extended in THz frequency range. Cramer et al.[193] presented a complete dynamic conductivity spectra of the fast-ion conducting silver iodide/silver selenite glasses at frequencies between 4 Hz and 10 THz and at temperatures between 93 K and 573 K (this temperature range covers the glassy and molten state of matter). In the spectra, they clearly distinguished between the hopping conductivity at low frequencies, and the vibrational regime at very high frequencies. After removing the vibrational contributions, they had studied the spectra in terms of the hopping motion of the silver ions. They proposed a superposition of two power laws to describe the complete hopping spectra. One of them was the 'Jonscher power law' with an exponent 0.62, while the additional power law had an exponent larger than one. Barrau et al.[183] studied the d.c. and a.c. conductivities of CNT/polyepoxy composites from 20 to 110 °C in the frequency range  $10^2$ - $10^6$  Hz as a function of the conductive weight fraction ' $p$ ' ranging from 0.04 to 2.5 weight percentage. The frequency dependence of the measured conductivity was found to be obeying the UDR model with a power law exponent  $s \sim 0.6$ -1.0. They found that the conduction behaviour was governed by tunnelling type conduction and the nature of conduction process was independent of the nature of the polymer used in preparing the matrix. Chakroborty et al.[182] studied the d.c. and a.c. electrical transport properties of MWNT/PVA composites within a temperature range 77-300 K and in the frequency range 20 Hz-1 MHz in presence as well as in absence of a transverse magnetic field up to 1 T. The d.c. conductivity followed variable range hopping model. The magneto-conductivity of the samples changed sign from positive to negative with an increase in temperature, which was interpreted by the dominance of the quantum

---

interference effect over the wave function shrinkage effect. The a.c. conductivity followed a power law and the temperature dependence of frequency exponent 's' was explained by correlated barrier hopping model. The dielectric behaviour of the samples was found to be governed by the grain and grain boundary resistance and capacitance. The a.c. conductivity got reduced with the application of magnetic field. Kilbride et al.[181] studied a.c. and d.c. conductivities for a range of concentrations of MWNTs in two different polymer hosts. In general, the a.c. conductivity displayed two distinct regions, a frequency independent region of magnitude  $\sigma_0$  at low frequency and a frequency dependent region at higher frequency. Both  $\sigma_{DC}$  and  $\sigma_0$  followed a percolation scaling law of the form  $\sigma \propto (p - p_c)^t$  with  $p_c = 0.055\%$  by mass and  $t = 1.36$ , which when extrapolated gave to a conductivity of  $10^{-3}$  S/m for 100% nanotube content. The presence of a thick polymer coating, resulting in poor electrical connection between tubes was reflected by such a low conductivity value. The charge transport was found to be controlled by fluctuation induced tunnelling. In the high frequency regime, the conductivity was found to be increasing with frequency according to an approximate power law with exponent  $s \approx 0.92$ , indicative of hopping transport. Dyre et al.[185] reviewed the conduction mechanism in different disordered materials in the frequency region of d.c. to several GHz using two different approaches; i) symmetric hopping model and ii) macroscopic model. Despite their fundamental differences, both models predicted a.c. universality in the extreme disorder limit and the two universal a.c. conductivities were found to be similar. Kahouli et al.[194] studied the electrical conduction mechanisms of semicrystalline thermoplastic parylene C thin films in a large temperature and frequency regions. The a.c. electrical conduction in parylene C was governed by two processes namely: i) correlated barrier hopping (CBH) model at low[77-155 K] and high[473-533 K] temperature and ii) the small polaron tunnelling mechanism (SPTM) from 193 to 413 K within the framework of the UDR law. They explained the conduction mechanism with the help of Elliot's theory and determined the Elliot's parameters. From frequency and temperature dependent conductivity characteristics, the activation energy was found to be 1.27 eV for d.c. conduction interpreted in terms of ionic conduction mechanism. The power law dependence of a.c. conductivity was interpreted in terms of electron hopping with a density  $N(E_F)$  ( $\sim 10^{18}$  eV  $\text{cm}^{-3}$ ) over a 0.023-0.03 eV high barrier across a distance of 1.46-1.54 Å.

Scientists were trying to manipulate the conductivity of CNT composites using various techniques ranging from acid treatment of CNT, CNT doping, CNT sidewall decoration etc.. Shehzad et al.[184] studied the effect of AR (of MWNT) on the conductivity

and dielectric properties of MWNT/polymer composites in the frequency range of 100 Hz to 10 MHz. Quantitatively, the frequency responses of electrical properties were found to be independent of nominal AR, concentration, percolation threshold, and the diameter of the MWNT. Instead, frequency response of electrical properties was dependent on the MWNT length and initial electrical conductivity of the composites. With the same initial conductivity of the MWNT composites, frequency-conductivity sensitivity varied inversely with the nominal length of the MWNTs.

The surface walls of CNTs decorated via a variety of nanoparticles offers an easy and exciting way to tune the frequency dependent conductivity properties of the respective CNTs. McAndrew et al.[195] studied electrical conductance enhancement in sparse SWNT networks by decoration with Au nanoparticles (AuNP). Their optimized hybrid network exhibited a sheet resistance of  $650 \Omega \text{ sq}^{-1}$ , 1/1500 of the resistance of the host undecorated network, with a negligible optical transmission penalty ( $> 90\%$  transmittance at 550 nm wavelength). The electrical transport at room temperature in the host and decorated networks were dominated by 2D variable range hopping. The high conductance enhancement was due to positive charge transfer from the decorating AuNP in intimate contact with the host network causing a Fermi energy shift into the high density of states at a van Hove singularity and enhanced electron delocalization relative to the host network. For higher than optimal values of nanoparticle coverage or nanoparticle diameter, the conductance enhancement was countered by metallic inclusions in the current pathways that are of higher resistance than the variable range hopping-controlled elements. Jung et al.[186] studied the effect of metallic, semiconducting and insulating nanocrystal decoration on the surfaces of SWNT, DWNT, MWNT and graphene oxide (GO) flakes in their THz conductivity properties. They found that, the presence of nanocrystals was responsible for the decrement of the THz conductivity of CNTs irrespective of the electronic nature of the nanocrystals. The effect being decreasing in the following order (SWNT  $>$  DWNT  $>$  MWNT  $>$  GO). They explained their experimental results in terms of coulomb trap potential of nanocrystals trapping the necessary free electrons of the CNTs. Subramaniam et al.[196] reported a CNT/copper composite exhibiting similar conductivity ( $2.3\text{-}4.7 \times 10^5 \text{ S cm}^{-1}$ ) as copper ( $5.8 \times 10^5 \text{ S cm}^{-1}$ ), but with a hundred times higher ampacity ( $6 \times 10^8 \text{ A cm}^{-2}$ ). Using vacuum experiments, they demonstrated that CNTs suppressed the primary failure pathways in copper due to the increased copper diffusion activation energy ( $\sim 2.0 \text{ eV}$ ) in CNT/copper composite, explaining its higher ampacity. This composite material was the only material with both

---

high conductivity and high ampacity, making it uniquely suited for applications in microscale electronics and inverters.

### 6.3. Basic Theory

For a composite system like SWNT/PVA composite film, the total conductivity of the composite material rather than the intrinsic conductivity of the SWNT is the most important parameter. In such materials, SWNT inclusion is considered to be the conductive inclusion in the otherwise non-conducting or poorly conducting dielectric (polymer) matrix. The conductivity spectra of such a disordered composite material obey a power law behaviour described by the following relation[183];

$$\sigma_{real}(\omega) = \sigma_{D.C.} + A\omega^s, \quad (45)$$

where,  $\sigma_{D.C.}$  is the d.c. plateau observed in the low frequency regime,  $A$  is a parameter which depends on the temperature,  $s$  is the frequency exponent which in turn depends upon the conductive properties of the sample and the temperature and can take values in the limit of  $0 < s < 1$ . The d. c. plateau region ( $\sigma_{D.C.}$ ) is obtained up to a critical frequency  $\omega_C$  defined as  $\sigma_{real}(\omega=\omega_C) = 1.1\sigma_{D.C.}$ [183] and beyond this critical frequency limit, conductivity spectra maintain a sub linear frequency dependence ( $s < 1$ ). In a large number of earlier studies[181-185, 193], this model has been used to analyze the dielectric relaxation of a composite material in MHz or GHz frequency range. The d.c. plateau region was found to be a function of the temperature and the concentration of CNT in a particular composite film. The critical frequency for CNT/PVA composites in general lies in the MHz frequency range and therefore does not appear in the present THz spectroscopic investigation where the frequency range of interest is several orders of magnitude higher. Such power law behaviour is a characteristic of different transient phenomenon in disordered systems including a.c. conductivity due to the random walk of charge carriers through the percolation pathways. This is referred to as the UDR model, as it finds applicability to a wide class of disordered materials. The conductivity spectra of SWNT/PVA films in the probed frequency range are analyzed using a modified UDR model as explained below. As the probing frequency reaches near the phonon frequency ( $10^{12}$  Hz), deviation from UDR model can be anticipated as the conductivity spectra get affected by the lowest lying vibrational component or some cross terms resulting from a coupling between vibrational and hopping motion of some carriers[193]. Treatment of all these effects in separate ways is a challenging task and a super-linear frequency dependence (i.e.,  $1 < s < 2$ ) has been proposed to qualitatively explain such spectra[193].

The physical interpretation of such behaviour has been elucidated by confined motion of carriers in the vicinity of coulomb traps. Hopping or tunnelling type of conduction of carriers is described by a sub-linear frequency dependence ( $0 < s < 1$ ) and in case of  $1 < s < 2$ , motion of carriers get disturbed by columbic traps and there movement is limited only in the local environment[193]. A matlab code as given in the appendices is used to analyse the real conductivity spectra using the UDR model.

## **6.4. Length Dependent Conductivity in SWNT/Polymer Composite**

### **6.4.1. Introduction**

It was already reported that, the AR, and more importantly the length of CNT and CNT weight fraction in a CNT/polymer composite were the dominant factor in determining the conductivity and dielectric relaxation of the composite material [184]. Here, we have employed similar idea in the THz frequency range, where the THz response of SWNT/polymer composite material has been studied by varying the SWNT effective length and SWNT weight fraction in the composite material.

In this chapter, we have dispersed two different types of SWNT samples namely S\_L (dia ~ 1-2 nm, average length ~ 15  $\mu\text{m}$ ) and S\_S (dia ~ 1-2 nm, average length ~ 2  $\mu\text{m}$ ) in PVA matrix at room temperature via slow drying process at three different weight fractions (0.1%, 0.8% and 1.6%). They are denoted as S\_L1, S\_L8, S\_L16, S\_S1, S\_S8, S\_S16 respectively. THz-TDS measurements are performed at room temperature in transmission geometry in the frequency window of 0.3-2.0 THz. THz conductivity spectra of the composite films are extracted from the time domain data and analyzed using a modified UDR model[193]. A super linear frequency exponent is found for all S\_S and S\_L1 samples whereas sub linear frequency exponent ( $s < 1$ ) is observed for S\_L8 and S\_L16 samples and are explained in the light of motion of electrons in restricted atmosphere. THz conductivity is shown to be increased significantly from S\_S to S\_L in the entire frequency window for all weight fractions in a controlled manner. The discussions based on these results have exposed intriguing aspects on THz response of SWNT/Polymer composite films and their possible application in future THz devices.

### 6.4.2. Sample Preparation

SWNTs (> 90% carbon content, dia ~ 1.0-1.2 nm) of two different lengths (15  $\mu\text{m}$  and 2  $\mu\text{m}$ ) were purchased from NanoAmor, USA at highest available purity and processed without further purification. All the SWNTs were bundled and no special isolation technique was employed to separate them. PVA (99% hydrolyzed, M.W. 89,000) was purchased from Sigma Aldrich and Millipore DI water was used for sample preparations. 1 gm granular PVA was dissolved in 10 ml DI water with continuous magnetic stirring for 45 min at 80  $^{\circ}\text{C}$  to produce a clear solution. Required amount of SWNT powder was mixed with 5 ml DI water, ultrasonicated for 30 min and added to the clear PVA solution. The SWNT/PVA solution was then magnetically stirred for another 45 min before pouring into a glass Petri dish, which was kept at an ambient condition for slow drying for 10 days to prepare composite films of thickness  $300 \pm 20 \mu\text{m}$  for spectroscopic measurements.

### 6.4.3. Results and Discussions

Fig. 6.2 shows the THz time domain waveform (and frequency domain as shown at the inset) passing through S\_L1, S\_S1, S\_L8, S\_S8 and S\_L16, S\_S16 samples respectively in the frequency range of 0.3-2.0 THz. It is distinctly evident from the FFT amplitude that optical parameters of the films can effectively be extracted in the frequency range of 0.3-2.0 THz due to reduced S/N ratio beyond that. The peak to peak time domain THz amplitude is found out to be larger in shorter length SWNT films compared to longer length SWNT films for all the three SWNT weight fractions. The change in the transmission spectra between the long and short SWNT films increases with increasing the SWNT weight fraction of the composites, which is more clearly visible in the frequency domain spectra. This implies higher THz conductivity (i.e. larger absorption of THz waves by the samples) for the longer length SWNT composites and the increment in conductivity is larger for larger SWNT weight fraction in the composite. The frequency dependent complex refractive index and the complex dielectric constants for the composite films are deduced by numerically solving Fresnel's transmission coefficient for each film by using the THz transmission spectra[197]. Special care has also been taken to account for the thickness distribution of different films during calculation of frequency dependent optical properties.

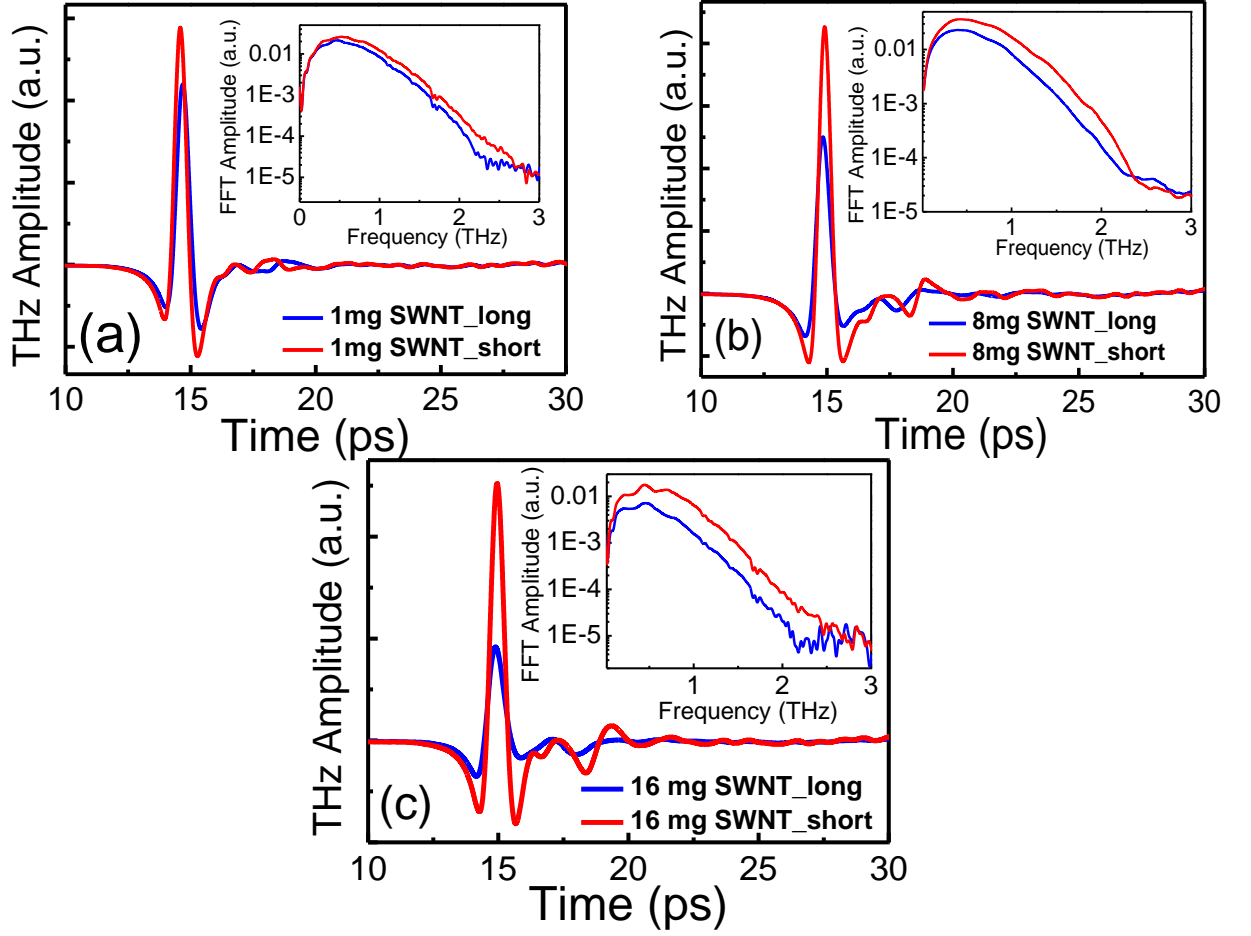


**Fig. 6.2: Transmitted THz amplitude in time domain and the corresponding FFT amplitude in frequency domain (shown at the inset of every graph) for a) 1 mg, b) 8 mg and c) 16 mg SWNT long and short samples**

THz conductivity is retrieved from complex optical constant using the following relations;

$$\tilde{n}(\omega) = n(\omega) + ik(\omega), \quad (46)$$

$$\begin{aligned} \tilde{\epsilon}(\omega) &= \tilde{n}^2(\omega) = n^2(\omega) - k^2(\omega) + i2n(\omega)k(\omega) \\ &= \epsilon_{real}(\omega) + i\epsilon_{ima}(\omega), \end{aligned} \quad (47)$$

$$\tilde{\epsilon}(\omega) = \epsilon_{\infty} + i \frac{\tilde{\sigma}(\omega)}{\epsilon_0 \omega}, \quad (48)$$

$$\tilde{\sigma}(\omega) = \sigma_{real}(\omega) + i\sigma_{ima}(\omega), \quad (49)$$

where,  $\tilde{n}(\omega)$  is the complex refractive index with  $n(\omega)$  as its real part and  $k(\omega)$  as its imaginary part,  $\tilde{\epsilon}(\omega)$  is the complex dielectric constant of the system,  $\epsilon_{\infty}$  is the infinite dielectric constant,  $\epsilon_0$  is the permittivity of free space,  $\omega$  is the angular frequency of

radiation and  $\tilde{\sigma}(\omega)$  is the complex conductivity of the system with  $\sigma_{real}(\omega)$  and  $\sigma_{ima}(\omega)$  representing its real and imaginary part, respectively.

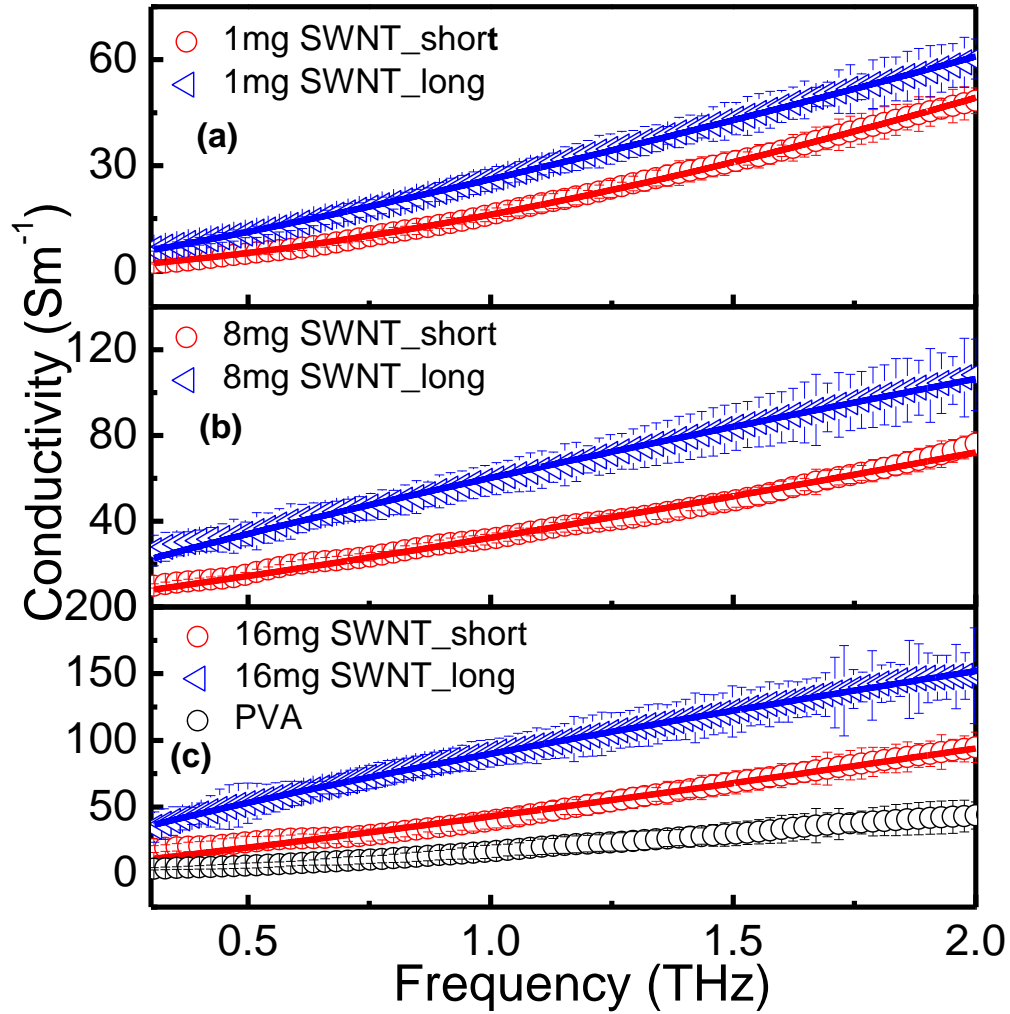


**Fig. 6.3: Real THz conductivity in the frequency range of 0.3-2.0 THz for S<sub>L</sub> and S<sub>S</sub> samples at different SWNT weight fractions (a, b, c) in the polymer composite. THz conductivity of a bare PVA film of similar thickness is given for reference**

The frequency dependent real conductivity spectra of S<sub>L</sub> and S<sub>S</sub> films at different SWNT weight fractions are shown in Fig. 6.3. It is observed that conductivity of all the samples increases with increasing probing frequency corroborating the observations reported in previous experiments[161]. Conductivity of short SWNT composites is found to be always smaller than that of the long SWNT composites due to weak scattering capability and more damaged sidewall of the latter. Previously, the appearance of a broad THz peak near 3 THz in SWNT/Polymer composites has been reported by Akima et al.[189]. They explained the appearance of the peak in the light of surface plasmonic excitation. We probe only the tail part of this TCP due to our restricted frequency window

(0.3-2.0 THz). According to the plasmon excitation model TCP frequency increases with decreasing SWNT effective length and the intensity of the tail of the conductivity spectra decreases simultaneously. We found out this decreased conductivity tail for the short SWNT sample as a fingerprint of plasmonic excitation model. For both types of SWNTs, conductivity increases with increasing SWNT weight fraction in the PVA matrix, a phenomenon[161] attributed to the introduction of conductive element well above the percolation threshold and local aggregation, and offers important application is THz shielding devices and THz attenuator devices.

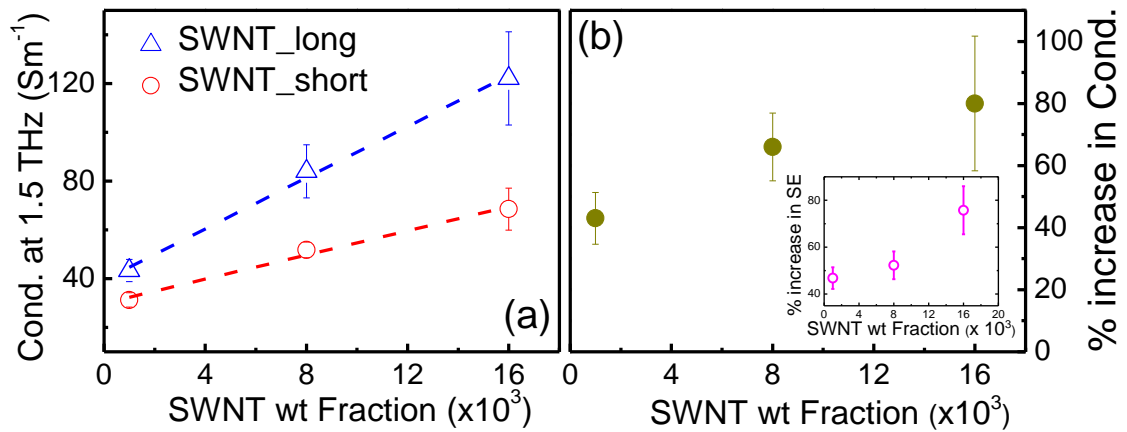


**Fig. 6.4:** (a) Real THz conductivities at 1.5 THz of S\_L and S\_S films and (b) the relative increment of real THz conductivity as a function of SWNT weight fraction. Inset shows the increment in shielding efficiency as a function of SWNT weight fraction

Real THz conductivities at 1.5 THz of SWNT\_long and SWNT\_short samples have been plotted as a function of SWNT weight fractions in Fig. 6.4a. It is found that, THz conductivity of SWNT/PVA composites at 1.5 THz increases linearly with increasing SWNT weight fraction in the polymer inclusion. Good linear fits are obtained with the slope being higher for longer SWNT films. Real THz conductivity of such a composite at any particular frequency and SWNT inclusion can be estimated using only three factors; i) real THz conductivity of the bare PVA matrix at that particular frequency, ii) SWNT weight fraction, iii) slope of the fitted straight line at that particular frequency as shown later. Real THz conductivity of a bare PVA matrix can be experimentally measured easily in the frequency range of interest and we know the slope of fitted straight lines at different frequencies for over a significant range of SWNT inclusions. This enables us to prepare a conducting composite device working at a particular frequency, according to the required THz conductivity using appropriate amount of SWNT inclusion inside the polymer matrix. THz conductivity at 1.5 THz can be calculated for any given SWNT weight fraction within

the range of the present measurement window using the relation  $[39.4 + (SWNT\ wt\ fraction \times 1000 \times 5.24)]$  in  $Sm^{-1}$  for longer SWNT/PVA composites and  $[29.9 + (SWNT\ wt\ fraction \times 1000 \times 2.47)]$  in  $Sm^{-1}$  for shorter SWNT/PVA composites. The relative increment of real THz conductivity at different SWNT weight fraction is given by

$$\% \text{ change in conductivity} = \left( \frac{|\sigma_{SWNT\_long} - \sigma_{SWNT\_short}|}{\sigma_{SWNT\_short}} \times 100 \right), \quad (50)$$

and plotted in Fig. 6.4b at the probing frequency of 1.5 THz. It is evident from the figure that THz conductivity can be increased up to as high as 80% for the highest SWNT weight fraction upon SWNT length modification and the increment can be modulated by simply varying the SWNT weight fraction in the PVA matrix. Such an easy conductivity tuning is important in different high frequency device applications such as EMIS and storage devices. As the conductivity of a composite is closely related with its shielding capability[161], we have also studied the EMIS property of the composite films and calculated the SE using the following relation;  $SE = -10 \log_{10} \left( \left| \frac{E_t}{E_i} \right|^2 \right)$  where,  $E_t$  and  $E_i$  are the complex electric field transmitted through the sample and incident on the sample. The relative increment of SE is given by;

$$\% \text{ change in SE} = \left( \frac{|SE_{SWNT\_long} - SE_{SWNT\_short}|}{SE_{SWNT\_short}} \times 100 \right), \quad (51)$$

and shown in the inset of Fig. 6.4b as a function of SWNT weight fraction. SE can also be engineered by changing the effective SWNT length in the composite as clearly observed in the figure. The highest relative increment in SE is found out to be more than 75% in longer SWNT samples.

## **6.5. Conductivity Manipulation in Surface Decorated Carbon Nanotube Composite**

### **6.5.1. Introduction**

In some recent studies[186, 195, 196], the conductivity of CNT composites have been tried to modulate by decorating the sidewalls of CNT with nanostructures. Different studies in various frequency region suggests either an increment or decrement in the observed composite conductivity after the decoration. However, as the deposited nanostructures either acts as carrier trapping potential to decrease the effective conductivity or as an alternative carrier conduction pathway to increase the effective conductivity, we tried to

vary the percentage of decoration of CNT sidewalls to manipulate the conductivity mechanism associated with the composite in THz frequency range. In this section, we will study how THz conductivity of CNT composite films can be engineered (either increase or decrease from parent composite conductivity) in a small range using gold nanoparticles (AuNP) decoration on the surface of CNTs. In the present chapter, we have synthesized AuNP and attached them to the surface of different types of CNTs (SWNT and MWNT) with varying the AuNP concentration. Then the frequency dependent conductivity of the composite films has been studied in THz frequency range and analysed using modified UDR model to find the role of AuNP in modulating the effective THz conductivity of the composite.

### 6.5.2. Sample Preparation

SWNTs (dia ~ 1-2 nm, purity ~ 90%) and MWNTs (outer dia ~ 30-50 nm, purity ~ 95%) were obtained from NanoAmor, U.S.A. and used without further purification. Chloroauric Acid ( $\text{HAuCl}_4$ ), tri-sodium citrate ( $\text{Na}_3\text{C}_6\text{H}_5\text{O}_7$ ), PVA (all from Sigma Aldrich), Ethanol (from Merck) and Millipore DI water were used for sample preparation. No special care was taken for CNT isolation procedure. Colloidal AuNP (dia ~ 15 nm) had been synthesized by reducing gold chloride solution by tri-sodium citrate.

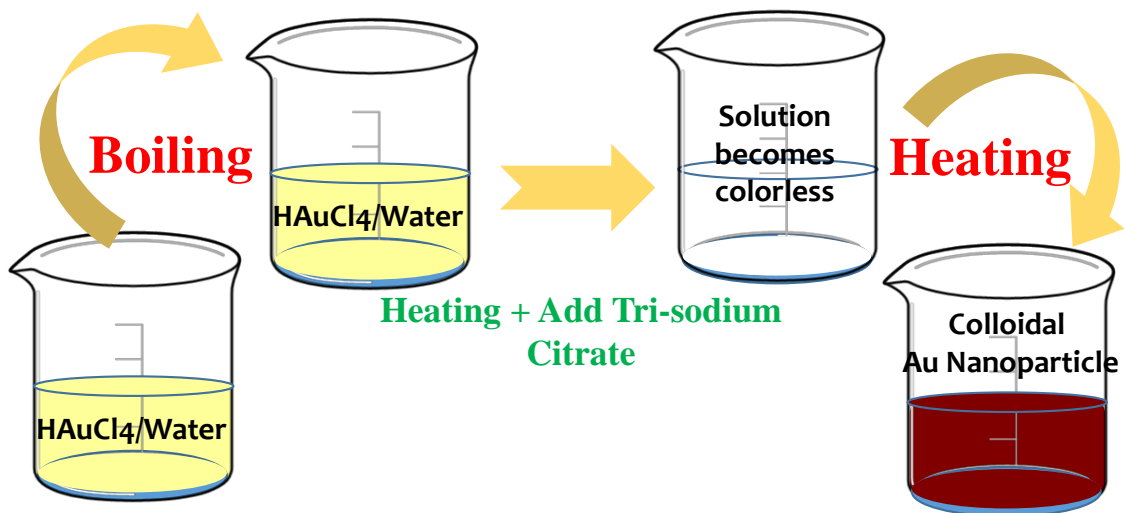


**Fig. 6.5: Schematic of colloidal gold nanoparticle preparation**

0.5 mM aqueous chloroauric acid solution was prepared by dissolving gold salt in 300 ml DI water using magnetic stirrer at room temperature. Then the solution was kept in a hot plate at an elevated temperature of 90-100 °C and strongly stirred magnetically. After 10 minutes, the gold salt solution was reduced by adding 38.8 mM aqueous tri-sodium citrate

(30 ml). The solution became colourless from light golden. Now, the solution was kept on the hot plate with strong magnetic stirring and after around 40 minutes the formation of the colloidal gold nanoparticles were indicated by the change of the colour of the solution to dark red wine. After cooling, the colloidal AuNP were used for characterization and CNT decoration. The process of the AuNP preparation is pictorially depicted in Fig. 6.5.

**Table 5: Reactants for the sample preparation**

Reactants or External Perturbations	Amount
Gold Salt	0.5 mM
Tri-sodium Citrate	38.8 mM
Poly-Vinyl Alcohol	1 g
Ethanol	Required Amount

A simple wet chemical method following the prescription described by Yu Shi et al.[198] is employed to decorate the sidewalls of CNTs with these AuNP. The reactants for the preparation of the AuNP colloidal solution and the CNT surface decoration are tabulated in Table 5.

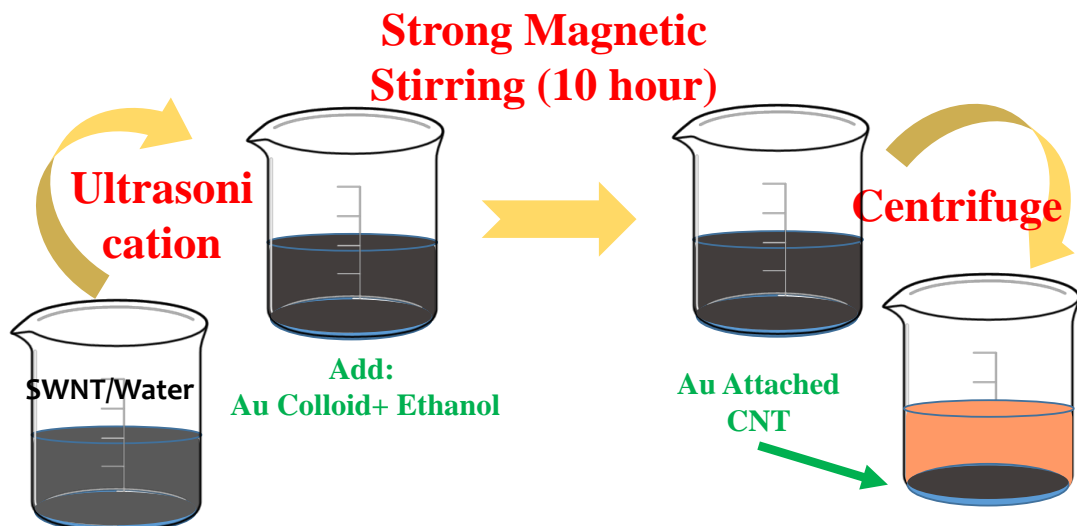


**Fig. 6.6: Schematic of CNT surface decoration with AuNP**

For the successful decoration of CNT sidewalls with the chemically synthesized AuNP, we have followed the following procedure, which is also pictorially depicted in Fig. 6.6. In a typical procedure, a measured amount of CNTs (8 mg) was added to 1-40 mL of the as-

prepared AuNP suspension. The amount of the AuNP colloidal suspension was varied to provide the AuNP density variation on the sidewalls of the tubes. About 5 or 6 mL ethanol was added immediately under vigorous magnetic stirring for 10 hours. After that, the black solid was separated by centrifuging, washed with DI water for several cycles, and then dried for 4 hours in a hot plate at 80 °C. We optimized the time required for magnetic stirring (i.e. 10 hour) for the complete decoration of the CNT using 10 ml AuNP suspension and applied the same time for the lower AuNP concentrations also. The SWNT/AuNP and MWNT/AuNP structures were then used to prepare the polymer composite films (the detailed procedure is described in previous chapter) via a slow drying technique. The thickness of the composite films was kept constant in  $300 \pm 20 \mu\text{m}$ . Total six films were prepared; three each using SWNT and MWNT inclusion and the amount of colloidal AuNP solution varied from 1, 10 and 40 ml in both SWNT and MWNT composites. Reference SWNT, MWNT and bare PVA films of similar thicknesses were also prepared for comparison.

### 6.5.3. Results and Discussions

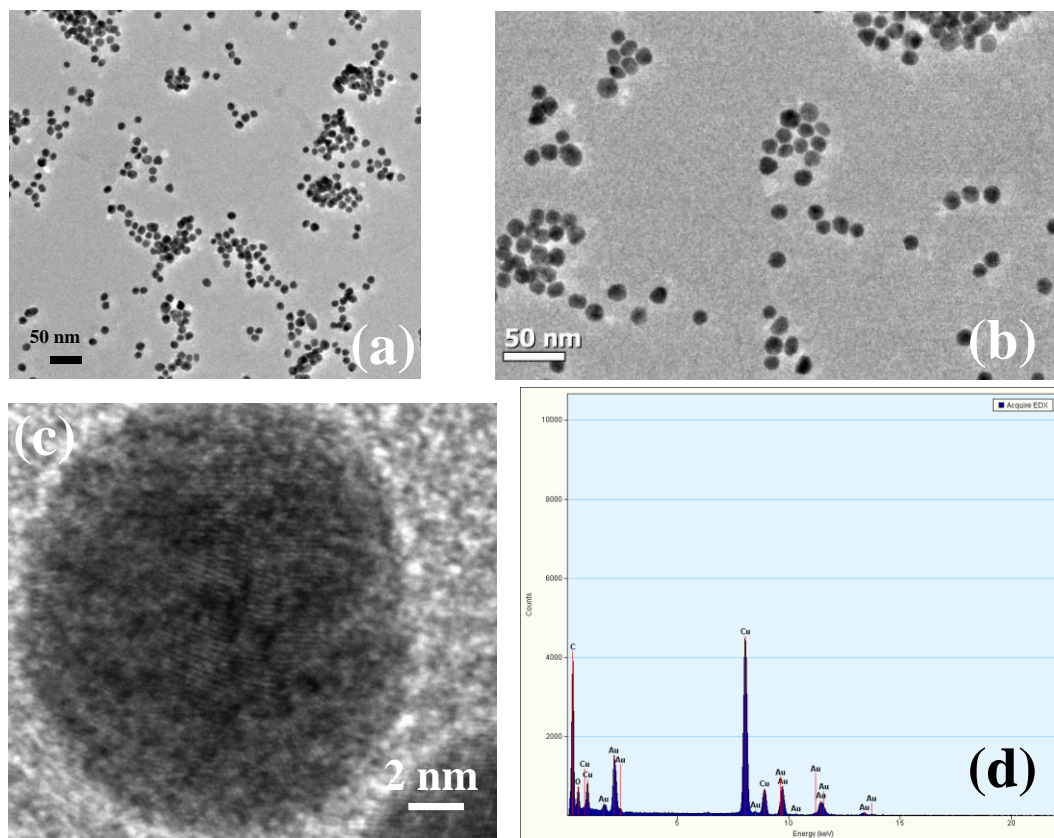


**Fig. 6.7: Transmission microscopy images of AuNP in different magnification (a-c), and (d) the corresponding EDAX spectrum showing the chemical purity of the synthesized particles**

The chemically synthesized AuNP solution is characterized using TEM for the shape and size of the AuNP. The average diameter of the AuNP is found to be 15 nm as shown in Fig. 6.7a-c. The EDX spectra as shown in Fig. 6.7d, confirms the chemical purity of the AuNP. The oxygen peak might be coming from the oxidation of the copper TEM grids and not from the particles itself. It is a well-known fact that metallic nanoparticles support surface plasmon (SP) in visible frequency range and the SP oscillation frequency significantly depend on the size and shape of the particles. The SP frequency of circular AuNP are well studied and documented[199, 200]. We have also used UV-visible spectroscopy to excite these surface plasmon resonance frequencies in the AuNP to qualitatively estimate the AuNP diameters as the SP frequency depend significantly on the AuNP diameter. The AuNP colloid is diluted twenty times before the experiment to get rid of the saturation effects. The UV-visible spectra of the diluted AuNP colloid solution is shown in the Fig. 6.8a.

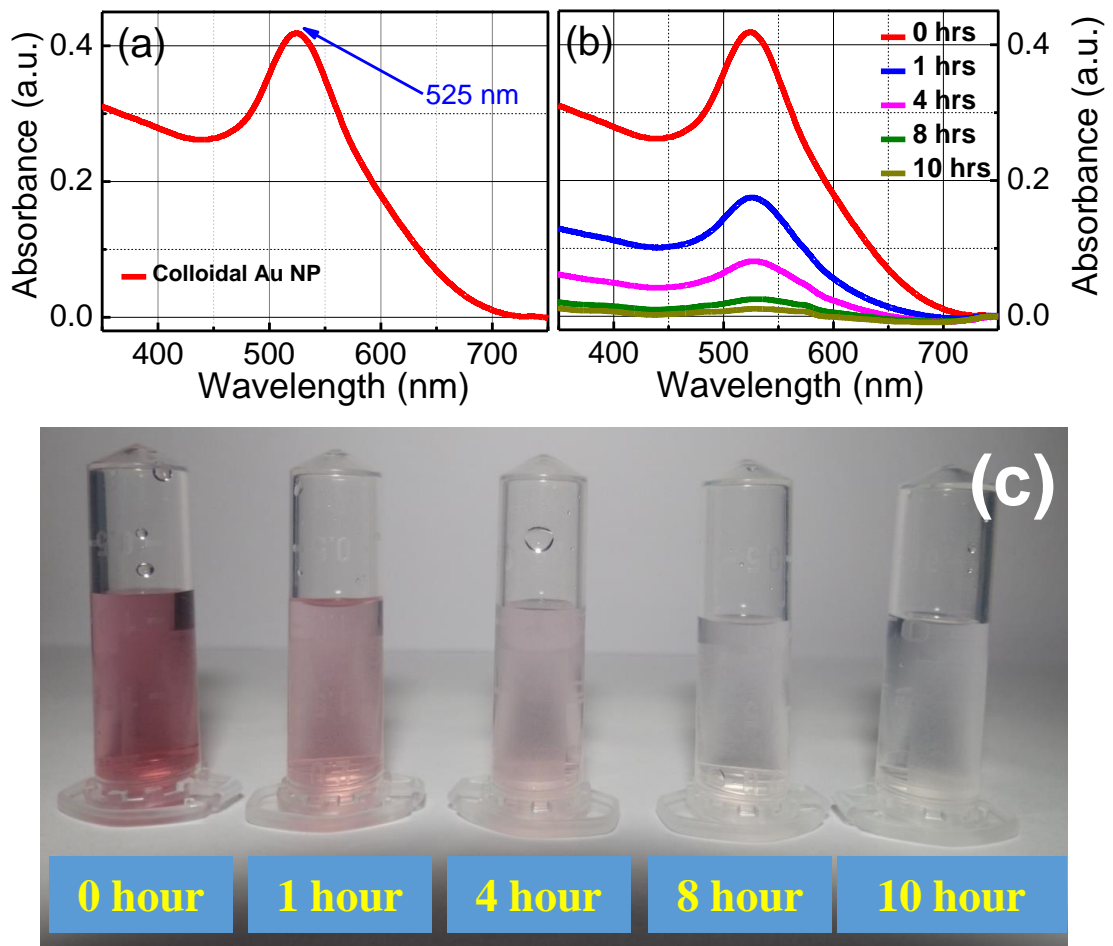


**Fig. 6.8: UV-visible absorption resonance in (a) colloidal Au NPs and (b) the supernatant of the CNT/AuNP mixture (8mg SWNT/40 ml Au NP) after different ultra-sonication time and (c) the optical image of the supernatants**

The resonance frequency appears at  $\sim 525$  nm (corresponds to the AuNP diameter of  $\sim 15$  nm), as observed in the figure. Now the AuNP decoration on the sidewalls of different types of CNTs are performed by strong ultrasonication (for 10 hours) of CNT (8 mg) and the required amount of AuNP solution in presence of a small amount of ethanol (5-6 ml for 10 ml AuNP solution). We have also studied how well the AuNP got attached to the CNT walls as we are increasing the sonication time. For this measurement, we performed ultrasonication at different times (0, 1, 4, 8 and 10 hours) and then centrifuged the solution to extract the AuNP coated CNT. A small amount from the supernatant in each cases are transferred to the cell for UV-visible spectroscopy and the UV-visible spectra is shown in Fig. 6.8b. With increasing ultra-sonication time, larger amount of AuNP got attached to the CNT surface. Hence, the UV-visible absorption intensity decreases with increasing sonication time as seen in the figure as lower number of AuNP are present in the supernatant.

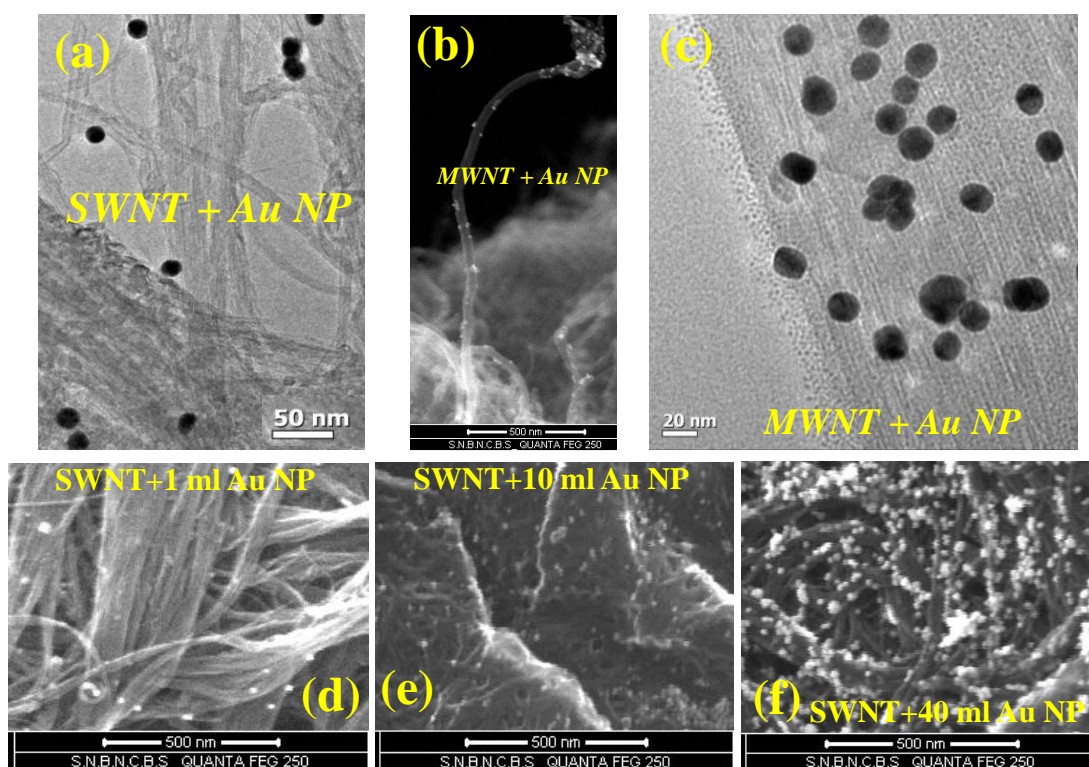


**Fig. 6.9:** TEM images of (a) SWNT/AuNP, (b) SEM images of MWNT/AuNP, (c) TEM image of MWNT/AuNP and SEM image of SWNT/AuNP structures with varying AuNP density (d-f)

After 10 hours of ultra-sonication, the UV-visible peak almost vanishes confirming the attachment of all the Au NP that were previously present in the solution at the CNT sidewalls and the supernatant contains very small amount of AuNP. This is also clearly visible in the optical images of the supernatants as shown in Fig. 6.8c. The dark red wine

colour, which is the signature of the colloidal gold nanoparticles, is continuously getting faded in the supernatant with increasing sonication time. This implies that more number of AuNP are being attached to the tube surface and hence less number of particles are present in the supernatant with increasing sonication time. SEM and TEM images as shown in Fig. 6.9 confirms the attachment of AuNP on the tube surfaces. SWNT/AuNP and MWNT/AuNP structures with different AuNP density are clearly visible giving us a fare idea about the AuNP attachment with different types of CNTs. In the SEM images as shown in Fig. 6.9 (d-f), the AuNP density variation has been clearly observed with increasing AuNP solution in SWNT/PVA composites. THz spectroscopic measurements are carried out at room temperature in transmission geometry in the frequency range of 0.3-2.0 THz using SWNT/AuNP and MWNT/AuNP composites with varying AuNP density. Transmitted THz field in SWNT and MWNT composites are shown in Fig. 6.10. The change observed in transmitted THz amplitude in SWNT/AuNP composites has been explained rigorously using THz conductivity concepts later. Qualitatively we can say that, after introducing 1 ml AuNP in the SWNT composites, THz absorption increases and then it decreases with increasing AuNP content. The MWNT/AuNP samples does not show any visible change in the THz spectrum (not shown here).

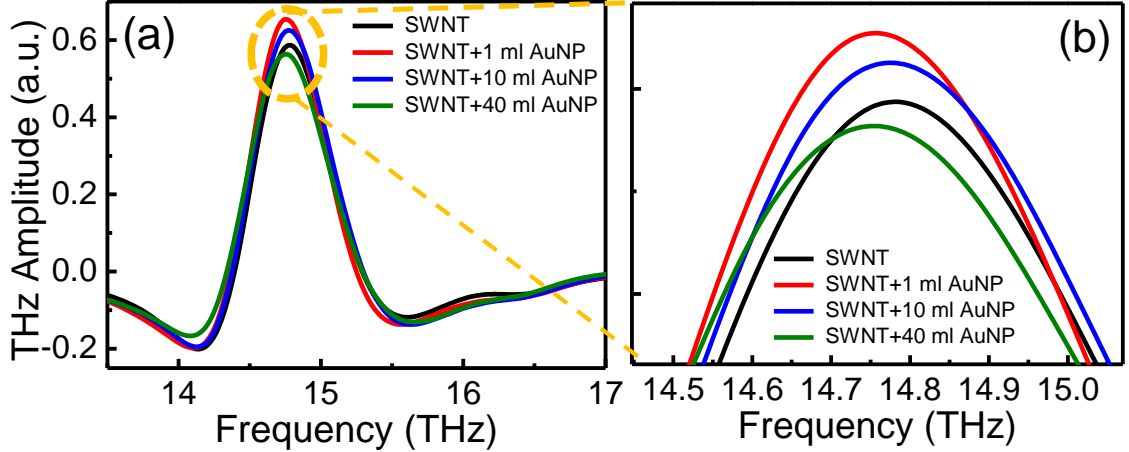


**Fig. 6.10:** (a) Transmitted THz field through SWNT/AuNP composites and the (b) zoomed in view

Small changes in the THz peak amplitude occurs due to the change in THz conductivity of the system. THz conductivity has been derived from complex optical constants using the following relation,

$$\tilde{\epsilon}(\omega) = \tilde{n}^2(\omega), \tilde{\epsilon}(\omega) = \epsilon_{\infty} + i \left( \frac{\tilde{\sigma}(\omega)}{\epsilon_0 \omega} \right) \quad (52)$$

where,  $\tilde{n}(\omega)$  is the complex refractive index,  $\tilde{\epsilon}(\omega)$  is the complex dielectric constant of the system,  $\epsilon_\infty$  is the dielectric constant at infinite frequency,  $\epsilon_0$  is the permittivity of free space,  $\omega$  is the angular frequency of radiation and  $\tilde{\sigma}(\omega)$  is the complex conductivity. Real THz conductivity profiles of SWNT and MWNT films are shown in Fig. 6.11 and fitted with UDR model. THz conductivity of CNTs increases with increasing probing frequency and can be evaluated as the tail of THz conductivity peak near 3 THz as observed in different CNT films. AuNP on the sidewalls of CNTs act as a local potential in which free carriers of CNTs get trapped, consequently THz conductivity decreases and in SWNT/1 ml AuNP sample THz conductivity is smaller than pristine SWNT sample (17% decrement at 1.5 THz) confirming this concept. However, with sufficiently increased AuNP concentration (SWNT/40 ml Au NP), THz conductivity offers a higher value than that of bare SWNT (12% increment at 1.5 THz). This is possibly due to carrier conduction through percolated SWNT/Au NP path at higher concentration, wherein AuNP act as a conduction path instead of a local carrier trapping potential. SWNT/10 ml composite suffers a competition between carrier trapping and variable range hopping conduction and THz conductivity is lower than pristine SWNT but higher than SWNT/40 ml Au NP film. Such controlled conductivity tuning could be found useful in different THz device applications like THz resistor. THz conductivity does not change much for MWNT/AuNP composites as seen in Fig. 6.11b.

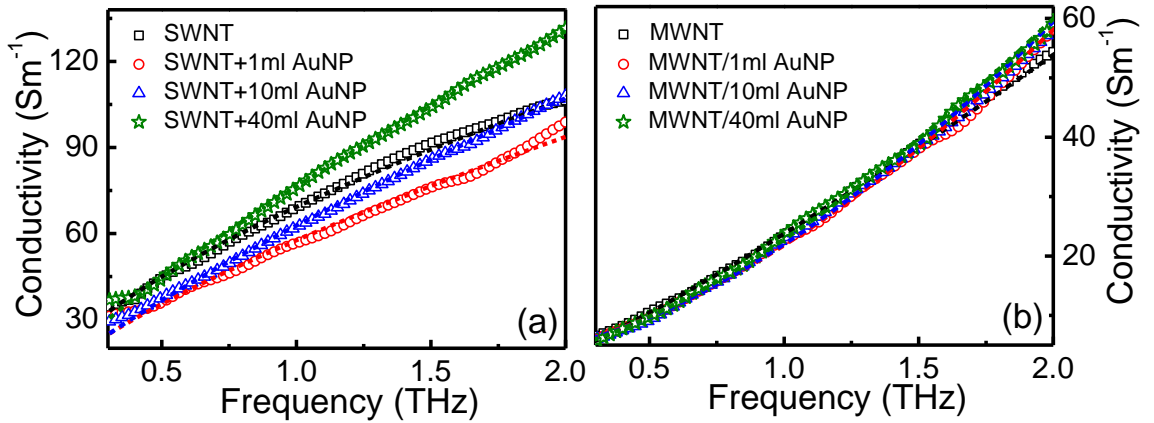


**Fig. 6.11: Real THz conductivity in (a) SWNT/AuNP and (b) MWNT/AuNP composites and fitted with UDR model**

The percentage change in THz conductivity in SWNT/AuNP composites is calculated using the following relation;

$$\text{\% change in conductivity} = \frac{|\sigma_{SWNT+x \text{ ml AuNP}} - \sigma_{SWNT}|}{\sigma_{SWNT}} \times 100, \quad (53)$$

and plotted in Fig. 6.12. We can see that, THz conductivity can either be increased or decreased depending on the AuNP concentration than the bare SWNT composite.

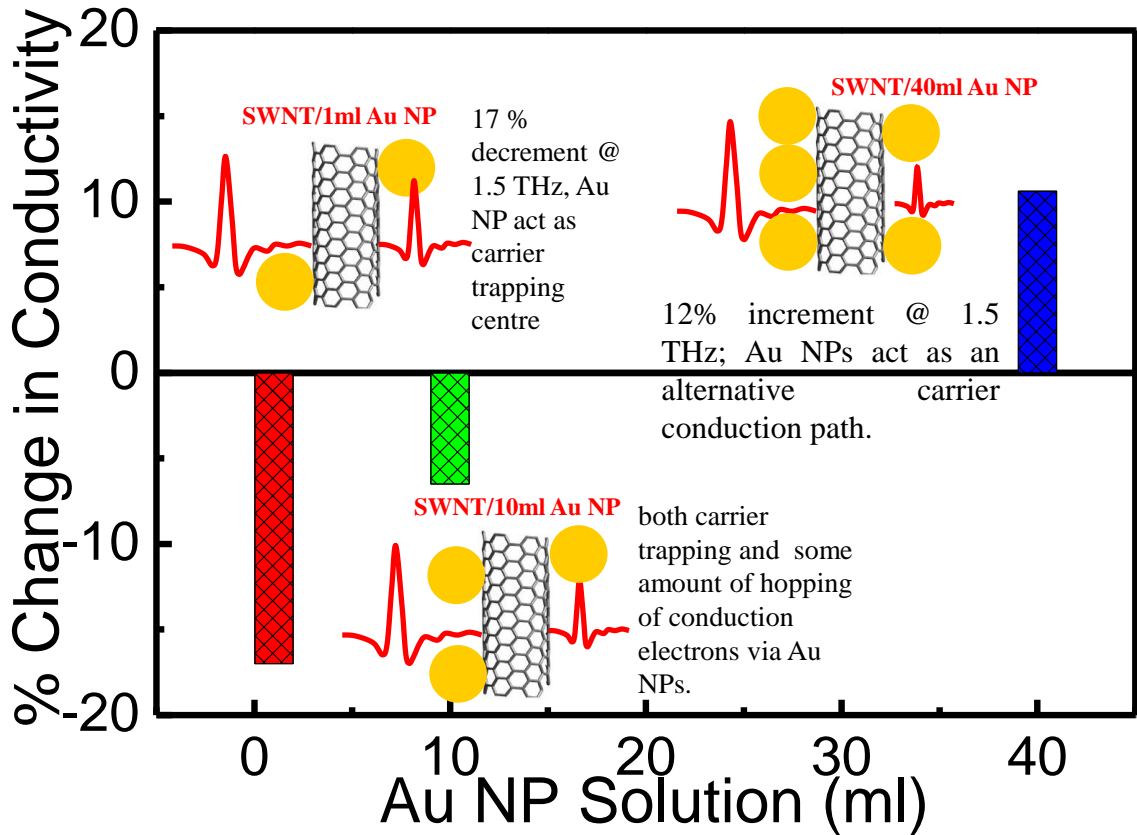


**Fig. 6.12: Percentage change in conductivity of SWNT/AuNP composites as a function of AuNP inclusion**

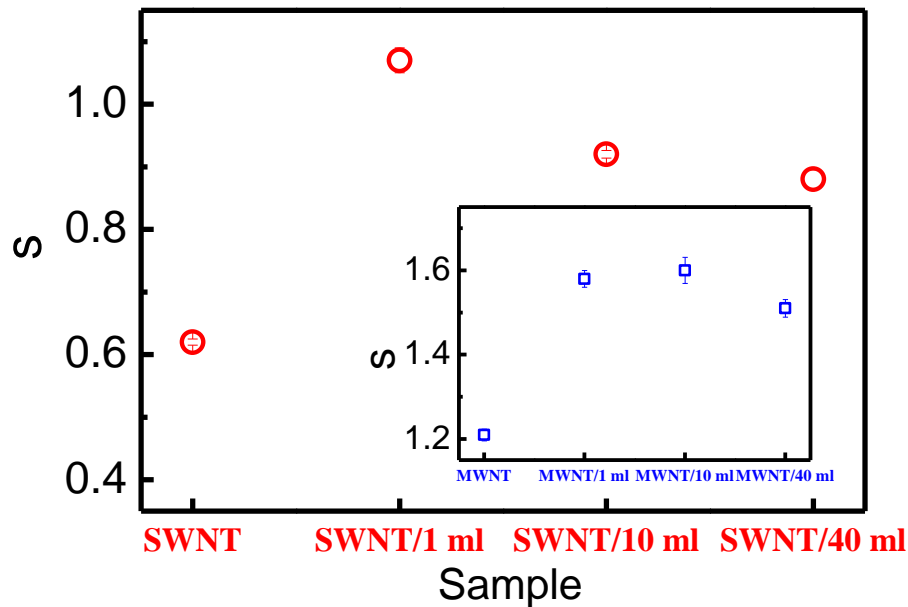
A short description of the conduction mechanism related to this kind of conductivity behaviour is also given in Fig. 6.12 and as well as described previously. Conductivity variation is trivial for MWNT samples as the intrinsic conductivity of MWNT itself is much smaller than SWNT due to its higher level of surface defects and weak scattering probability, to be affected by carrier trapping phenomenon. As AuNP diameter ( $\sim 15$  nm) is much larger than SWNT diameter ( $\sim 1$ -2 nm), the possibility of successful conduction increases at higher Au NP concentration, which is however not possible in MWNT sample due to the large tube diameter ( $\sim 30$ -50 nm).

THz conductivity spectra of these films has been using a modified UDR model as discussed earlier in this chapter. The exponent values ( $s$ ) found in different films after fitting the conductivity spectra using UDR model are depicted in Table 6.

**Table 6: The fitted  $s$  parameters for different SWNT/AuNP and MWNT/AuNP films**

Property	Type	SWNT Films	MWNT Films
Exponent " $s$ "	Pristine	$0.62 \pm 0.005$	$1.21 \pm 0.014$
	1ml Au NP	$1.09 \pm 0.020$	$1.58 \pm 0.020$
	10 ml Au NP	$0.92 \pm 0.006$	$1.60 \pm 0.031$
	40 ml Au NP	$0.88 \pm 0.015$	$1.51 \pm 0.021$

In pristine SWNT film,  $s$  is 0.62 and hopping type conduction mechanism is predominant. With increasing Au NP content, at first  $s$  value increases to 1.09 for SWNT/1ml Au NP film indicating increasing coulomb traps and confined motion of carriers in the vicinity of those traps. As we further increase Au NP content, conductivity increases indicating a possible conduction mechanism through percolated Au NP/SWNT structures itself and that motion is reflected in the decreasing value of  $s$  indicating somewhat less confined movement of the carriers.

**Fig. 6.13: The value of  $s$  for SWNT/AuNP and MWNT/AuNP (shown at the inset) films**

The value of  $s$  is larger than 1 in all MWNT films indicating the semiconducting nature of those samples as it should be due to the damaged sidewalls, higher surface defects and weak scattering capability of MWNT films. The value of  $s$  for all the SWNT/AuNP and

MWNT/AuNP films are shown in Fig. 6.13. With the inclusion of Au NP in MWNT samples,  $s$  value initially increases and then remains almost constant at  $1.55 \pm 0.5$  for all higher Au NP concentrations. This indicates confined motion of carriers near coulomb traps for all the samples and negligible dependence of the motion of carriers on AuNP concentration, which is reflected in the conductivity spectra of MWNT samples.

## 6.6. Conclusion

In this chapter we have investigated two different procedures, namely; i) changing the effective length and weight fraction of the SWNT inclusion inside the PVA matrix and ii) variation of AuNP decoration at the sidewalls of SWNT, to modulate the THz conductivity of SWNT/PVA composites. We found out that increasing the effective length of the SWNT from 2  $\mu\text{m}$  to 15  $\mu\text{m}$ , THz conductivity of the composite can be increased  $\sim 80\%$  at 1.5 THz. We also found that, surface wall modification of SWNT can be emerged as a useful technique to engineer the THz conductivity of the polymer composite material and THz conductivity of the composite can either be increased or decreased  $\sim 15\%$  by varying the density of AuNP decoration on the SWNT wall. The length dependent high frequency conductivity of SWNTs is discussed in the light of surface plasmon resonance. Adjustable THz conductivity of SWNT/PVA composites is successfully analysed with a modified UDR model. A tunable THz conductivity is observed with SWNT/AuNP films and such a system can emerge as a simple and potential THz resistor, whereas the conductivity spectra of MWNT/AuNP films remains unchanged with varying AuNP content. THz conductivity of the composites decreased from the parent composite upon 1ml AuNP attachment and then it increased with increasing AuNP content. A modified UDR theory is applied to analyse the conductivity spectra of SWNT/AuNP and MWNT/AuNP samples. A controlled way of THz conductivity modulation of SWNT/PVA composites will help the possible future applications of such composites in solar cells and high frequency EMI shielding devices.

# **Chapter Seven**

# 7. Terahertz Shielding Effectiveness and Conductivity of Self-Standing MWNT Film

---

---

## 7.1. Introduction

One of the primary advantages of using THz spectroscopy in material sciences is the possibility of label free non-destructive measurement of different nanostructures, recording the full complex optical constants of the material over a frequency range (which remains unpolluted by the present day wireless technology) and offering an unexplored regime for future communication bandwidth. Researchers have already demonstrated CNT and graphene based THz transistors[201], THz amplifiers[202] and wireless communication[24] as fast as 2.5 GB/s at 0.625 THz, paving the gateway of this frequency bandwidth, which extends roughly from 0.1-10 THz, as a potential candidate for future day electronics and communication systems. Different types of CNT, namely SWNT, DWNT and MWNT are being widely explored as the core material for different devices like transistors, polarizers, absorbers, frequency selective devices, EMIS devices working in the THz frequency range[5, 6, 161, 162, 187, 201]. THz EMIS devices and the modulation of THz shielding are becoming key research areas with the invention of different THz electronic devices, which need to be properly shielded from unwanted external THz radiations for their unhindered operations. Manipulation of conductivity and SE have also been demonstrated using different dopant on CNT, surface modification of CNT, conductive filler in CNT composites, changing the AR of CNT etc.[159, 203]. In all such applications the primarily important property is the high and anisotropic THz conductivity provided by different types of CNT and their composites. Researchers are intrigued about the origin of this extremely high THz conductivity and the much debated TCP of CNT, which has universally been observed in the frequency range of 4-30 THz[192] and the peak frequency is a function of CNT structure parameters. The origin of this TCP remains a topic of discussion with two possible explanations being offered. One of the theories states that TCP arises due to the excitation of surface plasmon resonance and

---

the peak frequency varies inversely with the length of the CNT[190, 192]. According to the other theory the peak frequency arises due to the intra-band transition at the curvature induced band gap in CNT and the peak frequency varies inversely with the diameter of CNT[204]. In a recent study from our group, we have examined the composite SE and THz conductivity of SWNT/Polymer film[187] and found out that both can be controlled by tailoring the length of the SWNT but any conclusive idea on the intrinsic nature of THz conductivity and TCP cannot be drawn due to the composite nature of the material. In the present chapter, we will study the THz conductivity and SE of MWNT as a function of MWNT average length and diameter.

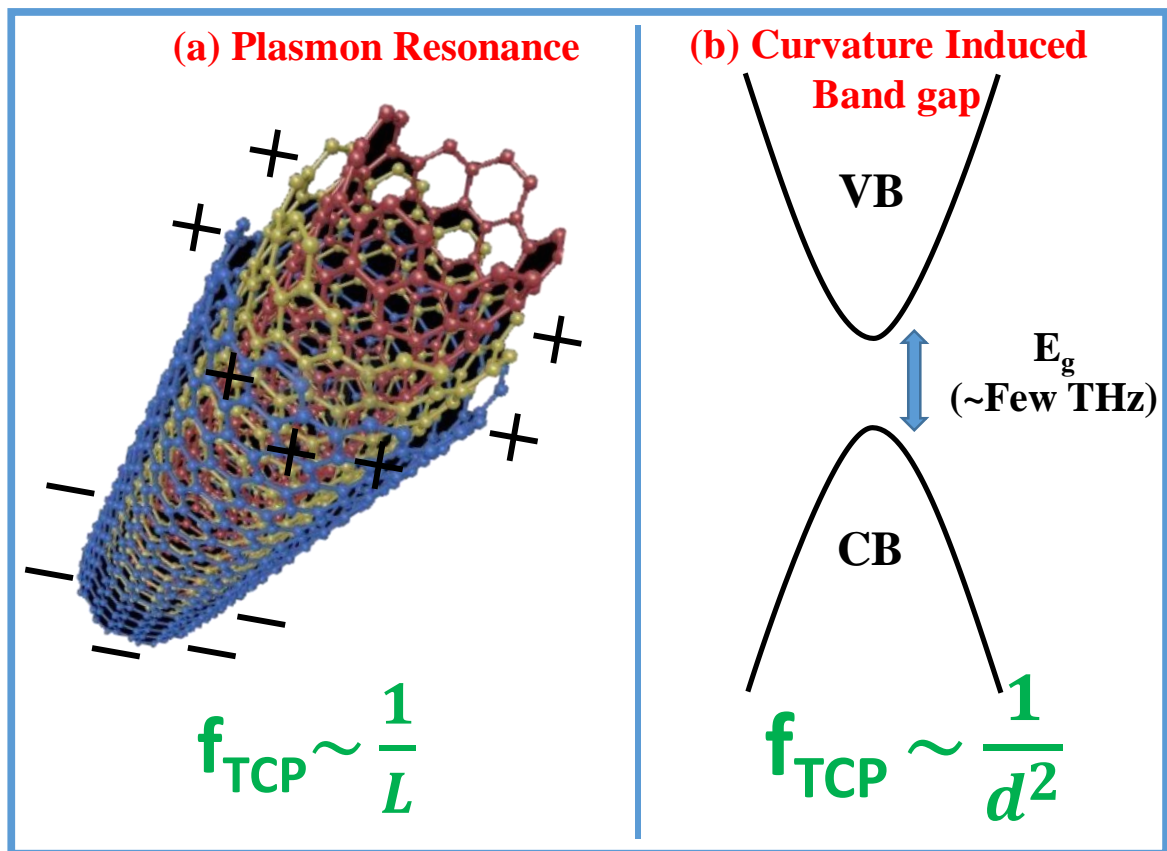


**Fig. 7.1: Schematic of two competing theories about the origin of THz conductivity peak in carbon nanotube films; (a) surface plasmon resonance mechanism and (b) curvature induced band gap**

## 7.2. Background Study

In the last few years, researchers have studied the appearance of the universally observed broad TCP in different types of CNTs and their composites with the peak frequency varying from  $\sim 0.5$  THz [140] to 30 THz depending on the different types of CNTs. The

two competing theories; i) surface plasmon resonance, ii) curvature induced bandgap, explaining the origin of the THz conductivity peak is pictorially depicted in Fig. 7.1.

Jeon et al.[205] studied the THz spectroscopy of anisotropically oriented SWNTs in the frequency range of 0.1-0.8 THz. SWCNT powder was synthesized using a traditional arc discharge with catalytic transition metals and then the film was prepared on glass slides. The power absorption showed maximum at parallel film orientation to the THz beam polarization, and reached minimum for perpendicular orientation. The a.c. conductivity of the aligned films increased with increasing frequency, following the Maxwell-Garnett (MG) model. A persistent decrease in anisotropy with increasing frequency was explained by the electromagnetic wave interactions between CNTs in the mat. They also performed a similar study[140] in the extended frequency range of 0.2-2.0 THz and theoretically modelled their experimental results using MG theory and Drude-Lorentz (DL) theory. Han et al.[206] made a theoretical study on the THz conductivity of SWNT films in the frequency range of 0.1-10 THz using a combination of DL theory and MG theory. They found that the THz conductivity decreased beyond 1 THz and the related dielectric constant reached a negative value. Kang et al.[207] studied the THz conductivity of hydrogen functionalized SWNT in the frequency range of 0.2-1.5 THz. They found that the magnitude of the index of refraction and electrical conductivity decreased after hydrogen functionalization. The reduced plasma frequency in functionalized CNTs resulted in a decrease in the number of free carriers, which could be the evidence of bonding change from  $sp^2$  to  $sp^3$  by hydrogen functionalization. In other words, the bonding change by functionalization induced the reduction of free carriers, resulting in the reduction of conductivity. Akima et al.[189] used two types of SWNTs namely L-SWNT (laser-ablation grown) and H-SWNT (commercially available high-pressure CO disproportionation process grown) and conducted optical spectroscopy in the wide frequency range of 6-10,000  $cm^{-1}$  in stretched and un-stretched condition in a polymer matrix. They found that the far-infrared peak was strongly polarized parallel to the tube direction, which also displayed remarkable morphology dependence, in sharp contrast to the morphology-insensitive spectra in the near-infrared region. They postulated an alternative model (plasmon-resonance model) for the peak around near 100  $cm^{-1}$ . Kampfrath et al.[208] studied optical properties of SWNT sheets over a wide frequency range from 1 THz to 40 THz. They derived the complex dielectric function of the nanotube sample and excellently reproduced it with DL model. They found that the centre and width of the Lorentz absorption peak reflect the average gap energy of the

---

small-gap tubes and the width of the gap distribution, respectively. After a few years later, they published another article[204] on the far-infrared absorption mechanisms in CNTs in the frequency range of 1-40 THz. They concluded that the THz conductivity peak around  $\sim 4$  THz appeared due to inter-band transition in tubes with an energy gap  $\sim 10$  meV. They also constructed a simple model based on an ensemble of two-level systems naturally explaining the weak temperature dependence of the far-infrared conductivity by the tube-to-tube variation of the chemical potential. Meang et al.[172] studied the comparative THz conductivity of SWNT and DWNT in the frequency range of 0.1-2.5 THz. They mixed CNT powder with the KBr powder, because KBr has a good transparency and a low refractive index in the far-infrared range and prepared pellets for measurements. They found that the power absorption, complex indices of refraction, and conductivity of DWNTs were smaller than those of SWNTs and concluded that this was because of the smaller carrier density of the DWNTs due to the smaller number of their tubes and interlayer interaction. Pekker et al.[191] presented a wide-range (3 meV-6 eV) optical characterization on freestanding transparent CNT films, made from nanotubes with different diameter distributions. In the far-infrared region, they found a low-energy gap in all investigated films. They determined that the average diameters of both the semiconducting and metallic species from the near-infrared and visible features of the spectra and established the dependence of the gap value on the mean diameter. They concluded that the frequency of the low-energy gap was increasing with increasing curvature. Their results strongly supported the explanation of the low-frequency feature as arising from a curvature-induced gap instead of effective-medium effects. Zhang et al.[190] studied the conductivity properties of metallic and semiconducting SWNT in both annealed and un-annealed state in a wide range of frequencies starting from 0.1-1000 THz to disclose the true nature of the conductivity peak in SWNT composites. Their experimental results showed that the broad THz peak originated from a plasmon resonance in both the metallic and the doped semiconducting CNT rather than the inter-band excitation of the curvature-induced gap in non-armchair metallic nanotubes. The intra-band free electron response also contributed to the low-energy excitation spectrum, especially in the metal-enriched film after annealing. They provided fundamental insight into the low-energy excitation in SWCNTs, while the broadband spectroscopy of semiconducting and metallic type-separated nanotube samples also provided basic knowledge useful for emerging applications of SWCNTs in plasmonics and optoelectronics in the technologically important THz frequency range. In recent review article[209] by

---

Hartman et al., they have discussed the various important works using carbon nanomaterials particularly SWNT and graphene on THz science ranging from fundamental studies such as THz dynamic conductivity, THz nonlinearities, and ultrafast carrier dynamics as well as THz applications such as THz sources, detectors, modulators, antennas, and polarizers.

## 7.3. Basic Theory

### 7.3.1. Shielding Analysis

The analysis of shielding has been described in detail in section 5.3. The experimental data has been analysed using the same theoretical models.

### 7.3.2. Effective Medium Theory

The MG and Bruggeman (BR) effective medium theories are derived for the average dielectric permeability of heterogeneous materials from a unified theoretical approach. It starts by specifying two random unit cells which represent different microstructures[210]. Inhomogeneous materials can exhibit different types of microstructures. They depict two possibilities as shown schematically in Fig. 7.2; a separated-grain structure in which particles of material *A* are dispersed in a continuous host of material *B*, and an aggregate structure being a space-filling random mixture of the two constituents. The volume fraction of material *A* (i.e., the filling factor) is denoted by *f*. Other types of microstructure are conceivable, but most heterogeneous materials can be approximated by either of the two cases as shown here.

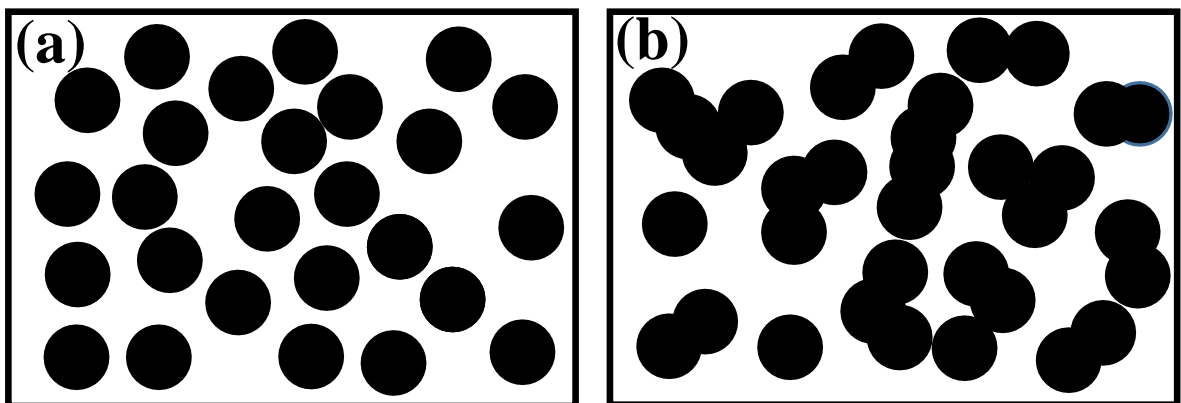


**Fig. 7.2: Schematic of (a) Maxwell-Garnett and (b) Bruggemann model**

The MG approximation[211], also known as the Clausius-Mossotti (CM) approximation, is one of the most widely used methods for calculating the bulk dielectric

properties of inhomogeneous materials. It is useful when one of the components can be considered as a host in which inclusions of the other components are embedded. It involves an exact calculation of the field induced in the uniform host by a single spherical or ellipsoidal inclusion and an approximate treatment of its distortion by the electrostatic interaction between the different inclusions. This distortion is caused by the charge dipoles and higher multipoles induced in the other inclusions. The induced dipole moments cause the longest range distortions and their average effect is included in the MG approximation which results in a uniform field inside all the inclusions. This approach has been extensively used for studying the properties of two-component mixtures in which both the host and the inclusions are isotropic materials with scalar dielectric coefficients[212]. In the derivation of the MG theory[213], it is assumed that the composite material consists of grains that are much smaller than the wavelength of light, but are large enough so that they can be characterized by macroscopic dielectric constants. In linear dielectric, the polarization is,

$$\vec{P} = \epsilon_0 \chi_e \vec{E}, \quad (54)$$

when the electric field  $\vec{E}$  is weak. However, this electric field is the total field i.e.  $\vec{E}_{tot} = \vec{E}_{ext} + \vec{E}_{pol}$  external and that due to polarization. For non-polar material, the induced dipole moment is  $\vec{p} = \alpha \vec{E}_{ext}$ , where  $\alpha$  is the atomic polarizability. If we are working with weak fields, then we may approximate,

$$\begin{aligned} \vec{P} &= N\vec{p}, \\ \epsilon_0 \chi_e \vec{E} &= N\alpha \vec{E}_{ext}, \\ \chi_e &= \frac{N\alpha}{\epsilon_0}, \end{aligned} \quad (55)$$

where N is the number of molecules per unit volume and is small. If we consider the non-polar molecule to be a uniformly charged sphere of radius R, then total charge is equal to the volume integration of the charge density over the entire volume of sphere with radius R and,

$$N = \frac{1}{\frac{4}{3}\pi R^3}. \quad (56)$$

Next, let us calculate  $\vec{E}_{pol}$  when the molecule is placed in  $\vec{E}_{ext}$ , using Gauss's law. According to Gauss Law, the electric flux through any closed surface S, enclosing a volume V is related by the following equation;

---

$$\phi = Q/\epsilon_0 \text{ or } \oiint \vec{E}_{pol} \cdot dA = \frac{\int \rho dV}{\epsilon_0}. \quad (57)$$

Where the surface integral is over the surface S which encloses the volume V.

$$\begin{aligned} \vec{E}_{pol} \cdot 4\pi r^2 &= \frac{4/3 \pi r^3 \rho}{\epsilon_0} \hat{r} \\ &= \frac{4/3 \pi r^3}{\epsilon_0} \cdot \frac{Q}{4/3 \pi R^3} \hat{r} \end{aligned} \quad (58)$$

So, this can be simplified as,

$$\begin{aligned} \vec{E}_{pol} &= \frac{1}{4\pi\epsilon_0} \cdot \frac{Q\vec{r}}{R^3} \\ \vec{E}_{pol} &= \frac{\vec{p}}{4\pi\epsilon_0 R^3}. \end{aligned} \quad (59)$$

Now, this polarization field will act opposite to the external field. So,

$$\vec{E}_{pol} = \frac{-\alpha \vec{E}_{ext}}{4\pi\epsilon_0 R^3}. \quad (60)$$

Hence, the total field is,

$$\begin{aligned} \vec{E}_{tot} &= \vec{E}_{ext} + \vec{E}_{pol} = \vec{E}_{ext} \left(1 - \frac{\alpha}{4\pi\epsilon_0 R^3}\right), \\ \vec{E}_{tot} &= \vec{E}_{ext} \left(1 - \frac{N\alpha}{3\epsilon_0}\right). \end{aligned} \quad (61)$$

The susceptibility ( $\chi_e$ ) and polarizability ( $\alpha$ ) get connected by the following relation,

$$\begin{aligned} \vec{P} &= N\vec{p} = N\alpha \vec{E}_{ext} = \frac{N\alpha \vec{E}_{tot}}{\left(1 - \frac{N\alpha}{3\epsilon_0}\right)}, \\ \epsilon_0 \chi_e \vec{E}_{tot} &= \frac{N\alpha \vec{E}_{tot}}{\left(1 - \frac{N\alpha}{3\epsilon_0}\right)}. \end{aligned} \quad (62)$$

So,

$$\chi_e = \frac{N\alpha}{\epsilon_0 \left(1 - \frac{N\alpha}{3\epsilon_0}\right)}. \quad (63)$$

Solving for  $\alpha$ , we obtain Clausius-Mossotti relation for non-polar molecule;

$$\frac{N\alpha}{3\epsilon_0} = \frac{\chi_e}{3 + \chi_e} = \frac{\epsilon_r - 1}{\epsilon_r + 2}. \quad (64)$$

Where the relative permittivity ( $\epsilon_r$ ) is defined as  $\epsilon_r = \chi_e + 1$ . This can be exploited to calculate the effective permittivity ( $\epsilon_{eff}$ ) of this inhomogeneous medium, where  $f_p$  is the volumetric content of the particles,

$$\frac{\epsilon_{eff} - 1}{\epsilon_{eff} + 2} = f_p \frac{\epsilon_p - 1}{\epsilon_p + 2}. \quad (65)$$

If the particles are embedded in a host material with given permittivity  $\epsilon_h$ , the equation changes into the MG equation as the following;

$$\frac{\epsilon_{eff} - \epsilon_h}{\epsilon_{eff} + 2\epsilon_h} = f_p \frac{\epsilon_p - \epsilon_h}{\epsilon_p + 2\epsilon_h}. \quad (66)$$

So, if we write the relative permittivity of the in terms of the permittivity of host and particle, it would look like the following;

$$\epsilon_{eff} = \epsilon_h \left( \frac{\epsilon_p(1 + 2f_p) + 2\epsilon_h(1 - f_p)}{\epsilon_p(1 - f_p) + \epsilon_h(2 + f_p)} \right). \quad (67)$$

Now, if we include a term 'g' to include the effect of finite AR and anisotropic nature of the tubes, the modified MG equation looks like the following[214, 215];

$$\epsilon_{eff} = \epsilon_h \left( \frac{\epsilon_p[g + f_p(1 - g)] + \epsilon_h[(1 - f_p)(1 - g)]}{\epsilon_p[g(1 - f_p)] + \epsilon_h(f_p g + 1 - g)} \right). \quad (68)$$

This equation has been used to extract the permittivity and consequently the THz conductivity of the MWNT in this chapter.

### 7.3.3. Drude-Lorentz Theory

The Drude model was developed at the turn of the 20th century by Paul Drude. It came a few years after J.J. Thompson discovered the electron in 1897. It predates quantum theory, but still can tell us a lot about electrons in metals. It is basically the application of kinetic theory of gases in electron conduction in a metal. The basic assumptions of the Drude model are the following;

1. Between collisions electrons move in straight line (in the absence of any electromagnetic field), effect of electron-electron interaction is ignored (independent electron approximation), effect of electron-ion in ignored (independent-electron approximation). We will treat collisions between electrons and ions are instantaneous, uncorrelated events.

2. Mean free time between collisions is  $\tau$  (probability of collision per unit time is  $1/\tau$ , probability of having a collision in infinitesimal time interval  $dt$  is  $dt/\tau$ ),  $\tau$  is independent of electron's position or velocity.

3. Electrons achieve thermal equilibrium by collisions with lattice, they emerge after collision at a random direction with speed appropriate to the temperature of the region where collision happened. The hotter the region; the higher the speed of the emerging electrons.

At first, we will establish the average equation of motion for an electron. To find this let's start with the momentum of an electron (mass  $m$ ) at time  $t$ ,  $p_m(t)$ , and find it at time  $t + dt$ . If the electrons had a collision it would on average have no momentum ( $\vec{p}_c(t + dt) = 0$ ) at time  $t + dt$  and by the third assumption above this has the probability,  $P_c = dt/\tau$ . This means that the probability of no collision is  $P_{nc} = (1 - dt/\tau)$  this is because  $P_c + P_{nc} = 1$ . If there were no collision the electrons would have evolved normally and the electrons momentum becomes,

$$\vec{p}_{nc}(t + dt) = \vec{p}_m(t) + \vec{F}(t)dt. \quad (69)$$

This makes the new momentum;

$$\begin{aligned} \vec{p}_m(t + dt) &= P_c \cdot \vec{p}_c(t + dt) + P_{nc} \cdot \vec{p}_{nc}(t + dt) \\ &= \left(1 - \frac{dt}{\tau}\right) [\vec{p}_m(t) + \vec{F}(t)dt]. \end{aligned} \quad (70)$$

Using this to find the derivative take,

$$\frac{d\vec{p}_m(t)}{dt} = \frac{\vec{p}_m(t + dt) - \vec{p}_m(t)}{dt} = \frac{-\vec{p}_m(t)}{\tau} + \vec{F}(t). \quad (71)$$

This is the equation of motion averaged over electrons. If we consider  $\vec{x}(t)$  to be the displacement vector at time  $t$  for the electron with mass  $m$ , and  $1/\tau = \Gamma_p$ , then the equation of motion becomes the following;

$$m \frac{d^2 \vec{x}(t)}{dt^2} = -m\Gamma_p \frac{d\vec{x}(t)}{dt} + \vec{F}(t). \quad (72)$$

We can extract the a.c. conductivity of a metallic system using this equation of motion. The a.c. electric field  $\vec{E}(t) = E_0 e^{-i\omega t}$  provides a force  $-e\vec{E}$  to an electron. So, the equation of motion becomes,

$$m \frac{d^2 \vec{x}(t)}{dt^2} = -m\Gamma_p \frac{d\vec{x}(t)}{dt} - e\vec{E}(t). \quad (73)$$

The well-known solution of this differential equation is  $\vec{x}(t) = x_0 e^{-i\omega t}$  and putting this solution into the equation we get,

$$-m\omega^2 \vec{x}(t) = im\omega\Gamma_p \vec{x}(t) - e\vec{E}(t), \quad (74)$$

$$\vec{x}(t) = \frac{e/m}{\omega^2 + i\omega\Gamma_p} \vec{E}(t), \quad (75)$$

Now, if  $\vec{p} = -e\vec{x}$ , is the polarization due to the electron displacement and the polarization density is  $\vec{P} = n\vec{p}$ , then we can write;

$$\vec{P} = n\vec{p} = -ne\vec{x} = -\frac{ne^2/m}{\omega^2 + i\omega\Gamma_p} \vec{E} = \varepsilon_0 \chi_e \vec{E}, \quad (76)$$

where,  $\chi_e$  is the susceptibility of the material. Hence, we can write,

$$\chi_e = -\frac{ne^2/m\varepsilon_0}{\omega^2 + i\omega\Gamma_p}, \quad (77)$$

$$\varepsilon_r = 1 + \chi_e.$$

$$\varepsilon_r = 1 - \frac{ne^2/m\varepsilon_0}{\omega^2 + i\omega\Gamma_p}. \quad (78)$$

Now, this theory is not always applicable for real life materials, especially in nanostructured materials, thin films and in resonant materials. So, alternative modifications to the very simplified Drude model has been proposed to satisfactorily explain the experimentally observed behaviour of metals and semiconductors. One of the mostly used such a modified model is called the Drude-Lorentz model. Now, we will establish the DL theory.

Now, we will establish the Lorentz theory. In this theory, to describe the interaction between atoms and electric fields in classical terms, Lorentz proposed that the electron (a particle with some small mass) is bound to the nucleus of the atom (with a much larger mass) by a force that behaves according to Hooke's Law - that is, a spring-like force ( $-m\omega_0^2 \vec{x}(t)$ ). An applied electric field would then interact with the charge of the electron, causing "stretching" or "compression" of the spring, which would set the electron into oscillating motion. This is the so-called Lorentz oscillator model. We have the conventional damping term ( $-m\Gamma_k \frac{d\vec{x}(t)}{dt}$ ) and the force on the electron due to the

---

application of an electric field  $(-e\vec{E}(t))$  as usual. So, the equation of motion becomes the following,

$$m \frac{d^2 \vec{x}(t)}{dt^2} = -m\Gamma_k \frac{d\vec{x}(t)}{dt} - m\omega_0^2 \vec{x}(t) - e\vec{E}(t). \quad (79)$$

Again, the well-known solution of this differential equation is  $\vec{x}(t) = x_0 e^{-i\omega t}$  and putting this solution into the equation we get,

$$-m\omega^2 \vec{x}(t) = im\omega\Gamma_k \vec{x}(t) - m\omega_0^2 \vec{x}(t) - e\vec{E}(t), \quad (80)$$

$$\vec{x}(t) = \frac{-e/m}{(\omega_0^2 - \omega^2) - i\omega\Gamma_k} \vec{E}(t). \quad (81)$$

Now, following the procedures of Drude theory, we can establish the effective permittivity of the system is,

$$\epsilon_r = 1 + \frac{ne^2/m\epsilon_0}{(\omega_0^2 - \omega^2) - i\omega\Gamma_k}. \quad (82)$$

Now, in real life materials, sometimes both the Drude and Lorentz model is required to explain the di-electric properties and conductivity of a system. The analysis of MWNT in this study is also incorporated both the theories and the combined di-electric function or the Drude-Lorentz Model as applied in the analysis is the following formula;

$$\tilde{\epsilon}_{DL}(\omega) = \epsilon_\infty - \frac{\Omega_p^2}{\omega^2 + i\Gamma_p\omega} + \sum_k \frac{\Omega_k^2}{(\omega_k^2 - \omega^2) - i\Gamma_k\omega}, \quad (83)$$

where, where,  $\epsilon_\infty$  is the high frequency dielectric constant,  $\frac{\Omega_p}{2\pi}$  is the Drude plasma frequency,  $\frac{\Gamma_p}{2\pi}$  is the free electron scattering rate,  $\frac{\Omega_k}{2\pi}$  is the oscillator strength,  $\frac{\omega_k}{2\pi}$  is the exciton frequency (plasmon in this case) and  $\frac{\Gamma_k}{2\pi}$  is the plasmon scattering rate. The summation over k for Lorentz oscillator term extends over all possible oscillatory phonon modes in the frequency region of consideration.

---

## 7.4. Length Dependent Shielding and THz Conductivity

### 7.4.1. Sample Preparation

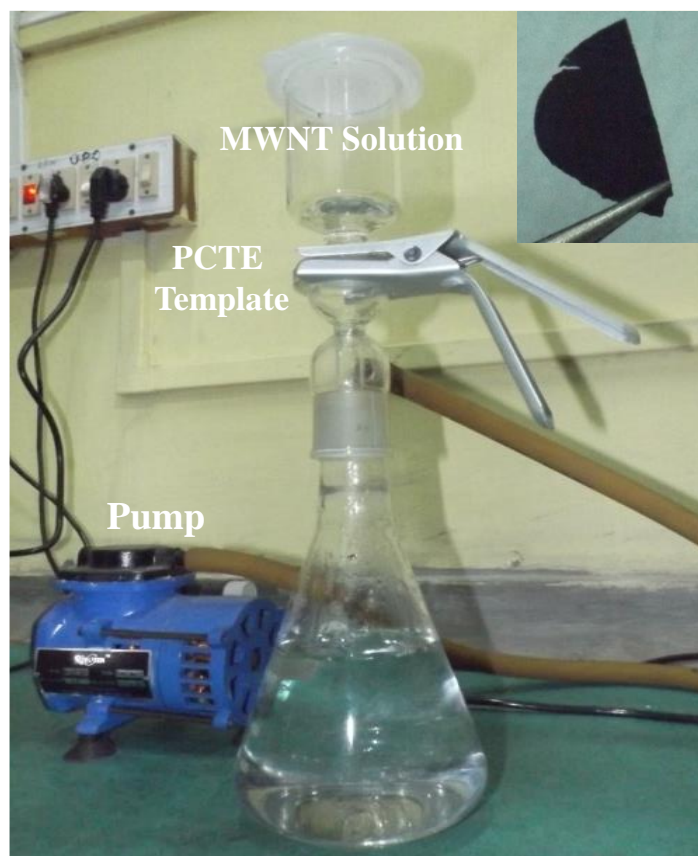


**Fig. 7.3: Vacuum Filtration Unit used for self-standing MWNT film preparation and an image of a self-standing MWNT film is given at the inset**

MWNT (> 90% carbon content, dia ~ 25 nm) of two different lengths (average length of ~ 15 and 2  $\mu\text{m}$ ; henceforth denoted as L\_MWNT and S\_MWNT, respectively) were purchased from NanoAmor, USA at the highest available purity and used without further purification. N,N-dimethylformamide (DMF), dichloromethane (DCM) were purchased from Merck. Nucleopore polycarbonate track etched (PCTE) membrane having a pore size of 0.2  $\mu\text{m}$  was purchased from Whatman. Millipore DI water was used in different steps of sample preparations. Required amount of MWNT was dispersed in 15 ml DMF by strong ultrasonication for 20 minutes. Dispersed MWNT were mixed with required amount of DI water and then filtered through PCTE membrane using a vacuum filtration unit and then washed several times with DI water. MWNT film on PCTE template was then transferred onto a silicon substrate and treated with DCM and DI water repeatedly

to dissolve the PCTE membrane and obtain the self-standing MWNT film of thickness  $\sim 14 \mu\text{m}$ . Two films of similar thickness were prepared using the two different MWNTs following the same procedure. The optical image of the vacuum filtration unit along with the pump which is installed in the lab and an optical image of the self-standing MWNT film is shown in Fig. 7.3. THz measurements were carried out in a commercial THz time domain spectrometer[197] (TERA K8, Menlo Systems). The frequency dependent power and phase of the transmitted pulse was obtained by using Fourier analysis of the measured time domain electric field amplitude  $E_{\text{THz}}(t)$ . Dielectric properties of the samples are analysed using a combination of MG model and DL model. THz conductivity of MWNT is extracted for both the films in the extended frequency region of 0-20 THz using the DL parameters which gives important insight about the electronic structures and origin of the TCP in MWNTs.

#### 7.4.2. Results and Discussions

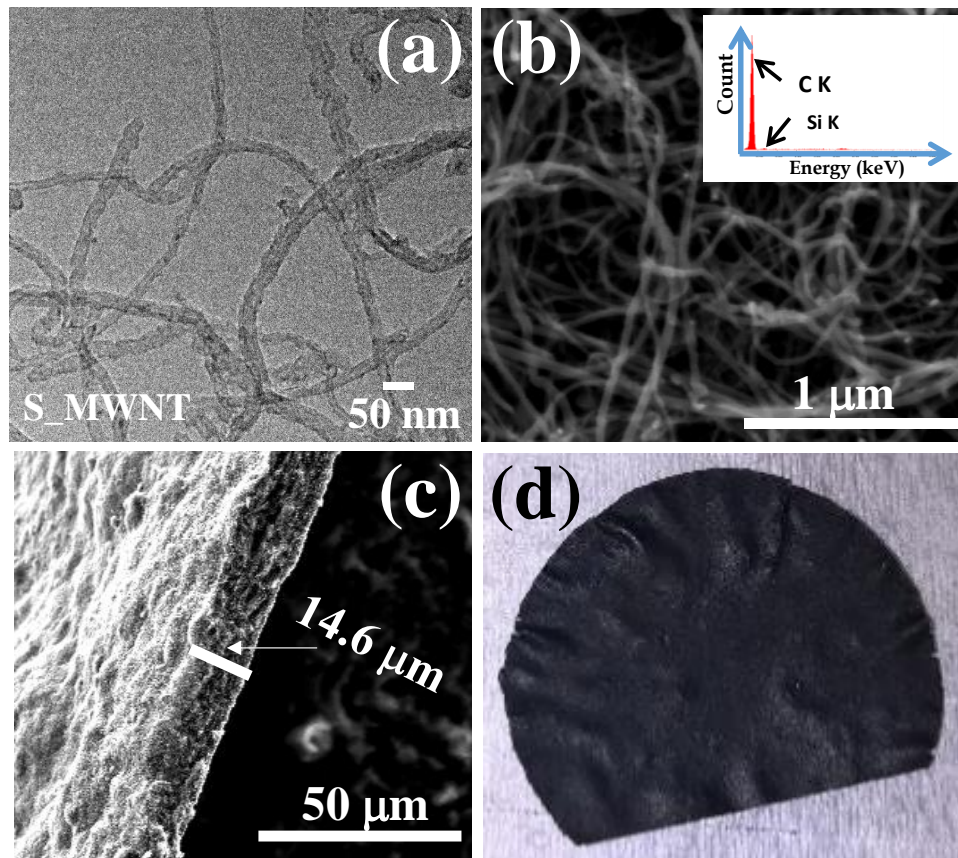


**Fig. 7.4:** (a) TEM image of S\_MWNT, (b) SEM image of the MWNT film and the corresponding EDAX spectra, (c) cross-sectional SEM image of MWNT self-standing film, (d) optical image of the self-standing MWNT paper

TEM image of the S\_MWNT film is shown in Fig. 7.4a and the detailed analysis using the TEM images confirm the diameter of the MWNT to be  $\sim 25 \pm 3$  nm which is close to the nominal value. Cross sectional view of the self-standing L\_MWNT film is shown in the SEM image of Fig. 7.4c and the thickness of the film is found to be  $\sim 14$   $\mu\text{m}$ . This thickness is later used while analyzing the measured data. EDX spectrum of the S\_MWNT film is given in the index of Fig. 7.4b and it shows the chemical purity of the MWNT (greater than 95% carbon content). A photograph of the self-standing L\_MWNT film of diameter 1.5 cm is shown in Fig. 7.4d. Transmitted THz spectra in time domain for both S\_MWNT and L\_MWNT films are shown in Fig. 7.5a and the corresponding FFT amplitude is shown in Fig. 7.5b.

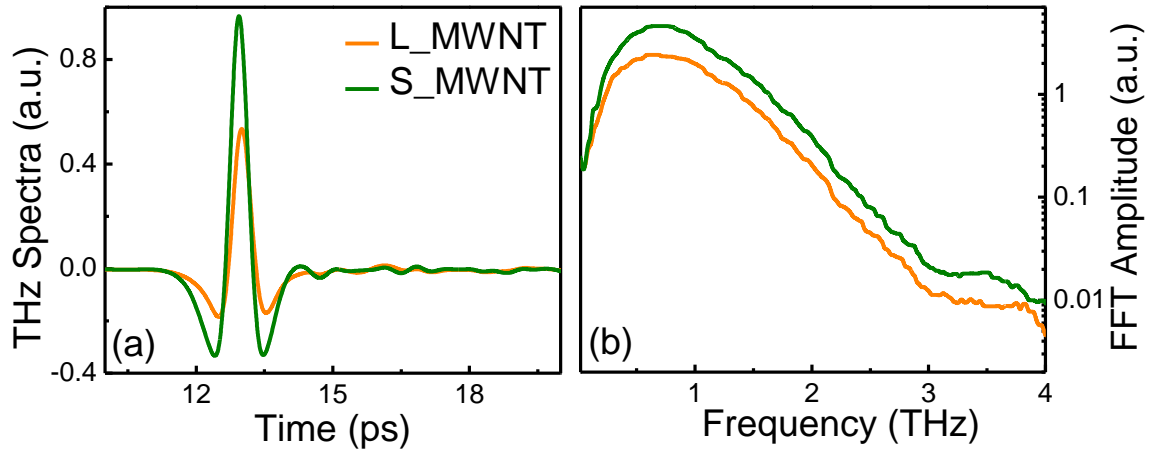


**Fig. 7.5: (c) Transmitted THz spectra for L-MWNT and S\_MWNT self-standing film and the corresponding (b) Fast Fourier Transfer (FFT) spectra of those samples**

Transmitted THz radiation is found to be much smaller in L\_MWNT than that of S\_MWNT having the same MWNT weight fraction indicating higher THz absorption in the former as observed in earlier THz studies in SWNT. It can be shown [75, 156] that SE of a composite system can be written as (also elaborately described in chapter 5);

$$\begin{aligned}
 SE(\omega) &= SE_A(\omega) + SE_R(\omega) + SE_{MIR}(\omega) \\
 &= 8.68\alpha(\omega)l + 20 \log_{10} \left( \frac{|1 + \tilde{n}(\omega)|^2}{4|\tilde{n}(\omega)|} \right) + 20 \log_{10} \left| 1 - \frac{(1 - \tilde{n}(\omega))^2}{(1 + \tilde{n}(\omega))^2} e^{(-2\alpha(\omega)l)} \right|,
 \end{aligned}$$

where  $\tilde{n}(\omega)$ ,  $\tilde{\gamma}(\omega)$  and  $l$  are the complex refractive index, complex propagation constant and thickness of the sample under consideration. The contributions of reflection and absorption to the total shielding are shown in Fig. 3a for all the MWNT films. Shielding due to multiple internal reflection ( $SE_{MIR}(\omega)$ ) are dominant for films where the thickness of the film is comparable or smaller than the skin depth at a particular frequency. If the

thickness of the film is thicker than the skin depth, the reflected wave from the internal surface will be absorbed by the conductive material, and thus multiple-reflection can be ignored. However, if the shield is thinner than the skin depth, the influence of multiple-reflection will be significant in decreasing overall EMI shielding[155]. It was theoretically shown in many literatures that the effect of multiple internal reflection can be neglected if  $SE_R(\omega) \geq 15 \text{ dB}$ [164, 165]. It was also found that the contribution of multiple internal reflection may be negative in some samples[155, 216].

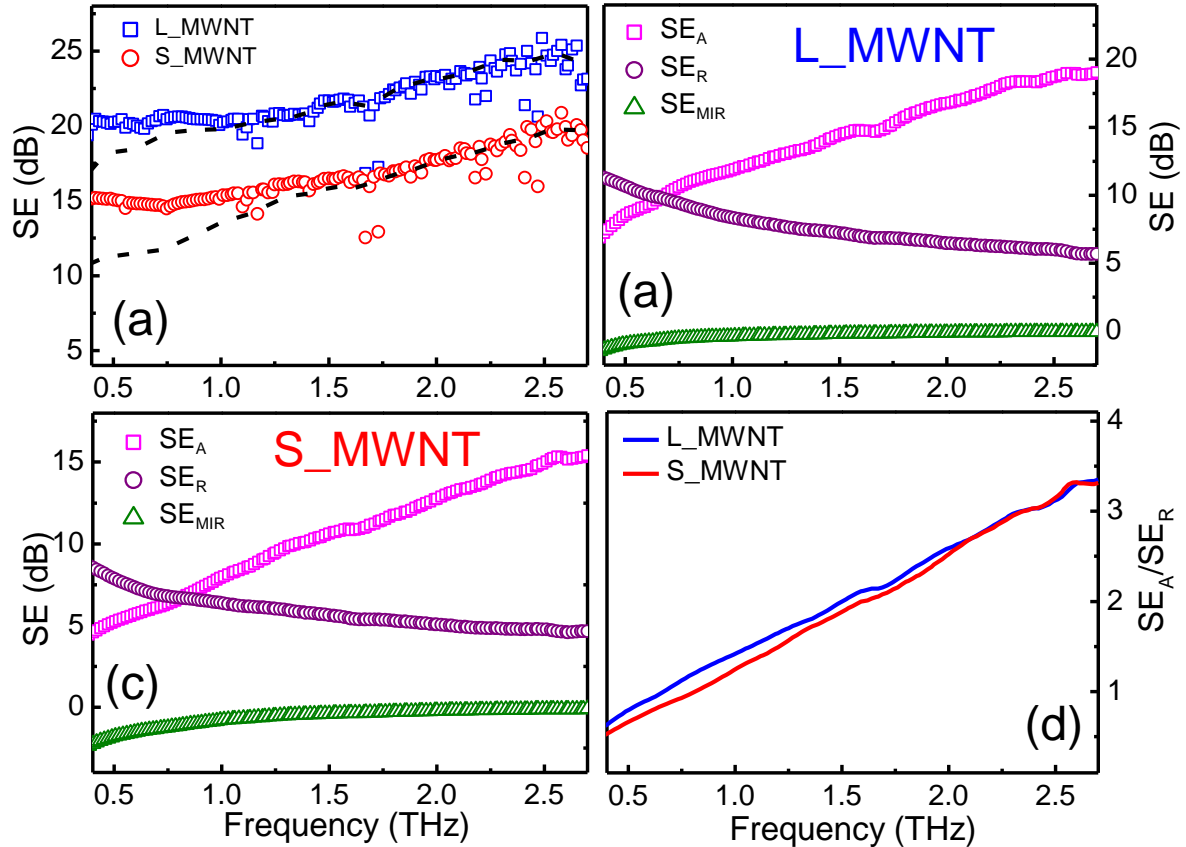


**Fig. 7.6: (a) Total SE of L\_MWNT and S\_MWNT films, contribution of absorption and reflection and multiple internal reflection for (b) L\_MWNT and (c) S\_MWNT films, and (d) relative contribution of absorption to reflection in L\_MWNT and S\_MWNT films**

The total shielding as shown in Fig. 7.6a has been excellently fitted using Eq. 43 in the frequency range of 0.4-2.7 THz. SE is much larger in L\_MWNT films than S\_MWNT films due to larger THz attenuation in long MWNT samples as observed in other literatures for longer SWNTs. This is mainly due to presence of larger number of free electrons, relatively less number of defect states and less junction resistance (MWNT-MWNT junction acts as a resistive lump in the otherwise conducting MWNT forest structure) in L\_MWNT film than S\_MWNT films. The individual contribution of absorptive shielding ( $SE_A(\omega)$ ),

reflective shielding ( $SE_R(\omega)$ ) and shielding due to multiple internal reflection ( $SE_{MIR}(\omega)$ ) is shown in Fig. 7.6b and Fig. 7.6c for L-MWNT and S\_MWNT films respectively. For both the films, initially, reflective shielding is larger than absorptive shielding and  $SE_R(\omega)$  decreases while  $SE_A(\omega)$  increases with increasing frequency. Beyond 0.75 THz, the contribution of absorption is greater than the contribution of reflection and is kept on increasing with increasing frequency for both the samples. In the higher frequency range, shielding is predominantly via absorption for both type of MWNT films. ( $SE_R(\omega)$ ) remains small and negative and increases to 0 beyond 1.2 THz for both the films. Another important observation is that the mechanism of shielding does not change with change in the length of MWNT under consideration although the magnitude of shielding increases with increasing MWNT length. We observed a different phenomenon, when we varied the diameter of the MWNT under consideration and is discussed in detail in the later part of this chapter. MWNTs are connected with each other forming a bird's nest like structure inside the films as has clearly been observed in the SEM images (Fig. 7.4b) and the volume fraction of MWNT is sufficiently large. In order to quantitatively estimate the optical constants of the films at THz frequency region we have applied DL model with a combination of MG EMT[215] and simulated the conductivity spectra of MWNT in the frequency range of 0-20 THz. In EMT, we have considered the MWNT self-standing film as a composite containing air and MWNT with MWNT volume fraction ( $f$ ) very high (as seen in the SEM image) and taken to be 0.98. The dielectric functions obtained from experiments are considered as an effective dielectric function ( $\epsilon_{eff}(\omega)$ ) of a composite material containing MWNT and air gaps in between. The corresponding dielectric function of the MWNT ( $\epsilon_{DL}(\omega)$ ) is extracted by applying the MG EMT as shown by the following equation[214, 215],

$$\tilde{\epsilon}_{eff}(\omega) = \epsilon_{air} \frac{[g + f(1 - g)]\tilde{\epsilon}_{DL}(\omega) + (1 - g)(1 - f)\epsilon_{air}}{g(1 - f)\tilde{\epsilon}_{DL}(\omega) + (fg + 1 - g)\epsilon_{air}}, \quad (84)$$

which is then used in the DL model to extract the DL parameters and conductivity of MWNT in THz frequency range. We also consider a geometrical factor ( $g$ ) to take into account the AR or shape of MWNT in the composite. Smaller value of ' $g$ ' corresponds to larger aspect ratio of the tubes. DL theory models the dielectric properties of a material considering the contribution from the free electrons (the Drude term) and the contributions from the bound electrons/excitons (the Lorentz oscillator term). Drude term considers free electrons not to possess any resonant frequency whereas the resonant behaviour for all the vibrational modes of bound electrons/excitons are taken into

consideration in the Lorentz oscillator term[173, 190]. The DL model is mathematically represented by the following equation (described before),

$$\tilde{\epsilon}_{DL}(\omega) = \epsilon_{\infty} - \frac{\Omega_p^2}{\omega^2 + i\Gamma_p\omega} + \sum_k \frac{\Omega_k^2}{(\omega_k^2 - \omega^2) - i\Gamma_k\omega}, \quad (85)$$

where,  $\epsilon_{\infty}$  is the high frequency dielectric constant,  $\frac{\Omega_p}{2\pi}$  is the Drude plasma frequency,  $\frac{\Gamma_p}{2\pi}$  is the free electron scattering rate,  $\frac{\Omega_k}{2\pi}$  is the oscillator strength,  $\frac{\omega_k}{2\pi}$  is the exciton frequency (plasmon in this case) and  $\frac{\Gamma_k}{2\pi}$  is the plasmon scattering rate. The summation over k for Lorentz oscillator term extends over all possible oscillatory phonon modes in the frequency region of consideration, however in the present scenario only one phonon mode is enough[173, 190] to successfully reproduce the data. We have applied MG EMT where the film is considered as an effective medium. The effective dielectric constant of the S\_MWNT and L\_MWNT films fitted with the combination of MG and DL models are shown in Fig. 7.7 in the frequency range of 0.3-2.7 THz and the obtained DL parameters are shown in Table 7. The DL parameters are closely related to the electronic structure of the samples in consideration hence, by analyzing the parameters listed in Table 7, one can have an insight to the electronic structure of S\_MWNT and L\_MWNT films.

**Table 7: DL Parameters for L\_MWNT and S\_MWNT Films**

Sample	$\epsilon_{\infty}$	$\frac{\Omega_p}{2\pi}$ (THz)	$\frac{\Gamma_p}{2\pi}$ (THz)	$\frac{\Omega_k}{2\pi}$ (THz)	$\frac{\omega_k}{2\pi}$ (THz)	$\frac{\Gamma_k}{2\pi}$ (THz)	g
L_MWNT	4.00	32.25	14.46	32.33	6.95	7.02	0.09
S_MWNT	4.00	10.60	3.51	48.70	9.37	35.66	0.16

The plasma frequency  $\frac{\Omega_p}{2\pi}$  is proportional to the square root of free electron density of the system which is found to be 32.25 THz for L\_MWNT and 10.60 THz for S\_MWNT film, indicating higher abundance of free electrons in L\_MWNT films which satisfactorily justifies its high THz conductivity and SE. During the fitting procedure we have kept the volume fraction of the MWNT ( $f$ ) fixed at 0.98 for both the films which is approximated from their SEM images. The free electron scattering rate  $\frac{\Gamma_p}{2\pi}$ , which is also proportional with the free electron density of the sample, decreased from 14.46 THz to 3.51 THz confirming the abundance of free electrons in the L\_MWNT films than S\_MWNT.

Plasmon frequency increases from 6.95 THz to 9.37 THz as the length of the MWNT get shortened. Such a decrement in plasmon frequency confirms that the resonance term is indeed arising due to the length dependent surface plasmon phenomenon in the MWNTs. It can also be noted that the width of the lorentzian peak  $\frac{\Gamma_k}{2\pi}$  is of the same order with the exciton frequency for longer MWNTs, however, for shorter MWNTs, it increases almost four times than the exciton frequency. This may be due to the presence of closely placed additional vibrational peaks (which are of course not resolved) in S\_MWNTs.

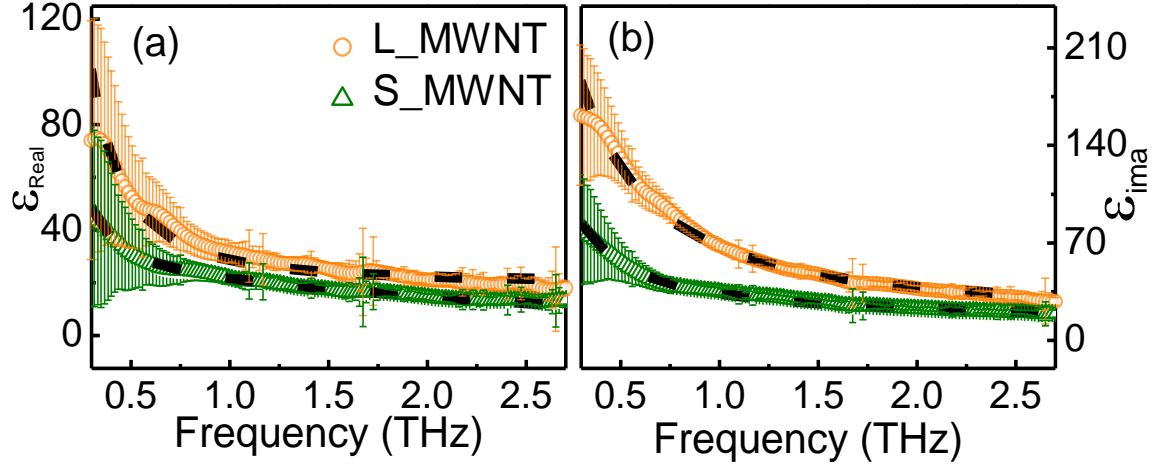


**Fig. 7.7: (a) Real and (b) Imaginary dielectric function of L\_MWNT and S\_MWNT films fitted with MG and DL Model**

From the fitted DL parameters, we have also extracted the complex THz conductivity of the MWNTs using the following formula;

$$\sigma(\omega) = \left( \frac{\Omega_p^2}{\omega^2 + i\Gamma_p\omega} - \frac{\Omega_k^2}{(\omega_k^2 - \omega^2) - i\Gamma_k\omega} \right) i\epsilon_0\omega. \quad (86)$$

Real THz conductivity is found to be positive and increasing while the imaginary THz conductivity found to be negative and decreasing in the measured frequency range which indicates that the famous THz conductivity peak lies outside the measured frequency range for the present samples. Hence, we have extrapolated the complex THz conductivity in the frequency range of 0-20 THz (measured frequency range is 0.4-2.7 THz) to observe the behaviour of the THz conductivity peak as a function of MWNT effective length. We indeed observed the TCP while the imaginary THz conductivity undergoes a change in sign (from negative to positive). The THz conductivity peak is observed at 6.6 THz for L\_MWNT films and at 7.5 THz for S\_MWNT films. The increment of THz peak frequency is found to be 0.9 THz in the shorter MWNT samples. Such a change has been proposed

by surface plasmonic excitation model of THz conductivity in carbon nanotubes and has been experimentally realized in a handful of studies.

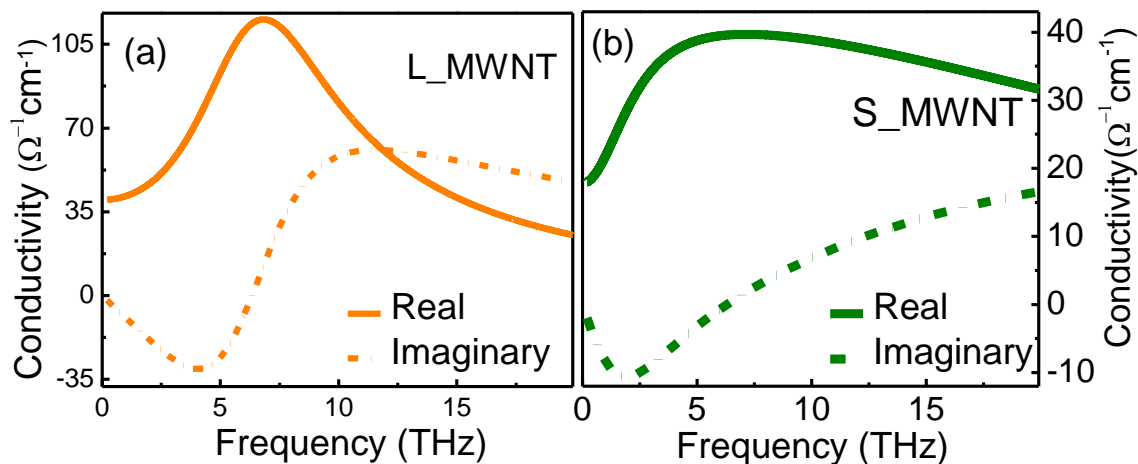


**Fig. 7.8: Real and Imaginary conductivity of (a) L\_MWNT and (b) S\_MWNT films extracted from DL parameters in the frequency range 0-20 THz.**

## 7.5. Diameter Dependent Shielding and THz Conductivity

### 7.5.1. Sample Preparation

MWNT (> 90% carbon content, average length  $\sim 1 \mu\text{m}$ ) of three different diameters (7 nm, 25 nm and 40 nm) were purchased from NanoAmor, USA at the highest available purity and used without further purification and named as MWNT\_7nm, MWNT\_25nm and MWNT\_40nm respectively. DMF and DCM were purchased from MERCK at highest available purity. PCTE membrane of pore diameter  $0.2 \mu\text{m}$  were purchased from Whatman. Same amount of the required type of MWNT powder was dispersed in 15 ml DMF via strong ultra-sonication for 20 minutes and then poured in the vacuum filtration unit with sufficient amount of DI water to be filtered through PCTE membrane. Depending on the nature of the solution, 10-20 hours were required for the complete filtration process. MWNT coated PCTE template was then transferred onto silicon substrate, carefully washed with DI water several times, dissolved in DCM and dried to obtain the self-standing MWNT film of thickness  $\sim 15\text{-}25 \mu\text{m}$ .

## 7.5.2. Results and Discussions

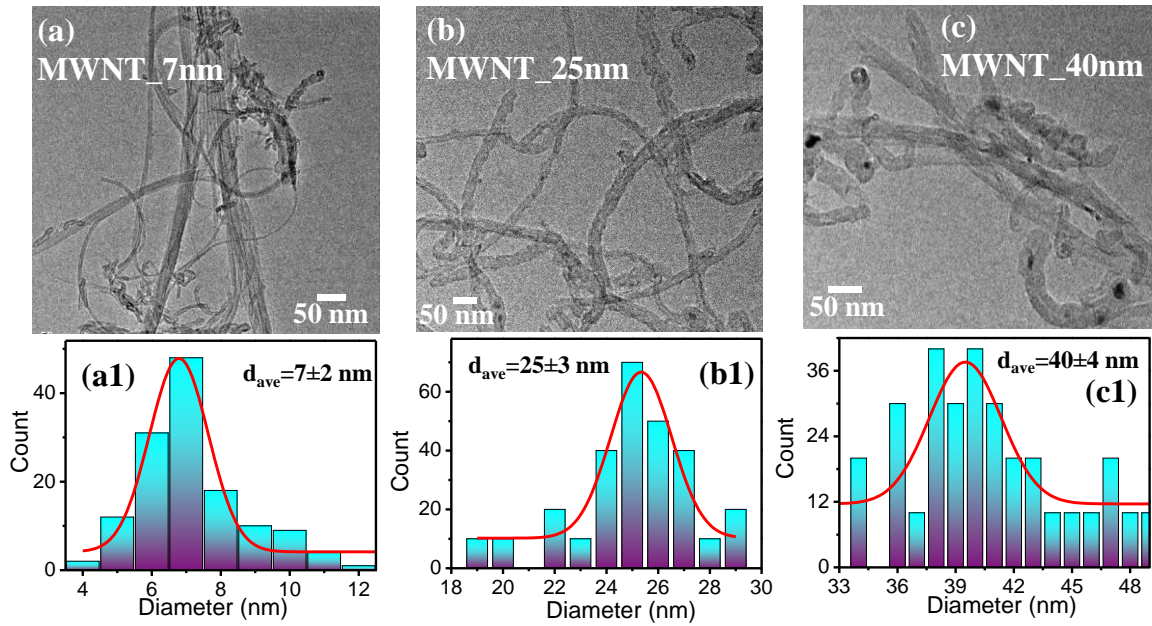


**Fig. 7.9: TEM image of (a) MWNT\_7nm, (b) MWNT\_25nm and (c) MWNT\_40nm and corresponding TEM analysis for diameter distribution is shown in (a1), (b1) and (c1)**

Diameters of the different MWNT samples are calculated from the TEM images and then fitted using a Gaussian curve as shown in Fig. 7.9 to determine the average diameter of each set of samples. The diameter of MWNT\_7nm, MWNT\_25nm and MWNT\_40nm samples are found to be  $7 \pm 2$  nm,  $25 \pm 3$  nm and  $40 \pm 4$  nm respectively after extensive TEM image analysis. The transmitted THz field for the MWNT films with varying MWNT diameter is shown in Fig. 7.10a. The peak to peak transmitted THz field is highest for the smallest diameter MWNT film and then decreases with increasing MWNT diameter in a non-linear fashion. It is interesting to observe that even with the same MWNT weight fraction, transmitted THz field drastically differs depending on the diameter of the MWNT in consideration, which indicates that bigger diameter MWNT films absorb THz radiation more efficiently compared to the smaller diameter MWNT films. The corresponding SE of the films are plotted in Fig. 7.10b and fitted with a theoretical model as described later. SE is found to be smallest for MWNT\_7nm but increases with increasing MWNT diameter and at 1.5 THz can be increased up to 330% and 380% by using MWNT\_25nm and MWNT\_40nm films respectively as observed from the figure. A SE as high as 30 dB has been achieved at 2.2 THz for MWNT\_40nm sample and it can be manipulated using MWNT tube diameter. A SE of 30 dB is considered to be of adequate

level for EMI shielding in the case of many applications as it can attenuate  $\sim 99.9\%$  of EMI radiation power[155].

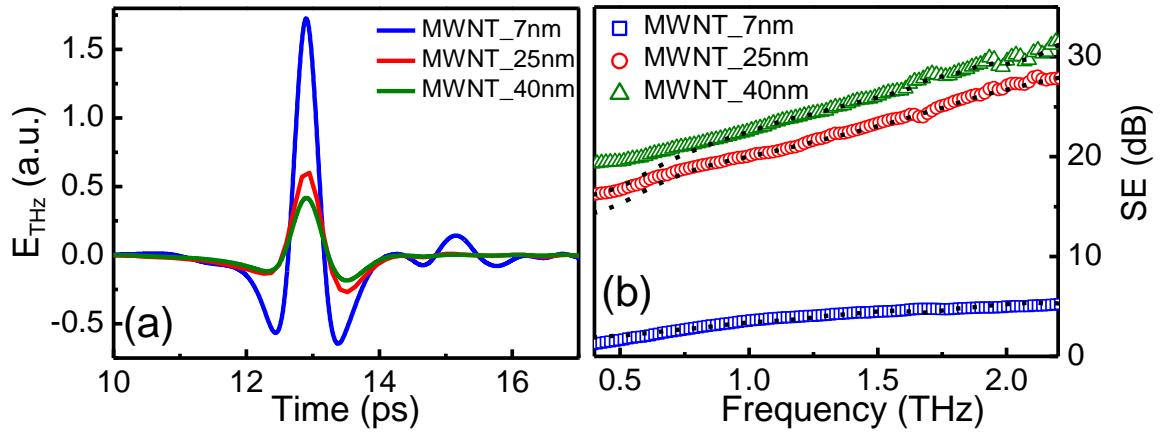


**Fig. 7.10: (a) Transmitted THz pulse in time domain passing through the samples and (b) the corresponding SE in the frequency range of 0.4-2.2 THz**

The shielding properties of these films has been analysed using the Eqn. 43 and Eqn. 44 which is already described in the chapter 5 and the contribution of each type of shielding (absorption, reflection and multiple internal reflection) has also been extracted. Shielding due to multiple internal reflection ( $SE_{\text{MIR}}(\omega)$ ) is dominant for films where the thickness of the film is comparable or smaller than the skin depth at a particular frequency. If the thickness of the film is thicker than the skin depth, the reflected wave from the internal surface will be absorbed by the conductive material, and thus multiple-reflection can be ignored.

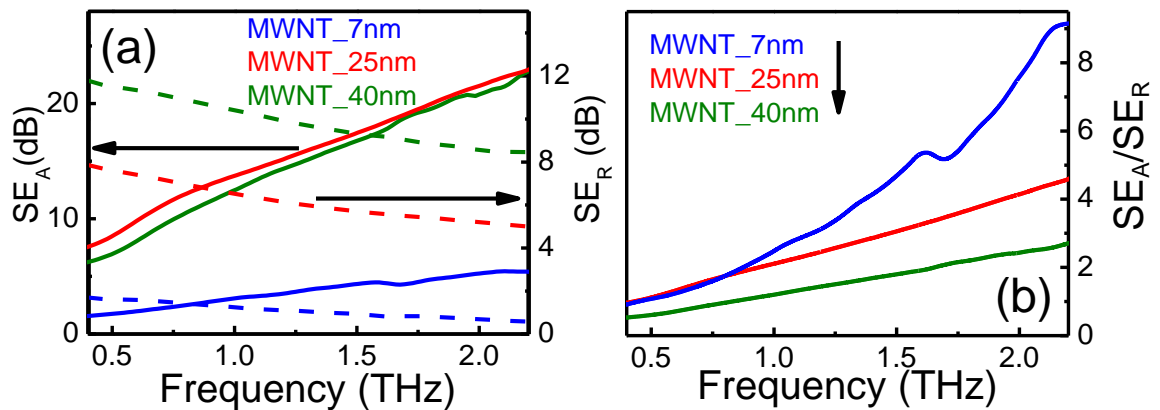


**Fig. 7.11: Contribution of absorption and reflection to the total shielding and (b) the relative ratio of contribution of absorption to reflection in the frequency range of 0.4-2.2 THz**

However, if the shield is thinner than the skin depth, the influence of multiple-reflection will be significant in decreasing the overall EMI shielding. In the present experiment, we

find that  $SE_R(\omega)$  decreases and  $SE_A(\omega)$  increases with increasing frequency as also theoretically prescribed by Shuba et al.[217] in sub-THz and THz frequency range. The dominant shielding mechanism is absorption for the three different MWNT films particularly in higher frequency range. For a particular frequency,  $SE_R(\omega)$  increases with increasing MWNT diameter. However, for MWNT\_25nm and MWNT\_40nm films,  $SE_A(\omega)$  is almost the same and much larger than MWNT\_7nm at a particular frequency. The ratio of absorption to reflection is shown in Fig. 7.7b. The relative contribution of absorption to reflection is larger in higher frequency range and it decreases with increasing MWNT diameter. Such diameter dependent change in THz shielding mechanism which is being studied here for the first time is really interesting. It was previously reported in numerous literatures that high frequency ( $\sim$  GHz) shielding of CNT based composites are primarily due to reflection and contribution from absorption is pretty less[156-158] and with increasing frequency contribution of reflection decreases and absorption increases. So, it can be understood that in sufficiently higher frequency range (THz) as in the present study, the effect of absorption may be the dominant shielding mechanism rather than reflection. It was also observed that, depending on the concentration of MWNT in a composite system, absorptive shielding or reflective shielding may dominate in a particular frequency range of interest[155].

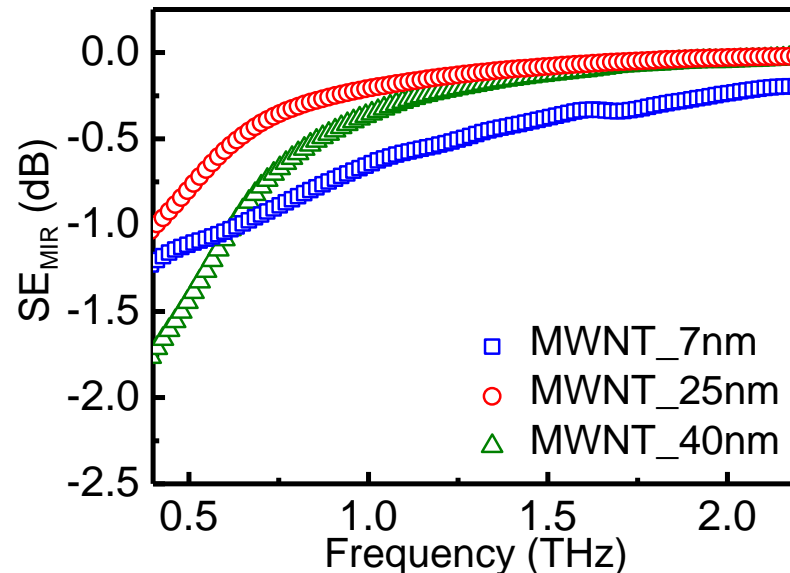


**Fig. 7.12: Contribution of Multiple internal reflection to the total shielding for different MWNT films**

It was also speculated that either reflection based or absorption based shielding is required for particular applications. Here, we have observed that, by choosing appropriate

MWNT diameter, we can choose to tune the dominant shielding mechanism. In the smaller frequency region ( $< 0.8$  THz), for MWNT\_40nm, shielding turns out to be mostly by reflection mechanism (as the ratio  $\frac{SE_A}{SE_R} < 1$ ) and in higher frequency range, although the effect of absorption increases than reflection, it remains comparable. However, in the other two MWNT films the shielding effect due to absorption is much larger than reflection especially in the higher frequency region. The effect of multiple internal reflection remains negative and negligibly small for all the samples and for MWNT\_25nm and MWNT\_40nm films, it reaches  $\sim 0$  beyond 1.2 THz as shown in Fig. 7.12. As the total shielding itself is much smaller in MWNT\_7nm, the effect of multiple internal reflection increases as clearly observed in the figure. Although, the negative value of shielding for multiple internal reflection is nothing new and has been observed in various literatures, it is somewhat counter intuitive at the first glance. As we know that skin depth of the material is closely related with the multiple internal reflective shielding, we have estimated the skin depth of the films in the frequency range of interest using the following formula:  $skin\ depth = abs\sqrt{\left(\frac{2}{\omega\mu\sigma}\right)}$ ; where  $\omega$  is the angular frequency,  $\mu$  is the permeability and  $\sigma$  is the complex conductivity of the sample. The skin depth and thickness of the films are shown in Fig. 7.13.

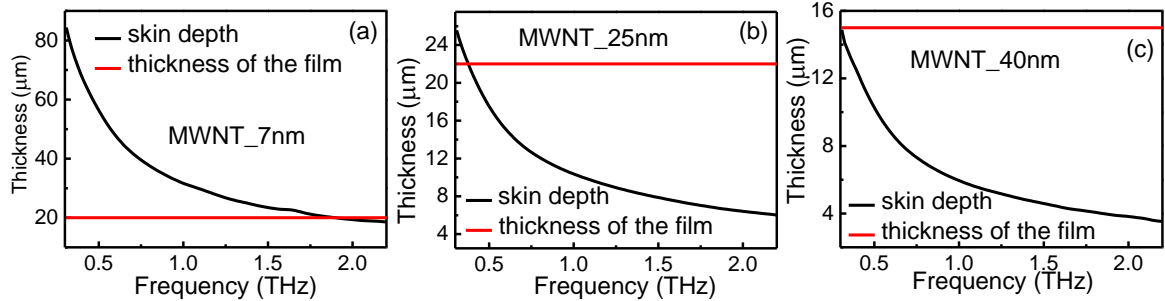


**Fig. 7.13: Comparison of skin depth and the thickness of the (a) MWNT\_7nm, (b) MWNT\_25nm and (c) MWNT\_40nm films**

The relative contribution of the multiple internal reflection shielding as shown in Fig. 7.12 is perfectly consistent with the skin depth and thickness of the films. When, the thickness of the film is smaller than the skin depth of the film, the effect of multiple internal reflection is strongest (most negative contribution) in reducing the overall SE of the system. Accordingly, for MWNT\_7nm film, effect of multiple internal reflection is maximum and it remains negative in almost at the entire frequency range. For MWNT\_25nm and MWNT\_40nm, as thickness of the film is smaller than the skin depth

only in the initial frequency range, the effect of multiple internal reflection is negative only in the initial frequency range. Then, as the skin depth of the films becomes smaller than the thickness, the effect of multiple internal reflection reduces to zero.

These films can be considered as composite material containing MWNT inclusions and air gaps in between as we have considered in our previous study. Hence, in order to quantitatively estimate the optical parameters of the films at THz frequency region we have used a combination of MG EMT and the DL model according as described in previous section.

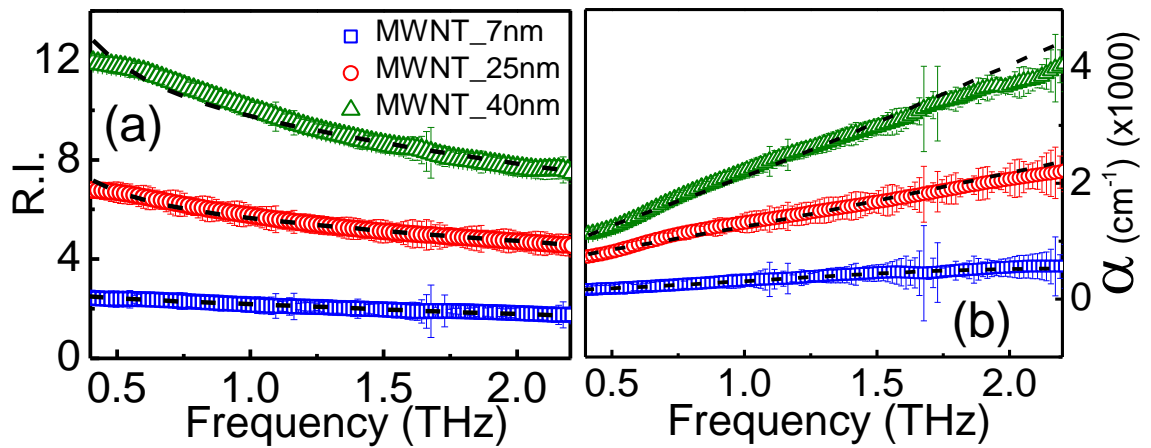


**Fig. 7.14: (a) Refractive Index (b) Absorption coefficient of MWNT films of different average diameters in the frequency range of 0.4-2.2 THz fitted with a combination of MG-DL model**

We have successfully fitted the experimentally observed refractive index and absorption coefficient of the films as shown in Fig. 7.14 in the frequency range of 0.4-2.2 THz. We obtained reasonably good fits within the error bars using the MG-DL model as shown in Fig. 7.14 and fitted value of DL parameters are given in Table 8 which is then used to simulate the complex conductivity spectra of the samples in the frequency range of 0.4-2.2 THz depicted in Fig. 7.15. Important information about the electronic structures of the samples can be estimated from the fitted DL parameters. The Drude plasma frequency  $\frac{\Omega_p}{2\pi}$ , which is proportional to the square root of free electron density, increases with increasing MWNT diameter indicating the increase in the free electron density. A twentyfold rise in the plasma frequency from 2.35 THz to 45.33 THz and a tenfold increase in scattering rate from 2.08 THz to 22.09 THz, is observed with enhanced MWNT diameter due to increase in the free electron number density. The large increase in both the parameters indicates increased free electron density with increasing MWNT diameter, which also gets reflected in the THz conductivity spectra of the MWNTs as

observed in Fig. 7.15. The plasma frequency has been found to be much larger than isolated small gap nanotubes as they are bundled together and no special care has been taken during the sample fabrication for nanotube isolation. For the largest MWNT diameter, free electron response ( $\frac{\Omega_p}{2\pi}$ ) is much larger than the Lorentzian response ( $\frac{\Omega_k}{2\pi}$ ), while for the other two smaller diameter MWNT samples  $\frac{\Omega_k}{2\pi} > \frac{\Omega_p}{2\pi}$ . This result indicates that intertube free carrier migration is enhanced because of the enhanced contact area between the carbon nanotubes due to its large diameter in MWNT\_40 nm sample. The exciton frequency ( $\frac{\omega_k}{2\pi}$ ) has been explained by different groups either originating from diameter dependent phenomenon or from length dependent phenomenon. The exciton frequency which is related to the TCP frequency does not vary monotonically with MWNT diameter as shown in table 8. This indicates that TCP does not necessarily arise only due to the curvature induced band gap of the CNTs, otherwise TCP frequency would have decreased with increasing MWNT diameter and this trend would have got reflected in the decreased exciton frequency as observed in previous literatures. The peak frequency is found to be 2.12, 9.37 and 5.01 THz for MWNT\_7 nm, MWNT\_25 nm and MWNT\_40 nm films, respectively. In the present experiment, the average length is same for all the samples are kept same however average diameters have been changed as given in the TEM image in Fig. 7.9.

**Table 8: Fitted DL parameters for different MWNT films**

Type of CNT	$\epsilon_\infty$	$\frac{\Omega_p}{2\pi}$ (THz)	$\frac{\Gamma_p}{2\pi}$ (THz)	$\frac{\Omega_k}{2\pi}$ (THz)	$\frac{\omega_k}{2\pi}$ (THz)	$\frac{\Gamma_k}{2\pi}$ (THz)
MWNT_7nm	4.00	2.35	2.08	4.42	2.12	3.78
MWNT_30nm	4.00	10.60	4.11	50.13	9.37	37.98
MWNT_50nm	4.00	45.33	22.09	43.45	5.01	14.99

So, the change in the exciton frequency as observed in Table 8, might be coming from the diameter dependence phenomenon. In the two larger diameter MWNT films, exciton frequency monotonically decreases with increasing diameter however the corresponding peak frequencies are quite large considering the large diameter of the tubes. People have observed TCP in the range of 3-10 THz in SWNT samples with diameters of the order of  $\sim 1$  nm[189, 208, 218]. Here, similar TCP have been found but in MWNTs with large diameter and this may be due to the screening effect of MWNTs under consideration[219]. These indicates that TCP does not necessarily arise only due to the curvature induced

band gap of the CNTs, otherwise TCP frequency would decrease with increasing MWNT diameter and this trend would get reflected in the decreased exciton frequency as observed in various literatures. Using the fitted DL parameters according to the following equation;

$$\sigma(\omega) = \left( \frac{\Omega_p^2}{\omega^2 + i\Gamma_p\omega} - \frac{\Omega_k^2}{(\omega_k^2 - \omega^2) - i\Gamma_k\omega} \right) i\varepsilon_0\omega. \quad (87)$$

we have extracted the conductivity spectra of intrinsic MWNT in the frequency range of 0.4-2.2 THz. Although the TCP does not vary systematically with the MWNT diameter, THz conductivity systematically increases with increasing MWNT diameter under consideration. Macutkevic et al.[220] have also showed that the TCP frequency does not necessarily vary with MWNT diameter.

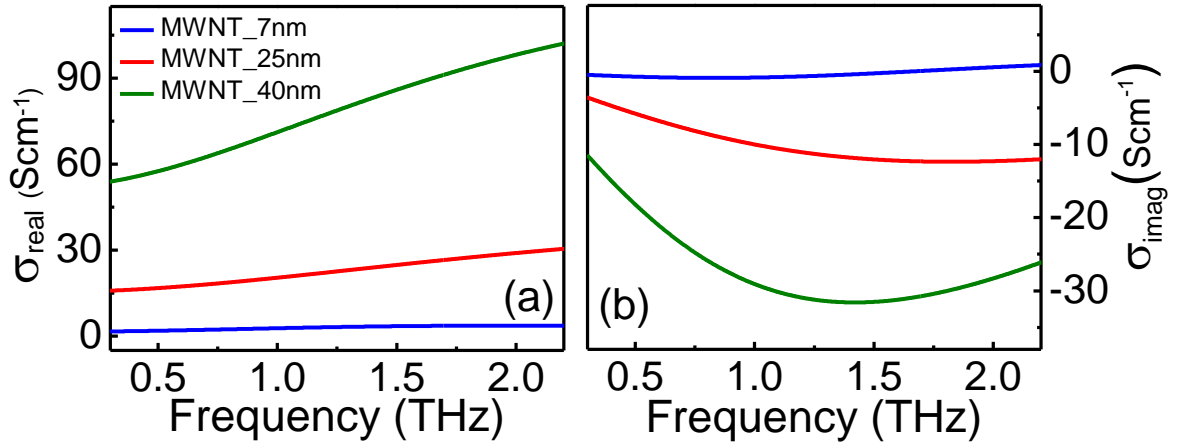


**Fig. 7.15: (a) Real and (b) Imaginary THz conductivity of MWNT films with varying diameters extracted from the fitted DL parameters in the frequency range of 0.4-2.2 THz**

They also showed THz conductivity does not change much with increasing MWNT diameter, which must be due to their limited choice of MWNT diameters (~ 9 and 12-14 nm) as observed from our detailed study.

## 7.6. Conclusion

We have prepared self-standing MWNT films with varying diameter and lengths using vacuum filtration technique and performed THz spectroscopic measurements at room temperature in transmission geometry. The effect of MWNT length and diameter on the shielding effectiveness and conductivity has been studied in THz frequency range. The shielding mechanism remains same with varying the MWNT length but depends significantly on MWNT diameter. THz conductivity of these films has been analysed using

a combination of MG EMT and DL model and dependence of TCP on the MWNT structure parameters has been observed.

S\_MWNT and L\_MWNT films of thickness  $14 \pm 1 \mu\text{m}$  are prepared by using vacuum filtration technique. SE of these films are extracted in the frequency range of 0.4-2.7 THz and analysed using a phenomenological model. SE is found to be larger than 34 dB for S\_MWNT and 46 dB for L\_MWNT in the entire frequency range and it increases weakly with increasing frequency. SE can be increased by  $\sim 30\%$  at 1.5 THz by simply changing the average MWNT length and thereby emerges as a potential candidate for application in THz EMIS devices. The relative contributions of absorption, multiple internal reflection and reflection to the total SE of the films are calculated using theoretical models and the weak frequency dependence observed in the SE occurs solely from the absorption mechanism in the films. The origin of THz conductivity peak is discussed in the light of excitation of surface plasmon resonance in MWNT by analyzing the obtained DL parameters and the conductivity spectra. Our investigation concludes that the TCP arises due to the excitation of plasmon resonances in MWNT films and the peak frequency is inversely proportional to the length of the MWNT.

We have also prepared self-standing MWNT films using three different MWNT's having the same average length ( $\sim 1 \mu\text{m}$ ) but of different average diameters ( $\sim 7 \text{ nm}$ ,  $25 \text{ nm}$  and  $40 \text{ nm}$ ). Detailed TEM analysis has been showed to confirm the variation of diameters in different MWNT samples. SE of the films are found to be increased to a gigantic 350 % by simply migrating to a suitable MWNT diameter. The SE has been analysed using a modified phenomenological model after carefully considering the skin depth and thickness of the samples. For MWNT\_7nm and MWNT\_25nm films  $SE_A$  turns out to be as the dominant shielding mechanism, but for the largest diameter MWNT film (MWNT\_40nm),  $SE_R$  becomes the dominant contributor to the total shielding mechanism especially in smaller frequency region ( $< 0.8 \text{ THz}$ ). A MG-DL model has been applied to extract important electronic information of the samples and extract the THz conductivity of the MWNT itself. Though TCP does not found to vary systematically on MWNT diameter, THz conductivity is found to be significantly dependent on the MWNT diameter and is mainly due to the enhanced free electron number density with increasing MWNT diameter. A controlled way of THz conductivity modulation of MWNT films will help the possible future applications of such composites in solar cells and high frequency EMI shielding device.

# **Chapter Eight**

---

# 8. Probing Oxidation in Copper Thin Film

---

## 8.1. Introduction

Metallic thin films are continuously being studied as transparent conducting electrode, ARC, shielding coating in THz frequency range. Oxidation of the films remains a grave concern upon the performance of these devices. In the present study, we have used THz spectroscopy as a delicate tool to detect and study the oxidation of Copper (Cu) thin films. Cu thin films of 20 nm are deposited via UHV d.c. magnetron sputtering technique and oxidized at 150 °C for 1, 4 and 6 hours. Further analysis on the complex THz conductivity of these films have been performed using Drude model. Ultrafast relaxation timescales increase from 20 fs to 200 fs upon oxidation. Thus, we have provided the use of THz spectroscopy as a sensitive tool to detect oxidation in Cu thin films.

## 8.2. Background Study

The complex frequency dependent conductivity of different types of semiconducting, metallic thin films and carbon nanostructures had been studied using THz spectroscopy in a non-invasive way in the last few years. Important conclusions about the electronic structure of the material had been extracted by analysing the THz conductivity spectra. Walther et al.[167] used THz-TDS to measure the complex conductivity of nanometer-thick gold films evaporated on silicon substrates in the frequency region from 0.2 to 2.7 THz. Laman et al.[168] prepared thin films of different metallic systems namely aluminium (Al), gold (Au) and silver (Ag) and studied their complex conductivity in THz frequency range at two different temperatures (77 K and 295 K). They found that the Ag film had much higher conductivity than Al and Au films of the same thickness, although their conductivity was much smaller than their d.c. value. Jameson et al.[221] studied the carrier dynamics of nickel-titanium (Ni-Ti) alloy using THz-TDS by varying the Ti concentration which also changed the thickness of the sample. They found that transmitted THz amplitude increased linearly with increasing Ti concentration in the alloy. They also studied the resistivity of the system and found sudden and sharp jumps in the resistivity curve for Ti concentration 22%, 44% and 62%, at which phase transitions

---

occurred at the growth temperature. They had also confirmed their THz spectroscopic data from conventional four probe measurements. Their results implied that the alloy films undergo significant structural disordering near the phase-transition concentrations. Zhu et al.[222] reported the THz transmission through vanadium dioxide (VO<sub>2</sub>) thin films grown on *c*-, *m*-, and *r*-plane sapphire substrates. Their results revealed that THz amplitude modulation as large as 84% for VO<sub>2</sub> films grown on *r*-plane sapphire substrates was possible upon crossing the metal–insulator phase transition temperature. Ramanandan et al.[223] studied the oxidation kinetics of Cu thin films using THz-TDS. They measured the transmission of broadband THz pulses from 1 to 7 THz through the Cu film (21 nm) while the film got oxidized at an elevated temperature (120, 130, 140 and 150 °C) in ambient air for up to three hours. The THz transmission through a freshly deposited Cu film was very low, which increased with time as the film was oxidized at different elevated temperature. The rate of increase was much higher at a temperature of 150 °C than at 120 °C, even though the temperature difference was only 30 °C. For the three highest temperatures used, the transmission had reached its highest, final value within 3 hours, suggesting that the oxidation was complete. The change in the transmitted THz electric field was correlated with the growth of the cuprous oxide layer and the decrease in thickness of the Cu layer. According to their analysis, a thin layer of cuprous oxide, which fully transmitted the THz pulses, was grown during Cu oxidation. The THz transmission through the oxidizing sample was found to be depended only on the thickness of the existing Cu film. Knowing the thickness of the Cu film which corresponded to a particular value of the THz transmission, one could determine the instantaneous remaining Cu film thickness during oxidation. Using Arrhenius law, they calculated the activation energy for diffusion to be 0.55-0.06 eV, which suggested a fast diffusion mechanism, such as diffusion of Cu atoms through the grain boundaries as the dominant diffusion mechanism. Yang et al.[224] studied the frequency-dependent complex conductivities, refractive indices and absorption coefficients of indium-tin oxide (ITO) nanowhiskers, which were also considered as a graded refractive index material, using THz-TDS in the frequency range of 0.2-2.0 THz. They had studied the conductivity spectra using Drude-Smith model and found that the ITO nanowhiskers exhibited longer carrier scattering times than ITO thin films. For whiskers with different heights (418 and 698 nm),  $\omega_p$  were in the range of 864~920 rad. THz, and  $\tau$  was in the range of 60~69 fs. Hong et al.[92] studied the THz conductivity of GO and rGO in the frequency range of 0.3-2.0 THz. They had prepared GO and rGO films of varying thickness ranging from 5 nm to

---

30 nm and studied the THz conductivity using the well-known Drude model. Their films demonstrated good shielding of electromagnetic waves with the conductivity of  $\sim 10^3$  S/cm in the THz range. For 30 nm rGO film, fitted value of plasma frequency and scattering rate were 100 THz and 26 fs respectively indicating a Drude roll-off frequency larger than probing frequency. Minami et al.[225] studied linear and nonlinear electron dynamics of polycrystalline Au ultrathin films with thicknesses ranging from 1.4 to 5.8 nm using THz spectroscopy.

### 8.3. Basic Theory

A thin film conductivity formula is used to extract the THz conductivity of 20 nm thick as-prepared and oxidized Cu films. The complex transmitted THz field through the substrate ( $\tilde{E}_{subs}$ ) and deposited film ( $\tilde{E}_{subs+film}$ ) is related with the complex refractive index of the substrate ( $\tilde{n}_{subs}$ ) and complex conductivity of the sample  $\tilde{\sigma}(\omega)$  according to the following equation,

$$\left| \frac{\tilde{E}_{subs+film}}{\tilde{E}_{subs}} \right| = \frac{1 + \tilde{n}_{substrate}}{1 + \tilde{n}_{substrate} + Z_0 \tilde{\sigma}(\omega) d}, \quad (88)$$

where,  $Z_0$  and  $d$  are the free space resistance ( $377 \Omega$ ) and the thickness of the thin film. The complex THz conductivity is then extracted easily using the following reconfigured formula,

$$\tilde{\sigma}(\omega) = \frac{\left( \left( \frac{1 + n_{subs}}{\left| \frac{\tilde{E}_{subs+Film}}{\tilde{E}_{subs}} \right|} \right) - 1 - \tilde{n}_{subs} \right)}{Z_0 d}. \quad (89)$$

High resistive silicon is used as a substrate for growing the Cu films because of its very low THz absorption and almost constant refractive index ( $\sim 3.4$ ) in the probed frequency range. A MATLAB code given at the appendices is used to extract the complex THz conductivity of the Cu thin films. The complex THz conductivity extracted using the abovementioned formula is analysed using the famous Drude formula. The Drude formula is given below,

$$\tilde{\sigma}(\omega) = \frac{\epsilon_0 \omega_p^2 \tau}{1 - i\omega\tau}, \quad (90)$$

where,  $\omega_p$  and  $\tau$  are the plasma frequency and the carrier scattering time, respectively. The parameters  $\omega_p$  and  $\tau$  can be extracted by fitting the experimentally obtained

conductivity with the Drude model. Further, the carrier concentration ( $N_e$ ) and mobility ( $\mu$ ) can also be determined from the relations

$$N_e = \varepsilon_0 \omega_p^2 m^* / e^2 \text{ and } \mu = e\tau / m^* \quad (91)$$

respectively, where  $m^*$  is the electron effective mass;  $m_e = 9.109 \times 10^{-31} \text{ kg}$ , is the electron's mass;  $e = 1.602 \times 10^{-19} \text{ C}$ , is the electron charge. DC conductivity ( $\sigma_{DC}$ ) can be calculated from the following formula,

$$\sigma_{DC} = \varepsilon_0 \omega_p^2 \tau. \quad (92)$$

The complex conductivity is analysed using origin software to extract the electronic parameters of the films.

## 8.4. Sample Preparation

Four Cu thin films of 20 nm thickness are deposited on top of a high resistive silicon substrate using a d.c. magnetron sputtering unit and then three of those films are put in an oven which is previously set at 150 °C. The films are taken out after 1 h, 4 h and 6 h respectively to perform different degree of oxidation in the Cu thin films and these films are named as Cu\_1, Cu\_4 and Cu\_6 respectively. Cu\_0 corresponds to un-oxidized Cu film.

## 8.5. Measurement and Analysis

Transmitted THz amplitude increases with increasing oxidation time as clearly shown in Fig. 8.1.

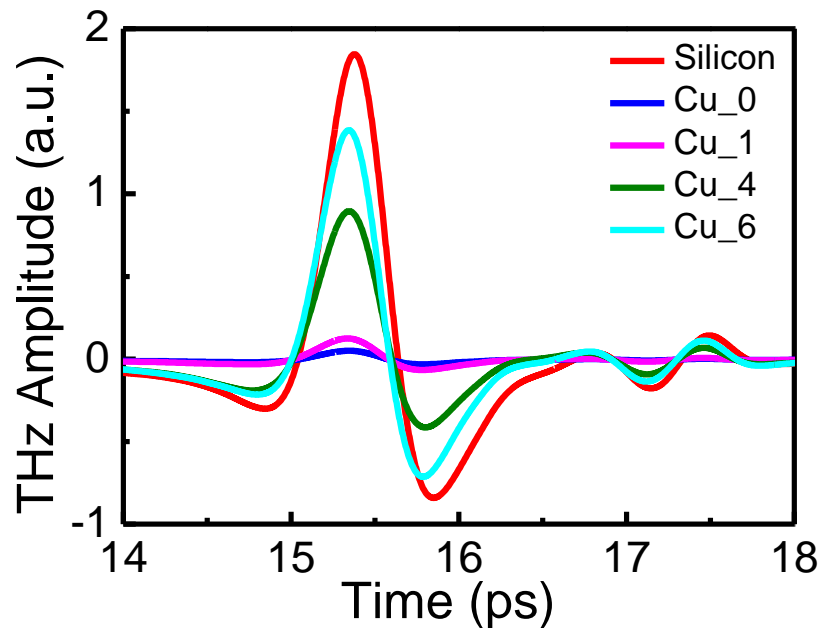
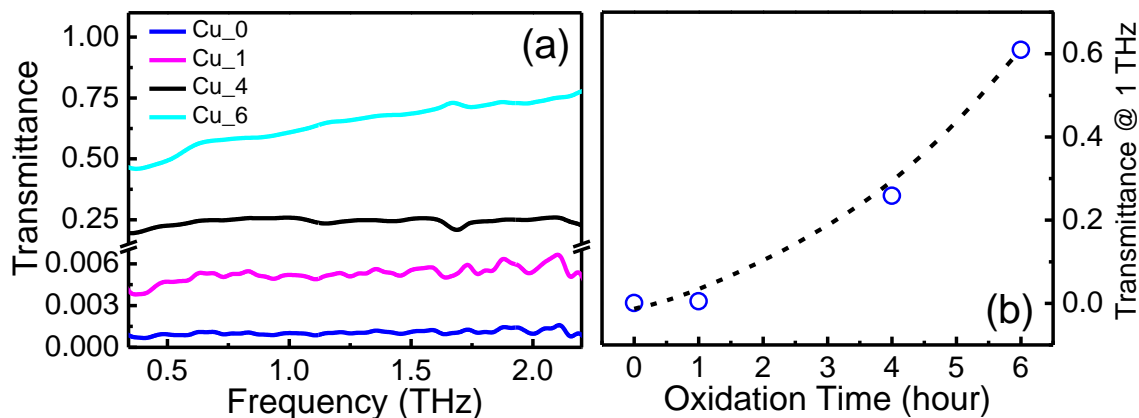


Fig. 8.1: Transmitted THz amplitude in time domain through the oxidized Cu films

This is due to the fact that with increasing oxidation time, the metallic nature of the Cu film decreases and the semiconductor nature increases. The transmittance in frequency domain has been calculated using the following relation  $T(\omega) = \left| \frac{\tilde{E}_{subs+film}(\omega)}{\tilde{E}_{subs}(\omega)} \right|^2$ , where  $\tilde{E}_{subs+film}(\omega)$  and  $\tilde{E}_{subs}(\omega)$  are the complex THz field passing through the sample and silicon substrate respectively. Transmittance spectrum has been shown in Fig. 8.2a. For as prepared Cu film, THz transmittance is nearly zero and then with increasing oxidation time it increases non-linearly, as observed in other studies[223] also. It is also noticeable that transmittance is nearly frequency independent for the as-prepared Cu film and also for low oxidized Cu films, but it increases with increasing frequency for Cu\_6. This frequency dependence has been explained later in the chapter. The transmittance at 1 THz is plotted in Fig. 8.2b and fitted with an exponential curve. So, the transmittance increases exponentially with increasing oxidation time.



**Fig. 8.2: (a) Transmittance spectrum of the Cu films, (b) transmittance at 1 THz as a function of oxidation time and fitted with exponential law**

Copper can oxidize to form two oxides, cuprous oxide ( $\text{Cu}_2\text{O}$ ) or cupric oxide ( $\text{CuO}$ ). However, for heating temperatures below  $225^\circ\text{C}$ , it is known[223] that the oxide formed is predominantly cuprous oxide. So, in the present scenario, we can safely assume that, Cu gets oxidized due to the formation  $\text{Cu}_2\text{O}$  layer because of heating and the greater the oxidation or heating time, larger amount of  $\text{Cu}_2\text{O}$  layer is formed. Ramachandan et al. analysed this oxide layer as a fully THz transparent thin layer (as most dielectric, non-absorbing thin layers behave in THz frequency range). They studied the transmission through the oxidized sample, which was dependent only on the thickness of the copper film and this thickness got decreased with increasing oxidation temperature. However, we have tried to visualize this phenomenon from a different angle. Because in our experimental transmittance data, we observe that, THz transmittance not only increased

with increasing oxidation time but also becomes highly frequency dependent. For the conductivity analysis, at first, we extracted the frequency dependent THz conductivity of the films using the thin film formula as given below (described in the theory section earlier in this chapter);

$$\tilde{\sigma}(\omega) = \frac{\left( \left( \frac{1 + n_{subs}}{\left| \frac{\tilde{E}_{subs+film}}{\tilde{E}_{subs}} \right|} \right) - 1 - \tilde{n}_{subs} \right)}{Z_0 d}, \quad (93)$$

where  $\tilde{n}_{subs}$  is the complex refractive index of the silicon substrate (almost constant  $\sim 3.41$  in the frequency range of interest),  $Z_0$  is the free space impedance ( $377 \Omega$ ) and  $d$  is the thickness of the Cu film ( $\sim 20$  nm).

We modelled oxidized Cu film as a poor metallic layer having the same thickness of the as-prepared Cu film (Cu\_0). In our calculation, the thickness of the material remains same, only the average electronic properties of the oxidized Cu film changes with increasing oxidation time.

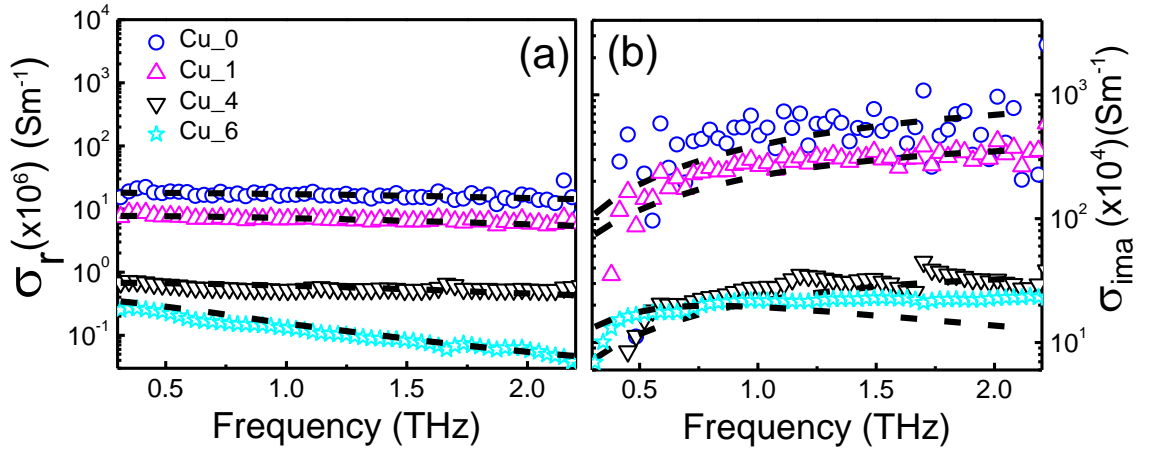


**Fig. 8.3: (a) Real and (b) imaginary THz conductivity of the Cu films fitted with Drude model**

The complex conductivity spectra of the Cu films are shown in Fig. 8.3. The real THz conductivity of the as prepared 20 nm Cu film is  $\sim 10^7 \text{ Sm}^{-1}$  and is almost frequency independent which matches well with the published values. The real and imaginary conductivity of these films at 1 THz has been tabulated in the Table 9. We can see that the real THz conductivity spectra not only decreases with increasing oxidation time but also becomes highly frequency dependent (for Cu\_4 and Cu\_6 films). So, we infer that, the conductivity changes may be related to the intrinsic changes in electronic properties of

the Cu films upon oxidation. The conductivity spectrum is fitted well using the conventional Drude model (described earlier in the chapter in the theory section).

**Table 9: Real and Imaginary Conductivity at 1 THz**

Sample Name	Real conductivity ( $\text{Sm}^{-1}$ )	Imaginary Conductivity ( $\text{Sm}^{-1}$ )
Cu_0	$16.28 \times 10^6$	$613.92 \times 10^4$
Cu_1	$6.048 \times 10^6$	$282.32 \times 10^4$
Cu_4	$0.50 \times 10^6$	$31.62 \times 10^4$
Cu_6	$0.08 \times 10^6$	$20.69 \times 10^4$

From the Drude fitting, we directly obtained the plasma frequency and the scattering times of the Cu films which has been shown in Table 10.

**Table 10: Plasma frequency and scattering rate of the Cu films**

Sample Name	Plasma Frequency $[\frac{\omega_p}{2\pi}]$ (THz)	Scattering Time $[\tau]$ (fs)
Cu_0	$1194.11 \pm 50.59$	$36 \pm 3$
Cu_1	$679.85 \pm 13.63$	$48 \pm 3$
Cu_4	$187.76 \pm 4.84$	$55 \pm 5$
Cu_6	$75.62 \pm 1.42$	$190 \pm 10$

Plasma frequency decreases with increasing oxidation time and the scattering time increases. A reduced plasma frequency can be rationalized by the fact that not all the carriers contribute equally[167] to the conduction process or the number of free carriers decreases with increasing oxidation time. Heating at high temperature may also create defect states on the surface of the film. The scattering time also increases as the defect state density increases with increasing oxidation time. It was also argued that for gold film thickness  $\geq 20$  nm, the plasma frequency should reach the bulk value of the material.

The value of plasma frequency  $(\frac{\omega_p}{2\pi})$  for bulk Cu is calculated to be  $\sim 2240$  THz[226, 227] or  $\sim 1912$  THz[228]. Here, for the as-prepared Cu film, we observed plasma frequency of  $\sim 1194$  THz. This discrepancy may be due to the quality of the film or we may need a

thicker sample to reproduce the bulk value in Cu films. The scattering time for as prepared 20 nm Cu film is found to be  $\sim 36$  fs which is pretty close to the bulk value of  $\sim 20$  fs[228]. The plasma frequency ( $\omega_p$ ) and the scattering time ( $\tau$ ) along with the error bars are plotted in Fig. 8.4.

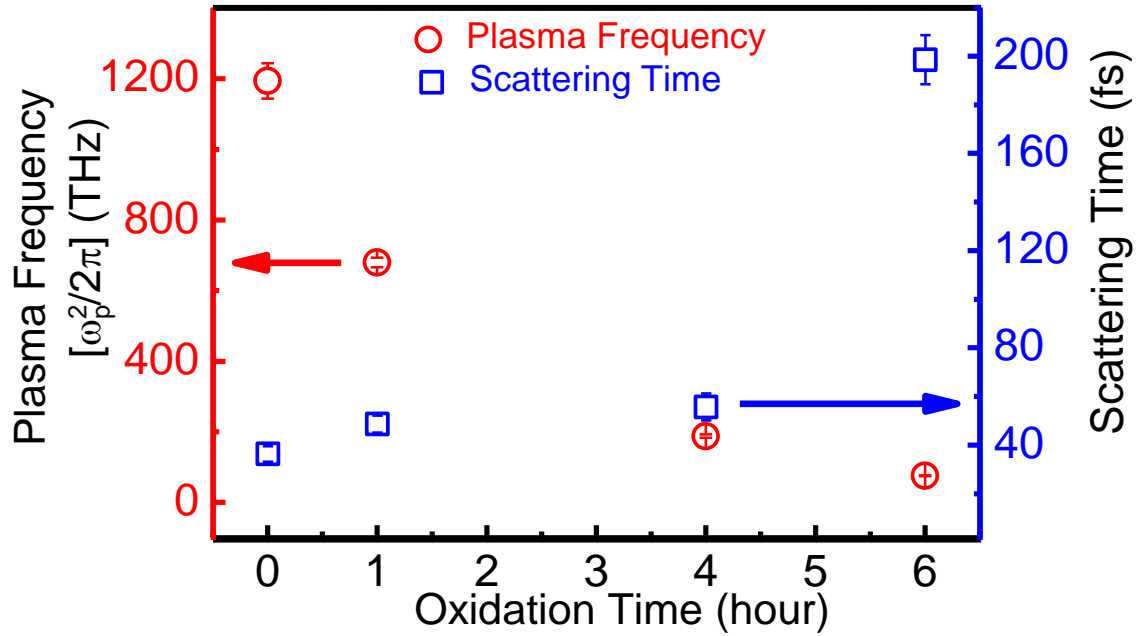


**Fig. 8.4: Scattering time (a) and DC conductivity (b) as a function of oxidation time**

The d.c. conductivity ( $\sigma_{DC}$ ), free carrier density ( $N_e$ ) and mobility ( $\mu$ ) can be obtained from the Drude parameters using the previously mentioned formula and the obtained values for the Cu thin films are shown in Table 11.

**Table 11: Different electronic parameters for the Cu films**

Sample	$\sigma_{DC}$ (Sm <sup>-1</sup> )	$N_e$ (cm <sup>-3</sup> )	$\mu$ (cm <sup>2</sup> V <sup>-1</sup> s <sup>-1</sup> )
Cu_0	$1.76 \times 10^7$	$2.5 \times 10^{22}$	44.5
Cu_1	$7.7 \times 10^6$	$8.1 \times 10^{21}$	59.4
Cu_4	$6.7 \times 10^5$	$6.2 \times 10^{20}$	68.1
Cu_6	$3.8 \times 10^5$	$1.0 \times 10^{20}$	235.2

The effective mass for Cu is taken  $1.42m_e$  according to published values. So, we observe a decreasing trend in d.c. conductivity and carrier density with increasing oxidation time

as the metallic character of the Cu films gets destroyed due to heating. Upon 6 hour of heating at 150<sup>o</sup> C, d.c. conductivity has been destroyed to 22 % than its original value.

## 8.6. Conclusion

We have prepared Cu thin films of 20 nm thicknesses using a sputtered d.c. magnetron deposition unit and then heated the films at 150 °C in air for different times (1, 4 and 6 hours) for oxidation. THz spectroscopic measurements are performed on these oxidized Cu films at room temperature in transmission geometry. One as-prepared Cu film (Cu\_0) of similar thickness was also studied. We know that the due to the oxidation of Cu films, a layer of Cu<sub>2</sub>O forms on the surface of the Cu films which creates a severe problem destroying the metallic character of the film. Previously, it was concluded that, the oxidized Cu films can be considered safely as a Cu film with reduced thickness to characterize it because Cu<sub>2</sub>O layer does not interact with the probing THz frequency. We found from the THz transmittance behaviour, that after oxidation, not only the transmittance increases but also a frequency dependence is introduced to the otherwise frequency independent transmittance spectra. We studied samples as thin films of same thickness but with degraded electronic properties with increasing oxidation time. Complex THz conductivity of these films were extracted using a well-known thin film formula and studied using the Drude model. Both the real and imaginary THz conductivity is found to be decreasing with increasing oxidation time. We found out that upon oxidation the plasma frequency decreases and scattering time increases due to decreasing free carrier density and increasing defect states/scattering centres respectively.

# **Chapter Nine**

## 9. Conclusion and Future Direction

---

---

This thesis is devoted in understanding the electro-optic properties of different types of nanostructures in the THz frequency range and using those nanostructures efficiently in manipulating THz radiation in application purposes. Some of these nanomaterials have been prepared in the lab while other types of nanostructures (different types of CNTs) have been commercially procured. In this crucial time, thanks to the pioneering works of many groups, THz spectroscopy is leaving behind its initial problems regarding efficient and compact THz sources and detectors, which has limited the applications of this techniques in the initial years of late 1980s to early 2000s, and moving towards a direction of unlimited and unforeseen opportunities in terms of its application in diverse gasp of science ranging from medical imaging, weather and space science, public security to ultrafast communication, THz opto-electronic devices, THz metamaterials, THz field induced demagnetization and THz ultrafast dynamics of nanostructures. Although the search for powerful THz sources is still ongoing which would eventually solve this technique's limited applicability in the fields of free space ultrafast communication and open air imaging, most of the studies are now being directed either in understanding fundamental physical properties of low energy ultrafast dynamics or applicability of THz devices. In this significant junction, we have studied the ground state opto-electronic properties of aligned Ni nanostructures, CNTs and their polymer (PVA) composites and Cu thin films in this frequency range and their use in manipulating this frequency band. As large number of studies are now motivated towards the THz electronic device fabrication and THz ultrafast communications, low cost durable THz manipulating devices like THz polarizer, THz EMIS films are becoming essential. CNTs act as the building block of these passive devices due to their fascinating high frequency properties and often the performance of the devices boils down to the efficient tuning of high frequency conductivity of these tubes. Although CNTs are being studied using THz spectroscopy since 2000s, the origin of extremely high THz conductivity in CNTs still remains a subject of debate and its relation with the geometrical parameters of the tubes is worth investigating.

Nanostructures other than CNTs have been prepared using chemical synthesis and vacuum filtration technique and characterized using conventional SEM, TEM and UV-

---

visible spectrometer. The experiments are performed using THz-TDS at room temperature in transmission geometry. Data is analysed using a commercial software (Teralyzer) for complex optical refractive index extraction and using matlab interface for others. Sufficient theoretical analysis has also been performed to explain the experimentally obtained data mainly using matlab interface.

## 9.1. Conclusion

[Chapter 1](#) provides the general introduction of the THz radiation, its potential application in diverse areas of science and the spectroscopic measurements possible using this technique and its advantage over the conventional spectroscopic technique.

[Chapter 2](#) provides the general background of this spectroscopic technique. It includes brief history about the development of this field starting from the early 1980s, which mainly consists of the study of new types of antenna based, and photo-mixer based structures for THz generation and THz detection and the subsequent optimization of the field and also the theory and demonstration of THz generation and detection using photo conductive antenna. A brief description of different application based recent works (within last ten years) on THz spectroscopy of different types of exotic nanostructures which is not within the scope of the present thesis is also provided.

[Chapter 3](#) is dedicated for the description of the instruments and data analysis procedure. The different components of the THz spectrometer (Menlo Tera K-8 spectrometer) that I have used is described in detail. The alignment procedure and working principle of the spectrometer is discussed. Though the alignment procedure is not unique and it depends on the individual, an overall idea about the alignment procedure can be found here. It mainly combines the ideas provided by the Menlo system engineers Rafal and Chris during their installation, technical visits, email assistance, my own hand-on experience while handling the instrument over four years and valuable inputs from my lab mates. General description about SEM, TEM, UV-visible Spectrometer has also been provided. These instruments are mainly used for additional sample characterization during experiments. The data analysis procedure and the corresponding theory is also discussed.

[Chapter 4](#) to [chapter 8](#) is based upon the experimental works that I have performed during my PhD. In [chapter 4](#), we demonstrate an easy route to prepare robust and durable THz polarizer and its performance in THz frequency range. NiNP with average diameter  $\sim 165$  nm and NiNC with average diameter  $\sim 300$  nm and average length  $\sim 4$   $\mu\text{m}$  has been chemically synthesized and aligned in liquefied polymer matrices under the influence of

---

external magnetic field. Anisotropic THz transmittance is observed with these structures in THz frequency range. For NiNP polarizer, the effective polarizer bandwidth is 0.2 to 0.9 THz with very high DOP  $\sim 0.98 \pm 0.03$  which then decreases with increasing probing frequency further. However, using the NiNC polarizer, we obtained a large polarizer bandwidth of 0.3-2.4 THz but with limited DOP of  $0.76 \pm 0.03$ . Our study revealed that the alignment of nanostructures could easily be tuned by using more uniform external magnetic field, which could ultimately control the DOP and polarizer bandwidth of the structure. Considering the good polarizing performance, easy and cheap preparation process, durability, robustness and tunability, we found that aligned magnetic nanostructures offer bright prospect to emerge as a popular THz polarizer.

[Chapter 5](#) is based on the study of THz electromagnetic shielding in SWNT-polymer composites. The composite polymer films are prepared via slow drying method with varying SWNT content in PVA matrices. Transmittance is found to be significant at lower frequencies (between 0.3 and 0.8 THz) but close to zero at higher frequencies (beyond 1.25 THz) showing a possible application of these composites especially with higher amount of SWNT contents for low band-pass THz filters. Shielding properties of the samples are studied in the frequency range of 0.3 THz to 2.1 THz with highest SE of  $\sim 29$  dB at 2.1 THz. SE shows a linear relationship with SWNT weight fraction at a particular probing frequency and in a broad frequency range from 1.2 to 2.0 THz, SE can be expressed as  $SE \propto (0.73 \pm 0.075)w$  where  $w$  is the SWNT weight fraction. Thus we have showed the performance of a low-cost and durable THz EMI shield using SWNT composites.

[Chapter 6](#) is dedicated in studying two different and unique ways of conductivity manipulation in SWNT/polymer composites.

In the first part we have demonstrated how the average length of SWNTs effect the overall THz conductivity of the SWNT/PVA composite films. The films are prepared via a slow drying process with a constant thickness of  $300 \pm 20$   $\mu\text{m}$  with varying SWNT length ( $\sim 2$   $\mu\text{m}$  and  $\sim 15$   $\mu\text{m}$ ) and SWNT weight fraction in the PVA matrix. THz conductivity spectra are obtained for these films in transmission geometry in the frequency range of 0.3 - 2.0 THz. It is explicitly shown that real conductivity of such films can be tuned up to 80% in a controlled manner by carefully choosing the length and weight fraction of the SWNT's. The length dependent high frequency conductivity of SWNTs is discussed in the light of surface plasmon resonance.

In the next part, we have tried to modulate the THz conductivity of SWNT/PVA and MWNT/PVA composites by decorating the sidewalls of the tubes with chemically synthesized AuNP and varying the density of AuNP decoration. The attachment of Au NP on the sidewalls of CNTs are confirmed by UV- visible spectroscopy as well as from SEM and TEM images. Surfaced decorated SWNT composites show either conductivity decrement or enhancement up to  $\pm 15\%$  depending on the AuNP concentration than the undecorated SWNT composites. The results are explained qualitatively by suggesting the role of AuNP as carrier trapping potential or alternative carrier conduction path depending on its density.

A controlled way of THz conductivity modulation of SWNT/PVA composites will help the possible future applications of such composites in solar cells and high frequency EMI shielding devices.

In [chapter 7](#), we have discussed the THz shielding effectiveness and THz conductivity of self-standing MWNT films as a function of MWNT diameter and MWNT length. The relative contributions of absorption, multiple internal reflection and reflection to the total SE of the films are calculated using theoretical models. Intrinsic THz conductivity of the MWNTs have been extracted using MG EMT and analysed with DL model.

Self-standing MWNT films of thicknesses  $\sim 15\text{-}25\ \mu\text{m}$  is prepared using vacuum filtration technique of two different MWNT average lengths (S\_MWNT and L\_MWNT having average length  $\sim 2\ \mu\text{m}$  and  $15\ \mu\text{m}$ ) and three different MWNT average outer diameters (MWNT\_7nm, MWNT\_25nm and MWNT\_40nm). SE can be increased by  $\sim 30\%$  at 1.5 THz by simply changing the average MWNT length whereas the increment can be as high as 350% by changing the MWNT diameter. The mechanism of shielding does not change with length variation; absorptive shielding increases while reflective shielding decreases with increasing frequency and the effect of multiple internal reflection is negative and almost negligible. However, the shielding mechanism is found to be MWNT diameter dependent. For the two smaller diameter MWNT films  $SE_A$  turns out to be the dominant shielding mechanism in the entire frequency range, but for the largest diameter MWNT film,  $SE_R$  becomes the dominant contributor to the total shielding mechanism in smaller frequency region ( $< 0.8\ \text{THz}$ ), although their frequency response remains the same. Our study on THz conductivity spectra concludes that the TCP arises due to the excitation of plasmon resonances in MWNT films and the peak frequency is inversely proportional to the length of the MWNT and it does not vary systematically on MWNT

---

diameter. However, THz conductivity is found to be significantly and systematically increasing both with increasing MWNT length and diameter.

In [chapter 8](#), on a slightly different note, we have studied the effect of oxidation in Cu thin films on the THz conductivity property of the films. We have prepared Cu thin films of 20 nm thicknesses using a sputtered magnetron d.c. deposition unit and then heated the films at 150 °C in air for different times for oxidation. We found that the THz conductivity of the oxidized Cu films can be described using the conventional Drude model but with significantly reduced metallic properties. Both the real and imaginary THz conductivity are found to be decreasing with increasing oxidation time. We found out that upon oxidation the plasma frequency decreases due to decreasing free carrier density and scattering time increases due to increasing defect states/scattering centres. The relation of the opto-electronic properties of Cu films with the oxidation time is experimentally established.

## 9.2. Future Direction

Ample scope exists to extend the works of the present thesis for more complete understanding of the fundamental properties of the nanostructures and their fruitful applications.

We have studied aligned nanoparticles and nanochains for the preparation of THz polarizer. However, from my understanding aligned nanowires and CNTs should provide a better DOP because of the large anisotropic AR of the structures. People have studied aligned CNTs grown on Si or quartz substrates using CVD technique however that makes the procedure to be expensive and the sample to be brittle. Some studies have shown promising ways to align CNTs inside polymer matrices which would provide a durable film. One can systematically study the THz polarizing behavior of such high AR nanostructures. One can also study metallic wire grid like polarizer structure on Si substrates and a graphene film and electrode sandwiched between them. The gate voltage will significantly alter the resistance of the graphene in THz frequency range which should in turn effect the THz transmittance of the polarizer both parallel and perpendicular orientation. Such an active THz polarizer may provide us interesting pathways to manipulate the polarization property of THz waves. Numerous literatures exist in studying THz metamaterials, however, there are plenty of room in studying the ARC in THz frequency range to minimize the problem of FP reflections in THz devices. We have started some preliminary measurements on anti-dot metallic structures and they

gave us better ARC performance than the conventional metallic thin film coatings. Thorough investigation is ongoing to study the effect of anti-dot thickness and structure constants on the ARC behavior. While anti-dot structure will provide the high transmission of main THz pulse, the geometry of the anti-dot will provide the necessary impedance matching condition for FP reflection peak suppression.

We have studied the SE and THz conductivity of SWNT/PVA composite films. One immediate extension of this works should be measuring the temperature dependent THz conductivity of the polymer composites, which would actually enable us to dictate the exact conductivity mechanism like variable range hopping, correlated barrier hopping, or small polaron tunneling mechanisms associated with the polymer composite structures. The role of SWNT and MWNT structure constants can also be explored. The highest SE we have obtained in SWNT composites is  $\sim 30$  dB in THz frequency range. One can also try to increase the SE of the composites by introducing conductive polymer instead of PVA to disperse the CNTs and also additional conductive inclusion like metallic nanowires/nanochains can be incorporated into the composite material to make it much more absorptive thus helping to increase its shielding behavior.

Due to limited frequency window of our spectrometer, we have studied the conductivity spectra of the self-standing MWNT films up to 2.7 THz and then simulated the spectra up to 20 THz to get knowledge about the TCP of the MWNT. However, using an ultra-broadband THz spectrometer, it is possible to directly measure the THz response of the films in the frequency range of interest and obtain a first-hand knowledge about the relation of TCP with the geometrical parameters of the tubes. Although such studies have already been performed using THz and FTIR technique; a thorough study using a single THz spectrometer with large number of different types of carefully chosen MWNT samples may provide us some much needed conclusive results.

I have studied the effect of nanostructured materials and their composites in manipulating THz radiation, now I am interested in using external influences like magnetic field, temperature, current to the material under investigation to manipulate THz radiation like magnetic field or temperature induced THz transparency, current induced THz conductivity etc.. It is also high time to study THz spintronics using ferromagnetic/non-magnetic multilayer films and their interaction with polarized THz waves in the presence of external magnetic field. Such studies will also provide us the fundamental carrier lifetimes of the system in a neutral way because of the extremely low temperature/energy of THz radiation.

---

## 10. References

---

---

1. C. Wai Lam, D. Jason, and M. M. Daniel, "Imaging with terahertz radiation," *Reports on Progress in Physics* **70**, 1325-1379 (2007).
2. B. Ferguson and X.-C. Zhang, "Materials for terahertz science and technology," *Nature Materials* **1**, 26-33 (2002).
3. L. Ren, C. L. Pint, L. G. Booshehri, W. D. Rice, X. Wang, D. J. Hilton, K. Takeya, I. Kawayama, M. Tonouchi, R. H. Hauge, and J. Kono, "Carbon Nanotube Terahertz Polarizer," *Nano Letters* **9**, 2610-2613 (2009).
4. J. Kyoung, E. Y. Jang, M. D. Lima, H.-R. Park, R. O. Robles, X. Lepró, Y. H. Kim, R. H. Baughman, and D.-S. Kim, "A Reel-Wound Carbon Nanotube Polarizer for Terahertz Frequencies," *Nano Letters* **11**, 4227-4231 (2011).
5. L. Ren, C. L. Pint, T. Arikawa, K. Takeya, I. Kawayama, M. Tonouchi, R. H. Hauge, and J. Kono, "Broadband Terahertz Polarizers with Ideal Performance Based on Aligned Carbon Nanotube Stacks," *Nano Letters* **12**, 787-790 (2012).
6. D. Polley, A. Ganguly, A. Barman, and R. K. Mitra, "Polarizing effect of aligned nanoparticles in terahertz frequency region," *Optics Letters* **38**, 2754-2756 (2013).
7. J.-B. Masson and G. Gallot, "Terahertz achromatic quarter-wave plate," *Optics Letters* **31**, 265-267 (2006).
8. I. Yamada, K. Takano, M. Hangyo, M. Saito, and W. Watanabe, "Terahertz wire-grid polarizers with micrometer-pitch Al gratings," *Optics Letters* **34**, 274-276 (2009).
9. M. A. Seo, J. W. Lee, and D. S. Kim, "Dielectric constant engineering with polymethylmethacrylate-graphite metastate composites in the terahertz region," *Journal of Applied Physics* **99**, 066103, (2006).
10. E. N. Agnandji, V. Vigneras, J. L. Miane, and P. Mounaix, "Shielding effectiveness in terahertz domain of monolayer-doped polyaniline films," in *Electronics Letters*, (2007), pp. 1271-1273.
11. M. A. Seo, J. H. Yim, Y. H. Ahn, F. Rotermund, D. S. Kim, S. Lee, and H. Lim, "Terahertz electromagnetic interference shielding using single-walled carbon nanotube flexible films " *Applied Physics Letters* **93**, 231905 (2008).
12. Q. Shi, W. Huang, Y. Zhang, J. Yan, Y. Zhang, M. Mao, Y. Zhang, and M. Tu, "Giant Phase Transition Properties at Terahertz Range in VO<sub>2</sub> films Deposited by Sol-Gel Method," *ACS Applied Materials & Interfaces* **3**, 3523-3527 (2011).
13. Z. Jin, A. Tkach, F. Casper, V. Spetter, H. Grimm, A. Thomas, T. Kampfrath, M. Bonn, M. Klaui, and D. Turchinovich, "Accessing the fundamentals of magnetotransport in metals with terahertz probes," *Nature Physics* **11**, 761-766 (2015).
14. D. E. Endean, J. N. Heyman, S. Maat, and E. D. Dahlberg, "Quantitative analysis of the giant magnetoresistance effect at microwave frequencies," *Physical Review B* **84**, 212405 (2011).
15. C. J. E. Straatsma, M. Johnson, and A. Y. Elezzabi, "Terahertz spinplasmonics in random ensembles of Ni and Co microparticles," *Journal of Applied Physics* **112**, 103904 (2012).
16. N. Horiuchi, "Terahertz spectroscopy: Magneto measurements," *Nature Photonics* **9**, 553-553 (2015).
17. C. Vicario, C. Ruchert, F. Ardana Lamas, P. M. Derlet, B. Tudu, J. Luning, and C. P. Hauri, "Off-resonant magnetization dynamics phase-locked to an intense phase-stable terahertz transient," *Nature Photonics* **7**, 720-723 (2013).

18. J. Ahn, D. Hutchinson, C. Rangan, and P. Bucksbaum, "Quantum phase retrieval of a Rydberg wave packet using a half-cycle pulse," *Physical Review Letters* **86**, 1179-1182 (2001).
19. T. Qi, Y.-H. Shin, K.-L. Yeh, K. A. Nelson, and A. M. Rappe, "Collective coherent control: synchronization of polarization in ferroelectric PbTiO<sub>3</sub> by shaped THz fields," *Physical Review Letters* **102**, 247603 (2009).
20. D. S. Rana, I. Kawayama, K. Mavani, K. Takahashi, H. Murakami, and M. Tonouchi, "Understanding the nature of ultrafast polarization dynamics of ferroelectric memory in the multiferroic BiFeO<sub>3</sub>," *Advanced Materials* **21**, 2881-2885 (2009).
21. K. Lee, B. Sussman, M. Sprague, P. Michelberger, K. Reim, J. Nunn, N. Langford, P. Bustard, D. Jaksch, and I. Walmsley, "Macroscopic non-classical states and terahertz quantum processing in room-temperature diamond," *Nature Photonics* **6**, 41-44 (2012).
22. J. A. Hutchby, G. I. Bourianoff, V. V. Zhirnov, and J. E. Brewer, "Extending the road beyond CMOS," *IEEE Circuits and Devices Magazine* **18**, 28-41 (2002).
23. X. Wang, M. Afzelius, N. Ohlsson, U. Gustafsson, and S. Kröll, "Coherent transient data-rate conversion and data transformation," *Optics Letters* **25**, 945-947 (2000).
24. L. Moeller, J. Federici, and K. Su, "2.5 Gbit/s duobinary signalling with narrow bandwidth 0.625 terahertz source," in *Electronics Letters*, (2011), pp. 856-858.
25. T. Kleine-Ostmann and T. Nagatsuma, "A review on terahertz communications research," *Journal of Infrared, Millimeter, and Terahertz Waves* **32**, 143-171 (2011).
26. J. M. Jornet and I. F. Akyildiz, "Joint energy harvesting and communication analysis for perpetual wireless nanosensor networks in the terahertz band," *Nanotechnology, IEEE Transactions on* **11**, 570-580 (2012).
27. T. Schneider, A. Wiatrek, S. Preußler, M. Grigat, and R.-P. Braun, "Link budget analysis for terahertz fixed wireless links," *Terahertz Science and Technology, IEEE Transactions on* **2**, 250-256 (2012).
28. M. D. Rotaru and J. K. Sykulski, "Improved sensitivity of terahertz label free bio-sensing application through trapped-mode resonances in planar resonators," *Magnetics, IEEE Transactions on* **47**, 1026-1029 (2011).
29. T. de Graauw, "THz Astronomy from Space," in *New Directions in Terahertz Technology* (Springer, 1997), pp. 237-244.
30. E. Klisch, T. Klaus, S. Belov, G. Winnewisser, and E. Herbst, "Laboratory rotational spectrum of CN in the 1 THz region," *Astronomy and Astrophysics* **304**, L5 (1995).
31. S. Withington, "Terahertz astronomical telescopes and instrumentation," *Philosophical Transactions of the Royal Society of London A: Mathematical, Physical and Engineering Sciences* **362**, 395-402 (2004).
32. B. J. Drouin, S. Yu, J. C. Pearson, and H. Gupta, "Terahertz spectroscopy for space applications: 2.5–2.7 THz spectra of HD, H<sub>2</sub>O and NH<sub>3</sub>," *Journal of molecular structure* **1006**, 2-12 (2011).
33. S. Nakajima, H. Hoshina, M. Yamashita, C. Otani, and N. Miyoshi, "Terahertz imaging diagnostics of cancer tissues with a chemometrics technique," *Applied Physics Letters* **90**, 41102 (2007).
34. Q. Wu, T. Hewitt, and X. C. Zhang, "Two-dimensional electro-optic imaging of THz beams," *Applied Physics Letters* **69**, 1026-1028 (1996).
35. S. Hunsche, M. Koch, I. Brener, and M. Nuss, "THz near-field imaging," *Optics Communications* **150**, 22-26 (1998).
36. Q. Chen, Z. Jiang, G. Xu, and X.-C. Zhang, "Near-field terahertz imaging with a dynamic aperture," *Optics Letters* **25**, 1122-1124 (2000).
37. P. Knobloch, C. Schildknecht, T. Kleine-Ostmann, M. Koch, S. Hoffmann, M. Hofmann, E. Rehberg, M. Sperling, K. Donhuijsen, and G. Hein, "Medical THz imaging: an

- investigation of histo-pathological samples," *Physics in Medicine and Biology* **47**, 3875-3884 (2002).
38. H.-T. Chen, R. Kersting, and G. C. Cho, "Terahertz imaging with nanometer resolution," *Applied Physics Letters* **83**, 3009-3011 (2003).
  39. J. F. Federici, B. Schulkin, F. Huang, D. Gary, R. Barat, F. Oliveira, and D. Zimdars, "THz imaging and sensing for security applications—explosives, weapons and drugs," *Semiconductor Science and Technology* **20**, S266 (2005).
  40. J. Chen, Y. Chen, H. Zhao, G. J. Bastiaans, and X.-C. Zhang, "Absorption coefficients of selected explosives and related compounds in the range of 0.1–2.8 THz," *Optics Express* **15**, 12060-12067 (2007).
  41. W. Fan, A. Burnett, P. Upadhyaya, J. Cunningham, E. Linfield, and A. Davies, "Far-infrared spectroscopic characterization of explosives for security applications using broadband terahertz time-domain spectroscopy," *Applied spectroscopy* **61**, 638-643 (2007).
  42. M. Tonouchi, "Cutting-edge terahertz technology," *Nature Photonics* **1**, 97-105 (2007).
  43. S. L. Dexheimer, ed., *Terahertz Spectroscopy Principles and Applications* (CRC Press, 2007).
  44. D. H. Auston, A. M. Glass, and P. LeFur, "Tunable far-infrared generation by difference frequency mixing of dye lasers in reduced (black) lithium niobate," *Applied Physics Letters* **23**, 47-48 (1973).
  45. D. H. Auston, "Picosecond optoelectronic switching and gating in silicon," *Applied Physics Letters* **26**, 101-103 (1975).
  46. P. LeFur and D. H. Auston, "A kilovolt picosecond optoelectronic switch and Pockel's cell," *Applied Physics Letters* **28**, 21-23 (1976).
  47. D. H. Auston, K. P. Cheung, and P. R. Smith, "Picosecond photoconducting Hertzian dipoles," *Applied Physics Letters* **45**, 284-286 (1984).
  48. P. R. Smith, D. H. Auston, and M. C. Nuss, "Subpicosecond photoconducting dipole antennas," *IEEE Journal of Quantum Electronics* **24**, 255-260 (1988).
  49. M. B. Ketchen, D. Grischkowsky, T. C. Chen, C. C. Chi, I. N. Duling, N. J. Halas, J. M. Halbout, J. A. Kash, and G. P. Li, "Generation of subpicosecond electrical pulses on coplanar transmission lines," *Applied Physics Letters* **48**, 751-753 (1986).
  50. D. Grischkowsky, "Optical pulse compression," *Applied Physics Letters* **25**, 566-568 (1974).
  51. H. Nakatsuka and D. Grischkowsky, "Recompression of optical pulses broadened by passage through optical fibers," *Optics Letters* **6**, 13-15 (1981).
  52. C. Fattering and D. Grischkowsky, "Terahertz beams," *Applied Physics Letters* **54**, 490-492 (1989).
  53. K. A. McIntosh, E. R. Brown, K. B. Nichols, O. B. McMahon, W. F. DiNatale, and T. M. Lyszczarz, "Terahertz photomixing with diode lasers in low-temperature-grown GaAs," *Applied Physics Letters* **67**, 3844-3846 (1995).
  54. S. Matsuura, M. Tani, and K. Sakai, "Generation of coherent terahertz radiation by photomixing in dipole photoconductive antennas," *Applied Physics Letters* **70**, 559-561 (1997).
  55. S. Kono, M. Tani, P. Gu, and K. Sakai, "Detection of up to 20 THz with a low-temperature-grown GaAs photoconductive antenna gated with 15 fs light pulses," *Applied Physics Letters* **77**, 4104-4106 (2000).
  56. M. Tani, K. Sakai, and H. Mimura, "Ultrafast Photoconductive Detectors Based on Semi-Insulating GaAs and InP," *Japanese Journal of Applied Physics* **36**, L1175 (1997).
  57. M. Tani, S. Matsuura, K. Sakai, and S.-i. Nakashima, "Emission characteristics of photoconductive antennas based on low-temperature-grown GaAs and semi-insulating GaAs," *Applied Optics* **36**, 7853-7859 (1997).

58. T.-A. Liu, M. Tani, M. Nakajima, M. Hangyo, K. Sakai, S.-i. Nakashima, and C.-L. Pan, "Ultrabroadband terahertz field detection by proton-bombarded InP photoconductive antennas," *Optics Express* **12**, 2954-2959 (2004).
59. B. Salem, D. Morris, V. Aimez, J. Beerens, J. Beauvais, and D. Houde, "Pulsed photoconductive antenna terahertz sources made on ion-implanted GaAs substrates," *Journal of Physics: Condensed Matter* **17**, 7327-7333 (2005).
60. A. Dreyhaupt, S. Winnerl, T. Dekorsy, and M. Helm, "High-intensity terahertz radiation from a microstructured large-area photoconductor," *Applied Physics Letters* **86**, 121114 (2005).
61. P. C. Upadhyaya, W. Fan, A. Burnett, J. Cunningham, A. G. Davies, E. H. Linfield, J. Lloyd-Hughes, E. Castro-Camus, M. B. Johnston, and H. Beere, "Excitation-density-dependent generation of broadband terahertz radiation in an asymmetrically excited photoconductive antenna," *Optics Letters* **32**, 2297-2299 (2007).
62. F. Miyamaru, Y. Saito, K. Yamamoto, T. Furuya, S. Nishizawa, and M. Tani, "Dependence of emission of terahertz radiation on geometrical parameters of dipole photoconductive antennas," *Applied Physics Letters* **96**, 211104 (2010).
63. S.-G. Park, Y. Choi, Y.-J. Oh, and K.-H. Jeong, "Terahertz photoconductive antenna with metal nanoislands," *Optics Express* **20**, 25530-25535 (2012).
64. L. Hou and W. Shi, "An LT-GaAs Terahertz Photoconductive Antenna With High Emission Power, Low Noise, and Good Stability," *IEEE Transactions on Electron Devices* **60**, 1619-1624 (2013).
65. X. Ropagnol, F. Blanchard, T. Ozaki, and M. Reid, "Intense terahertz generation at low frequencies using an interdigitated ZnSe large aperture photoconductive antenna," *Applied Physics Letters* **103**, 161108 (2013).
66. S. Gupta, J. F. Whitaker, and G. A. Mourou, "Ultrafast carrier dynamics in III-V semiconductors grown by molecular-beam epitaxy at very low substrate temperatures," *IEEE Journal of Quantum Electronics* **28**, 2464-2472 (1992).
67. N. Sekine, K. Hirakawa, F. Sogawa, Y. Arakawa, N. Usami, Y. Shiraki, and T. Katoda, "Ultrashort lifetime photocarriers in Ge thin films," *Applied Physics Letters* **68**, 3419-3421 (1996).
68. H. Erlig, S. Wang, T. Azfar, A. Udupa, H. R. Fetterman, and D. C. Streit, "LT-GaAs detector with 451 fs response at 1.55  $\mu\text{m}$  via two-photon absorption," *Electronics Letters* **35**, 173-174 (1999).
69. M. Tani, K.-S. Lee, and X.-C. Zhang, "Detection of terahertz radiation with low-temperature-grown GaAs-based photoconductive antenna using 1.55  $\mu\text{m}$  probe," *Applied Physics Letters* **77**, 1396-1398 (2000).
70. M. Suzuki and M. Tonouchi, "Fe-implanted InGaAs photoconductive terahertz detectors triggered by 1.56  $\mu\text{m}$  femtosecond optical pulses," *Applied Physics Letters* **86**, 163504 (2005).
71. H. Roehle, R. J. B. Dietz, H. J. Hensel, J. Böttcher, H. Künzel, D. Stanze, M. Schell, and B. Sartorius, "Next generation 1.5  $\mu\text{m}$  terahertz antennas: mesa-structuring of InGaAs/InAlAs photoconductive layers," *Optics Express* **18**, 2296-2301 (2010).
72. B. Sartorius, H. Roehle, H. Künzel, J. Böttcher, M. Schlak, D. Stanze, H. Venghaus, and M. Schell, "All-fiber terahertz time-domain spectrometer operating at 1.5  $\mu\text{m}$  telecom wavelengths," *Optics Express* **16**, 9565-9570 (2008).
73. C. Baker, I. S. Gregory, M. J. Evans, W. R. Tribe, E. H. Linfield, and M. Missous, "All-optoelectronic terahertz system using low-temperature-grown InGaAs photomixers," *Optics Express* **13**, 9639-9644 (2005).

74. J.-M. Ramer, F. Ospald, G. von Freymann, and R. Beigang, "Generation and detection of terahertz radiation up to 4.5 THz by low-temperature grown GaAs photoconductive antennas excited at 1560 nm," *Applied Physics Letters* **103**, 021119 (2013).
75. D. Griffiths, *Introduction to Electrodynamics (3rd Edition)* (Benjamin Cummings, 1998).
76. J. D. Jackson, *Classical Electrodynamics, 3rd Edition* (Wiley, 1998).
77. M. Dressel and G. Gruner, *Electrodynamics of Solids* (Cambridge University Press, 2002).
78. S. Sirbu, "Induced Excitations In Some Metal Oxides," (Ph. D. Thesis, Rijksuniversiteit Groningen, 2008).
79. D. Turchinovich, "Study of ultrafast polarization and carrier dynamics in semiconductor nanostructures: a THz spectroscopy approach," (Ph. D. Thesis, University of Freiburg, 2004).
80. J. T. Darrow, X. C. Zhang, D. H. Auston, and J. D. Morse, "Saturation properties of large-aperture photoconducting antennas," *IEEE Journal of Quantum Electronics* **28**, 1607-1616 (1992).
81. Y. R. Shen, *The Principles of Nonlinear Optics* (Wiley, 2002).
82. A. J. Taylor, P. K. Benicewicz, and S. M. Young, "Modeling of femtosecond electromagnetic pulses from large-aperture photoconductors," *Optics Letters* **18**, 1340-1342 (1993).
83. P. Parkinson, J. Lloyd-Hughes, Q. Gao, H. H. Tan, C. Jagadish, M. B. Johnston, and L. M. Herz, "Transient Terahertz Conductivity of GaAs Nanowires," *Nano Letters* **7**, 2162-2165 (2007).
84. E. Hendry, M. Koeberg, B. O'Regan, and M. Bonn, "Local Field Effects on Electron Transport in Nanostructured TiO<sub>2</sub> Revealed by Terahertz Spectroscopy," *Nano Letters* **6**, 755-759 (2006).
85. P. A. George, J. Strait, J. Dawlaty, S. Shivaraman, M. Chandrashekar, F. Rana, and M. G. Spencer, "Ultrafast optical-pump terahertz-probe spectroscopy of the carrier relaxation and recombination dynamics in epitaxial graphene," *Nano Letters* **8**, 4248-4251 (2008).
86. M. C. Hoffmann, J. Hebling, H. Y. Hwang, K.-L. Yeh, and K. A. Nelson, "THz-pump/THz-probe spectroscopy of semiconductors at high field strengths [Invited]," *Journal of the Optical Society of America B* **26**, A29-A34 (2009).
87. J. Hebling, M. C. Hoffmann, H. Y. Hwang, K.-L. Yeh, and K. A. Nelson, "Observation of nonequilibrium carrier distribution in Ge, Si, and GaAs by terahertz pump-terahertz probe measurements," *Physical Review B* **81**, 035201 (2010).
88. R. Ulbricht, E. Hendry, J. Shan, T. F. Heinz, and M. Bonn, "Carrier dynamics in semiconductors studied with time-resolved terahertz spectroscopy," *Reviews of Modern Physics* **83**, 543 (2011).
89. J. Shah, *Ultrafast spectroscopy of semiconductors and semiconductor nanostructures* (Springer Science & Business Media, 2013), Vol. 115.
90. J. J. Hannah, J. D. Callum, G. Qiang, H. H. Tan, J. Chennupati, L.-H. James, M. H. Laura, and B. J. Michael, "Electronic properties of GaAs, InAs and InP nanowires studied by terahertz spectroscopy," *Nanotechnology* **24**, 214006 (2013).
91. V. Ryzhii, M. Ryzhii, and T. Otsuji, "Negative dynamic conductivity of graphene with optical pumping," *Journal of Applied Physics* **101**, 083114 (2007).
92. J. T. Hong, K. M. Lee, B. H. Son, S. J. Park, D. J. Park, J.-Y. Park, S. Lee, and Y. H. Ahn, "Terahertz conductivity of reduced graphene oxide films," *Optics Express* **21**, 7633-7640 (2013).
93. M. Tamagnone, J. S. G3mez-D3az, J. R. Mosig, and J. Perruisseau-Carrier, "Reconfigurable terahertz plasmonic antenna concept using a graphene stack," *Applied Physics Letters* **101**, 214102 (2012).

94. A. Vakil and N. Engheta, "Transformation optics using graphene," *Science* **332**, 1291-1294 (2011).
95. J. Horng, C.-F. Chen, B. Geng, C. Girit, Y. Zhang, Z. Hao, H. A. Bechtel, M. Martin, A. Zettl, M. F. Crommie, Y. R. Shen, and F. Wang, "Drude conductivity of Dirac fermions in graphene," *Physical Review B* **83**, 165113 (2011).
96. G. Jnawali, Y. Rao, H. Yan, and T. F. Heinz, "Observation of a Transient Decrease in Terahertz Conductivity of Single-Layer Graphene Induced by Ultrafast Optical Excitation," *Nano Letters* **13**, 524-530 (2013).
97. F. Bonaccorso, Z. Sun, T. Hasan, and A. Ferrari, "Graphene photonics and optoelectronics," *Nature Photonics* **4**, 611-622 (2010).
98. L. Ju, B. Geng, J. Horng, C. Girit, M. Martin, Z. Hao, H. A. Bechtel, X. Liang, A. Zettl, Y. R. Shen, and F. Wang, "Graphene plasmonics for tunable terahertz metamaterials," *Nature Nanotechnology* **6**, 630-634 (2011).
99. L. Vicarelli, M. S. Vitiello, D. Coquillat, A. Lombardo, A. C. Ferrari, W. Knap, M. Polini, V. Pellegrini, and A. Tredicucci, "Graphene field-effect transistors as room-temperature terahertz detectors," *Nature Materials* **11**, 865-871 (2012).
100. S. H. Lee, M. Choi, T.-T. Kim, S. Lee, M. Liu, X. Yin, H. K. Choi, S. S. Lee, C.-G. Choi, S.-Y. Choi, X. Zhang, and B. Min, "Switching terahertz waves with gate-controlled active graphene metamaterials," *Nature Materials* **11**, 936-941 (2012).
101. H. Y. Hwang, N. C. Brandt, H. Farhat, A. L. Hsu, J. Kong, and K. A. Nelson, "Nonlinear THz Conductivity Dynamics in P-Type CVD-Grown Graphene," *The Journal of Physical Chemistry B* **117**, 15819-15824 (2013).
102. F. Xia, T. Mueller, Y.-m. Lin, A. Valdes-Garcia, and P. Avouris, "Ultrafast graphene photodetector," *Nature Nanotechnology* **4**, 839-843 (2009).
103. I. Maeng, S. Lim, S. J. Chae, Y. H. Lee, H. Choi, and J.-H. Son, "Gate-Controlled Nonlinear Conductivity of Dirac Fermion in Graphene Field-Effect Transistors Measured by Terahertz Time-Domain Spectroscopy," *Nano Letters* **12**, 551-555 (2012).
104. S. Chih-Chiang, H. Yu-Te, L. Lain-Jong, and L. Hsiang-Lin, "Charge Dynamics and Electronic Structures of Monolayer MoS<sub>2</sub> Films Grown by Chemical Vapor Deposition," *Applied Physics Express* **6**, 125801 (2013).
105. C. J. Docherty, P. Parkinson, H. J. Joyce, M.-H. Chiu, C.-H. Chen, M.-Y. Lee, L.-J. Li, L. M. Herz, and M. B. Johnston, "Ultrafast transient terahertz conductivity of monolayer MoS<sub>2</sub> and WSe<sub>2</sub> grown by chemical vapor deposition," *ACS nano* **8**, 11147-11153 (2014).
106. C. H. Lui, A. J. Frenzel, D. V. Pilon, Y. H. Lee, X. Ling, G. M. Akselrod, J. Kong, and N. Gedik, "Trion-Induced Negative Photoconductivity in Monolayer MoS<sub>2</sub>," *Physical Review Letters* **113**, 166801 (2014).
107. S. Kar, Y. Su, R. Nair, and A. Sood, "Probing Photoexcited Carriers in a Few-Layer MoS<sub>2</sub> Laminate by Time-Resolved Optical Pump-Terahertz Probe Spectroscopy," *ACS nano* **9**, 12004 (2015).
108. B. D. Kong, Z. Jin, and K. W. Kim, "Hot-Electron Transistors for Terahertz Operation Based on Two-Dimensional Crystal Heterostructures," *Physical Review Applied* **2**, 054006 (2014).
109. Y. Cao, S. Gan, Z. Geng, J. Liu, Y. Yang, Q. Bao, and H. Chen, "Optically tuned terahertz modulator based on annealed multilayer MoS<sub>2</sub>," *Scientific reports* **6**, 22899 (2016).
110. H. S. Lee, S. S. Baik, S.-W. Min, P. J. Jeon, J. S. Kim, K. Choi, S. Ryu, H. J. Choi, J. H. Kim, and S. Im, "Extremely high mobility over 5000 cm<sup>2</sup>/Vs obtained from MoS<sub>2</sub> nanosheet transistor with NiO<sub>x</sub> Schottky gate," *arXiv preprint arXiv:1406.6779* (2014).
111. L. Duvillaret, F. Garet, and J.-L. Coutaz, "Highly precise determination of optical constants and sample thickness in terahertz time-domain spectroscopy," *Applied Optics* **38**, 409-415 (1999).

112. T. D. Dorney, R. G. Baraniuk, and D. M. Mittleman, "Material parameter estimation with terahertz time-domain spectroscopy," *Journal of the Optical Society of America A* **18**, 1562-1571 (2001).
113. I. Pupeza, R. Wilk, and M. Koch, "Highly accurate optical material parameter determination with THz time-domain spectroscopy," *Optics Express* **15**, 4335-4350 (2007).
114. M. Scheller, C. Jansen, and M. Koch, "Analyzing sub-100- $\mu\text{m}$  samples with transmission terahertz time domain spectroscopy," *Optics Communications* **282**, 1304-1306 (2009).
115. P. U. Jepsen and B. M. Fischer, "Dynamic range in terahertz time-domain transmission and reflection spectroscopy," *Optics Letters* **30**, 29-31 (2005).
116. J. A. Nelder and R. Mead, "A Simplex Method for Function Minimization," *The Computer Journal* **7**, 308-313 (1965).
117. M. A. Belkin, F. Capasso, A. Belyanin, D. L. Sivco, A. Y. Cho, D. C. Oakley, C. J. Vineis, and G. W. Turner, "Terahertz quantum-cascade laser source based on intracavity difference-frequency generation," *Nature Photonics* **1**, 288 (2007).
118. J. F. O'Hara, J. M. O. Zide, A. C. Gossard, A. J. Taylor, and R. D. Averitt, "Enhanced terahertz detection via ErAs:GaAs nanoisland superlattices," *Applied Physics Letters* **88**, 251119 (2006).
119. G. P. Williams, "Filling the THz gap-high power sources and applications," *Reports on Progress in Physics* **69**, 301-326 (2006).
120. C. Kulesa, "Terahertz Spectroscopy for Astronomy: From Comets to Cosmology," *IEEE Transactions on Terahertz Science and Technology* **1**, 232-240 (2011).
121. M. C. Beard, G. M. Turner, and C. A. Schmittenmaer, "Terahertz Spectroscopy," *Journal of Physical Chemistry B* **106**, 7146-7159 (2002).
122. B. B. Hu and M. C. Nuss, "Imaging with terahertz waves," *Optics Letters* **16**, 1716-1718 (1995).
123. D. F. Plusquellic, K. Siegrist, E. J. Heilweil, and O. Esenturk, "Applications of Terahertz Spectroscopy in Biosystems," *ChemPhysChem* **8**, 2412-2431 (2007).
124. T. K. Ostmann and T. Nagatsuma, "A Review on Terahertz Communications Research," *Journal of Infrared, Millimeter, and Terahertz Waves* **32**, 143-171 (2011).
125. D. Qu, D. Grischkowsky, and W. Zhang, "Terahertz transmission properties of thin, subwavelength metallic hole arrays," *Optics Letters* **29**, 896-898 (2004).
126. V. Juve, A. Crut, P. Maioli, M. Pellarin, M. Broyer, N. Del Fatti, and F. Valle, "Probing Elasticity at the Nanoscale: Terahertz Acoustic Vibration of Small Metal Nanoparticles," *Nano Letters* **10**, 1853-1858 (2010).
127. T. Nagashima and M. Hangyo, "Measurement of complex optical constants of a highly doped Si wafer using terahertz ellipsometry," *Applied Physics Letters* **79**, 3917-3919 (2001).
128. T. Hofmann, C. M. Herzinger, A. Boosalis, T. E. Tiwald, J. A. Woollam, and M. Schubert, "Variable-wavelength frequency-domain terahertz ellipsometry," *Review of Scientific Instruments* **81**, 023101 (2010).
129. M. Neshat and N. P. Armitage, "Terahertz time-domain spectroscopic ellipsometry: instrumentation and calibration," *Optics Express* **20**, 29063-29075 (2012).
130. T. Hofmann, C. M. Herzinger, J. L. Tedesco, D. K. Gaskill, J. A. Woollam, and M. Schubert, "Terahertz ellipsometry and terahertz optical-Hall effect," *Thin Solid Films* **519**, 2593-2600 (2011).
131. H. Zhe, P. Hongkyu, E. P. J. Parrott, C. Hau Ping, and E. Pickwell-MacPherson, "Robust Thin-Film Wire-Grid THz Polarizer Fabricated Via a Low-Cost Approach," *IEEE Photonics Technology Letters* **25**, 81-84 (2013).

132. L. Sun, Z.-H. Lv, W. Wu, W.-T. Liu, and J.-M. Yuan, "Double-grating polarizer for terahertz radiation with high extinction ratio," *Applied Optics* **49**, 2066-2071 (2010).
133. L. Y. Deng, J. H. Teng, L. Zhang, Q. Y. Wu, H. Liu, X. H. Zhang, and S. J. Chua, "Extremely high extinction ratio terahertz broadband polarizer using bilayer subwavelength metal wire-grid structure," *Applied Physics Letters* **101**, 011101 (2012).
134. K. Shiraishi, S. Oyama, and C. S. Tsai, "A Polarizer Using Thin Metallic-Film Subwavelength Grating for Infrared to Terahertz Region," *Journal of Lightwave Technology* **29**, 670-676 (2011).
135. J. S. Cetnar, J. R. Middendorf, and E. R. Brown, "Extraordinary optical transmission and extinction in a Terahertz wire-grid polarizer," *Applied Physics Letters* **100**, 231912 (2012).
136. C. Berry and M. Jarrahi, "Broadband Terahertz Polarizing Beam Splitter on a Polymer Substrate," *Journal of Infrared, Millimeter, and Terahertz Waves* **33**, 127-130 (2012).
137. A. Das, T. M. Schutzius, C. M. Megaridis, S. Subhechha, T. Wang, and L. Liu, "Quasi-optical terahertz polarizers enabled by inkjet printing of carbon nanocomposites," *Applied Physics Letters* **101**, 243108 (2012).
138. N. K. Grady, J. E. Heyes, D. R. Chowdhury, Y. Zeng, M. T. Reiten, A. K. Azad, A. J. Taylor, D. A. R. Dalvit, and H.-T. Chen, "Terahertz Metamaterials for Linear Polarization Conversion and Anomalous Refraction," *Science* **340**, 1304-1307 (2013).
139. Z. Huang, E. P. J. Parrott, H. Park, H. P. Chan, and E. Pickwell-MacPherson, "High extinction ratio and low transmission loss thin-film terahertz polarizer with a tunable bilayer metal wire-grid structure," *Optics Letters* **39**, 793-796 (2014).
140. T.-I. Jeon, K.-J. Kim, C. Kang, I. H. Maeng, J.-H. Son, K. H. An, J. Y. Lee, and Y. H. Lee, "Optical and electrical properties of preferentially anisotropic single-walled carbon-nanotube films in terahertz region," *Journal of Applied Physics* **95**, 5736-5740 (2004).
141. D. Fragouli, A. Das, C. Innocenti, Y. Guttikonda, S. Rahman, L. Liu, V. Caramia, C. M. Megaridis, and A. Athanassiou, "Polymeric films with electric and magnetic anisotropy due to magnetically assembled functional nanofibers," *ACS Applied Materials & Interfaces* **6**, 4535-4541 (2014).
142. Y. Hirota, R. Hattori, M. Tani, and M. Hangyo, "Polarization modulation of terahertz electromagnetic radiation by four-contact photoconductive antenna," *Optics Express* **14**, 4486-4493 (2006).
143. C.-F. Hsieh, Y.-C. Lai, R.-P. Pan, and C.-L. Pan, "Polarizing terahertz waves with nematic liquid crystals," *Optics Letters* **33**, 1174-1176 (2008).
144. A. Wojdyla and G. Gallot, "Brewster's angle silicon wafer terahertz linear polarizer," *Optics Express* **19**, 14099-14107 (2011).
145. B. Scherger, M. Scheller, N. Vieweg, S. T. Cundiff, and M. Koch, "Paper terahertz wave plates," *Optics Express* **19**, 24884-24889 (2011).
146. L. Cong, W. Cao, X. Zhang, Z. Tian, J. Gu, R. Singh, J. Han, and W. Zhang, "A perfect metamaterial polarization rotator," *Applied Physics Letters* **103**, 171107 (2013).
147. F. Liu, S. Wang, M. Zhang, M. Ma, C. Wang, and J. Li, "Improvement of mechanical robustness of the superhydrophobic wood surface by coating PVA/SiO<sub>2</sub> composite polymer," *Applied Surface Science* **280**, 686-692 (2013).
148. S. Ensslin, K. P. Moll, T. Haefele-Racin, and K. Mäder, "Safety and Robustness of Coated Pellets: Self-Healing Film Properties and Storage Stability," *Pharmaceutical Research* **26**, 1534-1543 (2009).
149. J. J. Wang, F. Walters, X. Liu, P. Sciortino, and X. Deng, "High-performance, large area, deep ultraviolet to infrared polarizers based on 40 nm line/78 nm space nanowire grids," *Applied Physics Letters* **90**, 061104 (2007).
150. A. Rodger, "Linear Dichroism Spectroscopy: Theory," in *Encyclopedia of Biophysics*, G. C. K. Roberts, ed. (Springer Berlin Heidelberg, Berlin, Heidelberg, 2013), pp. 1244-1248.

151. M. Kargarian, M. Randeria, and N. Trivedi, "Theory of Kerr and Faraday rotations and linear dichroism in Topological Weyl Semimetals," *Scientific reports* **5**, 12683 (2015).
152. A. Rodger and B. Norden, *Circular Dichroism and Linear Dichroism* (Oxford University Press, Oxford, 1997).
153. D. D. L. Chung, "Electromagnetic interference shielding effectiveness of carbon materials," *Carbon* **39**, 279-285 (2001).
154. N. Li, Y. Huang, F. Du, X. He, X. Lin, H. Gao, Y. Ma, F. Li, Y. Chen, and P. C. Eklund, "Electromagnetic Interference (EMI) Shielding of Single-Walled Carbon Nanotube Epoxy Composites," *Nano Letters* **6**, 1141-1145 (2006).
155. M. H. Al-Saleh and U. Sundararaj, "Electromagnetic interference shielding mechanisms of CNT/polymer composites," *Carbon* **47**, 1738-1746 (2009).
156. Z. Liu, G. Bai, Y. Huang, Y. Ma, F. Du, F. Li, T. Guo, and Y. Chen, "Reflection and absorption contributions to the electromagnetic interference shielding of single-walled carbon nanotube/polyurethane composites," *Carbon* **45**, 821-827 (2007).
157. P. Saini, V. Choudhary, B. P. Singh, R. B. Mathur, and S. K. Dhawan, "Polyaniline–MWCNT nanocomposites for microwave absorption and EMI shielding," *Materials Chemistry and Physics* **113**, 919-926 (2009).
158. Y. Yang, M. C. Gupta, K. L. Dudley, and R. W. Lawrence, "Novel Carbon Nanotube–Polystyrene Foam Composites for Electromagnetic Interference Shielding," *Nano Letters* **5**, 2131-2134 (2005).
159. A. Das, C. M. Megaridis, L. Liu, T. Wang, and A. Biswas, "Design and synthesis of superhydrophobic carbon nanofiber composite coatings for terahertz frequency shielding and attenuation," *Applied Physics Letters* **98**, 174101 (2011).
160. D. Polley, A. Barh, A. Barman, and R. K. Mitra, "Nickel nanochain composite: An improved terahertz shielding material," in *2015 IEEE Applied Electromagnetics Conference (AEMC)*, 2015), 1-2.
161. D. Polley, A. Barman, and R. K. Mitra, "EMI shielding and conductivity of carbon nanotube-polymer composites at terahertz frequency," *Optics Letters* **39**, 1541-1544 (2014).
162. J. A. Berres and G. W. Hanson, "Multiwall Carbon Nanotubes at RF-THz Frequencies: Scattering, Shielding, Effective Conductivity, and Power Dissipation," *Antennas and Propagation, IEEE Transactions on* **59**, 3098-3103 (2011).
163. J. Macutkevic, R. Adomavicius, A. Krotkus, D. Seliuta, G. Valusis, S. Maksimenko, P. Kuzhir, K. Batrakov, V. Kuznetsov, S. Moseenkov, O. Shenderova, A. V. Okotrub, R. Langlet, and P. Lambin, "Terahertz probing of onion-like carbon-PMMA composite films," *Diamond and Related Materials* **17**, 1608-1612 (2008).
164. R. B. Schulz, V. C. Plantz, and D. R. Brush, "Shielding theory and practice," *IEEE Transactions on Electromagnetic Compatibility* **30**, 187-201 (1988).
165. J. Joo and A. J. Epstein, "Electromagnetic radiation shielding by intrinsically conducting polymers," *Applied Physics Letters* **65**, 2278-2280 (1994).
166. J. B. Baxter and C. A. Schmuttenmaer, "Conductivity of ZnO Nanowires, Nanoparticles, and Thin Films Using Time-Resolved Terahertz Spectroscopy," *The Journal of Physical Chemistry B* **110**, 25229-25239 (2006).
167. M. Walther, D. G. Cooke, C. Sherstan, M. Hajar, M. R. Freeman, and F. A. Hegmann, "Terahertz conductivity of thin gold films at the metal-insulator percolation transition," *Physical Review B* **76**, 125408 (2007).
168. N. Laman and D. Grischkowsky, "Terahertz conductivity of thin metal films," *Applied Physics Letters* **93**, 051105 (2008).
169. J. Lloyd-Hughes and T.-I. Jeon, "A Review of the Terahertz Conductivity of Bulk and Nano-Materials," *Journal of Infrared, Millimeter, and Terahertz Waves* **33**, 871-925 (2012).

170. H. Němec, P. Kužel, and V. Sundström, "Charge transport in nanostructured materials for solar energy conversion studied by time-resolved terahertz spectroscopy," *Journal of Photochemistry and Photobiology A: Chemistry* **215**, 123-139 (2010).
171. M. C. Beard, G. M. Turner, and C. A. Schmuttenmaer, "Size-Dependent Photoconductivity in CdSe Nanoparticles as Measured by Time-Resolved Terahertz Spectroscopy," *Nano Letters* **2**, 983-987 (2002).
172. I. Maeng, C. Kang, S. J. Oh, J.-H. Son, K. H. An, and Y. H. Lee, "Terahertz electrical and optical characteristics of double-walled carbon nanotubes and their comparison with single-walled carbon nanotubes," *Applied Physics Letters* **90**, 051914 (2007).
173. E. P. J. Parrott, J. A. Zeitler, J. McGregor, S.-P. Oei, H. E. Unalan, W. I. Milne, J.-P. Tessonier, D. S. Su, R. Schlögl, and L. F. Gladden, "The Use of Terahertz Spectroscopy as a Sensitive Probe in Discriminating the Electronic Properties of Structurally Similar Multi-Walled Carbon Nanotubes," *Advanced Materials* **21**, 3953-3957 (2009).
174. L. Min, Z. Wu, C. Liwei, S. Li, P. Ajayan, and X. Hao, "Terahertz Characterization of Single-Walled Carbon Nanotube and Graphene On-Substrate Thin Films," *IEEE Transaction on Microwave Theory and Techniques* **59**, 2719-2725 (2011).
175. C. Kang, I. H. Maeng, S. J. Oh, S. C. Lim, K. H. An, Y. H. Lee, and J.-H. Son, "Terahertz optical and electrical properties of hydrogen-functionalized carbon nanotubes," *Physical Review B* **75**, 085410 (2007).
176. D. J. P. Jung Taek Hong, Jin Young Moon, Soo Bong Choi, Jae Ku Park, and J.-Y. P. Farbian Rotermund, Soonil Lee, and Yeong Hwan Ahn, "Terahertz Wave Applications of Single-Walled Carbon Nanotube Films with High Shielding Effectiveness," *Applied Physics Express* **5**, 015102 (2012).
177. Y.-J. Chiang, C.-S. Yang, Y.-H. Yang, C.-L. Pan, and T.-J. Yen, "An ultrabroad terahertz bandpass filter based on multiple-resonance excitation of a composite metamaterial," *Applied Physics Letters* **99**, 191909 (2011).
178. M. E. MacDonald, A. Alexanian, R. A. York, Z. Popovic, and E. N. Grossman, "Spectral transmittance of lossy printed resonant-grid terahertz bandpass filters," *IEEE Transactions on Microwave Theory and Techniques* **48**, 712-718 (2000).
179. S. Iijima, "Helical microtubules of graphitic carbon," *Nature* **354**, 56-58 (1991).
180. S. Iijima and T. Ichihashi, "Single-shell carbon nanotubes of 1-nm diameter," *Nature* **363**, 603-605 (1993).
181. B. E. Kilbride, J. N. Coleman, J. Fraysse, P. Fournet, M. Cadek, A. Drury, S. Hutzler, S. Roth, and W. J. Blau, "Experimental observation of scaling laws for alternating current and direct current conductivity in polymer-carbon nanotube composite thin films," *Journal of Applied Physics* **92**, 4024-4030 (2002).
182. G. Chakraborty, K. Gupta, A. K. Meikap, R. Babu, and W. J. Blau, "Anomalous electrical transport properties of polyvinyl alcohol-multiwall carbon nanotubes composites below room temperature," *Journal of Applied Physics* **109**, 033707 (2011).
183. S. Barrau, P. Demont, A. Peigney, C. Laurent, and C. Lacabanne, "DC and AC Conductivity of Carbon Nanotubes-Polyepoxy Composites," *Macromolecules* **36**, 5187-5194 (2003).
184. K. Shehzad, Z.-M. Dang, M. N. Ahmad, R. U. R. Sagar, S. Butt, M. U. Farooq, and T.-B. Wang, "Effects of carbon nanotubes aspect ratio on the qualitative and quantitative aspects of frequency response of electrical conductivity and dielectric permittivity in the carbon nanotube/polymer composites," *Carbon* **54**, 105-112 (2013).
185. J. C. Dyre and T. B. Schröder, "Universality of ac conduction in disordered solids," *Reviews of Modern Physics* **72**, 873-892 (2000).
186. G. B. Jung, Y. Myung, Y. J. Cho, Y. J. Sohn, D. M. Jang, H. S. Kim, C.-W. Lee, J. Park, I. Maeng, J.-H. Son, and C. Kang, "Terahertz Spectroscopy of Nanocrystal-Carbon

- Nanotube and –Graphene Oxide Hybrid Nanostructures," *The Journal of Physical Chemistry C* **114**, 11258-11265 (2010).
187. D. Polley, A. Barman, and R. K. Mitra, "Controllable terahertz conductivity in single walled carbon nanotube/polymer composites," *Journal of Applied Physics* **117**, 023115 (2015).
  188. D. Polley, A. Patra, A. Barman, and R. K. Mitra, "Modulating conductivity of Au/CNT composites in THz frequency range: A THz resistor," in *2014 39th International Conference on Infrared, Millimeter, and Terahertz waves (IRMMW-THz)*, 2014), 1-2.
  189. N. Akima, Y. Iwasa, S. Brown, A. M. Barbour, J. Cao, J. L. Musfeldt, H. Matsui, N. Toyota, M. Shiraishi, H. Shimoda, and O. Zhou, "Strong Anisotropy in the Far-Infrared Absorption Spectra of Stretch-Aligned Single-Walled Carbon Nanotubes," *Advanced Materials* **18**, 1166-1169 (2006).
  190. Q. Zhang, E. H. Hároz, Z. Jin, L. Ren, X. Wang, R. S. Arvidson, A. Lüttge, and J. Kono, "Plasmonic Nature of the Terahertz Conductivity Peak in Single-Wall Carbon Nanotubes," *Nano Letters* **13**, 5991-5996 (2013).
  191. Á. Pekker and K. Kamarás, "Wide-range optical studies on various single-walled carbon nanotubes: Origin of the low-energy gap," *Physical Review B* **84**, 075475 (2011).
  192. M. V. Shuba, A. G. Paddubskaya, A. O. Plyushch, P. P. Kuzhir, G. Y. Slepyan, S. A. Maksimenko, V. K. Ksenevich, P. Buka, D. Seliuta, I. Kasalynas, J. Macutkevicius, G. Valusis, C. Thomsen, and A. Lakhtakia, "Experimental evidence of localized plasmon resonance in composite materials containing single-wall carbon nanotubes," *Physical Review B* **85**, 165435 (2012).
  193. C. Cramer and M. Buscher, "Complete conductivity spectra of fast ion conducting silver iodide/silver selenate glasses," *Solid State Ionics* **105**, 109-120 (1998).
  194. A. Kahouli, A. Sylvestre, F. Jomni, B. Yangui, and J. Legrand, "Experimental and Theoretical Study of AC Electrical Conduction Mechanisms of Semicrystalline Parylene C Thin Films," *The Journal of Physical Chemistry A* **116**, 1051-1058 (2012).
  195. F. M. Calum and B. Mark, "High electrical conductance enhancement in Au-nanoparticle decorated sparse single-wall carbon nanotube networks," *Nanotechnology* **24**, 305202 (2013).
  196. C. Subramaniam, T. Yamada, K. Kobashi, A. Sekiguchi, D. N. Futaba, M. Yumura, and K. Hata, "One hundred fold increase in current carrying capacity in a carbon nanotube-copper composite," *Nature Communications* **4**, 1-7 (2013).
  197. D. Polley, A. Patra, and R. K. Mitra, "Dielectric relaxation of the extended hydration sheath of DNA in the THz frequency region," *Chemical Physics Letters* **586**, 143-147 (2013).
  198. Y. Shi, R. Yang, and P. K. Yuet, "Easy decoration of carbon nanotubes with well dispersed gold nanoparticles and the use of the material as an electrocatalyst," *Carbon* **47**, 1146-1151 (2009).
  199. S. Eustis and M. A. El-Sayed, "Why gold nanoparticles are more precious than pretty gold: Noble metal surface plasmon resonance and its enhancement of the radiative and nonradiative properties of nanocrystals of different shapes," *Chemical Society Reviews* **35**, 209-217 (2006).
  200. S. K. Ghosh and T. Pal, "Interparticle Coupling Effect on the Surface Plasmon Resonance of Gold Nanoparticles: From Theory to Applications," *Chemical Reviews* **107**, 4797-4862 (2007).
  201. Y. Hu, J. Xiang, G. Liang, H. Yan, and C. M. Lieber, "Sub-100 Nanometer Channel Length Ge/Si Nanowire Transistors with Potential for 2 THz Switching Speed," *Nano Letters* **8**, 925-930 (2008).
  202. W. R. Deal, X. B. Mei, V. Radisic, K. Leong, S. Sarkozy, B. Gorospe, J. Lee, P. H. Liu, W. Yoshida, J. Zhou, M. Lange, J. Uyeda, and R. Lai, "Demonstration of a 0.48 THz Amplifier

- Module Using InP HEMT Transistors," *IEEE Microwave and Wireless Components Letters* **20**, 289-291 (2010).
203. J.-M. Thomassin, X. Lou, C. Pagnouille, A. Saïb, L. Bednarz, I. Huynen, R. Jérôme, and C. Detrembleur, "Multiwalled Carbon Nanotube/Poly( $\epsilon$ -caprolactone) Nanocomposites with Exceptional Electromagnetic Interference Shielding Properties," *The Journal of Physical Chemistry C* **111**, 11186-11192 (2007).
  204. T. Kampfrath, K. von Volkmann, C. M. Aguirre, P. Desjardins, R. Martel, M. Krenz, C. Frischkorn, M. Wolf, and L. Perfetti, "Mechanism of the Far-Infrared Absorption of Carbon-Nanotube Films," *Physical Review Letters* **101**, 267403 (2008).
  205. T.-I. Jeon, K.-J. Kim, C. Kang, S.-J. Oh, J.-H. Son, K. H. An, D. J. Bae, and Y. H. Lee, "Terahertz conductivity of anisotropic single walled carbon nanotube films," *Applied Physics Letters* **80**, 3403-3405 (2002).
  206. J. Han, Z. Zhu, Z. Wang, W. Zhang, L. Yu, L. Sun, T. Wang, F. He, and Y. Liao, "The conductivity of single walled nanotube films in Terahertz region," *Physics Letters A* **310**, 457-459 (2003).
  207. C. Kang, I. H. Maeng, S. J. Oh, J.-H. Son, T.-I. Jeon, K. H. An, S. C. Lim, and Y. H. Lee, "Frequency-dependent optical constants and conductivities of hydrogen-functionalized single-walled carbon nanotubes," *Applied Physics Letters* **87**, 041908 (2005).
  208. T. Kampfrath, L. Perfetti, K. von Volkmann, C. M. Aguirre, P. Desjardins, R. Martel, C. Frischkorn, and M. Wolf, "Optical response of single-wall carbon nanotube sheets in the far-infrared spectral range from 1 THz to 40 THz," *physica status solidi (b)* **244**, 3950-3954 (2007).
  209. R. R. Hartmann, J. Kono, and M. E. Portnoi, "Terahertz science and technology of carbon nanomaterials," *Nanotechnology* **25**, 322001 (2014).
  210. G. A. Niklasson, C. G. Granqvist, and O. Hunderi, "Effective medium models for the optical properties of inhomogeneous materials," *Applied Optics* **20**, 26-30 (1981).
  211. J. C. M. Garnett, "Colours in Metal Glasses and in Metallic Films," *Philosophical Transactions of the Royal Society of London A: Mathematical, Physical and Engineering Sciences* **203**, 385-420 (1904).
  212. O. Levy and D. Stroud, "Maxwell Garnett theory for mixtures of anisotropic inclusions: Application to conducting polymers," *Physical Review B* **56**, 8035-8046 (1997).
  213. J. I. Gittleman and B. Abeles, "Comparison of the effective medium and the Maxwell-Garnett predictions for the dielectric constants of granular metals," *Physical Review B* **15**, 3273-3275 (1977).
  214. T.-I. Jeon, J.-H. Son, K. H. An, Y. H. Lee, and Y. S. Lee, "Terahertz absorption and dispersion of fluorine-doped single-walled carbon nanotube," *Journal of Applied Physics* **98**, 34316-34316 (2005).
  215. J. Kim, I. Maeng, J. Jung, H. Song, J.-H. Son, K. Kim, J. Lee, C.-H. Kim, G. Chae, M. Jun, Y. Hwang, S. Jeong Lee, J.-M. Myoung, and H. Choi, "Terahertz time-domain measurement of non-Drude conductivity in silver nanowire thin films for transparent electrode applications," *Applied Physics Letters* **102**, 011109 (2013).
  216. W.-L. Song, M.-S. Cao, M.-M. Lu, S. Bi, C.-Y. Wang, J. Liu, J. Yuan, and L.-Z. Fan, "Flexible graphene/polymer composite films in sandwich structures for effective electromagnetic interference shielding," *Carbon* **66**, 67-76 (2014).
  217. M. V. Shuba, A. V. Melnikov, A. G. Paddubskaya, P. P. Kuzhir, S. A. Maksimenko, and C. Thomsen, "Role of finite-size effects in the microwave and subterahertz electromagnetic response of a multiwall carbon-nanotube-based composite: Theory and interpretation of experiments," *Physical Review B* **88**, 045436 (2013).
  218. H. Nishimura, N. Minami, and R. Shimano, "Dielectric properties of single-walled carbon nanotubes in the terahertz frequency range," *Applied Physics Letters* **91**, 011108 (2007).

219. S. A. Maksimenko, G. Y. Slepian, M. V. Shuba, and A. Lakhtakia, "Terahertz and sub-terahertz responses of finite-length multiwall carbon nanotubes," in *Electrical Design of Advanced Packaging and Systems Symposium (EDAPS), 2011 IEEE*, 2011), 1-4.
220. J. Macutkevic, D. Seliuta, G. Valusis, R. Adomavicius, A. Krotkus, P. Kuzhir, A. Paddubskaya, S. Maksimenko, V. Kuznetsov, I. Mazov, and I. Simonova, "Multi-walled carbon nanotubes/PMMA composites for THz applications," *Diamond and Related Materials* **25**, 13-18 (2012).
221. A. D. Jameson, J. W. Kevek, J. L. Tomaino, M. Hemphill-Johnston, M. J. Paul, M. Koretsky, E. D. Minot, and Y.-S. Lee, "Terahertz spectroscopy of Ni-Ti alloy thin films," *Applied Physics Letters* **98**, 221111 (2011).
222. Y. Zhu, Y. Zhao, M. Holtz, Z. Fan, and A. A. Bernussi, "Effect of substrate orientation on terahertz optical transmission through VO<sub>2</sub> thin films and application to functional antireflection coatings," *Journal of the Optical Society of America B* **29**, 2373-2378 (2012).
223. G. K. P. Ramanandan, G. Ramakrishnan, and P. C. M. Planken, "Oxidation kinetics of nanoscale copper films studied by terahertz transmission spectroscopy," *Journal of Applied Physics* **111**, 123517 (2012).
224. C.-S. Yang, C.-H. Chang, M.-H. Lin, P. Yu, O. Wada, and C.-L. Pan, "THz conductivities of indium-tin-oxide nanowhiskers as a graded-refractive-index structure," *Optics Express* **20**, A441-A451 (2012).
225. Y. Minami, J. Takeda, T. D. Dao, T. Nagao, M. Kitajima, and I. Katayama, "Nonlinear electron dynamics of gold ultrathin films induced by intense terahertz waves," *Applied Physics Letters* **105**, 241107 (2014).
226. H. Ehrenreich and H. R. Philipp, "Optical Properties of Ag and Cu," *Physical Review* **128**, 1622-1629 (1962).
227. J. P. Marton and B. D. Jordan, "Optical properties of aggregated metal systems: Interband transitions," *Physical Review B* **15**, 1719-1727 (1977).
228. M. A. Ordal, L. L. Long, R. J. Bell, S. E. Bell, R. R. Bell, R. W. Alexander, and C. A. Ward, "Optical properties of the metals Al, Co, Cu, Au, Fe, Pb, Ni, Pd, Pt, Ag, Ti, and W in the infrared and far infrared," *Applied Optics* **22**, 1099-1119 (1983).

# 11. Appendices

---

---

Some theories and few matlab codes used in the thesis are described below.

## 11.1. Kramers Kronig relation

This relation states that if  $\tilde{\chi}(\omega) = \chi_1(\omega) + i\chi_2(\omega)$ , is a complex function of a complex variable  $\omega$  and  $\chi_1(\omega)$  and  $\chi_2(\omega)$  real then the real and imaginary part of the complex function  $\tilde{\chi}(\omega)$  is related to each other according to the following equations;

$$\chi_1(\omega) = \frac{1}{\omega} \mathbb{P} \int_{+\infty}^{-\infty} \frac{\chi_2(\acute{\omega})}{\acute{\omega} - \omega} d\acute{\omega},$$
$$\chi_2(\omega) = -\frac{1}{\omega} \mathbb{P} \int_{+\infty}^{-\infty} \frac{\chi_1(\acute{\omega})}{\acute{\omega} - \omega} d\acute{\omega},$$

Where  $\mathbb{P}$  denotes the Cauchy principle value. So, the real and imaginary part of such a complex function are not independent and one of the part can be reconstructed from the other part.

## 11.2. Transmittance Calculation

---

---

### MATLAB Program 1: Transmittance Calculation

```
% Calculation of Transmittance and Its Plotting%
clearvars
ref1 = dlmread('test2_air_Hole_N2_001', '\t', 0, 0);
ref2 = dlmread('test2_air_Hole_N2_001', '\t', 0, 0);
ref3 = dlmread('test4_air_Hole_N2_001', '\t', 0, 0);
sample1= dlmread('test4_Silicon_Hole_N2_002', '\t', 0, 0);
sample2= dlmread('test4_Silicon_Hole_N2_002', '\t', 0, 0);
sample3= dlmread('test4_Silicon_Hole_N2_003', '\t', 0, 0);
data1=(ref1+ref2+ref3)/3;
data2=(sample1+sample2+sample3)/3;
ntime=data1(1:200,1);
ampref=data1(1:200,2);%Average Reference Data%
ampsample=data2(1:200,2);%Average Sample Data%
fs=1/(0.1146*1e-12);%Frequency Resolution%
L=length(ntime);
NFFT = 2^nextpow2(L);
```

```

REF = fft(ampref,NFFT);%Fast Fourier Transform%
SAMPLE =fft(ampsample,NFFT);
f1= ((fs*(0:NFFT/2+1)/NFFT)');
f = ((fs*(0:NFFT/2+1)/NFFT)/1e12)'; %THz Frequency%
L2=length(f);
REFmag=abs(REF);
REFmag=smooth(REFmag,0.05,'loess');
SAMPLEmag=abs(SAMPLE);
SAMPLEmag=smooth(SAMPLEmag,0.05,'loess');
T=abs((SAMPLE(1:NFFT/2)./REF(1:NFFT/2))).^2;%Transmittance or
simplified Transfer Function%
plot(f(10:64),T(10:64),'--k','LineWidth',4)
title('Transmittance of Silicon Substrate')
xlabel('Frequency (THz)')
ylabel('Transmittance')

```

---

## 11.3. Analysis of THz Polarizer

---

### MATLAB Program 2: Analysis of THz Polarizer

```
%Analysis of a Polarizer%
clearvars
ref1 = dlmread('test4_PVA_hole_N2_002','\t',0,0);
ref2 = dlmread('test4_PVA_hole_N2_002','\t',0,0);
ref3 = dlmread('test4_PVA_hole_N2_002','\t',0,0);
samp1_0 = dlmread('test3_NiNW_parallel_hole_N2_001','\t',0,0);
samp2_0 = dlmread('test3_NiNW_parallel_hole_N2_001','\t',0,0);
samp3_0 = dlmread('test3_NiNW_parallel_hole_N2_001','\t',0,0);
samp1_90 = dlmread('test3_NiNW_perpendicular_hole_N2_002','\t',0,0);
samp2_90 = dlmread('test3_NiNW_perpendicular_hole_N2_002','\t',0,0);
samp3_90 = dlmread('test3_NiNW_perpendicular_hole_N2_002','\t',0,0);
ntime=ref1(1:511,1);
ampref = (ref1(1:511,2)+ref2(1:511,2)+ref3(1:511,2))/3;
ampsamp_0 = ((samp1_0(1:511,2)+samp2_0(1:511,2)+samp3_0(1:511,2))/3);
ampsamp_90 = ((samp1_90(1:511,2)+samp2_90(1:511,2)+samp3_90(1:511,2))/3);
fs=1/(0.1146*1e-12);
NFFT = length(ntime)+1;
REF = fft(ampref,NFFT);
SAMP_0 =fft(ampsamp_0,NFFT);
SAMP_90 =fft(ampsamp_90,NFFT);
f = ((fs*(0:NFFT/2-1)/NFFT)/1e12)';%Frequency%
T_0 = smooth(((abs((SAMP_0(1:NFFT/2)./REF(1:NFFT/2))))).^2),0.2,'rloess');
T_90 = smooth(((abs((SAMP_90(1:NFFT/2)./REF(1:NFFT/2))))).^2),0.2,'rloess');
A_0 = -10*log10(T_0);%Parallel Absorption%
A_90 = -10*log10(T_90);%Perpendicular Absorption%
LD=A_0-A_90; %Linear Dicroism%
A_tot=(A_0+2.*A_90./3);
LDR=LD./A_tot;%Reduced Linear Dicroism%
DOP=(A_0-A_90)./(A_0+A_90);%Degree of Polarization%
ER=-10*log10(T_90./T_0);%Extinction Ratio%
subplot(1,2,1)
plot(f(7:142,1),T_0(7:142,1),':',f(7:142,1),T_90(7:142,1),'x');
Title('Transmittence')
subplot(1,2,2)
plot(f(7:142,1),DOP(7:142,1));
Title('Degree of Polarization')
```

---

## 11.4. Shielding Analysis

---

### MATLAB Program 3: Shielding Analysis

```
%Analysis of Shielding%
clearvars
ref1 = dlmread('test6_air_N2_001','\t',0,0);
ref2 = dlmread('test6_air_N2_002','\t',0,0);
ref3 = dlmread('test6_air_N2_003','\t',0,0);
sample1= dlmread('test6_4mgSWNT_N2_001','\t',0,0);
sample2= dlmread('test6_4mgSWNT_N2_002','\t',0,0);
sample3= dlmread('test6_4mgSWNT_N2_003','\t',0,0);
data1=(ref1+ref2+ref3)/3;
data2=(sample1+sample2+sample3)/3;
ntime=data1(1:511,1);
ampref=data1(1:511,2);%Reference Amplitude%
ampsample=data2(1:511,2);%Sample Amplitude%
fs=1/(0.1125*1e-12);
L=length(ntime);
NFFT = 2^nextpow2(L);
REF = fft(ampref,NFFT);
SAMPLE =fft(ampsample,NFFT);
f1= ((fs*(0:NFFT/2+1)/NFFT))';
f = ((fs*(0:NFFT/2+1)/NFFT)/1e12)';
L2=length(f);
REFmag=abs(REF);
REFmag=smooth(REFmag,0.05,'loess');
SAMPLEmag=abs(SAMPLE);
SAMPLEmag=smooth(SAMPLEmag,0.05,'loess');
T=abs((SAMPLE./REF)).^2;%Transmittance%
SE=-10*log10(T(18:157));%Total Shielding%
filename = '4mgSWNT_D=306';
ext='.csv';
data = xlsread(strcat(filename,ext));
thick=306*10^-6;%Thickness of the Sample%
neu1=data(:,1);
neu=data(:,1)/1e12;
omega=2*pi*neu;
wavelength=((3.*10.^8)./neu1);%wavelength in m%
e1=data(:,11);%Real Dielectric Constant%
e2=data(:,12);%Imaginary Dielectric Constant%
SE1=interp1(f(18:157),SE,neu);
D=e2./e1;
alpha=((2.*pi)./wavelength).*(sqrt(e1.*(sqrt((1+D.*D))-1)./2));
alpha1=((2.*pi)./wavelength).*(sqrt(e1.*(sqrt((1+D.*D))+1)./2));
e=(e1+1i*e2);
ein=1.00;
e0=8.854;
ep=e0.*e;
```

---

```

A=sqrt(2.*pi.*neu1.*4.*pi.*10.^-7);
con=(1i.*e0.*omega.*(ein-e));
real_con=e0.*omega.*e2;
del=(sqrt(sqrt(1+(omega.*ep./con).^2)+(omega.*ep./con)).*sqrt(2./(om
ega.*con.*4.*pi.*10^5)));
gamma=alpha+1i.*alpha1;
n=sqrt(e1+1i.*e2);
k=(imag(n))./(omega.*10.^12);
B=(1-n.*n)./(1+n.*n);
SEA=real(8.68.*thick.*alpha);%Absorption%
SER=20.*log10((abs(1+n).^2)./abs(4.*n));%Reflection%
SEMIR=20.*log10(abs((1-((1-n).^2./(1+n).^2).*(exp(-
2.*alpha.*thick)))));%Multiple Internal Reflection%
SET=SEA+SER+SEMIR;%Total Shielding%
plot(neu,SE1,'go',neu,SET,'--k','LineWidth',2)

```

---

## 11.5. Universal Di-electric Relaxation Model

---

### MATLAB Program 4: UDR Model

```
%UDR Model%
clearvars
filename = '4mgSWNT_long_D=315'
ext='.csv';
data = xlsread(strcat(filename,ext));
neu=data(1:110,1)/1e12;
omega=2*pi*neu;
e1=data(1:110,11);%Real Dielectric Function%
e2=data(1:110,12);%Imaginary Dielectric Function%
err_e1=data(1:110,28);
e0=8.854;
real_con=e0.*omega.*e2;%Real Conductivity%
a0=[1,10,3];
opt=optimset('GradObj','on','TolX',1e-
15,'MaxIter',4000,'MaxFunEvals',10000);
[a,fval,exitflag,output]=fminsearch(@UDR,a0,opt,neu,real_con);
fit1=a(1)+a(2).*(2.*pi.*neu).^a(3);
subplot(1,1,1);
plot(neu,real_con,'go',neu,fit1,'--k','LineWidth',2)
Title('Real Conductivity')
```

### UDR Function

```
function f = UDR(a0,neu,real_con)
f = sum((real_con-(a0(1)+a0(2).*(2.*pi.*neu).^a0(3))).^2);
```

---

## 11.6. Thin Film Conductivity

---

### MATLAB Program 5: Thin Film Conductivity

```
%Thin Film Conductiity%
clearvars
ref1 = dlmread('test2_air_hole_N2_Si_001','\t',0,0);
ref2 = dlmread('test2_air_hole_N2_Si_001','\t',0,0);
ref3 = dlmread('test2_air_hole_N2_Si_001','\t',0,0);
sample1= dlmread('test2_Cu(0hour)_hole_N2_001','\t',0,0);
sample2= dlmread('test2_Cu(0hour)_hole_N2_001','\t',0,0);
sample3= dlmread('test2_Cu(0hour)_hole_N2_001','\t',0,0);
data1=(ref1+ref2+ref3)/3;
data2=(sample1+sample2+sample3)/3;
ntime=data1(1:200,1);
ampref=data1(1:200,2);
ampsample=data2(1:200,2);
fs=1/(0.1146*1e-12);
L=length(ntime);
NFFT = 2^nextpow2(L);
REF = fft(ampref,NFFT);
SAMPLE =fft(ampsample,NFFT);
f1= ((fs*(0:NFFT/2+1)/NFFT))';
f = ((fs*(0:NFFT/2+1)/NFFT)/1e12)';
L2=length(f);
REFmag=abs(REF);
REFmag=smooth(REFmag,0.05,'loess');
SAMPLEmag=abs(SAMPLE);
SAMPLEmag=smooth(SAMPLEmag,0.05,'loess');
subplot(2,2,1); plot(ntime(1:L,1),ampref(1:L,1),'-
',ntime(1:L,1),ampsample(1:L,1),':')
xlabel('Time(ps)')
ylabel('amplitude(a.u.)')
title('Time Domain Data')
subplot(2,2,2); semilogy(f(1:L2,1),REFmag(1:L2,1),'-
',f(1:L2,1),SAMPLEmag(1:L2,1),':')
title('Frequency Domain Data')
xlabel('Frequency(THz)')
ylabel('FFTamplitude')
T1=(SAMPLE./REF);
T = abs(T1).^2;%Transmittance or simplified Transfer Function%
SE=-10*log10(T);
subplot(2,2,3); plot(f(8:70,1),T(8:70,1))
title('Shielding Effectiveness')
xlabel('Frequency(THz)')
ylabel('SE')
nsub=3.418+1i*0.03;
d=20*10^-9;
A=(1+nsub)./T1;
```

```
B=A-1-nsub;
sigma2 = (((1+nsub)./(T1))-1-nsub)./(377.*d);
sigmare=real(sigma2);
sigmaim=imag(sigma2);
sigma=smooth(sigma2,0.05,'loess');
subplot(2,2,4);plot(f(8:100,1),sigmare(8:100,1),'b',f(8:100,1),sigma
im(8:100,1),'r')
title('Complex Conductivity')
xlabel('Frequency(THz)')
ylabel('Real and Imaginary Conductivity')
```

---